

AFAL-TR-75-119

12

ADA 023257

ANALYSES OF VARIOUS PERIODIC SLOT ARRAY GEOMETRIES USING MODAL MATCHING

THE OHIO STATE UNIVERSITY
COLUMBUS, OHIO

FEBRUARY 1976



TECHNICAL REPORT AFAL-TR-75-119
INTERIM REPORT FOR PERIOD 1 JANUARY 1975 -- 31 JULY 1975

Approved for public release; distribution unlimited

AIR FORCE AVIONICS LABORATORY
AIR FORCE WRIGHT AERONAUTICAL LABORATORIES
Air Force Systems Command
Wright-Patterson Air Force Base, Ohio 45433

DDC
RECEIVED
APR 20 1976
RECEIVED
E

1. 2. 3.

When Government drawings, specifications, or other data are used for any purpose other than in connection with a definitely related Government procurement operation, the United States Government thereby incurs no responsibility nor any obligation whatsoever; and the fact that the government may have formulated, furnished, or in any way supplied the said drawings, specifications, or other data, is not to be regarded by implication or otherwise as in any manner licensing the holder or any other person or corporation, or conveying any rights or permission to manufacture, use, or sell any patented invention that may in any way be related thereto.

This report has been reviewed by the Information Office (OI) and is releasable to the National Technical Information Service (NTIS). At NTIS, it will be available to the general public, including foreign nations.

This technical report has been reviewed and is approved for publication.

LARRY E. CARTER
LARRY E. CARTER
Program Monitor

William F. Bahret
WILLIAM F. BAHRET
Actg Chief, Passive ECM Branch
Electronic Warfare Division

FOR THE DIRECTOR

Ollie H. Edwards
OLLIE H. EDWARDS
Colonel, USAF
Chief, Electronic Warfare Div

Copies of this report should not be returned unless return is required by security considerations, contractual obligations, or notice on a specific document.

ADDITION FOR

NTIS	WALLS C. 1981	<input checked="" type="checkbox"/>
DOC	BJH 1981	<input type="checkbox"/>
UNIV. OF CALIF.		<input type="checkbox"/>
JULY 1981		

BY

LIBRARY AVAILABILITY UNIT

U.S. DEPARTMENT OF COMMERCE

A

UNCLASSIFIED

SECURITY CLASSIFICATION OF THIS PAGE (When Data Entered)

REPORT DOCUMENTATION PAGE		READ INSTRUCTIONS BEFORE COMPLETING FORM
1. REPORT NUMBER AFAL-TR-75-119	2. GOVT ACCESSION NO.	3. RECIPIENT'S CATALOG NUMBER
4. TITLE (and Subtitle) ANALYSES OF VARIOUS PERIODIC SLOT ARRAY GEOMETRIES USING MODAL MATCHING		5. TYPE OF REPORT & PERIOD COVERED 1 Jan 75 - 31 Jul 75 Interim Report
7. AUTHOR(s) R. J. Luebbers		6. PERFORMING ORG. REPORT NUMBER ESL-3622-4
9. PERFORMING ORGANIZATION NAME AND ADDRESS The Ohio State University ElectroScience Lab. Department of Electrical Engineering Columbus, Ohio 43212		8. CONTRACT OR GRANT NUMBER(s) F33615-73-C-1173
11. CONTROLLING OFFICE NAME AND ADDRESS Air Force Avionics Laboratory, Air Force Systems Command, Wright-Patterson Air Force Base Ohio 45433		10. PROGRAM ELEMENT, PROJECT, TASK AREA & WORK UNIT NUMBERS Project 7633
14. MONITORING AGENCY NAME & ADDRESS (if different from Controlling Office)		12. REPORT DATE February 1976
		13. NUMBER OF PAGES 242
		15. SECURITY CLASS (of this report) UNCLASSIFIED
		15a. DECLASSIFICATION/DOWNGRADING SCHEDULE
16. DISTRIBUTION STATEMENT (of this Report) Approved for public release; distribution unlimited.		
17. DISTRIBUTION STATEMENT (of the abstract entered in Block 20, if different from Report)		
18. SUPPLEMENTARY NOTES		
19. KEY WORDS (Continue on reverse side if necessary and identify by block number) Modal analysis Metallic radome Periodic slot arrays Resonant slot surface Frequency selective surface Resonant dipole surface		
20. ABSTRACT (Continue on reverse side if necessary and identify by block number) A ground plane pierced periodically with resonant slots can, with proper design, transmit an incident plane wave with no loss at its resonant frequency but with loss at all other frequencies. Such a structure is known variously as a periodic slot array or as a resonant window. These structures have application as radomes and in dual frequency antenna feeds.		

UNCLASSIFIED

SECURITY CLASSIFICATION OF THIS PAGE (When Data Entered)

20.

In this work the properties of such structures are examined theoretically using a modal matching type of computer solution. Extensive experimental confirmation of the calculated results are included. Various types of resonant windows are analyzed, including 1) those fabricated from finitely thick metal screens, 2) those with various slot shapes, including rectangular and various transmission line loaded slots and 3) biplanar resonant windows. The above solutions include the effects of planar dielectric layers on one or both sides of the slot array. In conjunction with the investigation of thick arrays, the problem of a thick, rectangular resonant (pressure) window in a rectangular waveguide is solved, with extensive experimental verification of the results.

As a result of these numerical and experimental investigations various parameters of resonant window design are now more fully understood. Some of these parameters are: 1) Effects of panel thickness on resonance frequency, bandwidth, and incidence angle properties; 2) reduction of bandwidth changes with incidence angle through dielectric matching layers; 3) the effect of dielectric layers on the Wood's anomaly null frequencies, i.e., "blind angles" in resonant surfaces; 4) the interactions between dielectric loading and panel thickness; 5) cross polarization losses in certain loaded slot elements; 6) higher order resonances, and 7) dielectric filling of biplanar slot arrays. In conjunction with these parameter investigations several improved resonant window designs have been developed, with special emphasis on thick panel designs.

UNCLASSIFIED

SECURITY CLASSIFICATION OF THIS PAGE (When Data Entered)

FOREWORD

This report, Ohio State University Research Foundation Report No. 3622-4, was prepared by the ElectroScience Laboratory, Department of Electrical Engineering, The Ohio State University at Columbus, Ohio. Research was conducted under Contract F33615-73-C-1173 of the Air Force Avionics Laboratory, Air Force Wright Aeronautical Laboratories at Wright-Patterson Air Force Base, Ohio. Mr. L. E. Carter, AFAL/WRP was the AFAL Program Monitor for this research conducted under Project 7633. This report was submitted to the sponsor on 15 May 1975.

The author's advisor, Professor L. Peters, Jr., deserves special thanks for his guidance during the initial phases of this research, for his help in the development and organization of the material, and for his critical review during the preparation of this report.

This report could not have reached its present form without the helpful discussions, comments and suggestions of Professor B. A. Munk, which have been incorporated throughout. His insight into the various phenomena encountered was a great aid in the course of the work, and most especially so during his final review of the manuscript.

Finally, two other persons should be mentioned as having been influential on this work: Professor E. M. Kennaugh, for his thought-provoking questions during the very early stages, and Professor Jack H. Richmond for his critical review of the final manuscript.

The material contained in this report is also used as a dissertation submitted to the Department of Electrical Engineering, The Ohio State University as partial fulfillment for the degree Doctor of Philosophy.

TABLE OF CONTENTS

Chapter		Page
I	INTRODUCTION.....	1
	A. Resonant Reflectors and Resonant Windows	2
	B. Woods Anomaly and Grating Lobes	4
	C. Bandwidth vs. Incidence Angle	6
	D. Bandwidth vs. Array Spacing	6
	E. Resonant Frequency vs. Incidence Angle	9
	F. Comparison of the Various Types of Tuned Elements	9
	G. Biplanar Resonant Surfaces	22
	H. Discussion of Various Tuned Radome Configurations	22
	I. Methods of Analysis	29
II	RECTANGULAR WAVEGUIDE WINDOWS.....	31
	A. Modal Analysis Solution	31
	B. Finite Conductivity	48
	C. The Effect of Plate Thickness on Babinet's Principle	63
	D. Conclusions	64
III	MODAL EXPANSIONS.....	67
	A. Floquet Modes	67
	B. Internal Slot Modes	88
IV	THICKNESS AND DIELECTRIC EFFECTS.....	97
	A. Thick Panel Solution	98
	B. Convergence Properties of the Modal Solution	106
	C. Thin Arrays Covered with Dielectric Slabs	113
	D. Dielectric Layers and Wood's Anomaly	123
	E. The Brick Array and Wood's Anomaly	131
	F. Thick Slots Filled With Dielectric	135
	G. Thickness - Dielectric Interactions	141
V	THIN LOADED SLOT ARRAYS.....	146
	A. Derivation of Moment Method Solution	146
	B. Single Loaded Slots	153
	C. 4-legged Symmetric Slots	161
	D. 3-legged Symmetric Slots	173

Chapter		Page
VI	BIPLANAR SLOT ARRAYS.....	185
	A. Derivation of Solution	185
	B. Biplanar Arrays Without Dielectric Layers	195
	C. Dielectric Covered Biplanar Arrays	200
VII	SUMMARY.....	217
Appendix		
A	WAVEGUIDE MEASUREMENT OF EQUIVALENT IMPEDANCE.....	218
B	EVALUATION OF MODAL INTEGRATIONS.....	220
BIBLIOGRAPHY.....		238

LIST OF ILLUSTRATIONS

Figure		Page
1-1	Physical geometry and plane wave reflection coefficient curve for a resonant dipole array.....	2
1-2	Physical geometry and plane wave transmission coefficient curve for a resonant slot array.....	3
1-3	Wood's anomaly in a resonant slot array: a) Geometry of slot array. b) Plane wave incident at angle θ . c) Resonance curve showing Wood's anomaly.....	5
1-4	Measured transmission coefficient curves for an array of transmission line loaded slots for various E-plane incidence angles. The slots are 4-legged symmetric slots (Fig. 1-7e) spaced 1 cm apart.....	7
1-5	Measured transmission coefficient curves for an array of transmission line loaded slots for various H-plane incidence angles. The slots are 4-legged symmetric slots (Fig. 1-7e) spaced 1 cm apart.....	8
1-6	Calculated transmission for an array of rectangular slots illustrating the shift of the resonance frequency with incidence angle (H-plane incidence).....	10
1-7	Various types of tuned elements used in resonant surfaces: a) Flat dipole (rectangular slot). b) Circular disk (circular slot, circular hole). c) Loop (annular slot). d) Singly loaded dipole (slot). e) 4-legged symmetrically loaded dipole (slot). f) 3-legged loaded dipole (slot).....	11
1-8	Transmission coefficient curves for an array of annular slots for various incidence angles in the H-plane.....	12
1-9	Transmission coefficient curves for an array of annular slots for various incidence angles in the E-plane.....	13

Figure		Page
1-10	Computed transmission coefficients for an array of single-loaded slots for various E-plane incidence angles.....	14
1-11	Measured transmission curves showing the transmission loss at resonance for an array of loaded slots with H-plane incidence angles.....	15
1-12	Arrangement of single-loaded slots which eliminates cross polarized radiation for H-plane incidence angles.....	16
1-13	Measured transmission for an array of symmetric 4-legged loaded slots for various angles of incidence in the H-plane (b, c, and d are defined in Fig. 3-11).....	17
1-14	Effect of element design on bandwidth: a) A loaded element with a relatively wide bandwidth. b) The bandwidth is decreased by decreasing the width of the conductor. c) The bandwidth is further decreased by changing the shape of the element as shown.....	18
1-15	Measured H-plane transmission curves for an interlaced array of 4-legged loaded slots.....	19
1-16	Measured H-plane transmission curves for an array of 3-legged symmetric loaded slots.....	20
1-17	Measured E-plane transmission curves for an array of 3-legged symmetric loaded slots.....	21
1-18	Measured transmission curves for a biplanar slot array E-plane incidence. The two arrays are spaced 1.1 cm (0.33λ) apart.....	23
1-19	Measured transmission curves for a biplanar slot array H-plane incidence. The two arrays are spaced 1.1 cm (0.33λ) apart.....	24
1-20	Measured reflection curves for a single dipole array mounted on 1/32" thick dielectric material ($\epsilon_r=2.5$) for various incidence angles in the H-plane. The inset shows a full size section of the array.....	25

Figure		Page
1-21	Measured reflection curves for two dipole arrays of the type shown in Fig. 1-20 separated by $0.27 \lambda_0$, where $\lambda_0 = 3.2$ cm.....	26
1-22	Some possible configurations for tuned radomes: a) Thin film resonant window behind conventional radome. b) Thick metal radome. c) Multi-layer. d) Dielectric-resonant window sandwich.....	27
2-1	Geometry and coordinate system for a thick rectangular slot in a rectangular waveguide.....	32
2-2	Equivalent impedances for a thin slot.....	33
2-3	Equivalent impedances for a thick slot.....	36
2-4	Calculated and measured values of the equivalent impedance Z_{eq} for a 0.063" thick rectangular slot in a waveguide vs. frequency. Also shown are circles of Z_{eq} corresponding to transmission losses of 0.1, 0.5, 1.0, and 4.0 dB.....	42
2-5	Calculated and measured values of the transmission coefficient for a 0.063" thick rectangular slot in a waveguide vs. frequency.....	43
2-6	Calculated and measured values of the equivalent impedance Z_{eq} for a 0.125" thick rectangular slot in a waveguide vs. frequency.....	44
2-7	Calculated and measured values of the transmission coefficient for a 0.125" thick rectangular slot in a waveguide vs. frequency.....	45
2-8	Calculated and measured values of the equivalent impedance Z_{eq} for a 0.187" thick rectangular slot in a waveguide vs. frequency.....	46

Figure		Page
2-9	Calculated and measured values of the transmission coefficient for a 0.187" thick rectangular slot in a waveguide vs. frequency.....	47
2-10	Calculated and measured values of the equivalent impedance Z_{eq} for a 4.1" thick rectangular slot in a waveguide vs. frequency. Calculated values for both a lossless slot and a slot with finite conductivity are shown.....	50
2-11	Calculated and measured values of the equivalent impedance Z_{eq} for a 4.1" thick rectangular slot in a waveguide vs. frequency. This is a continuation of Fig. 2-10 and shows the second (longitudinal) resonance.....	52
2-12	Calculated values of the Transmission coefficient for lossy aluminum slots of various thicknesses vs. frequency.....	53
2-13	Calculated loss at resonance (3.5 GHz) vs. conductivity for a 0.5" thick rectangular slot in a waveguide.....	57
2-14	Calculated loss at resonance vs. resonance frequency for a 0.25" thick slot in a waveguide.....	58
2-15	Calculated values of the transmission coefficient vs. frequency for 0.125" wide rectangular slots of various thicknesses in a waveguide.....	59
2-16	Calculated values of the transmission coefficient vs. frequency for 0.87" wide rectangular slots of various thicknesses in a waveguide.....	60
2-17	Calculated values of the transmission coefficient vs. frequency for 0.2" wide rectangular slots of various thicknesses in a waveguide.....	61

Figure		Page
2-18	Calculated values of the transmission coefficient vs. frequency for 0.675" wide rectangular slots of various thicknesses in a waveguide.....	62
2-19	Calculated values of the transmission coefficient vs. frequency for very thin rectangular slots in a waveguide.....	63
2-20	Calculated values of the 3 dB bandwidth vs. slot thickness for a rectangular slot in a waveguide.....	65
2-21	Calculated values of the 3 dB bandwidth in λ vs. thickness in wavelengths for a rectangular slot in a waveguide.....	66
3-1	Geometry and coordinate system for a plane wave incident on a periodic slot array.....	68
3-2	Details of array geometry showing skewed coordinate system and periodic cell.....	69
3-3	Relationship between skewed coordinate system (S_1, S_2) and orthogonal (x, y) coordinate system.....	70
3-4	Grating lobe diagram for the array of Fig. 3-2 with $d_x = \lambda$. $T_x = \sin\theta \cos\phi$, $T_y = \sin\theta \sin\phi$	74
3-5	The unit periodic cell ABCD of Fig. 3-2 can be deformed to the shape GHIJ without affecting the orthogonality of the Floquet modes.....	75
3-6	Deformation of original periodic cell ABCD to the periodic cell GHIJ which includes only one slot.....	77
3-7	Slotted metal panel covered by dielectric with a plane wave incident. The different modes which may exist on the panel are illustrated schematically.....	79
3-8	Incident, reflected, and transmitted waves in the free space and dielectric regions.....	81

Figure		Page
3-9	Coordinates and dimensions used to express the single loaded slot modes.....	91
3-10	Coordinate system for expressing the approximate mode set for a narrow coaxial waveguide.....	93
3-11	Coordinates and dimensions for expressing the approximate mode set for the 4-legged symmetric loaded slot.....	95
3-12	Coordinates and dimensions for expressing the approximate mode set for the 3-legged loaded slot.....	96
4-1	Coordinates and dimensions for an array of slots in a thick metal panel covered with dielectric layers.....	97
4-2	A slot mode i excited when the incoming plane wave hits the panel at $z=0$ will excite other slot modes j, k, \dots , as well as mode i itself when it is reflected by the end of the slot at $z=-L$	100
4-3	Symmetric and anti-symmetric excitation of a slot in the array.....	101
4-4	Calculated curves (mutual impedance method) and measured points (from Munk, [3]) for the bistatic reflection coefficient for an array of dipoles; t is the thickness of the copper plates.....	107
4-5	Transmission curves for the slot array which is the complement of the dipole array of fig. 4-5 calculated using the modal analysis solution.....	108
4-6	Convergence data consisting of calculated transmission curves for an array of slots in a 0.0175 cm thick panel for near normal (1° E-plane) incidence vs. frequency. The slot mode index f has maximum values of 1, 3, 5, and 7 for the various curves. The number of Floquet modes is kept constant at 242.....	109

Figure		Page
4-7	Convergence data consisting of the transmission coefficient at 5 GHz for the array shown for various numbers of slot modes (f_{max}) vs. the number of Floquet modes; 80° H-plane incidence.....	111
4-8	Convergence data consisting of the transmission coefficient at 5 GHz for the array shown for various numbers of slot modes (only the odd modes are excited) vs. the number of Floquet modes; 80° E-plane incidence.....	112
4-9	Transmission coefficient vs. frequency for a slot array covered with varying thicknesses of dielectric material. Near normal ($\theta=1^\circ$, $\phi=90^\circ$) incidence.....	114
4-10	Calculated transmission coefficient curves for the slotted panel of Fig. 4-5 ($d_x=d_y=1.78$ cm, $a=1.32$ cm, $b=0.128$ cm, $\alpha=90^\circ$) covered on both sides by a dielectric layer 0.7 cm thick with $\epsilon_r=1.5$ in the dielectric layer and in the slot.....	116
4-11	Calculated transmission coefficient curves for the slotted panel of Fig. 4-5 ($d_x=d_y=1.78$ cm, $a=1.32$ cm, $b=0.128$ cm, $\alpha=90^\circ$) covered on both sides by a dielectric layer 0.7 cm thick with $\epsilon_r=2.6$ in the dielectric layer and in the slot.....	117
4-12	Calculated transmission coefficient curves for the slotted panel of Fig. 4-5 ($d_x=d_y=1.78$ cm, $a=1.32$ cm, $b=0.128$ cm, $\alpha=90^\circ$) covered on both sides by a dielectric layer 0.7 cm thick with $\epsilon_r=4.0$ in the dielectric layer and in the slot.....	119
4-13	Measured transmission curves for the dielectric coated array of Fig. 4-12.....	120
4-14	Calculated transmission coefficient curves for the slotted panel of Fig. 4-5 ($d_x=d_y=1.78$ cm, $a=1.32$ cm, $b=0.128$ cm, $\alpha=90^\circ$) covered on both sides by a dielectric layer 0.35 cm thick with $\epsilon_r=4.0$ in the dielectric layer and in the slot.....	121

Figure		Page
4-15	Measured transmission curves for the dielectric coated array of Fig. 4-14.....	122
4-16	Section of a dielectric covered slot array with a propagating grating lobe.....	124
4-17	The normalized surface wave null propagation constant vs. the dielectric thickness as calculated using 2 different methods; 1) full modal solution, 2) one Floquet mode. The dielectric thickness is measured in wavelengths (in the dielectric).....	126
4-18	Calculated transmission curves for the slot array shown using only the TE ₁₀ slot mode.....	132
4-19	Calculated transmission curves for the slot array of Fig. 4-18 but with 3 slot modes (TE ₁₀ , TE ₂₀ , TE ₃₀).....	134
4-20	Calculated transmission curves for an array of rectangular slots in a 0.1" thick metal panel ($\ell=.254$ cm). The slots are filled with dielectric of $\epsilon_r=5.0$ ($\epsilon_3=5\epsilon_0$).....	136
4-21	Measured transmission curves for a slot array chemically etched to approximate the design of Fig. 4-20. The slots were etched in a 0.1" thick aluminum panel and filled with Emerson and Cumming Stycast 35DA ($\epsilon_r=5$).....	138
4-22	Measured transmission curves for a slot array of the design used in Figs. 4-20 and 4-21 made using electrical discharge machining on a 0.1" thick aluminum panel. The slots are again filled with Emerson and Cumming Stycast 35DA ($\epsilon_r=5$).....	139
4-23	Calculated transmission curves for the array of Figs. 4-20 and 4-21 coated on both sides with a 0.635 cm thick dielectric layer with $\epsilon_r=1.5$ ($t=0.635$ cm, $\epsilon_1=1.5\epsilon_0$). The metal panel is 0.1" thick ($\ell=.254$ cm) and the slots are filled with dielectric of $\epsilon_r=5$ ($\epsilon_3=5\epsilon_0$).....	140
4-24	Calculated transmission curves for an array of rectangular slots in metallic panels of various thicknesses with no dielectric present.....	142

Figure		Page
4-25	Calculated transmission curves for the same slot arrays of Fig. 4-25 but with the slots filled with dielectric ($\epsilon_3=4\epsilon_0$).....	143
4-26	Calculated transmission curves for the same slot arrays of Figs. 4-24 and 4-25 but with a .159 cm thick dielectric layer on both sides of the array in addition to the dielectric material in the slots.....	145
5-1	Front and edge views of a periodic array of loaded slots covered by dielectric layers.....	147
5-2	Computed transmission coefficient curves using the mutual impedance method (Munk [3]) for an array of single loaded slots for various incidence angles in the E-plane ($\phi=90^\circ$) $\lambda=\lambda_1=0.38$ cm.....	154
5-3	Computed transmission curves using the modal matching solution for the loaded slot array of Fig. 5-2 for various E-plane incidence angles.....	155
5-4	Measured transmission curves showing the transmission loss at resonance for an array of loaded slots with H-plane ($\phi=0^\circ$) incidence.....	156
5-5	Calculated transmission curves for various incidence angles θ ($\phi=0^\circ$) for the single loaded slot array of Fig. 5-4.....	158
5-6	Measured transmission of the cross polarized radiation for the same loaded slot array of Figs. 5-4 and 5-5 for various incidence angles θ in the H-plane ($\phi=0^\circ$).....	159
5-7	Calculated transmission of the cross polarized radiation which corresponds to the measured curves of Fig. 5-6.....	160
5-8	Electric field polarities for the $n=1$ sine and cosine modes for the 4-legged symmetric loaded slot.....	161

Figure		Page
5-9	Electric field polarities for the $n=2$ sine and cosine modes for the 4-legged symmetric loaded slot.....	162
5-10	Calculated transmission curves for an array of 4-legged symmetric slots on a thin dielectric substrate ($t_2=0.072$ cm, $\epsilon_2=2.38\epsilon_0$; $t_1=0$), H-plane incidence.....	164
5-11	Measured transmission curves corresponding to the calculated curves of Fig. 5-10.....	165
5-12	Calculated transmission curves for an array of 4-legged symmetric slots on a thin dielectric substrate ($t_2=0.072$ cm, $\epsilon_2=2.38\epsilon_0$; $t_1=0$), E-plane incidence.....	166
5-13	Measured transmission curves corresponding to the calculated curves of Fig. 5-12.....	167
5-14	Calculated transmission curves for an array of 4-legged symmetric slots on a thin dielectric substrate ($t_2=0.072$ cm, $\epsilon_2=2.38\epsilon_0$; $t_1=0$), H-plane incidence. The frequency range includes the second resonance.....	169
5-15	Measured transmission curves corresponding to the calculated curves of Fig. 5-14.....	170
5-16	Calculated transmission curves for an array of 4-legged symmetric slots on a thin dielectric substrate ($t_2=0.072$ cm, $\epsilon_2=2.38\epsilon_0$; $t_1=0$), E-plane incidence. The frequency range includes the second resonance.....	171
5-17	Measured transmission curves corresponding to the calculated curves of Fig. 5-16.....	172
5-18	Calculated transmission curves for the array of Fig. 5-16 but with the even ordered cosine modes omitted.....	174
5-19	Calculated transmission curves for an array of 4-legged symmetric slots on a thin dielectric substrate, H-plane incidence.....	175

Figure		Page
5-20	Measured transmission curves corresponding to the calculated curves of Fig. 5-19.....	176
5-21	Electric field polarities for the $n=1$ sine and cosine modes for the 3-legged symmetric loaded slot.....	177
5-22	Calculated transmission curves for an array of 3-legged symmetric slots on a thin dielectric substrate ($t_2=0.08$ cm, $\epsilon_2=2.50\epsilon_0$; $t_1=0$), H-plane incidence ($\phi=90^\circ$).....	178
5-23	Measured transmission curves corresponding to the calculated curves of Fig. 5-22.....	179
5-24	Calculated transmission curves for an array of 3-legged symmetric slots on a thin dielectric substrate ($t_2=0.08$ cm, $\epsilon_2=2.5\epsilon_0$; $t_1=0$), E-plane incidence ($\phi=0^\circ$).....	180
5-25	Measured transmission curves corresponding to the calculated curves of Fig. 5-24.....	181
5-26	Calculated transmission curves for an array of 3-legged symmetric slots on a thin dielectric substrate ($t_2=0.08$ cm, $\epsilon_2=2.5\epsilon_0$; $t_1=0$), H-plane incidence ($\phi=0^\circ$).....	182
5-27	Measured transmission curves corresponding to the calculated curves of Fig. 5-26.....	183
6-1	Geometry and coordinates for a biplanar slot array: a) Typical geometry of one of the two thin slot arrays; b) arrangement of the two slot arrays to form a biplanar slot array.....	184
6-2	Transmission line model of the dielectric layers between the two slotted panels used to determine the modal impedance $Z_{0q}^{(2)}$ at the $z=0^-$ surface of the front panel.....	189
6-3	Calculated transmission curves for a biplanar array of 4-legged symmetric loaded slots. The two panels are separated 0.13 λ at resonance ($t_1=0.079$ cm, $\epsilon_1=2.56\epsilon_0$; $t_2=0$; $t_3=0.43$ cm, $\epsilon_3=\epsilon_0$).....	196

Figure		Page
6-4	Measured transmission curves corresponding to the calculated curves of Fig. 6-3.....	197
6-5	Calculated transmission curves for a biplanar array of 4-legged symmetric loaded slots. The two panels are separated 0.25λ at resonance ($t_1=0.079$ cm, $\epsilon_1=2.56\epsilon_0$; $t_2=0$; $t_3=0.83$ cm, $\epsilon_3=\epsilon_0$).....	198
6-6	Measured curves corresponding to the calculated curves of Fig. 6-5.....	199
6-7	Calculated transmission curves for a biplanar array of 4-legged symmetric loaded slots ($t_1=0.5$ cm, $\epsilon_1=4.0\epsilon_0$; $t_2=0$; $t_3=0.7$ cm, $\epsilon_3=1.9\epsilon_0$). These curves illustrate the bad performance which can result from a poorly designed dielectric covered biplanar array.....	201
6-8	Geometry of the biplanar array analyzed in the following series of calculated and measured curves: a) Grid arrangement for the 4-legged symmetric slots with dimensions $b=0.051$ cm, $c=0.32$ cm, $d=0.183$ cm. b) Arrangement of the dielectric layers showing $t_1=0.85$ cm, $\epsilon_1=1.5\epsilon_0$; $t_2=0.072$ cm, $\epsilon_2=2.38\epsilon_0$; and $t_3=0.556$ cm, $\epsilon_3=1.9\epsilon_0$	203
6-9	Calculated transmission curves for a biplanar array of 4-legged symmetric loaded slots arranged as shown in Fig. 6-8. E-plane incidence.....	204
6-10	Calculated transmission curves for the same biplanar array of Fig. 6-9 but with the relative dielectric constant of the t_2 substrate layer set equal to that of the t_3 center layer. E-plane incidence.....	205
6-11	Measured transmission curves corresponding to the calculated curves of Fig. 6-9.....	207
6-12	Calculated transmission curves for a biplanar array of 4-legged symmetric loaded slots arranged as shown in Fig. 6-8. H-plane incidence.....	208

Figure		Page
6-13	Measured transmission curves corresponding to the calculated curves of Fig. 6-12.....	209
6-14	Calculated transmission curves showing the second resonance for a biplanar array of 4-legged symmetric loaded slots arranged as shown in Fig. 6-8. E-plane incidence.....	210
6-15	Measured transmission curves corresponding to the calculated curves of Fig. 6-14.....	211
6-16	Calculated transmission curves showing the second resonance for a biplanar array of 4-legged symmetric loaded slots arranged as shown in Fig. 6-8. H-plane incidence.....	212
6-17	Measured transmission curves corresponding to the calculated curves of Fig. 6-16.....	213
6-18	Calculated transmission curves for a biplanar array of 4-legged symmetric loaded slots with d_x and d_y reduced to 1.2 cm to eliminate the passband null. $t_1=0.85$ cm, $\epsilon_1=1.5\epsilon_0$; $t_2=0$, $t_3=0.7$ cm, $\epsilon_3=1.9\epsilon_0$	215
6-19	Phase of transmission coefficient for a biplanar array. The curves marked "square" are for the biplanar array of Fig. 6-18. The curves marked "interlaced" are for the biplanar array of Fig. 6-18 but with the slots arranged in an interlaced grid, i.e., every other row of slots shifted right by $d_x/2$	216
A-1	Waveguide equipment used to measure the reflection coefficient and equivalent shunt impedance of a slot.....	219
B-1	Single loaded slot divided into linear regions by points P_1 through P_6	221

LIST OF TABLES

Table		Page
1	Calculated Losses at Resonance 1.68 x 0.0625 x λ Slot in S-Band W.G.	56
B-1	COMMON Inputs for Single Loaded Slot.....	227
B-2	COMMON Inputs for 4-legged Slots.....	228
B-3	COMMON Inputs for 3-legged Slots.....	229

CHAPTER I INTRODUCTION

The existence of a surface that, despite being composed primarily of metal, can transmit nearly all of the energy incident upon it suggests some very interesting applications. Among these is the radome application, where it appears possible to achieve improved operation over the present dielectric structures from both an electrical and mechanical point of view. The goal of this dissertation is to extend the analytic tools used in the study of such surfaces and to examine several new types of surfaces. The metallic radome developed by Pelton and described in [1,2] represents the state-of-the-art in metallic radomes as of 1973. Theoretical analyses, notably Munk's mutual impedance analysis [3], had previously been used to guide the experimental studies, but the intuition that had been developed through this analysis had suggested some novel designs (such as the radome indicated above) that at the time defied mathematical analysis. One of the goals of this dissertation is to extend the analytic techniques to "catch up" with the new designs. The need for such analytic tools lies in the requirement for a general design procedure for such surfaces, and an understanding of how and why they work.

Previous analytic studies of resonant windows have for the most part restricted their attention to thin surfaces where Babinet's principle could be applied. Another goal of this work was the development of analytic tools that would be applicable to thicker metallic resonant surfaces. Such structures composed of slots or holes of one form or another in a metallic surface also required the use of dielectric materials in the holes. Treatment of such dielectric filled slots is also incorporated in this analysis.

As a means of further improving metallic radomes Munk noted that dielectric layers placed on this resonant surface could lead to improved results [4]. An investigation into this phenomenon from two different viewpoints was initiated. The one reported in this work extends the modal analysis technique to obtain a solution. An alternate solution using a mutual impedance procedure has been pursued by Munk [5]. The two solutions complement one another in that the modal solution's strength is an analysis while the mutual impedance solution is more useful for design.

Primarily, then, this work is concerned with investigating several distinct new methods for designing better metallic radomes. However, before becoming involved in the specifics of individual cases and geometries, we shall devote some pages to a tutorial discussion of resonant periodic arrays in general.

A. Resonant Reflectors and Resonant Windows

There are two basic types of resonant surfaces; the resonant reflector and the resonant window. The resonant reflector is an array of resonant conducting elements which, with proper design, acts like a ground plane at its resonant frequency, but transmits varying amounts of power at other frequencies. A typical resonant reflector is shown in Fig. 1-1, along with a typical reflection coefficient curve for a

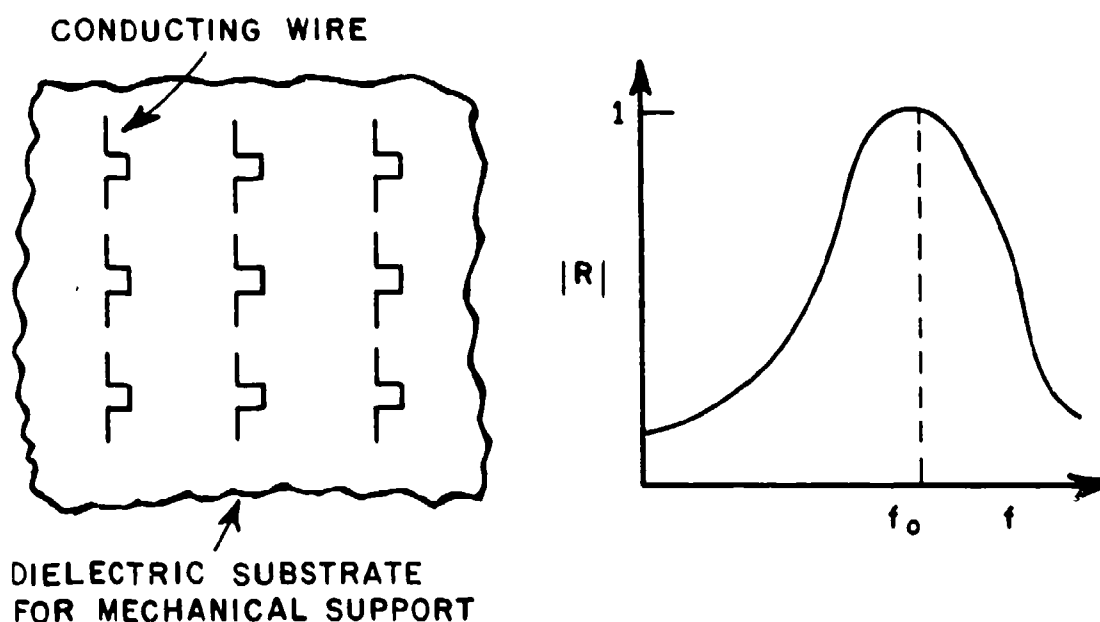


Figure 1-1.--Physical geometry and plane wave reflection coefficient curve for a resonant dipole array.

plane wave incident on the reflector. The dipoles are arranged in a periodic lattice. The field reflected by the resonant reflector is normalized to the field reflected by a flat plate of the same size. Thus the reflection coefficient curve actually represents the difference in the reflected field caused by replacing a ground plane with a resonant reflector of the same size, with the incident field unchanged. Although many applications require curved surfaces, it has been shown that the results obtained for flat panels are directly applicable to curved resonant arrays [2].

The resonant window is the complement of the resonant reflector. It is thus a resonant array of slots cut in a ground plane. With proper design, this resonant slot array will be transparent at its resonant frequency but will transmit varying amounts of power at other frequencies. A typical resonant slot array is shown in Fig. 1-2,

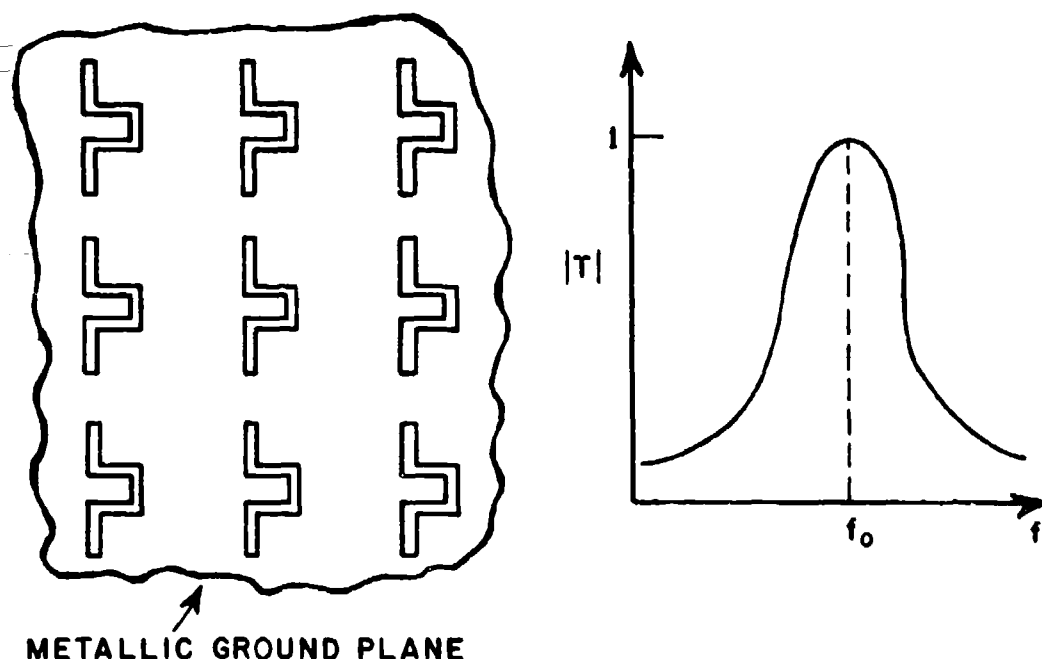


Figure 1-2.--Physical geometry and plane wave transmission coefficient curve for a resonant slot array.

along with a transmission coefficient curve. As with the resonant reflector, for a finite size window the transmission curve is obtained through a normalization process. For the resonant window the transmitted fields are normalized to the fields transmitted through an aperture of the same size as the resonant window, said aperture being in an infinite ground plane. Thus for a finite resonant slot array the transmission coefficient of Fig. 1-2 actually represents the difference between the fields transmitted through an aperture in a ground plane and the fields transmitted through the same aperture covered by the resonant slot array. In this work we are concerned primarily with resonant windows.

Both types have practical applications. Resonant reflectors have been used as components of dual frequency antenna feeds [6] and as lightweight parabolic antennas [7]. The resonant windows have their main application as radomes. The properties of these two devices are such that they no doubt are capable of much wider application.

As might be expected from examination of Fig. 1-1, the two types of resonant surfaces have many common properties. In fact, if we know the transmission coefficient of a slot array cut in an

infinitesimally thin, perfectly conducting ground plane, we can determine the reflection coefficient for complementary dipole array and vice versa, by applying Babinet's principle [8]. As applied here, Babinet's principle asserts that the transmission coefficient for a resonant slot array will be equal to the reflection coefficient for the complementary reflecting array provided that the \vec{E} field of the incident plane wave is rotated in space by 90° . While this applies exactly only for infinitesimally thin panels, it can be used to obtain good results for panels on the order of 0.001λ in thickness, λ being the free space wavelength (see Chapter II).

Now that we have established this basic relationship between slot and dipole arrays, let us investigate some of the properties which they have in common.

B. Woods Anomaly and Grating Lobes

Anyone concerned with designing these resonant surfaces of periodically placed dipoles or slots must be aware of a phenomenon known as Wood's anomaly. Wood's anomaly occurs when the phase delay between the currents or voltages on neighboring elements is $2n\pi$. An example is shown in Fig. 1-3 for a resonant surface with a rectangular lattice. In Fig. 1-3b it is evident that for a phase delay of $2n\pi$ radians between slot "a" and slot "b" we must have

$$(1-1) \quad d_x(1 \pm \sin\theta) = \pm n\lambda; \quad n=1,2,3,\dots$$

When the above condition is satisfied the transmission curve for a resonant window will have a null, i.e., total reflection will take place, as shown in Fig. 1-3c. Conversely, a resonant reflector will have a null in the reflection curve, i.e., total transmission will take place.

When the lattice is not rectangular, or when the incident angle is not in one of the cardinal planes, Eq. (1-1) does not apply and the determination of the Wood's anomaly frequency is somewhat more complicated (see Chapter III). However, a simple rule which always holds is that one can avoid Wood's anomaly for all incidence angles by keeping the spacing between elements less than $\lambda/2$. The rule must be modified in the presence of dielectric materials, since they can lower the null frequency as discussed in Chapter IV. For this situation the null is called a surface wave null, since it is caused by a propagating surface wave.

Another phenomenon connected with Wood's anomaly is the grating lobe onset. For frequencies below the frequency of the 1st Wood's anomaly null all of the energy scattered by the resonant surface

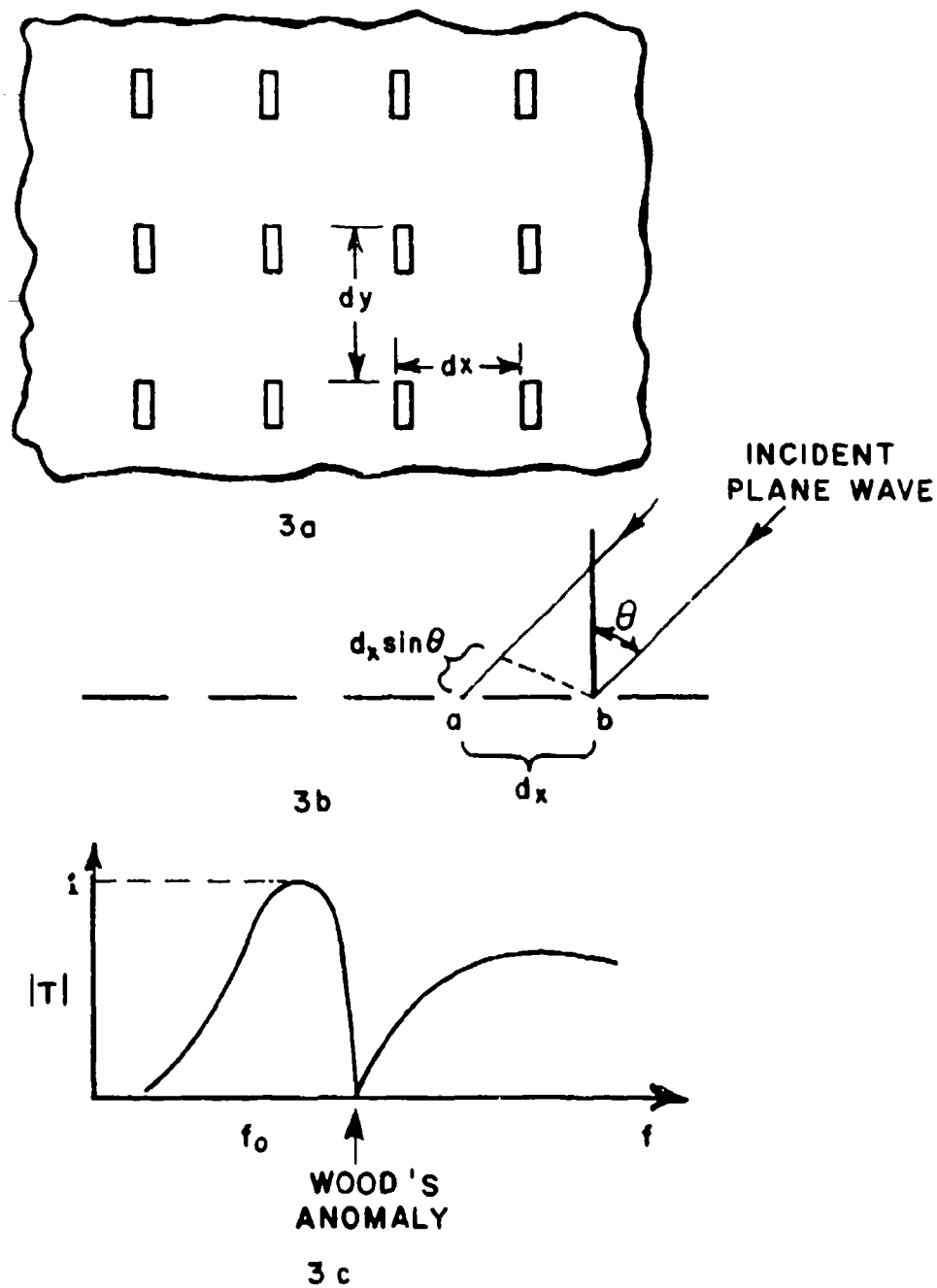


Figure 1-3.--Wood's anomaly in a resonant slot array:
a) Geometry of slot array.
b) Plane wave incident at angle θ .
c) Resonance curve showing Wood's anomaly

travels either straight through the resonant surface or else is reflected in the specular direction. However, at frequencies higher than the 1st Wood's anomaly null frequency the phasing between the currents or voltages on the elements is such that energy may propagate in other directions as well. These directions are called the grating lobe directions. Note in Fig. 1-3c that the transmission curve above the Wood's anomaly frequency shows a resonance, but does not attain a value of unity. This is because some of the energy is being radiated in the grating lobe directions.

C. Bandwidth vs. Incidence Angle

Suppose we have a resonant window whose transmission coefficient curve is as shown in Fig. 1-2 for a plane wave normally incident. This transmission curve will have a given bandwidth. Now further suppose that the incidence angle is changed so as to be at an angle θ in the E-plane, where E-plane incidence is defined so that the plane determined by the \vec{E} vector and the incident plane wave Poynting vector is perpendicular to the plane containing the resonant surface. As the angle θ is increased the bandwidth of the transmission curve is increased by approximately a factor of $1/\cos\theta$, with $\theta=0^\circ$ corresponding to normal incidence. For H-plane incidence, where the plane defined by the H-field vector and the incident plane wave Poynting vector is perpendicular to the plane containing the resonant surface, the bandwidth is decreased by a factor of $\cos\theta$. This behavior is illustrated by the curves in Figs. 1-4 and 1-5, which show the variation of bandwidth with incidence angle for an array of 4-legged loaded slots.

A resonant reflector has similar behavior. However, the bandwidth is increased by a factor of $1/\cos\theta$ for H-plane incidence and decreased by a factor of $\cos\theta$ for E-plane incidence.

D. Bandwidth vs. Array Spacing

The relationship between the interelement spacing (i.e., d_x and d_y of Fig. 1-3a) and the bandwidth of the resonant surface can be stated quite simply. The more closely packed the elements are the greater will be the bandwidth of the resonance curve. This relationship is true for both resonant reflectors and resonant windows; however, it is limited to cases where no grating lobes can propagate and where the elements are not touching one another.

If the interelement spacing d_x or d_y is reduced by $1/2$ the bandwidth of the resonant surface will approximately double. Thus, if both d_x and d_y are reduced by $1/2$ the resulting resonant surface will have a bandwidth approximately four times as large as the original.

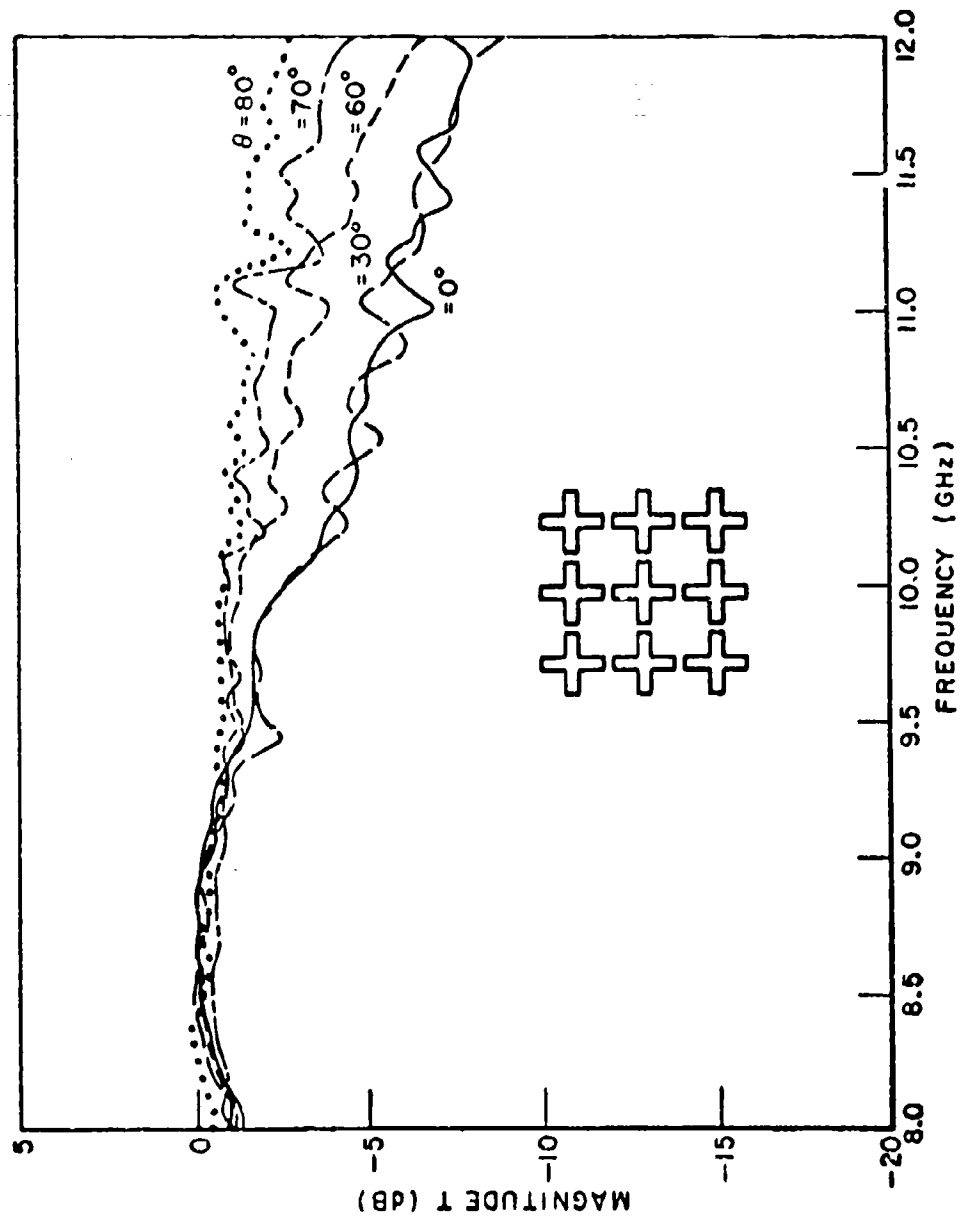


Figure 1-4.---Measured transmission coefficient curves for an array of transmission line loaded slots for various E-plane incidence angles. The slots are 4-legged symmetric slots (Fig. 1-7e) spaced 1 cm apart.

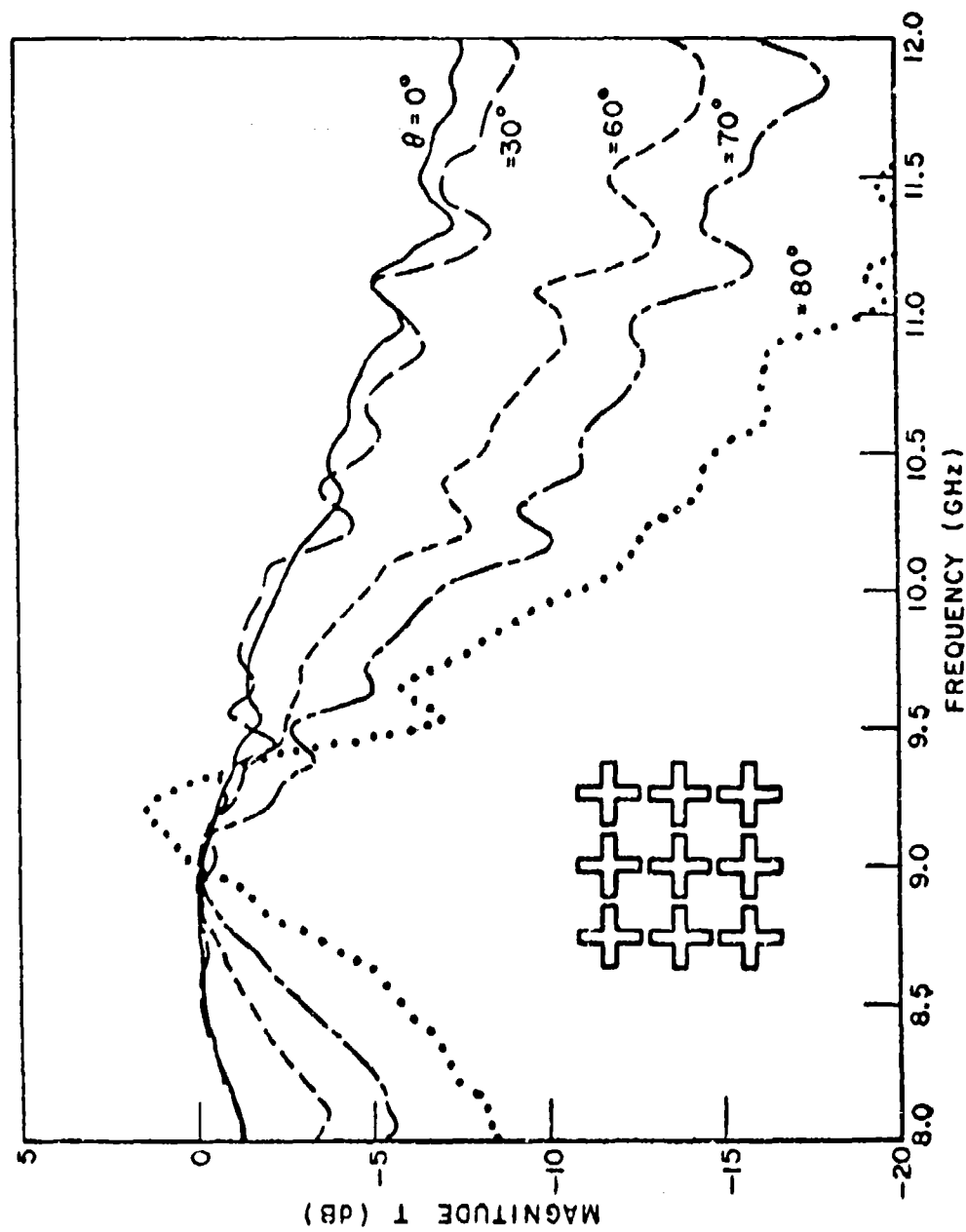


Figure 1-5.--Measured transmission coefficient curves for an array of transmission line loaded slots for various H-plane incidence angles. The slots are 4-legged symmetric slots (Fig. 1-7e) spaced 1 cm apart.

E. Resonant Frequency vs. Incidence Angle

In Figs. 1-4 and 1-5 a set of reflection curves vs. incidence angle are shown for an array of transmission line loaded dipoles. While the bandwidth of these curves varies greatly with incidence angle, the resonant frequency changes very little. In general, however, the resonant frequency of a resonant surface will change with incidence angle. An example of this is shown in Fig. 1-6 for an array of unloaded, rectangular slots. Thus the shape of the individual elements is very important in designing resonant surfaces. In the following section of this chapter we shall discuss the various shapes of elements which have been used in resonant surfaces.

F. Comparison of the Various Types of Tuned Elements

Figure 1-7 illustrates some of the different shapes of elements which have been used in periodic surfaces. Since the behavior of the different shapes will be the same whether they are used in a resonant reflector or resonant window (Babinet's Principle), the discussion of the relative merits of each element applies to both applications.

Historically, the first slot shapes investigated for use in resonant surfaces were the flat dipole and the circular hole. The shift of resonant frequency with incidence angle for resonant surfaces composed of straight flat dipoles has already been illustrated in Fig. 1-6. Resonant surfaces composed of circular slots also exhibit a similar shift of resonant frequency with incidence angle [9]. While radome models have been made and tested using these slot shapes [10,11], their usefulness is limited to designs where only a narrow range of incidence angles will be encountered.

Resonant surfaces composed of loops (Fig. 1-7c) have a resonant frequency which is much less dependent on incidence angle than was the case for the flat dipole and circular disk resonant surfaces. Transmission curves for a resonant window composed of annular slots are shown in Figs. 1-8 and 1-9 for various incidence angles. The improvement in angles of incidence stability is quite dramatic when compared with the flat dipoles of Fig. 1-6. Perhaps the major shortcoming of resonant surfaces composed of loops is that they have a fairly wide bandwidth when compared with the loaded elements to be discussed next. Nevertheless, resonant windows made from annular slots have been used in the fabrication of radomes [12].

The singly loaded element of Fig. 1-7d can be considered a variation of the flat dipole of Fig. 1-7a. This element has been analyzed by treating it as a dipole terminated with a short-circuited transmission line load [3], thus the term singly loaded dipole. This picture of the single loaded element enables the designer to predict quite simply how changes in the shape of a loaded element will affect

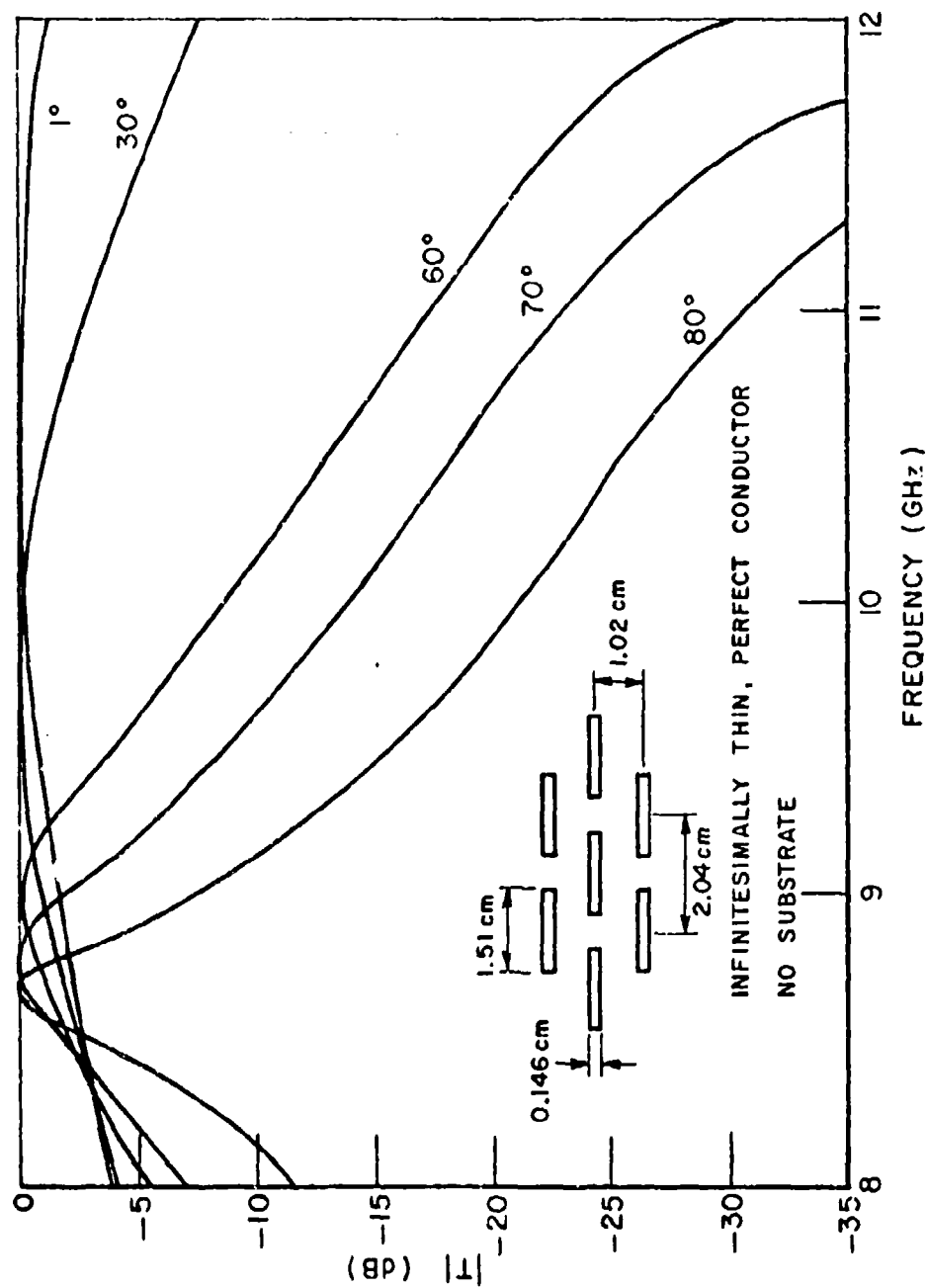


Figure 1-6.--Calculated transmission for an array of rectangular slots illustrating the shift of the resonance frequency with incidence angle (H-plane incidence).

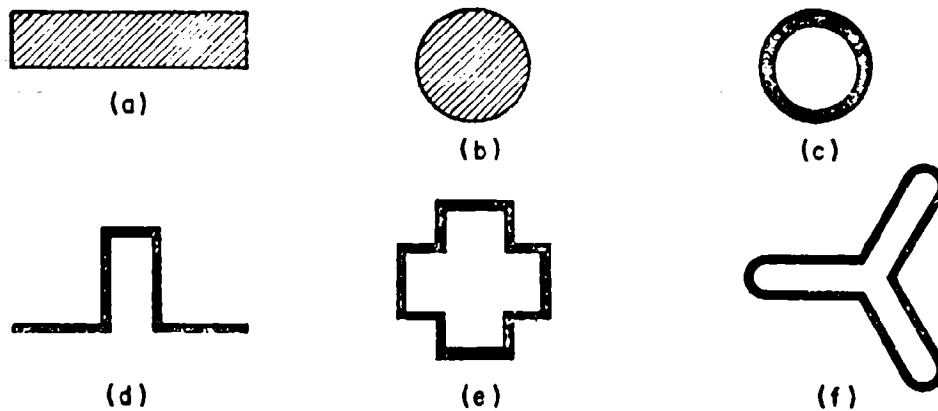


Figure 1-7.--Various types of tuned elements used in resonant surfaces:

- a) Flat dipole (rectangular slot).
- b) Circular disk (circular slot, circular hole).
- c) Loop (annular slot).
- d) Singly loaded dipole (slot).
- e) 4-legged symmetrically loaded dipole (slot).
- f) 3-legged loaded dipole (slot).

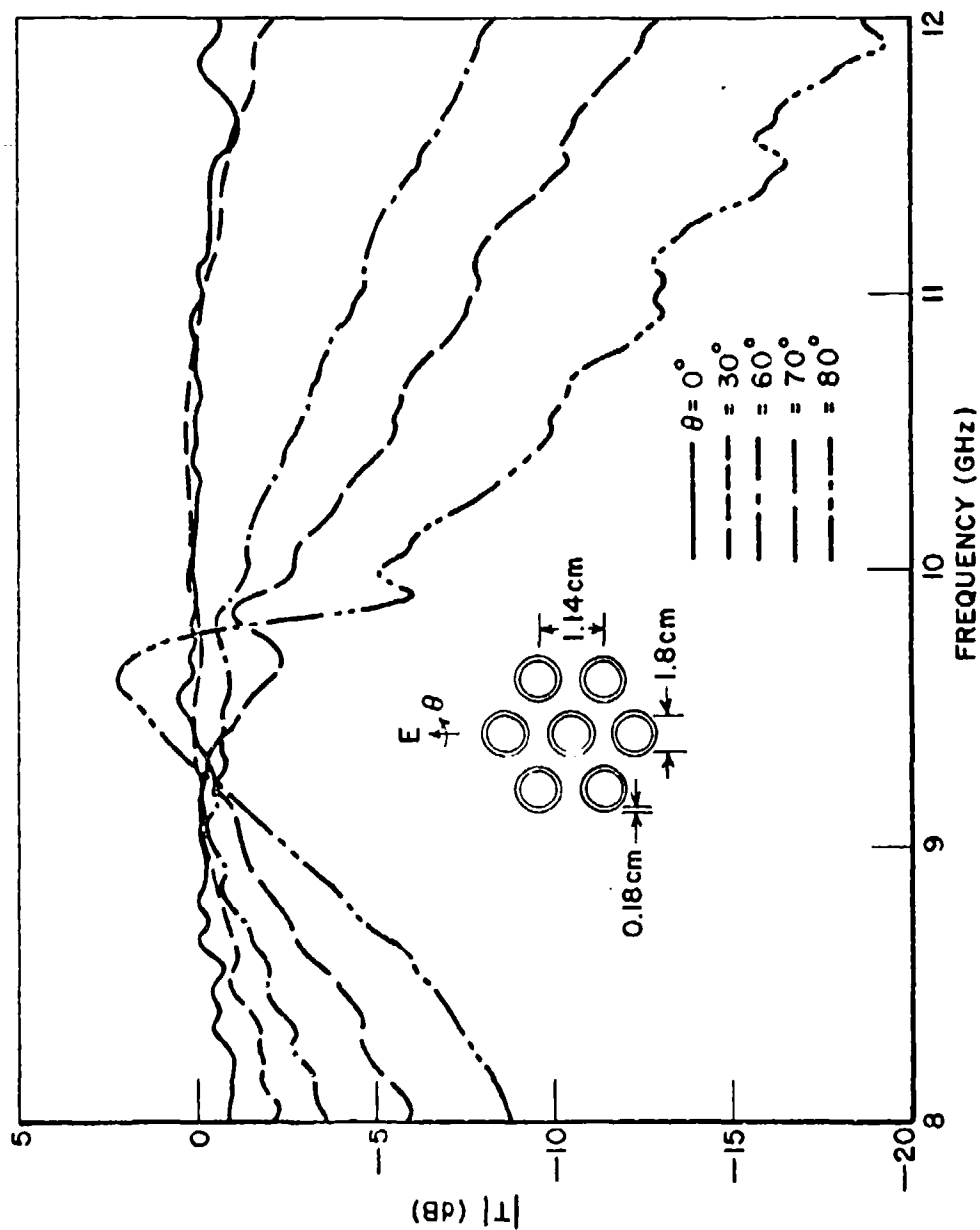


Figure 1-8.--Transmission Coefficient curves for an array of annular slots for various incidence angles in the H-plane.

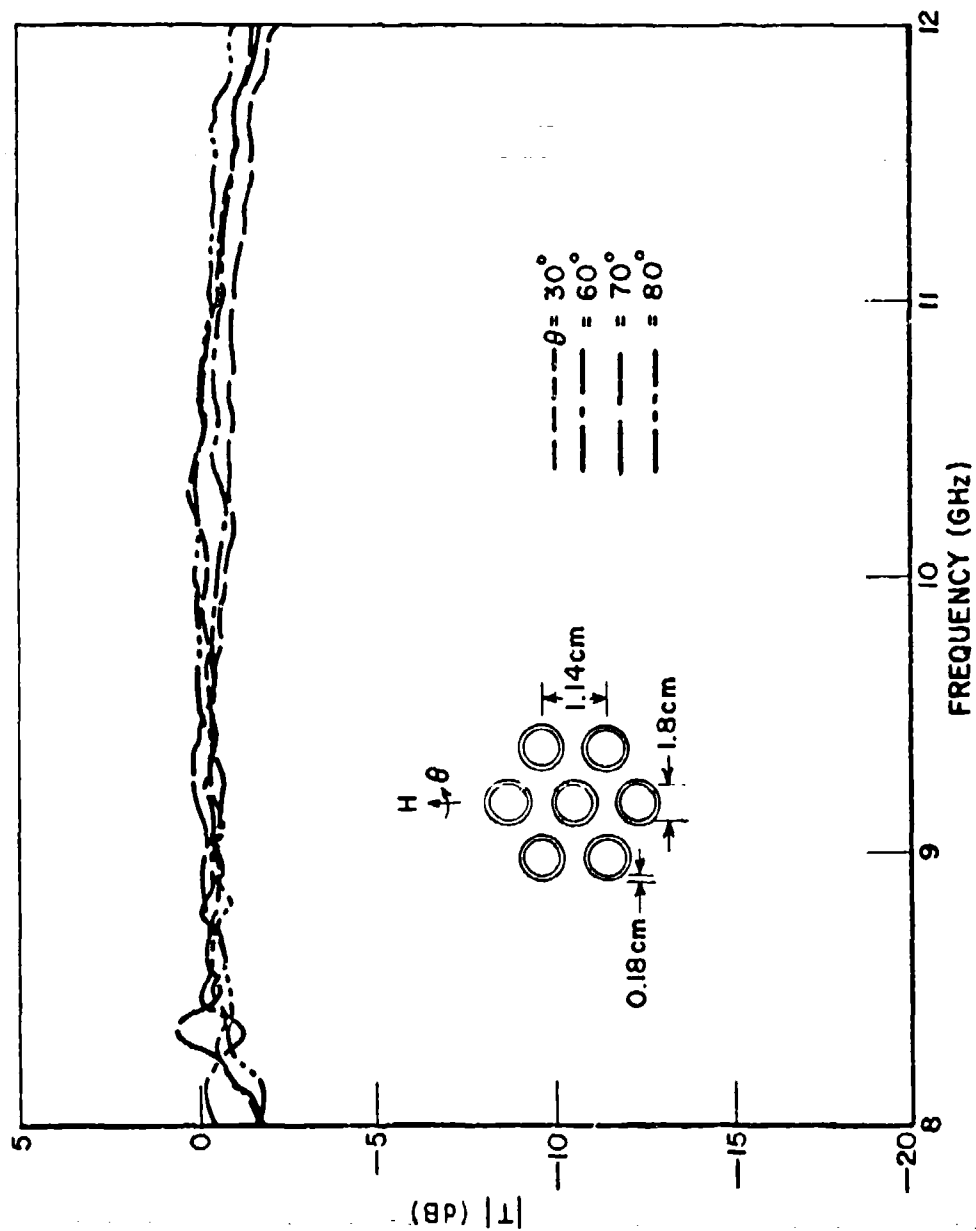


Figure 1-9.--Transmission Coefficient curves for an array of annular slots for various incidence angles in the E-plane.

bandwidth, resonant frequency, and angle of incidence properties [13]. A rule of thumb is that they will resonate when approximately $1/2$ wavelength long. Also, of all the elements shown in Fig. 1-7, this one will result in the most narrow banded resonant surface. An example of a typical resonance curve for a resonant window, E-plane scan, is shown in Fig. 1-10. If the array of slots shown in Fig. 1-10

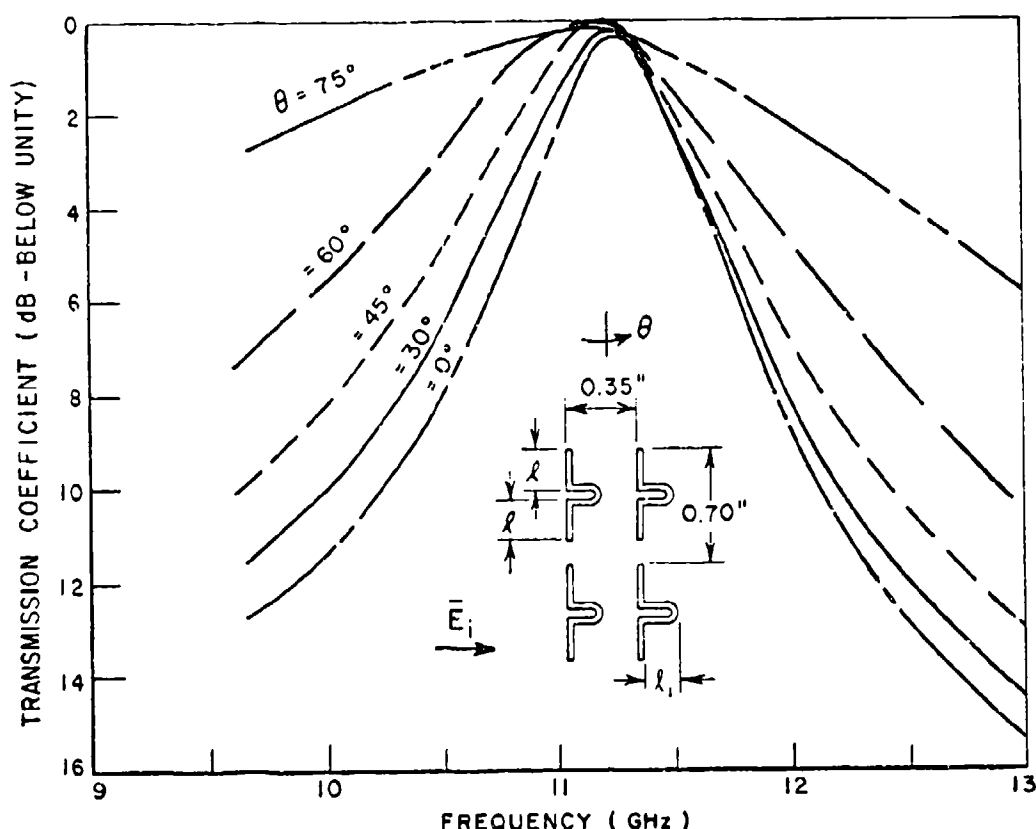


Figure 1-10.--Computed transmission coefficients for an array of single-loaded slots for various E-plane incidence angles.

is illuminated by a plane wave with H-plane incidence, there will be transmission losses at high incidence angles due to cross polarized radiation from the transmission line load (see Chapter V). This loss is illustrated in the curves of Fig. 1-11, which are taken from Chapter V. If, however, the slots are arranged as shown in Fig. 1-12 the cross polarized radiation from adjacent elements cancels out and lossless transmission can be obtained for both E- and H-plane incidence [14].

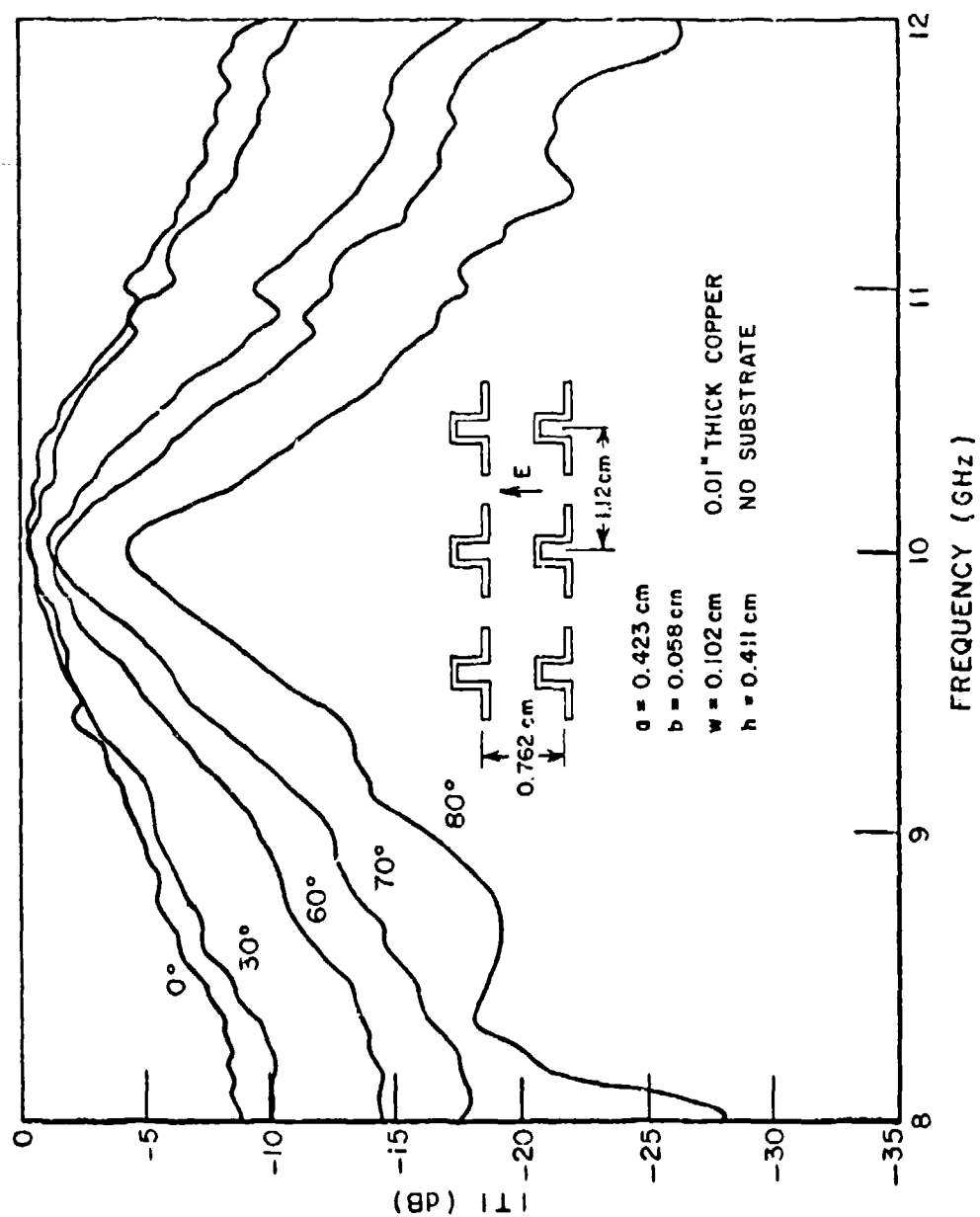


Figure 1-11.--Computed transmission coefficients for an array of single-loaded slots for various H-plane incidence angles.

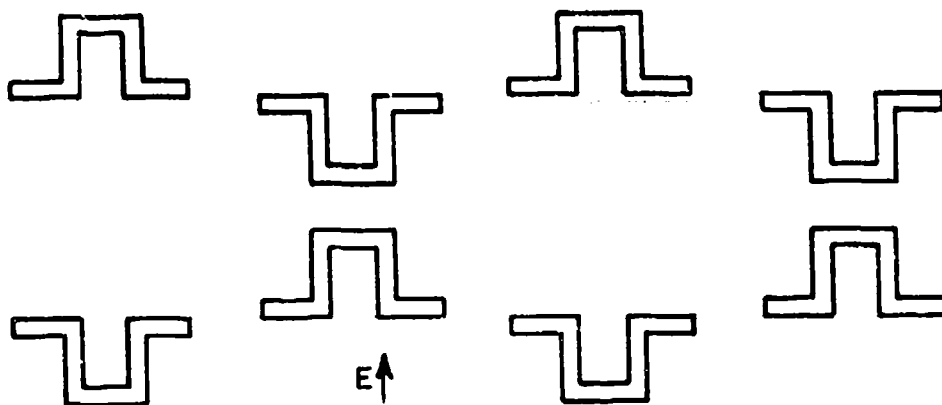


Figure 1-12.--Arrangement of single-loaded slots which eliminates cross polarized radiation for H-plane incidence angles.

An array of the type shown in Fig. 1-12 is linearly polarized. If a resonant surface capable of reflecting or transmitting arbitrarily polarized waves is desired then one can use elements of the type shown in Figs. 1-7e and 1-7f. These elements can be considered either as combinations of loaded dipoles or as variations of the circular loop. These elements will resonate when they are approximately 1 wavelength in circumference. Due to the symmetry of the 4-legged loaded element cross-polarized radiation is negligible, and thus it can have nearly lossless transmission for high incidence angles, as is illustrated in Fig. 1-13.

It is interesting to note that while the 4-legged loaded element is perhaps the most useful and sophisticated of all the element designs shown in Fig. 1-7, it is also one of the oldest. This element was conceived by Munk as a circularly polarized version of the single-loaded dipole of Fig. 1-7d, and its properties had been analyzed both experimentally and mathematically by early 1967 [15]. This predates by several years much of the work referenced previously which was concerned with arrays of circular holes, loops, and rectangular slots which do not perform nearly as well as the 4-legged symmetric slot arrays.

The bandwidth of the loaded elements can be adjusted over fairly wide limits by the means illustrated in Fig. 1-14. In addition, since the loaded elements are more compact than the circular loop, the resonant surface designer has more freedom in choosing the interelement spacing and lattice structure. As stated previously, this will give the designer even more control of the bandwidth of the resonant surface.

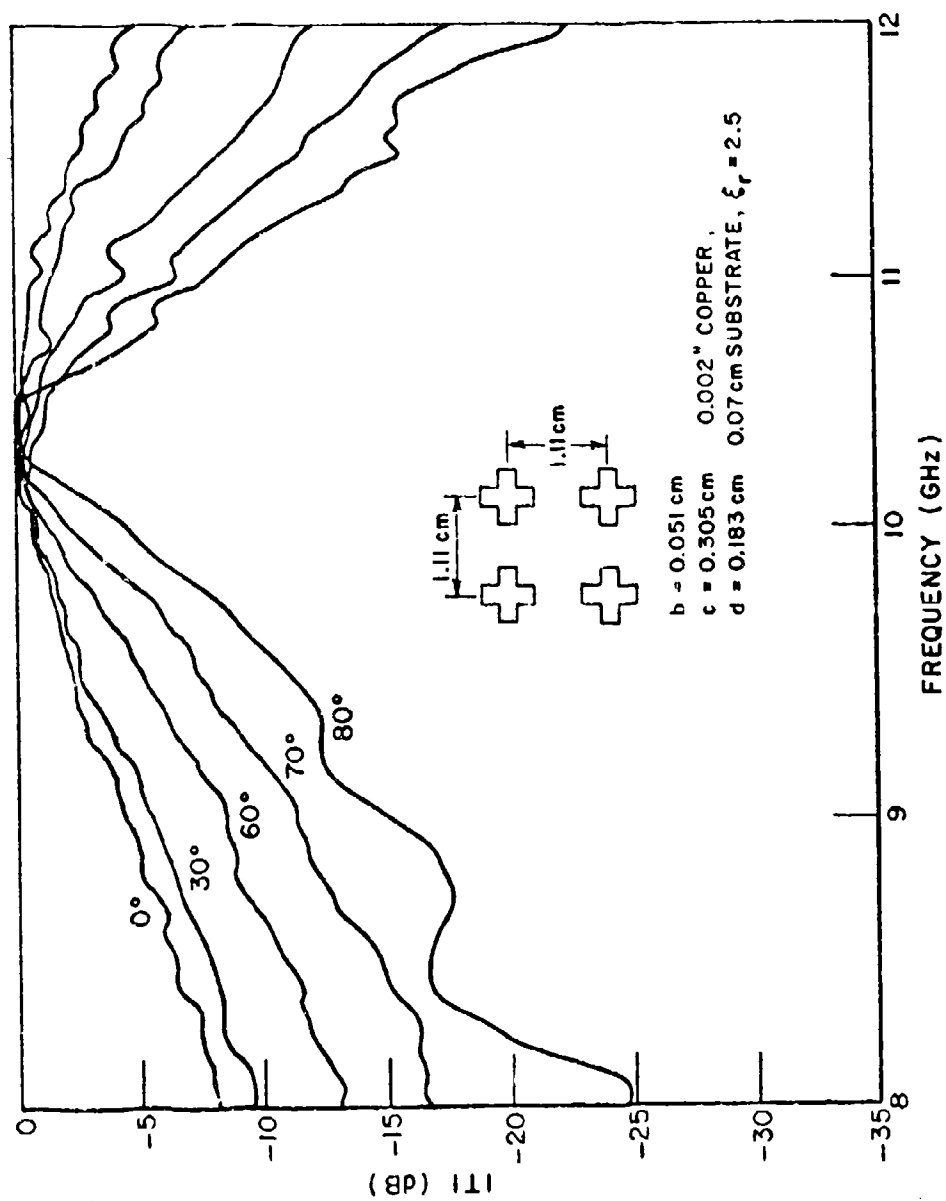


Figure 1-13.--Measured transmission for an array of symmetric 4-legged loaded slots for various angles of incidence in the H-plane (b, c, and d are defined in Fig. 3-11).

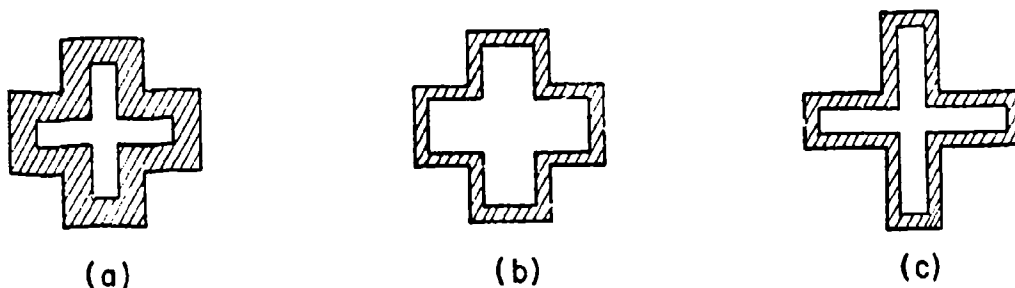


Figure 1-14.--Effect of element design on bandwidth:

- a) A loaded element with a relatively wide bandwidth.
- b) The bandwidth is decreased by decreasing the width of the conductor.
- c) The bandwidth is further decreased by changing the shape of the element as shown.

While Figs. 1-4, 1-5 and 1-13 illustrate the stability of resonance frequency with incidence angle which can be obtained with 4-legged loaded elements, it should be noted that this stability also depends on the interelement spacing and the orientation of the elements. If very close spacing is desired and the slots are interlaced the resonance frequency may shift, as illustrated in Fig. 1-15. To overcome this problem the 3-legged loaded element was developed. Because of its high degree of symmetry it can be packed very tightly. The 3-legged element shape can also be modified to better fit different array geometries. For example, the symmetrical 3-legged element fits quite naturally into an equilateral triangle grid. The symmetry of the element can be modified so that it can fit other array grids. This is discussed in some detail by Pelton who dealt with 3-legged unloaded (Y) elements [16]. In Figs. 1-16 and 1-17 transmission curves for various incidence angles are shown for an array of 3-legged elements. The resonance frequency is unchanged for incidence angles to 80° , and despite the close packing of elements the bandwidth is more narrow than for the loop array of Figs. 1-8 and 1-9. A resonant window of the type shown in Fig. 1-17 was used to fabricate a high performance metallic radome model with a 3-1 fineness ratio [1,2].

The power handling capability of these various element shapes has been investigated. All of them can be used to fabricate radomes or resonant reflectors capable of withstanding the power generated by most airborne radars. Actual, measured power transmission and reflection capabilities for various element types are contained in References [12,17]. When designing and fabricating resonant surfaces all corners should be rounded, array spacing should be small, and the elements should be embedded in a dielectric material if possible.

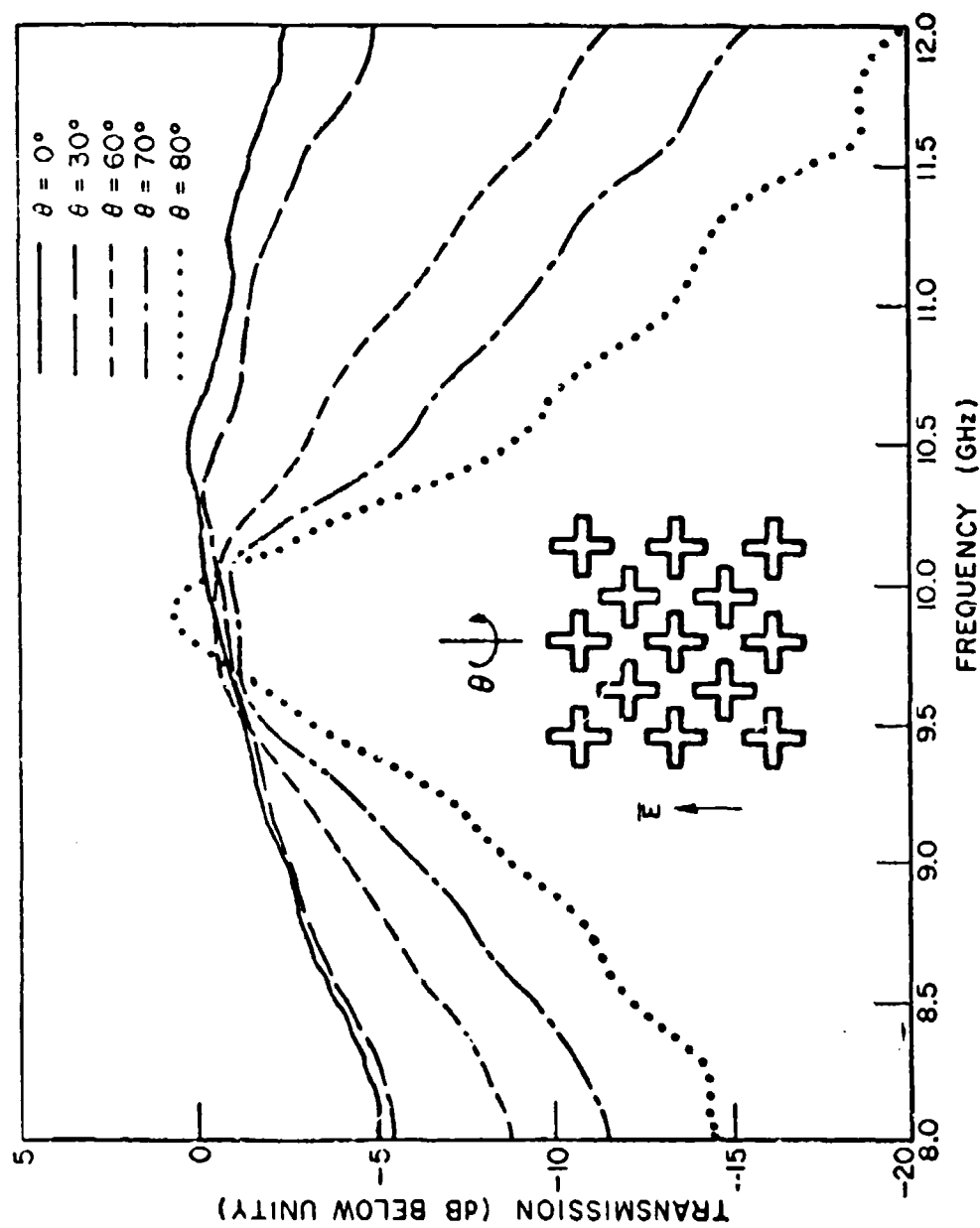


Figure 1-15.--Measured H-plane transmission curves for an interlaced array of 4-legged loaded slots.

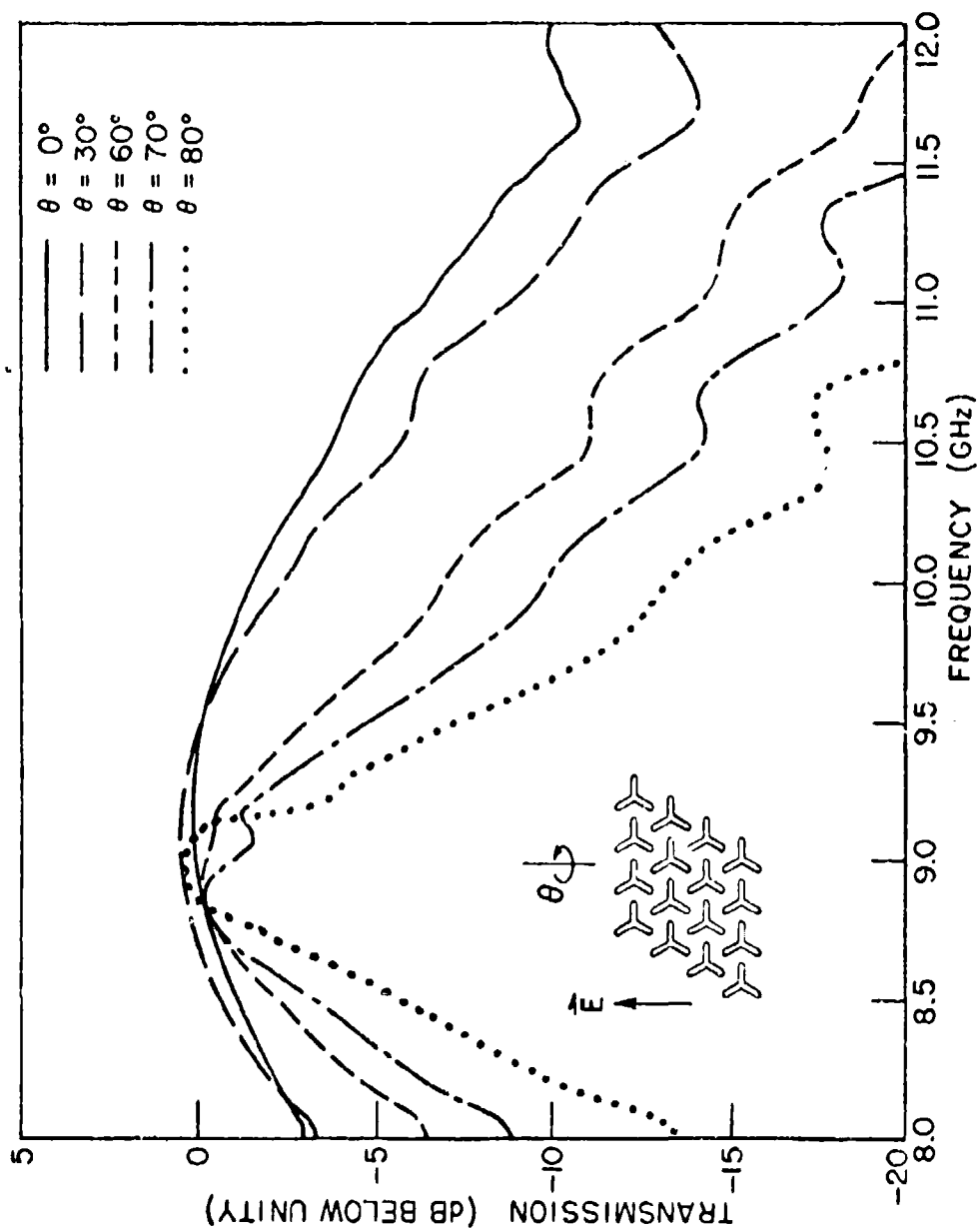


Figure 1-16.--Measured H-plane transmission curves for an array of 3-legged symmetric loaded slots.

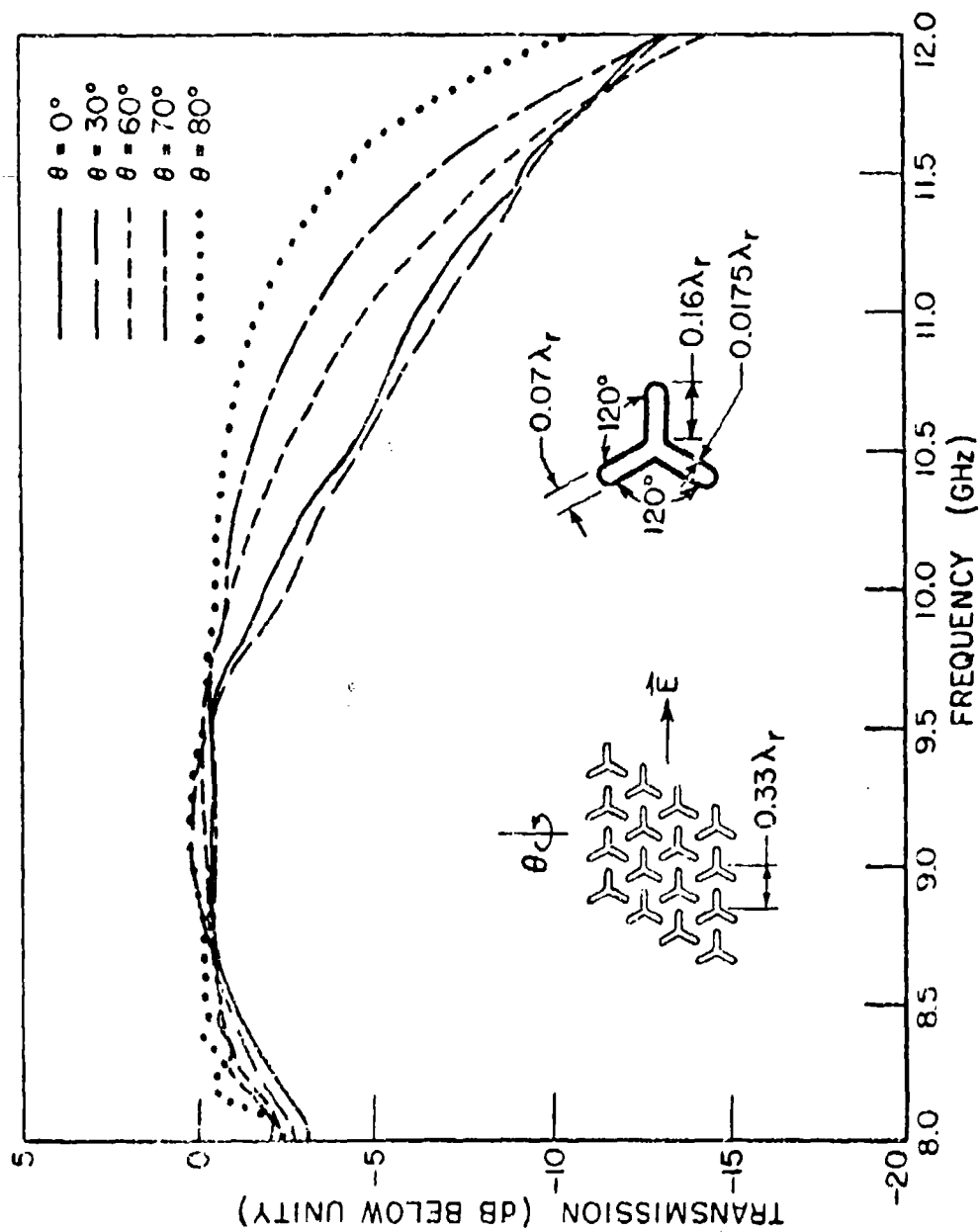


Figure 1-17.--Measured E-plane transmission curves for an array of 3-legged symmetric loaded slots.

G. Biplanar Resonant Surfaces

Some applications for resonant surfaces may require a relatively wide reflection/transmission band coupled with sharp skirt selectivity. These properties can be obtained from biplanar resonant surfaces [18,19,20].

An example of this for a resonant window is shown in Figs. 1-18 and 1-19. These curves are for a biplanar slot array made by taking two arrays of the type shown in Figs. 1-4 and 1-5, placing them parallel to one another, and separating them 1.1 cm (0.33λ). Thus, the improvement obtained in the usable transmission bandwidth and skirt selectivity by adding a second layer can be seen by comparing Figs. 1-18, 1-19 and Figs. 1-4, 1-5. When making the comparison note the change in the vertical scale. The improvement is quite marked. One problem with bi-planar resonant windows is the dip in the resonance curve for high H-plane incidence angles. This dip is caused by the near field coupling between the two panels and becomes deeper as the panels are moved close together [19]. Actually, the optimum spacing between the panels disregarding this dip would be $\sim .25\lambda$. However, the spacing shown, $.33\lambda$, is the result of a tradeoff between optimum selectivity and the depth of the dip at resonance for 80° H-plane incidence. Means for overcoming this and other problems of biplanar resonant windows are discussed in Chapter VI.

The usable reflection band and skirt selectivity for resonant reflectors can also be improved by using a two layer dipole array. This improvement is shown by comparing Figs. 1-20 and 1-21. By using the Butterworth filter design even more marked improvement can be obtained using 3 or more layers [21].

H. Discussion of Various Tuned Radome Configurations

We will now assume that the reader knows how to construct a metallic resonant window that has the required resonance, bandwidth, and incidence angle properties. The next problem is how to incorporate the resonant window into the overall radome design.

Several possible physical configurations for tuned radomes are illustrated in Fig. 1-22. The various configurations have relative trade-offs in relation to power handling capability, ease of fabrication, skirt selectivity, boresight error, multi-frequency capabilities, and lightning protection. In this section we shall discuss the various configurations and the relative strengths and weaknesses of each.

The most easily fabricated tuned radome is the thin film radome shown in Fig. 1-22a. This radome is protected from the environment by a conventional dielectric radome, and thus need only be strong enough to support its own weight. Normal construction would consist

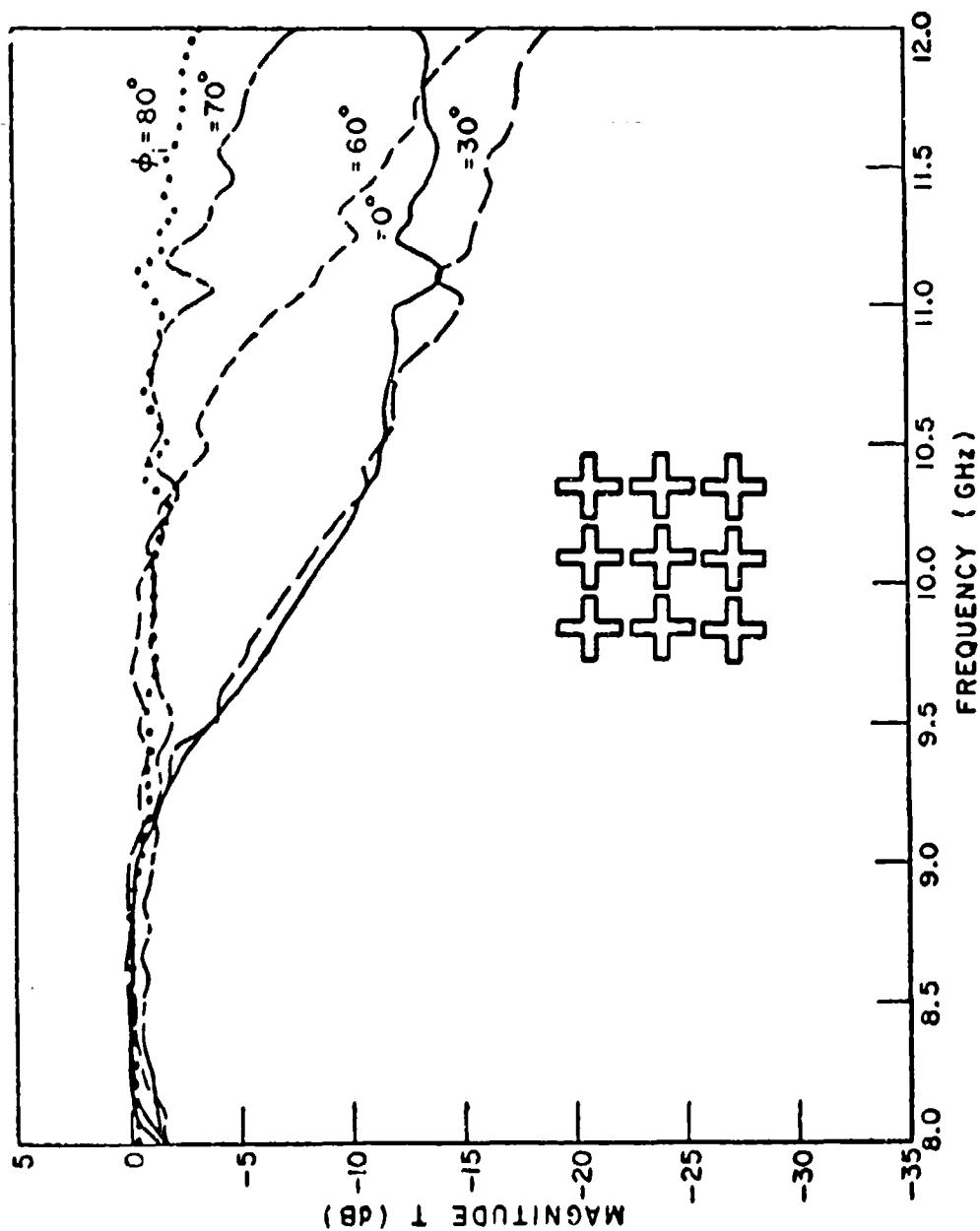


Figure 1-18.--Measured transmission curves for a biplanar slot array E-plane incidence. The two arrays are spaced 1.1 cm (0.33λ) apart.

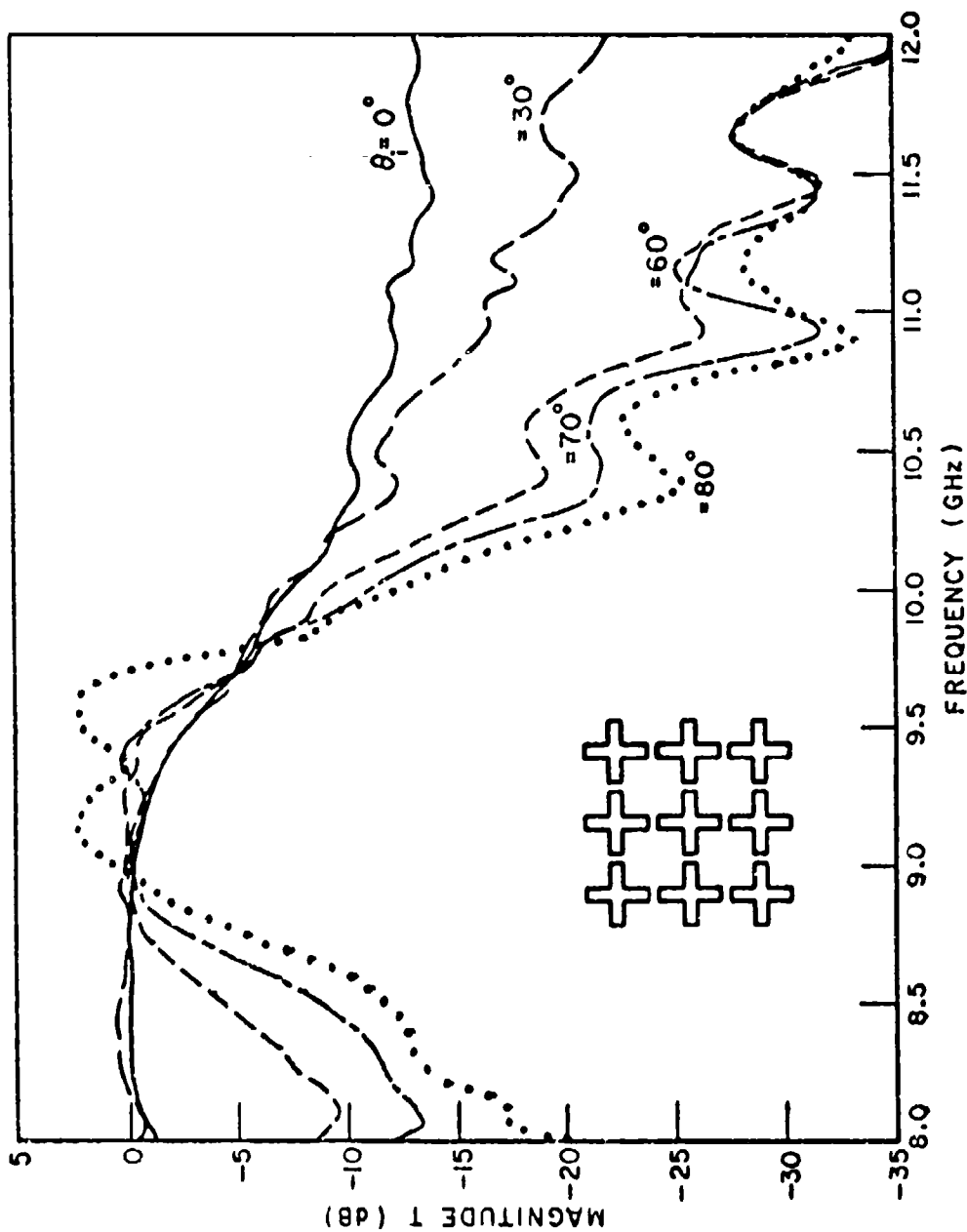


Figure 1-19.---Measured transmission curves for a biplanar slot array H-plane incidence. The two arrays are spaced 1.1 cm (0.33λ) apart.

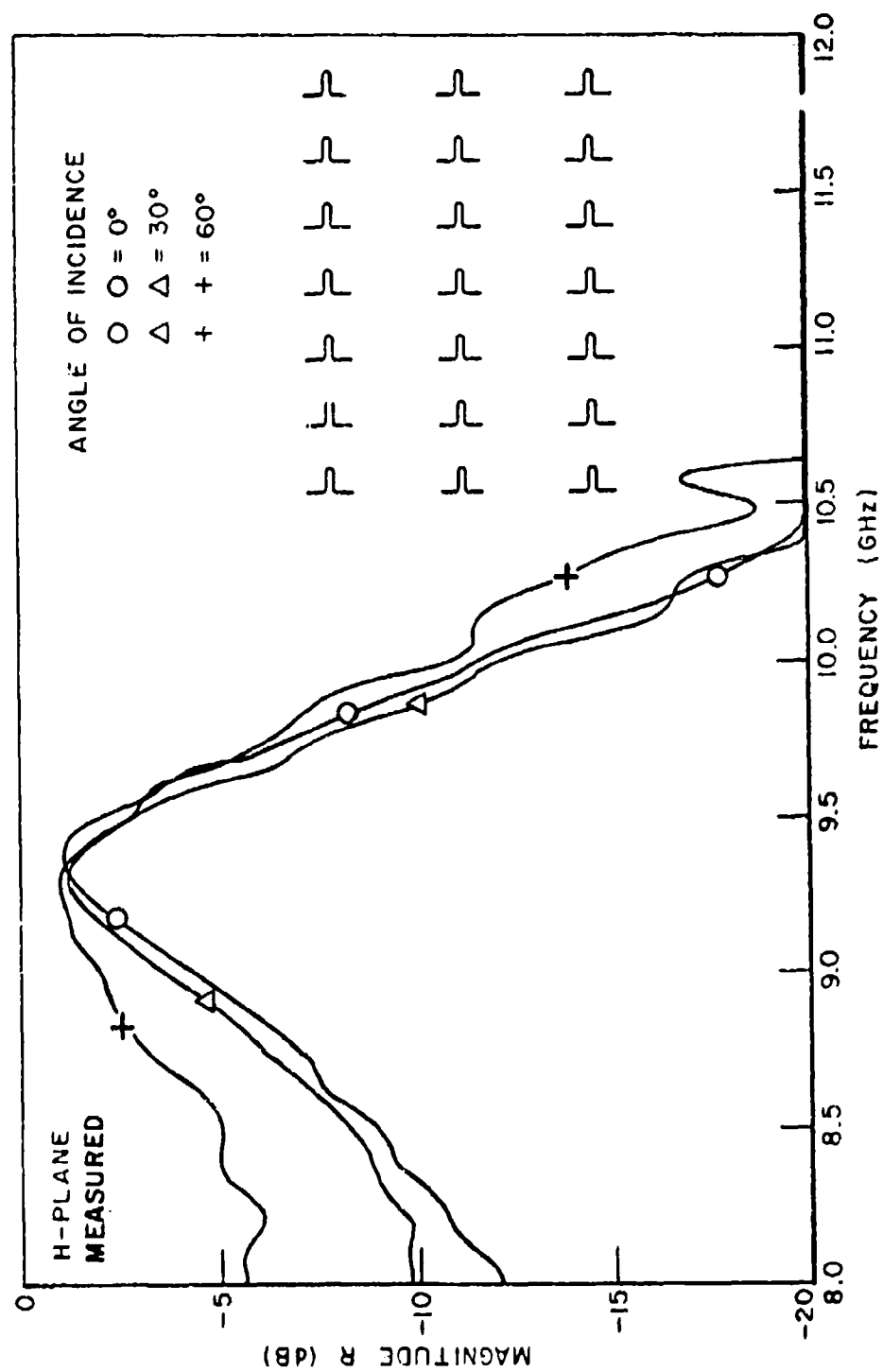


Figure 1-20.--Measured reflection curves for a single dipole array mounted on 1/32" thick dielectric material ($\epsilon_r=2.5$) for various incidence angles in the H-plane. The inset shows a full size section of the array.

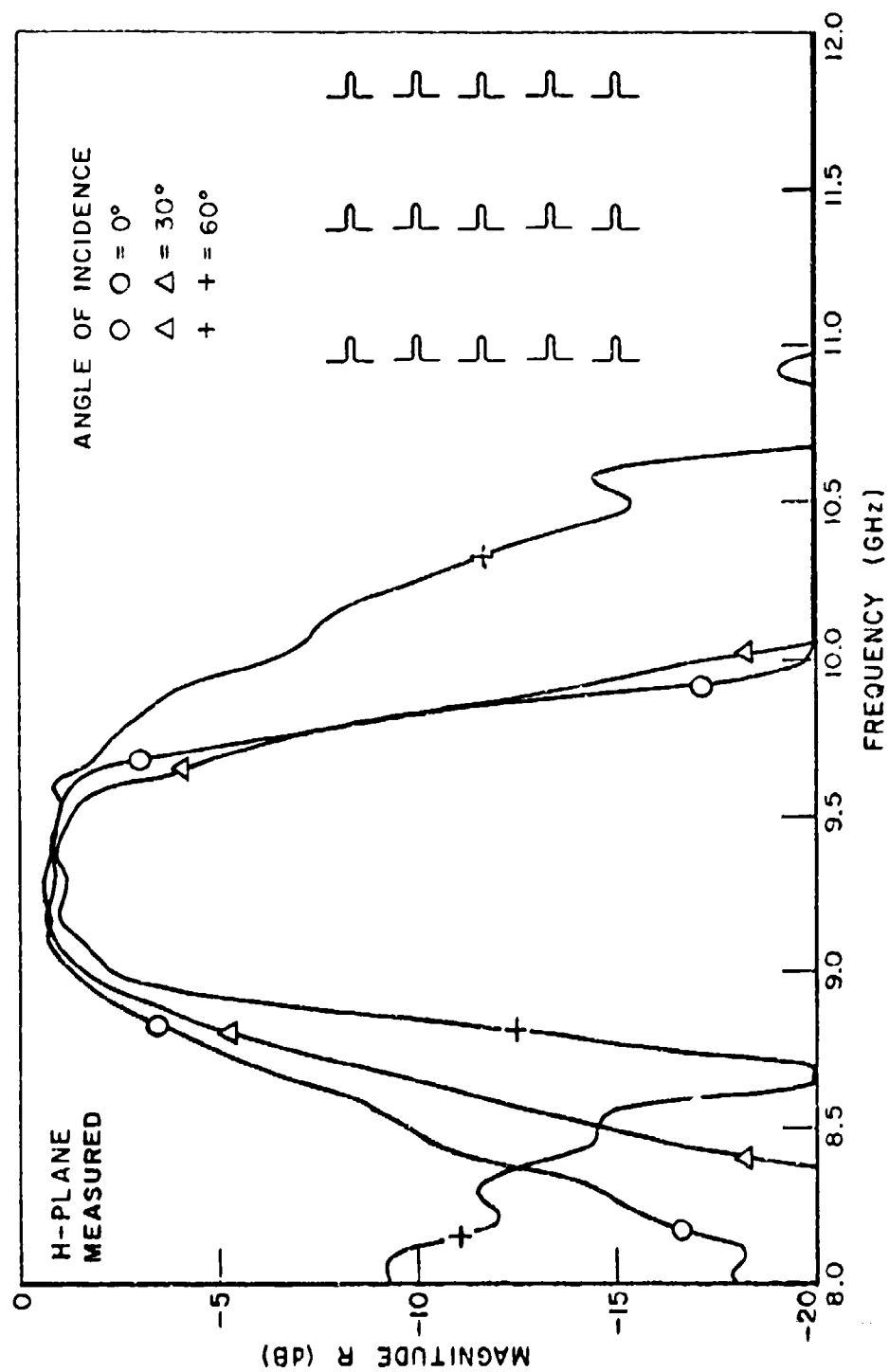


Figure 1-21.--Measured reflection curves for two dipole arrays of the type shown in Fig. 1-20 separated by $0.27 \lambda_0$, where $\lambda_0 = 3.2$ cm.

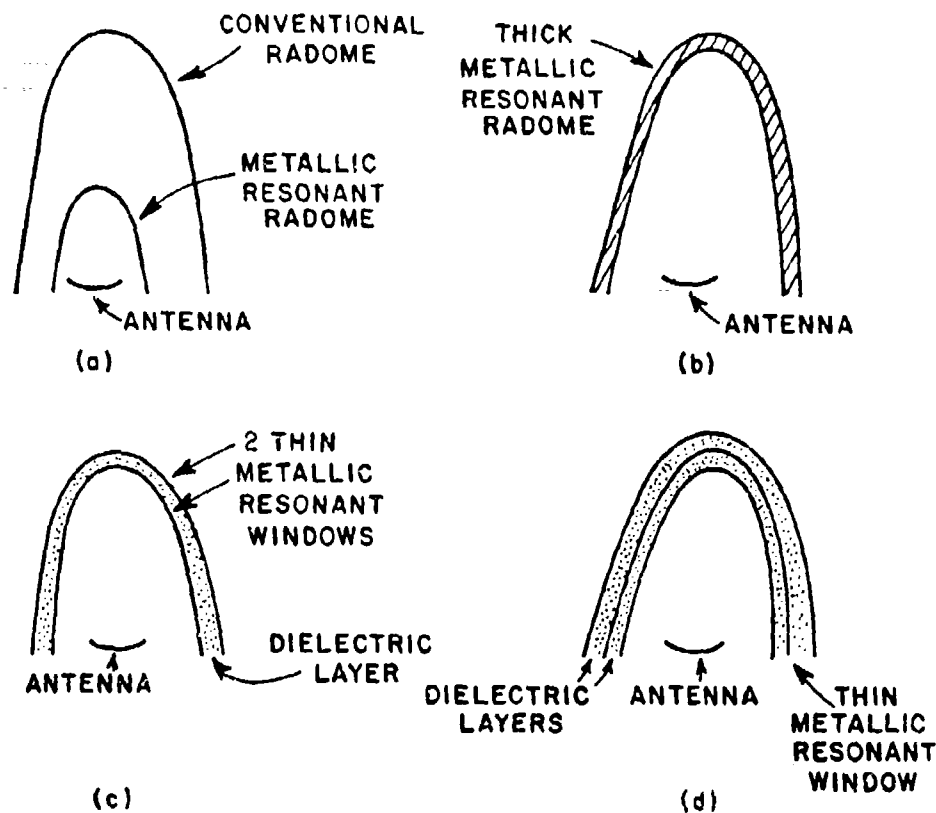


Figure 1-22.--Some possible configurations for tuned radomes:

- a) Thin film resonant window behind conventional radome.
- b) Thick metal radome.
- c) Multi-layer.
- d) Dielectric-resonant window sandwich.

of a thin film of conducting metal deposited on a thin dielectric substrate. The metal film is then chemically etched to produce the slotted resonant window. Successful prototypes of this type of tuned radome have been constructed [1,2,22]. Since fabrication is simple, holding the required tolerances is not a problem. This configuration, with proper design, yields a very low boresight error. Since the metal is not in contact with the external environment, this configuration does not give good lightning protection.

The next configuration to be considered is the thick metal radome, shown in Fig. 1-22b. Physically, the metal would be approximately 0.1" thick. In Chapters II and IV we show that the major effect of making the resonant window thicker is a narrowing of the bandwidth of the transmission curve. This is not a serious problem, as the narrowing bandwidth can be compensated by using a wide band element shape. The relative advantages of the thick metallic radome are increased strength and good lightning protection. However, it can be quite difficult to mill an array of resonant slots in a thick piece of metal with the tolerance and uniformity required for lossless transmission at resonance. One possible solution to this problem is to use simple shapes, i.e., rectangular or circular slots. The loading necessary to stabilize the resonance frequency when varying the incidence angle would be obtained from the dielectric material used to fill the slot. Theoretical investigations of this technique appear promising, as shown in Chapter IV.

The performance of the multi-layer radome is directly related to the performance of biplanar slot arrays, which were discussed in Section G and are further investigated in Chapter VI. The basic advantage of the multi-layer tuned radome over other configuration is the relatively wide passband coupled with sharp skirt selectivity. The configuration shown in Fig. 1-22c will also have good lightning protection. A variation of this design would have dielectric layers on the inner and outer surfaces as well as in the center. The advantage of this would be increased power handling capacity and relatively constant bandwidth with changing incidence angles, as discussed in Chapter VI.

The dielectric sandwich configuration is shown in Fig. 1-22d. For lossless transmission the two dielectric layers should have the same electrical thickness. This configuration would have a greater power handling capability than any of the other configurations shown. As with the multi-layer radome, there should be no gaps between the dielectric layers and the metal layer. As shown, lightning protection would be poor. However, this protection would be improved considerably by running wires from the metal layer, through the outer dielectric layer terminating at the outer surface of the radome. These wires would then drain accumulating static charges from the outer surface of the radome.

The four configurations presented are not the only ones possible. They are merely intended as an illustration of the options available to the tuned radome designer.

I. Methods of Analysis

There are basically four different methods which have been used to analyze periodic scattering arrays. They are: 1) variational; 2) point matching; 3) mutual impedance; and 4) modal matching. In this work we are concerned with the fourth type of solution, but we will also discuss the other three types briefly.

Early investigations of resonant slot arrays dealt with thin arrays of square or rectangular slots. In 1961 Kiebertz and Ishimaru [23] used variational methods to obtain the transmission coefficients for normal incidence. By 1965 a point matching solution using an entire domain basis was developed by Ott et.al. [24] to obtain the reflection coefficient for the complementary dipole array for normal incidence. For these thin arrays Babinet's principle applies, so that a solution to the dipole problem is also a solution for the complementary slot problem, and vice versa.

The solutions mentioned thus far could deal only with arrays of rectangular slots or dipoles. However, a definite breakthrough in both the performance and analysis of periodic arrays was made by Munk in 1967. He developed the transmission line loaded element of Fig. 1-7d [25], and also developed a method for calculating the reflection coefficient for an array of loaded dipoles [15]. This method of analysis involved the summation of mutual impedances to obtain the input impedance of an element in the array, and is thus known as the mutual impedance solution. With some approximations, the solution of Munk could also deal with arrays of 4-legged loaded slots, as shown in Fig. 1-7e. Pelton has since extended the mutual impedance solution so that it can deal with Y-shaped and cross shaped (+) dipoles as well [16]. The mutual impedance solution can include thickness effects when dealing with dipole (reflecting) arrays. However, only thin slot arrays can be analyzed with this method (Babinet).

Still another method for analyzing thin arrays was developed in 1970 by Chen, who used a modal matching technique to obtain the transmission coefficient for a periodic array of rectangular slots [26]. The array could be covered on one side by a dielectric layer. He also published, in a separate paper [27], a modal matching solution for the scattering from a periodic array of thin conducting plates. These modal solutions used the Floquet mode set developed by Galindo and Amitay for the analysis of phased array antennas [28]. This Floquet mode set is discussed in Chapter III. The thin plate solution did not allow for the presence of a dielectric layer. More recently, Montgomery [29] has also obtained a modal matching solution for the thin conducting plate problem which does allow a dielectric layer on one side of the array, while Chen has extended this solution to circular holes [30]. The performance of these arrays of rectangular or circular elements was, however, inferior to that of the arrays of loaded elements already analyzed by Munk.

The section of this work dealing with thin slot arrays (Chapter V) contains calculations of transmission coefficients for various slot array geometries. A modal analysis solution is employed. The solution is similar to that obtained by Chen. However, the solution has been extended to include dielectric layers on one or both sides. Also, in addition to rectangular apertures, arrays of single loaded, 4-legged loaded, and 3-legged loaded slots (Fig. 1-7) can be analyzed with the modal solution derived in Chapter V. A portion of the work presented in Chapter V has been previously published [31].

As mentioned previously in this chapter, biplanar slot and dipole arrays are of interest for many applications. To our knowledge these arrays have not been analyzed using variational or point matching solutions. Using the mutual impedance method, Munk [32] and more recently Munk and Luebbers have analyzed biplanar dipole arrays [18]. Also, Luebbers and Munk have extended the analysis to an N-layer array of dipoles [21]. The biplanar slot array has also been analyzed using mutual impedances [19,20].

In Chapter VI we present the first modal matching solution for a biplanar slot array. One limitation, which does not apply for the mutual impedance solution, is that the two slot arrays must be identical. Advantages of the modal solution of Chapter VI are that dielectric layers can be present, and that the analysis can handle all of the various loaded slot shapes. Munk, however, will soon publish a mutual impedance analysis of the biplanar slot array which includes dielectric layers [5].

Perhaps the greatest advantage of the modal matching type of solution is that it can be used to analyze thick slot arrays. Chen [33] formulated a modal matching solution for the transmission through a finitely thick conducting plate, and gave some results for rectangular and circular apertures. In Chapter IV a similar solution to this problem is presented. However, this solution can also handle the various loaded slot shapes, can accommodate dielectric layers on both sides of the thick slot array, and also allows the slots themselves to be filled with dielectric.

One final method of analyzing periodic slot arrays which has not yet been mentioned involves modeling the periodic slot array with one (or more) slots in a waveguide. This waveguide simulation can yield valuable information about resonant array parameters which do not strongly depend on incidence angle. Also, the waveguide simulator may be much easier to fabricate than an entire resonant slot array, especially when the slot array is thick. In Chapter II we will show how the transmission through a thick rectangular waveguide iris can be calculated using modal analysis [34,35], and how significant information concerning the effects of thickness on resonant slot arrays can be obtained from these calculations.

CHAPTER II RECTANGULAR WAVEGUIDE WINDOWS

The major portion of this work is concerned with transmission through periodic slot arrays. These arrays are analyzed using a modal matching solution. One of the main advantages of this type of solution is that it can be formulated to include the finite thickness of the slotted conducting panel.

Our earlier work on slots with walls of finite thickness was based on waveguide simulation of thick slot arrays. It is well known that the dominant mode field in a rectangular waveguide can be considered as composed of two plane waves. This fact, coupled with image theory, implies that a slot in a waveguide simulates an infinite array of slots with two incident plane waves. Thus if we are concerned with investigating properties of periodic slot arrays which do not strongly depend on incidence angle, a waveguide simulation can yield the desired information. The main advantages of the waveguide simulation were that 1) it was easier to fabricate one slot for a waveguide simulation than an entire array of slots, and 2) the transmission through the slot in the waveguide could be more accurately measured.

The modal solution presented in this chapter for the thick waveguide window is almost identical to that given in Chapter IV for the thick slot array. The only difference is that in Chapter IV the fields in the regions outside the slot are expanded in Floquet modes rather than in rectangular waveguide modes as is done here. Thus the solution given here will serve to introduce the reader to the basic method of solution which will be used throughout this work.

In conjunction with this work a modal analysis solution for the transmission through a rectangular waveguide window was developed. Using this solution the effects of thickness and finite conductivity were investigated and some interesting results were obtained. Since these results are applicable to periodic slot arrays and will not be repeated in later chapters, they are included herein for completeness.

A. Modal Analysis Solution

The geometry and coordinates of a thick, rectangular slot in a rectangular waveguide are shown in Fig. 2-1. It is assumed that only the dominant TE_{10} mode will propagate in the larger waveguide. The problem is to calculate the transmission and reflection coefficients of the slot. If the slot is infinitesimally thin, i.e., $b \rightarrow 0$, variational techniques can be used to obtain an expression for the

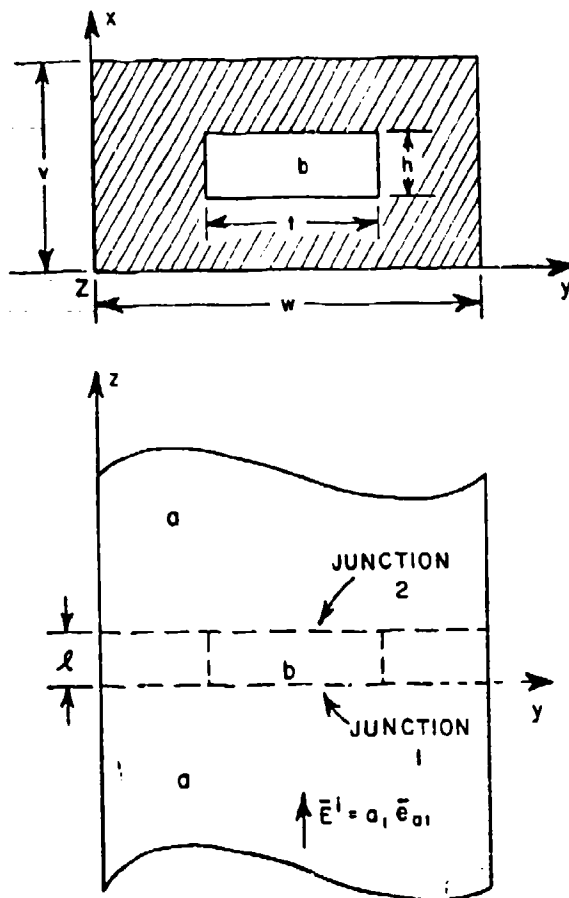
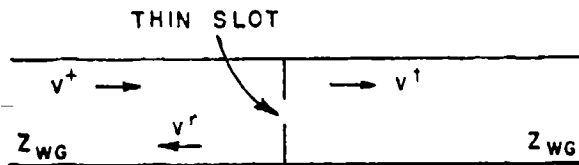


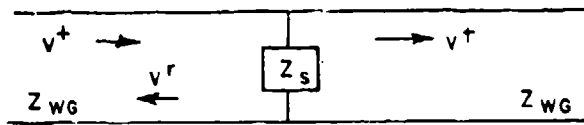
Figure 2-1.--Geometry and coordinate system for a thick rectangular slot in a rectangular waveguide.

equivalent shunt impedance Z_s (see Fig. 2-2), from which R and T can be calculated [10,36]. For finite values of l , however, this method appears to be difficult if not impossible to apply, except for the degenerate cases where the slot width equals the waveguide width (capacitive obstacle) or the slot height equals the waveguide height (inductive obstacle). Results for these cases are given by Marcuvitz [37]. However these results are not applicable to resonant slot arrays since these degenerate cases are not resonant structures.

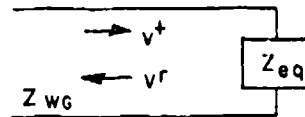
The modal analysis method for calculating the reflection and transmission coefficients of waveguide obstacles was developed by Wexler [38]. The method can be applied to almost any type of waveguide discontinuity providing the waveguide modes of each discontinuity region are known. For a rectangular slot the modes in the discontinuity region (i.e., the slot) are merely the usual modes for a



(a) THIN SLOT IN WAVEGUIDE



(b) SLOT REPLACED BY EQUIVALENT SHUNT IMPEDANCE Z



(c) Z_s COMBINED WITH Z_{wg} TO FORM EQUIVALENT IMPEDANCE Z_{eq}

Figure 2-2.--Equivalent impedances for a thin slot.

rectangular waveguide. The large waveguide is denoted as region "a" in Fig. 2-1. The slot will be considered to be a small waveguide, and be denoted as region "b". The geometry is now treated as a waveguide junction. The transverse components of the modes in region a are [39]

$$(2-1) \quad \bar{e}_{ai} = \sin\left(\frac{p\pi y}{w}\right) \cos\left(\frac{q\pi x}{v}\right) \hat{x}$$

$$(2-2) \quad \bar{h}_{ai} = y_{ai} \sin\left(\frac{p\pi y}{w}\right) \cos\left(\frac{q\pi x}{v}\right) \hat{y}$$

$$- j\sqrt{\frac{\epsilon}{\mu}} \frac{\lambda}{2\pi} \frac{\frac{pq\pi^2}{wv}}{\sqrt{\left(\frac{p\pi}{w}\right)^2 + \left(\frac{q\pi}{v}\right)^2 - \left(\frac{2\pi}{\lambda}\right)^2}} \cos\left(\frac{p\pi y}{w}\right) \sin\left(\frac{q\pi x}{v}\right) \hat{x}$$

where \hat{x} and \hat{y} are unit vectors, p and q the conventional mode numbers, (integers), and y_{ai} is the wave admittance of the i -th mode given by

$$(2-3) \quad y_{ai} = j\sqrt{\frac{\epsilon}{\mu}} \frac{\lambda}{2\pi} \cdot \frac{\left(\frac{2\pi}{\lambda}\right)^2 - \left(\frac{p\pi}{w}\right)^2}{\sqrt{\left(\frac{p\pi}{w}\right)^2 + \left(\frac{q\pi}{v}\right)^2 - \left(\frac{2\pi}{\lambda}\right)^2}}$$

The factor $e^{j\omega t}$ is suppressed, and $j = \sqrt{-1}$. Similarly in region b (i.e., $\frac{w-t}{2} < y < \frac{w+t}{2}$ and $\frac{v-h}{2} < x < \frac{v+h}{2}$) the transverse components of the modes are

$$(2-4) \quad \bar{e}_{bj} = \sin(r\pi \cdot \frac{2y-w+t}{2t}) \cos(s\pi \cdot \frac{2x-v+h}{2h}) \hat{x}$$

$$(2-5) \quad \bar{h}_{bj} = y_{bj} \sin(r\pi \cdot \frac{2y-w+t}{2t}) \cos(s\pi \cdot \frac{2x-v+h}{2h}) \hat{y}$$

$$-j\sqrt{\frac{\epsilon}{\mu}} \frac{\lambda}{2\pi} \frac{\frac{rs\pi^2}{th}}{\sqrt{\left(\frac{r\pi}{t}\right)^2 + \left(\frac{s\pi}{h}\right)^2 - \left(\frac{2\pi}{\lambda}\right)^2}} \cdot \cos(r\pi \cdot \frac{2y-w+t}{2t}) \sin(s\pi \cdot \frac{2x-v+h}{2h}) \hat{x}$$

where r and s are the mode numbers and y_{bj} is given by

$$(2-6) \quad y_{bj} = j\sqrt{\frac{\epsilon}{\mu}} \frac{\lambda}{2\pi} \frac{\left(\frac{2\pi}{\lambda}\right)^2 - \left(\frac{r\pi}{t}\right)^2}{\sqrt{\left(\frac{r\pi}{t}\right)^2 + \left(\frac{s\pi}{h}\right)^2 - \left(\frac{2\pi}{\lambda}\right)^2}}$$

These modes are neither TE nor TM to the Z axis, but are characterized by the absence of a y -directed E field. This mode set is more efficient for this problem than the usual TE_z and TM_z modes since we can match the tangential fields across the aperture with only one vector component. Modes are numbered consecutively, i.e., $i=1,2,3,\dots$, and $j=1,2,3,\dots$, with each value of i corresponding to a particular pair of values for p and q . Due to symmetry, not all modes are excited; p and r are always odd, q and s even (or 0) for this geometry and excitation.

Consider the mode $i=1$, i.e., the TE_{10} mode, with strength a_1 emanating from a matched source in waveguide a and impinging on waveguide b (the slot) at junction 1. Taking \vec{E} to be the total transverse electric field at the discontinuity, the field expanded in terms of modes just below junction 1 is

$$(2-7) \quad \vec{E} = (1+\rho) a_1 \vec{e}_{a1} + \sum_{i=2}^{\infty} a_i \vec{e}_{ai}$$

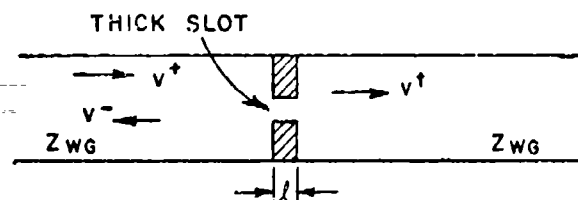
where ρ is the reflection coefficient for mode $i=1$, and the a_i are the coefficients of the backscattered modes. The total transverse magnetic field \vec{H} is expressed by

$$(2-8) \quad \vec{H} = (1-\rho) a_1 \vec{h}_{a1} - \sum_{i=2}^{\infty} a_i \vec{h}_{ai}.$$

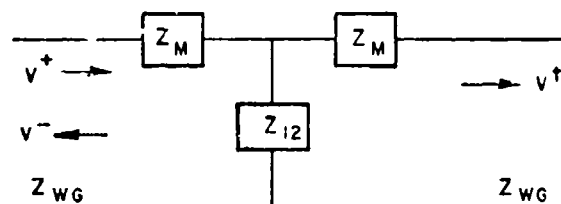
The fields in waveguide b just above junction 1 are to be expressed in terms of modes in b. However, one must account for the reflection of these modes from junction 2, since each transmitted mode j reaching junction 2 will scatter power into other modes k , some of which return to junction 1. It is therefore necessary to account for these returned waves as well as the positively directed ones when summing fields. In order to do this a scattering coefficient S_{jk} is defined as equal to the mode coefficient b_k of the k -th backscattered mode present just above junction 1 due to mode j scattering from junction 2. Clearly, to find the fields due to one wave incident on the slot the reflected fields from junction 2 must be found for each j mode. These tedious computations can be avoided for this problem since the obstacle is symmetric about the X-Y plane. By using symmetric and antisymmetric excitations we can find the T-equivalent circuit parameters (see Fig. 2-3) without evaluating a complete set of scattering coefficients. Symmetric excitation of the slot is obtained by having two incident modes in the waveguide, one traveling in the +Z direction and the other in the -Z direction, such that the E fields are in phase in the X-Y plane; antisymmetric excitation is obtained if these modes are 180° out of phase in the X-Y plane. For symmetric excitation an open circuit appears at the X-Y plane; antisymmetrical excitation produces a short circuit. Under these conditions $S_{jk}=0$ for $j \neq k$, and

$$(2-9) \quad S_{jj} = \pm e^{-\Gamma_j l}$$

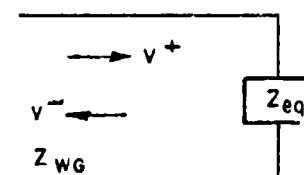
where Γ_j is the propagation constant for mode j in guide b. For a rectangular slot with modes as defined previously (Eqs. 2-4, 2-5, 2-6),



(a) THICK SLOT IN WAVEGUIDE



(b) SLOT REPRESENTED BY EQUIVALENT T CIRCUIT



(c) T CIRCUIT COMBINED WITH Z_{WG} TO FORM Z_{eq}

Figure 2-3.--Equivalent impedances for a thick slot.

$$(2-10) \quad \Gamma_j = \sqrt{\left(\frac{r_\pi}{t}\right)^2 + \left(\frac{s_\pi}{h}\right)^2 - \left(\frac{2\pi}{\lambda}\right)^2}.$$

The plus and minus signs in Eq. (2-9) correspond to symmetrical and antisymmetrical excitation respectively. With antisymmetrical excitation the computed input impedance of the slot is equal to the upper arm impedance of the equivalent T circuit so that once ρ is calculated for antisymmetric excitation (ρ_a) we can obtain Z_m from

$$(2-11) \quad \frac{Z_m}{Z_{wg}} = \frac{1+\rho_a}{1-\rho_a}$$

where ρ_a is the dominant mode reflection coefficient (see Eq. (2-7)) with antisymmetric excitation and Z_{wg} is the waveguide impedance. Once the ρ is obtained for symmetric excitation (ρ_s) the common branch impedance Z_{12} can be found from the above equation and the fact that for symmetrical excitation we have

$$(2-12) \quad \frac{Z_m + 2Z_{12}}{Z_{wg}} = \frac{1+\rho_s}{1-\rho_s}$$

with ρ_s the reflection coefficient for symmetric excitation.

With either symmetric or antisymmetric excitation the fields in region b just above junction 1 are given by

$$(2-13) \quad \vec{E} = \sum_{j=1}^{\infty} b_j \vec{e}_{bj} (1 + S_{jj})$$

$$(2-14) \quad \vec{H} = \sum_{j=1}^{\infty} b_j \vec{h}_{bj} (1 - S_{jj})$$

where b_j is the coefficient of the j -th mode.

To solve for the unknown coefficient ρ the boundary conditions at the discontinuity must be satisfied; continuity of transverse electric and magnetic fields across the aperture, and zero tangential \vec{E} at the surface of the conducting panel which contains the slot.

In waveguide region a it can be easily shown that

$$(2-15) \quad \int_a \vec{e}_{ai} \times \vec{h}_{am} \cdot \hat{z} \, ds = 0$$

where m is a mode number in waveguide a, $i \neq m$, and $\int_a ds$ denotes an integration over the cross-section of waveguide a. Following Wexler's procedure, we enforce continuity of transverse electric field across the aperture by equating Eq. (2-7) with Eq. (2-13), take the cross product with \vec{h}_{am} and integrate, keeping in mind the orthogonality relation of Eq. (2-15). The results are

$$(2-16) \quad (1 + \rho) a_1 \int_a \bar{e}_{a1} \times \bar{h}_{a1} \cdot \hat{z} \, ds =$$

$$\sum_{j=1}^{\infty} b_j \int_b \bar{e}_{bj} \times \bar{h}_{a1} \cdot \hat{z} \, ds \cdot (1 + S_{jj})$$

for $m=1$ and

$$(2-17) \quad a_m \int_a \bar{e}_{am} \times \bar{h}_{am} \cdot \hat{z} \, ds =$$

$$\sum_{j=1}^{\infty} b_j \int_b \bar{e}_{bj} \times \bar{h}_{am} \cdot \hat{z} \, ds \cdot (1 + S_{jj})$$

when $m \neq 1$, where $\int_b ds$ denotes an integration over the cross-section of waveguide b . This integration also enforces the boundary condition of zero tangential E at the surface of the panel.

To provide continuity of the transverse magnetic field through the aperture we equate Eq. (2-8) and Eq. (2-14), take a cross product with \bar{e}_{bn} , and integrate. By using the orthogonality relation

$$(2-18) \quad \int_b \bar{e}_{bn} \times \bar{h}_{bj} \cdot \hat{z} \, ds = 0$$

the result is

$$(2-19) \quad (1-\rho) a_1 \int_b \bar{e}_{bn} \times \bar{h}_{a1} \cdot \hat{z} \, ds - \sum_{i=2}^{\infty} a_i \int_b \bar{e}_{bn} \times \bar{h}_{ai} \cdot \hat{z} \, ds$$

$$= b_n (1 - S_{nn}) \int_b \bar{e}_{bn} \times \bar{h}_{bn} \cdot \hat{z} \, ds$$

If we now substitute Eq. (2-17) into Eq. (2-19) and change index m to i the a_i coefficients are eliminated, and we obtain the equation

$$\begin{aligned}
 (2-20) \quad \rho \int_b \bar{e}_{bn} \times \bar{h}_{a1} \cdot \hat{z} \, ds + \sum_{j=1}^N \frac{b_j}{a_1} \sum_{i=2}^M \frac{\int_b \bar{e}_{bj} \times \bar{h}_{ai} \cdot \hat{z} \, ds (1+S_{jj})}{\int_a \bar{e}_{ai} \times \bar{h}_{ai} \cdot \hat{z} \, ds} \\
 + \int_b \bar{e}_{bn} \times \bar{h}_{ai} \cdot \hat{z} \, ds + \frac{b_n}{a_1} (1-S_{nn}) \int_b \bar{e}_{bn} \times \bar{h}_{bn} \cdot \hat{z} \, ds = \\
 \int_b \bar{e}_{bn} \times \bar{h}_{a1} \cdot \hat{z} \, ds .
 \end{aligned}$$

Since the computer can solve only a limited number of equations the infinite series were truncated at M and N, where M and N are the number of modes used to approximate the fields in waveguide regions a and b respectively. Equation (2-20) is really N linear equations corresponding to $n=1,2,3,\dots,N$. There are N+1 unknowns, namely ρ and the N modal coefficients in waveguide b $(\frac{b_1}{a_1}, \frac{b_2}{a_1}, \dots, \frac{b_N}{a_1})$, but by dividing Eq. (2-16) by a_1 and rearranging we have

$$\begin{aligned}
 (2-21) \quad \rho \int_a \bar{e}_{a1} \times \bar{h}_{a1} \cdot \hat{z} \, ds - \sum_{j=1}^N \frac{b_j}{a_1} (1+S_{jj}) \int_b \bar{e}_{bj} \times \bar{h}_{a1} \cdot \hat{z} \, ds \\
 = - \int_a \bar{e}_{a1} \times \bar{h}_{a1} \cdot \hat{z} \, ds
 \end{aligned}$$

which in combination with Eq. (2-20) forms a system of N+1 linear equations with N+1 unknowns.

The integrations are fairly straightforward for this problem, and the results will be given here:

$$\begin{aligned}
 (2-22) \quad \int_a \bar{e}_{ai} \times \bar{h}_{ai} \cdot \hat{z} \, ds \\
 = y_{ai} \int_0^w \int_0^v \sin^2 \left(\frac{p\pi y}{w} \right) \cos^2 \left(\frac{q\pi x}{v} \right) dx \, dy \\
 = \begin{cases} .25 \, wv \, y_{ai} & \text{if } q \neq 0 \\ .50 \, wv \, y_{ai} & \text{if } q = 0 \end{cases}
 \end{aligned}$$

$$(2-23) \quad \int_b \bar{e}_{bj} \times \bar{h}_{bj} \cdot \hat{z} \, ds$$

$$= y_{bj} \int_{\frac{w-t}{2}}^{\frac{w+t}{2}} \int_{\frac{v-h}{2}}^{\frac{v+h}{2}} \sin^2(r\pi \cdot \frac{2y-w+t}{2t}) \cos^2(s\pi \cdot \frac{2x-v+h}{2h}) \, dx \, dy$$

$$= \begin{cases} .25 \, \text{th } y_{bj} & \text{if } s \neq 0 \\ .50 \, \text{th } y_{bj} & \text{if } s = 0 \end{cases}$$

$$(2-24) \quad \int_b \bar{e}_{bj} \times \bar{h}_{ai} \cdot \hat{z} \, ds$$

$$= y_{ai} \int_{\frac{w-t}{2}}^{\frac{w+t}{2}} \int_{\frac{v-h}{2}}^{\frac{v+h}{2}} \sin(r\pi \cdot \frac{2y-w+t}{2t}) \cdot \sin(\frac{p\pi y}{w})$$

$$\cdot \cos(s\pi \cdot \frac{2x-v+h}{2h}) \cos(\frac{q\pi x}{v}) \, dx \, dy$$

$$= \left\{ \frac{\cos[\frac{\pi}{2}(r-p)]}{\pi[\frac{r}{t} - \frac{p}{w}]} \cdot \sin[\frac{\pi}{2}(r - \frac{pt}{w})] \right.$$

$$- \frac{\cos[\frac{\pi}{2}(r+p)]}{\pi[\frac{r}{t} + \frac{p}{w}]} \sin[\frac{\pi}{2}(r + \frac{pt}{w})] \Bigg\}$$

$$\cdot \left\{ \frac{\cos[\frac{\pi}{2}(s+q)]}{\pi[\frac{s}{h} + \frac{q}{v}]} \sin[\frac{\pi}{2}(s + \frac{qh}{v})] \right.$$

$$+ \frac{\cos[\frac{\pi}{2}(s-q)]}{\pi[\frac{s}{h} - \frac{q}{v}]} \sin[\frac{\pi}{2}(s - \frac{qh}{v})] \Bigg\}$$

The calculations presented in this chapter were made by solving the system of equations (i.e., Eq. (2-20) and Eq. (2-21)) for ρ using both symmetric and antisymmetric excitation and the appropriate equation (i.e., Eq. (2-11) or Eq. (2-12)) to determine the equivalent-T circuit parameters. The reflection coefficient can be calculated by reducing the equivalent-T circuit to Z_{eq} , with complex T (transmission coefficient) given by transmission line techniques as

$$(2-25) \quad T = \frac{Z_{12} Z_{wg} (1+R)}{2 Z_m Z_{12} + Z_{12} Z_{wg} + (Z_m)^2 + Z_m Z_{wg}}$$

The number of modes used to approximate the fields did not appear to be critical. Values for the equivalent circuit parameters agreed to within a few per cent when the number of modes in waveguide b were varied from 6 to 9. A rule of thumb to follow when choosing the number of modes is that the ratio of the number of modes in waveguide a to the number of modes in waveguide b should be the same as the ratio of the area of waveguide a to the area of waveguide b [40].

The calculations were made using an IBM 360/75 (and later an IBM 370/165) computer. The simultaneous equations were solved using IBM software modified to handle complex arithmetic.

Using the waveguide measurement system described in Appendix A the value of the equivalent impedance was measured for 4 different slots as a function of frequency. All the measurements were made with S-band waveguide with dimensions $v=1.34$ ". The calculated values of Z_{eq} were made with the maximum values of the mode numbers p, q, r, and s being 19, 22, 11, and 0 respectively. This corresponds to 120 modes in the waveguide ($M = \frac{p+1}{2} \cdot \frac{q+2}{2}$) and 6 modes in the slot being used to approximate the fields, since p and r are always odd while q and s are always even.

Figures 2-4 through 2-9 are plots of calculated and measured values of Z_{eq} and $|T|$ for slots of dimensions $t=1.68$ inches, $h=.0625$ inches and thicknesses .0625, .125, and .1875 inches. At resonance, these thicknesses correspond to $.019\lambda$, $.037\lambda$, and $.056\lambda$ respectively. Circular loci of Z_{eq} corresponding to transmission losses of .1, .5, 1.0, and 4.0 dB are marked on Fig. 2-4 to illustrate how accurate the Smith Chart plots of Z_{eq} are for determining values of T near resonance. These figures show that the modal analysis method yields values of Z_{eq} which show good agreement with values obtained experimentally.

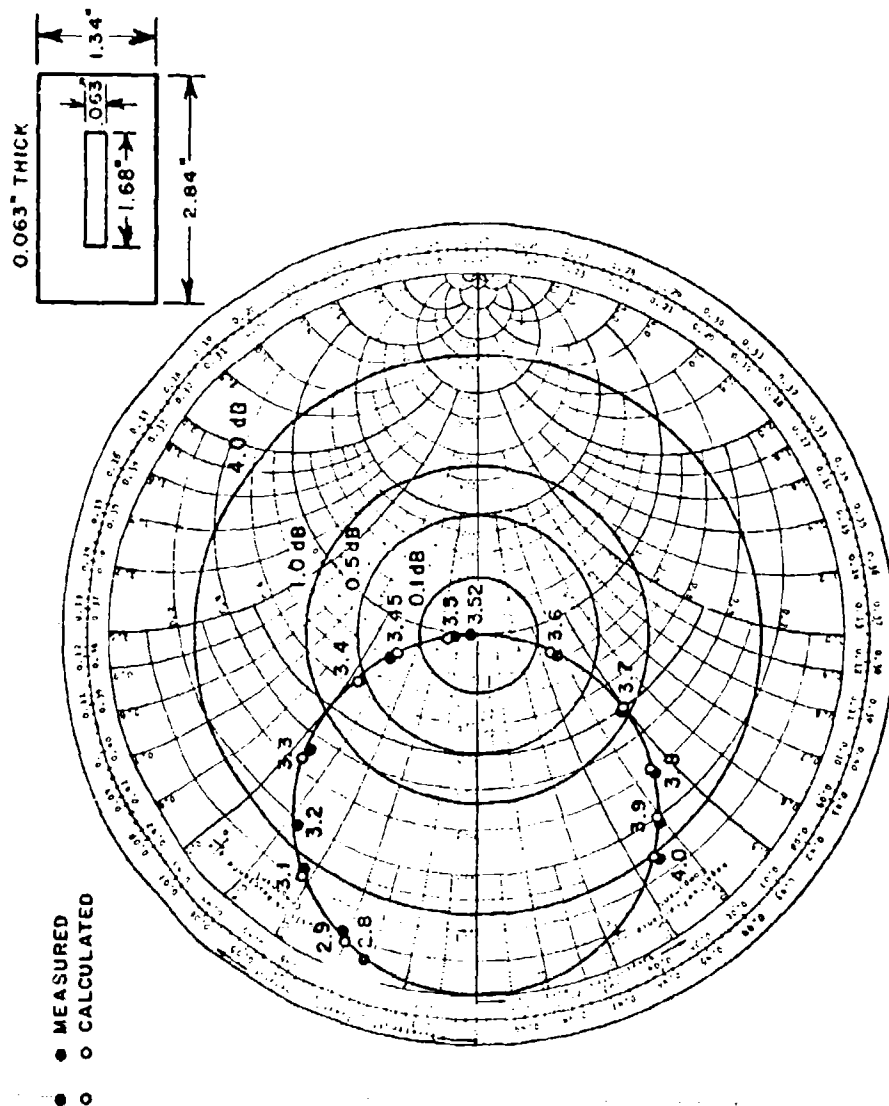


Figure 2-4.--Calculated and measured values of the equivalent impedance Z_{eq} for a 0.063" thick rectangular slot in a waveguide vs. frequency. Also shown are circles of Z_{eq} corresponding to transmission losses of 0.1, 0.5, 1.0, and 4.0 dB.

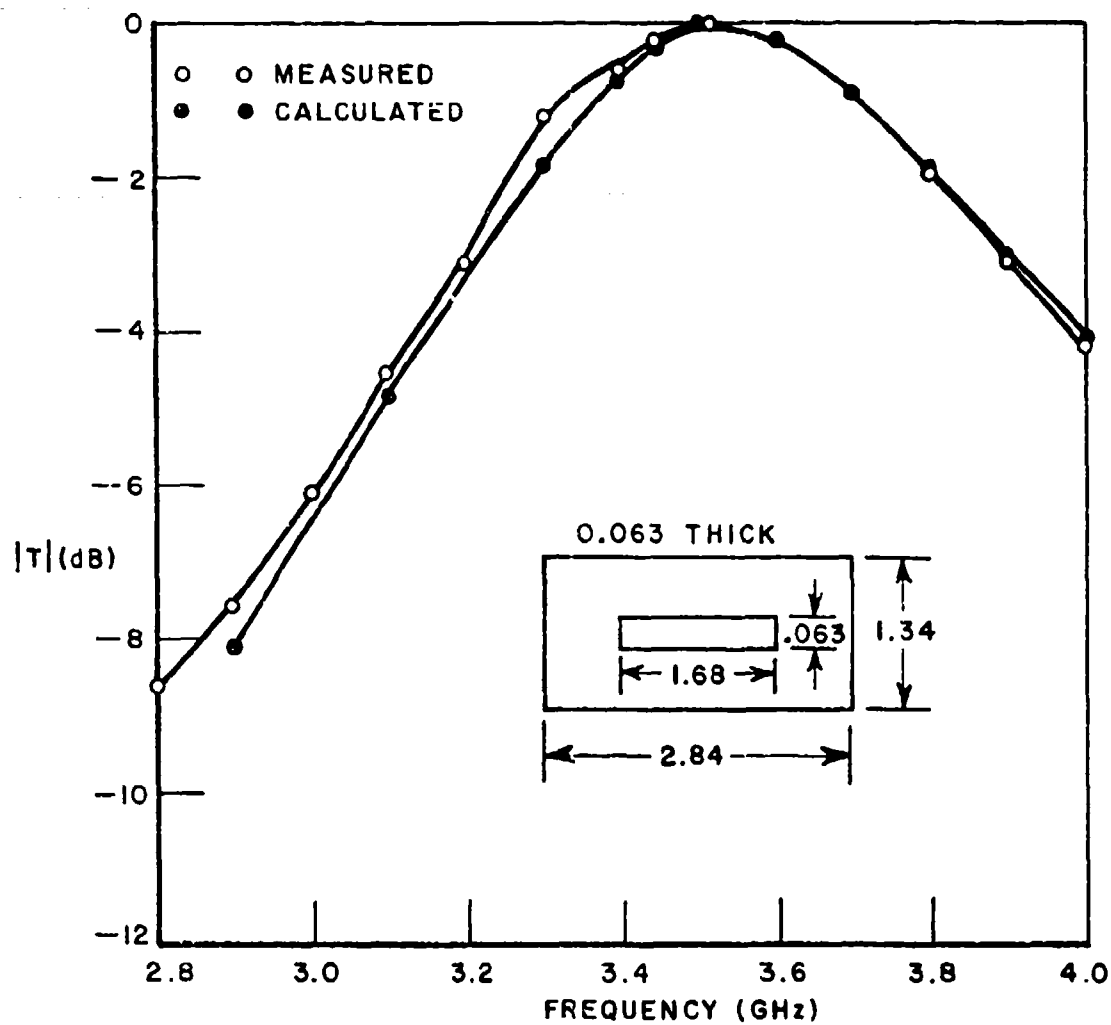


Figure 2-5.--Calculated and measured values of the transmission coefficient for a 0.063" thick rectangular slot in a waveguide vs. frequency.

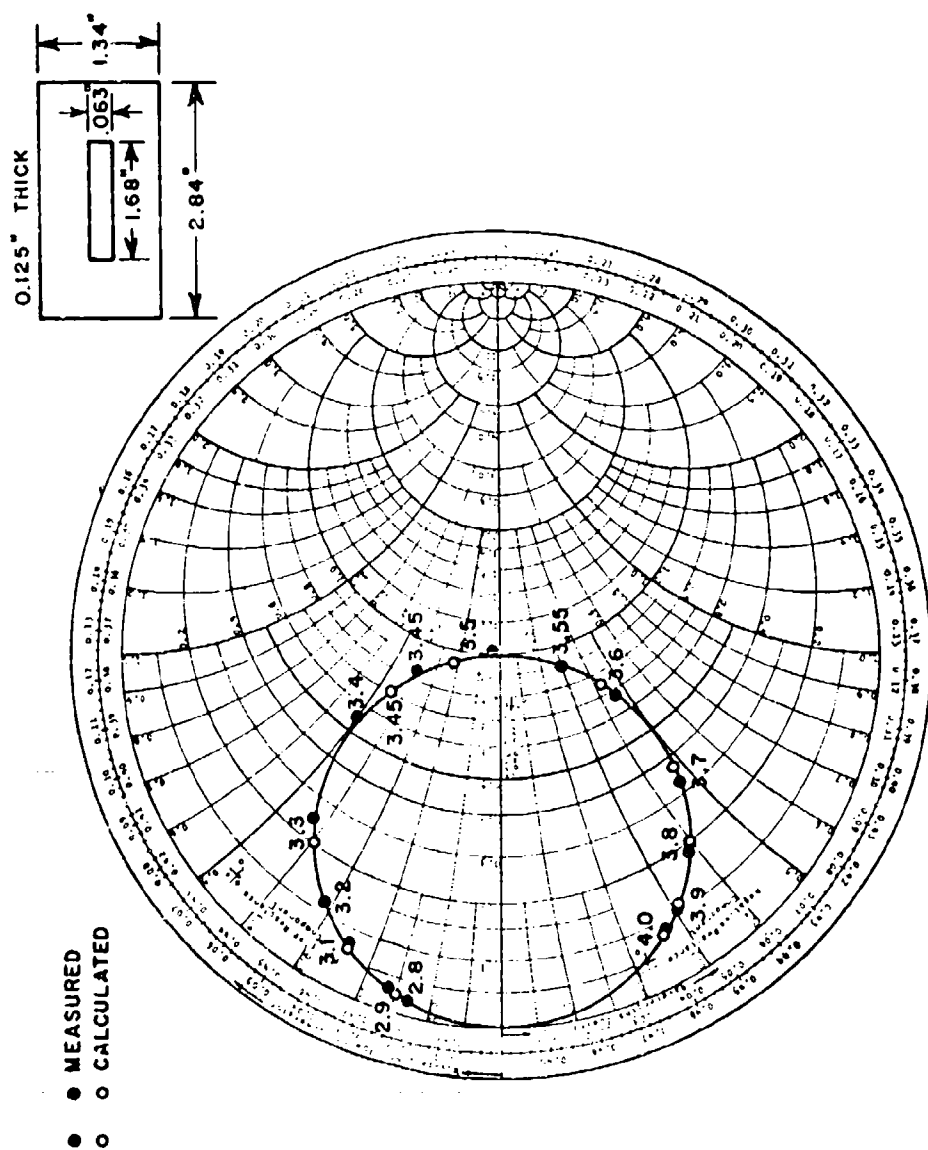


Figure 2-6.--Calculated and measured values of the equivalent impedance Z_{eq} for a 0.125" thick rectangular slot in a waveguide vs. frequency.

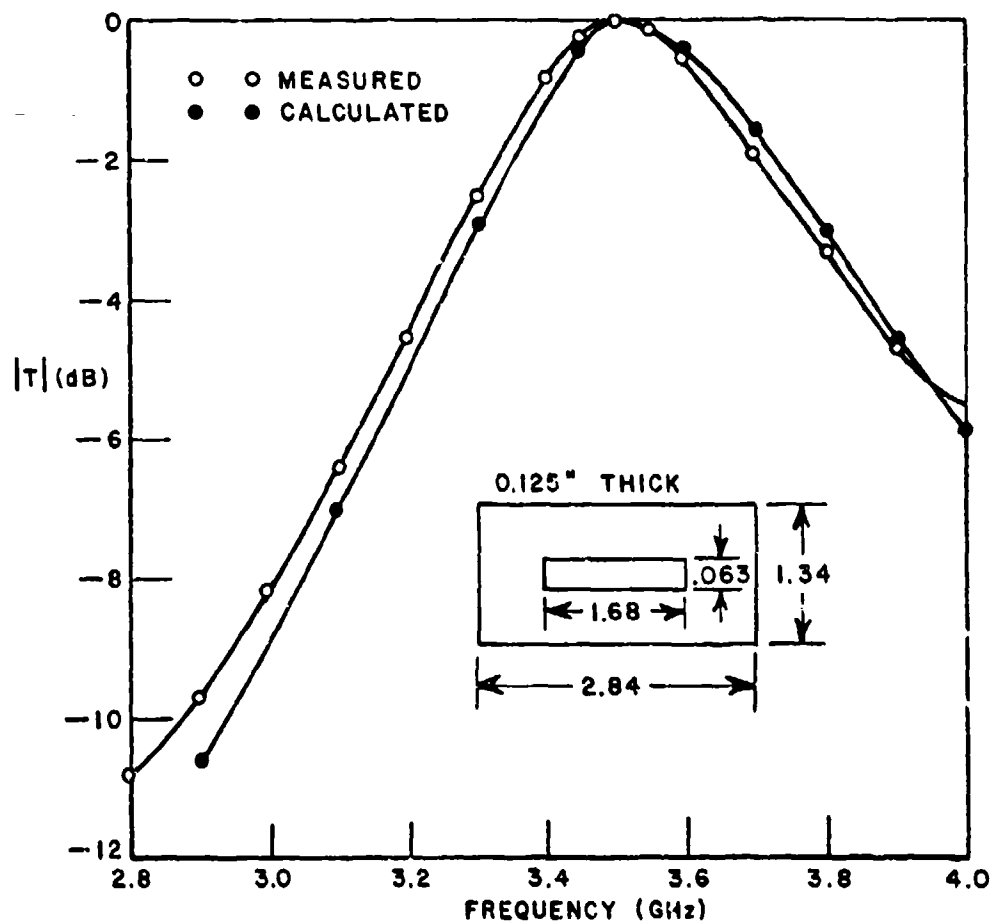


Figure 2-7.--Calculated and measured values of the transmission coefficient for a 0.125" thick rectangular slot in a waveguide vs. frequency.

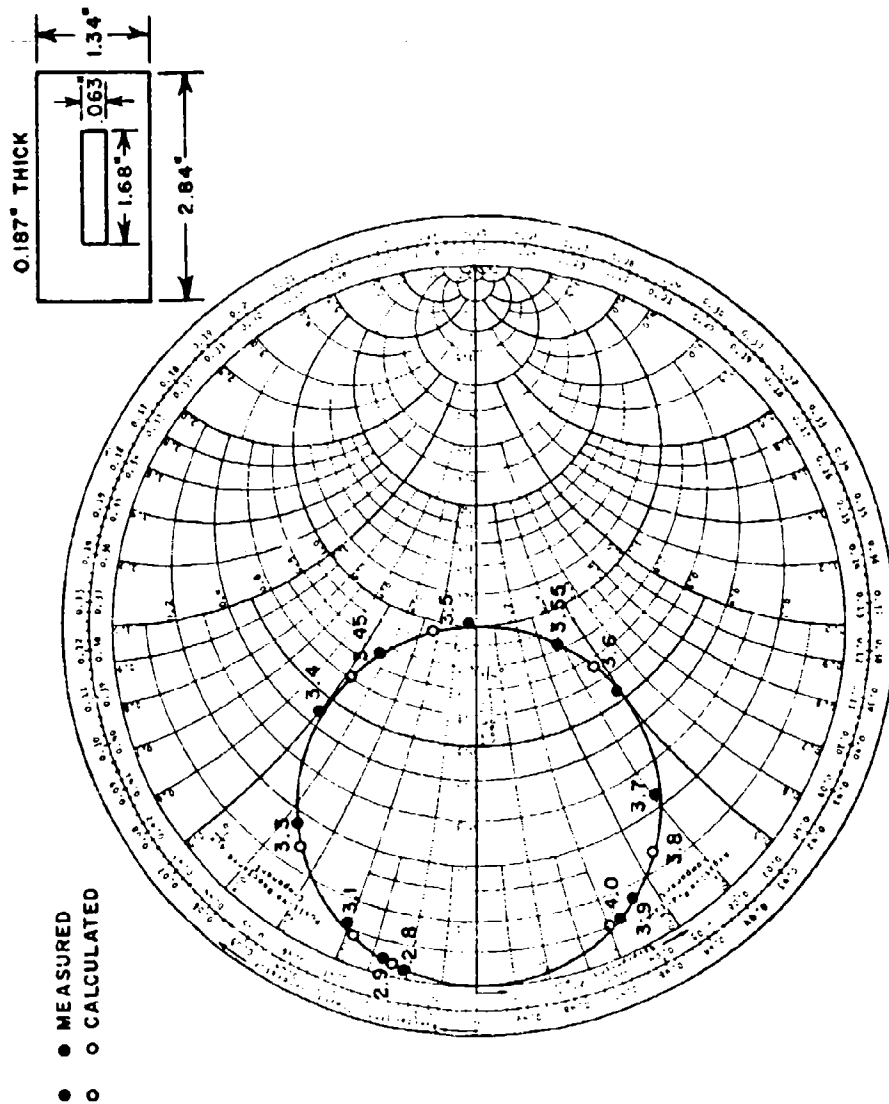


Figure 2-8.--Calculated and measured values of the equivalent impedance Z_{eq} for a 0.187" thick rectangular slot in a waveguide vs. frequency.

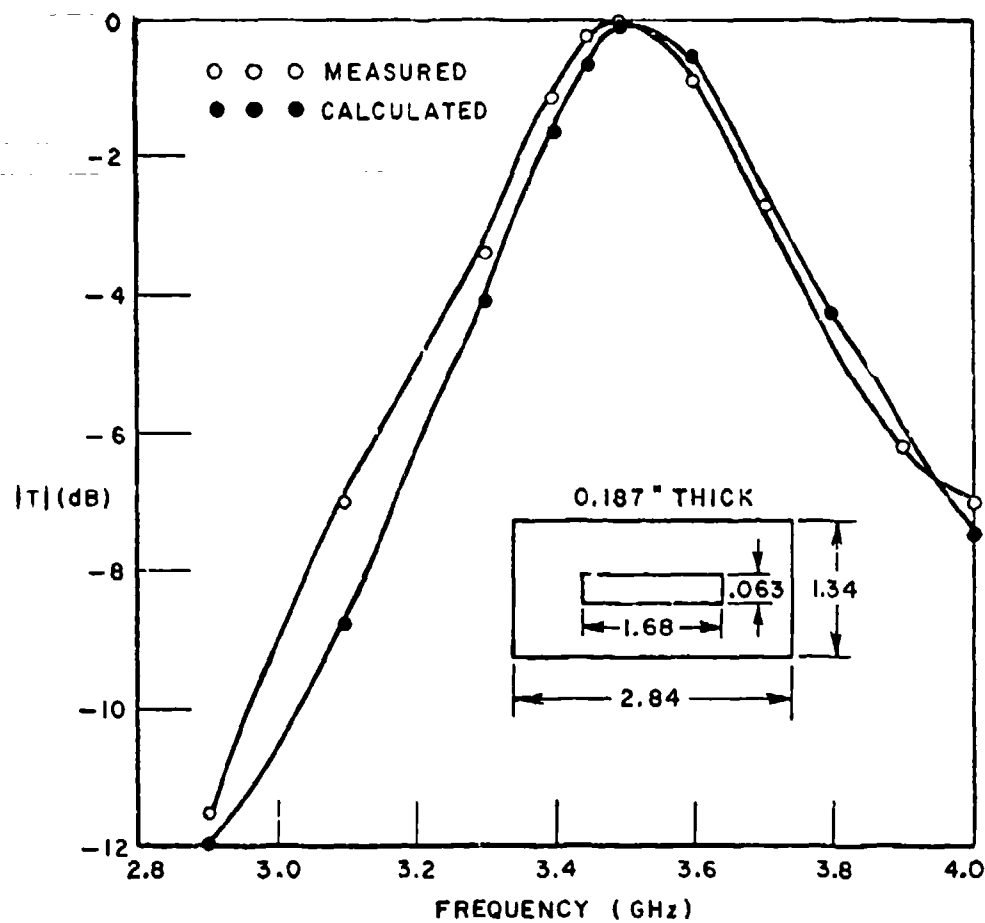


Figure 2-9.--Calculated and measured values of the transmission coefficient for a 0.187" thick rectangular slot in a waveguide vs. frequency.

B. Finite Conductivity

For thin slots (i.e., $\lambda < .1875"$ at S-band) the agreement between measured and calculated values of the equivalent impedance of the slot was excellent. However, the thickest measured slot ($\lambda > \lambda$) did not show such good agreement between measurements and calculations using the modal analysis method as described previously. The calculations predicted perfect transmission at resonance, whereas the measurements showed an appreciable transmission loss. Using a simple perturbational method, Harrington [41] gives the attenuation constant due to imperfectly conducting guide walls as

$$(2-26) \quad \alpha = \frac{R}{h\eta\sqrt{1 - (f_c/f)^2}} \left[1 + \frac{2h}{t} (f_c/f)^2 \right]$$

where R = surface resistance, $\eta = \sqrt{\frac{\mu}{\epsilon}}$, f_c = the cutoff frequency of the waveguide, and t and h are shown in Fig. 2-1. The waveguide of region a is operated well above cutoff, so that very little attenuation occurs. However, for a narrow (i.e., $h \ll \lambda$) slot at resonance, $t \approx \lambda/2$, so that resonance occurs at approximately the cutoff frequency of waveguide b (i.e., the slot), and $f \approx f_c$. Note that for $f = f_c$, Eq. (2-26) predicts $\alpha \rightarrow \infty$. Obviously this simple perturbational approach to finite conductivity of the waveguide is not valid near cutoff. However, it serves to indicate that the finite conductivity of the slot will have a definite effect on the transmission properties of a thick slot.

In order to account for the effects of finite conductivity of the slot walls near cutoff one must consider the mode coupling due to the surface currents. Collin [42] gives equations which contain the propagation constant γ as a function of the TE and TM mode coupling due to finite conductivity. For TE_{r0} modes the equations can be solved for γ . Substituting the correct values for the mode numbers we obtain

$$(2-27) \quad \frac{(\gamma_j^2 - \Gamma_j^2) j \omega \mu t h}{2 Z_m} + \left[\left(\frac{r\pi}{t} \right)^2 - \left(\frac{2\pi}{\lambda} \right)^2 \right] (2h+t) \\ - \frac{\Gamma_j^2}{2 \left[\left(\frac{r\pi}{t} \right)^2 - \left(\frac{2\pi}{\lambda} \right)^2 \right]} \cdot \frac{r^2 \pi^2}{t} = 0$$

Solving for γ_j^2 ,

$$(2-28) \quad \gamma_j^2 = \frac{-2 Z_m}{j\omega\mu} \left[r^2 \pi^2 \cdot \frac{2}{t^3} + \frac{4\pi^2}{h\lambda^2} \right] + r_j^2$$

where λ = free space wavelength and Z_m is the wave impedance of the metal panel containing the slot and is given by

$$(2-29) \quad Z_m = \left(\frac{j\omega}{2\sigma} \right)^{1/2} (1+j)$$

where σ is the conductivity of the metal. Note that for infinite conductivity Eq. (2-28) reduces to $\gamma_j^2 = r_j^2$ as expected. Using Eq. (2-28) to obtain γ_j , the scattering coefficient becomes

$$(2-30) \quad S_{jj} = \pm e^{-\gamma_j L}$$

The modes for waveguide b as given in Eqs. (2-4)-(2-6) are no longer correct, since they were derived for perfectly conducting walls. One can approximate the modes in the lossy waveguide by assuming that the shape of the waveguide modes, i.e., their sine-cosine dependence, remains unchanged but the wave admittance or ratio of H_y to E_x is changed. Using this approximation we have

$$(2-31) \quad y_{bj} = j\sqrt{\frac{\epsilon}{\mu}} \frac{\lambda}{2\pi} \left[\left(\frac{2\pi}{\lambda} \right)^2 - \left(\frac{r\pi}{t} \right)^2 \right] / \gamma_j$$

The calculations of reflection and transmission coefficients for lossy slots were made using the previously described modal analysis method except that Eqs. (2-30) and (2-31) were substituted for Eqs. (2-9) and (2-6) respectively. In order to evaluate the modal analysis method as modified to include losses a 4.1 inch long slot with $t=1.687$ inch, $h=.0625$ inch was machined from brass and measured. Some of the measured and calculated values of Z_{eq} for this slot are plotted in Fig. 2-10. The improvement gained by modifying the modal analysis method to account for the finite conductivity losses are shown by plotting calculated values for both the lossless and lossy cases. For these calculations the D.C. conductivity of brass ($\sigma = 1.43 \times 10^7$ mho/meter) was used. Although the agreement between the measured and calculated values of Z_{eq} is not as good as for the thinner slots, it is still quite good

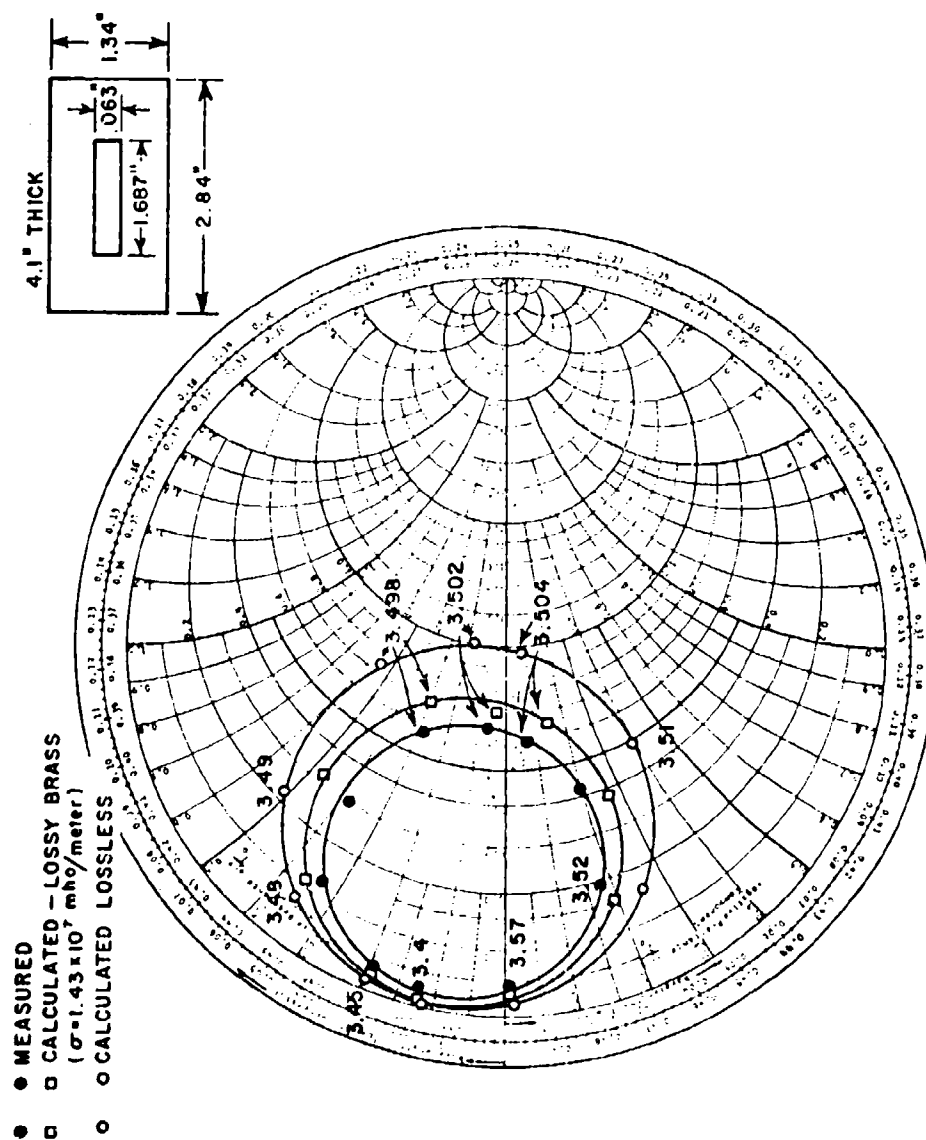


Figure 2-10.--Calculated and measured values of the equivalent impedance Z_{eq} for a 4.1" thick rectangular slot in a waveguide vs. frequency. Calculated values for both a lossless slot and a slot with finite conductivity are shown.

As a further check on the finite conductivity calculations the transmission loss of the 4.1 inch long slot was measured at resonance and found to be 2.94 dB. Using the above value of conductivity the calculated loss was 1.49 dB. One possible source for this error is the surface roughness inside the slot caused by the machining process used in its manufacture. Marcuvitz [43] gives a value of effective conductivity for a machined brass surface as 1.17×10^7 mho/meter. Using this value the transmission loss at resonance was calculated as 1.67 dB. (This value of σ provided very little change in the positions of the calculated points in Figs. 2-11 and 2-12.) This slight improvement indicates that the surface roughness is not the major source of error.

Another possible source of heat loss is the slot end walls (the hatched area in Fig. 2-1). We believe that this loss could be calculated using perturbation techniques, since the fields at the wall surface can be calculated with modal analysis. However, we have not attempted these calculations.

The 4.1" long slot also illustrates another phenomenon of thick arrays, namely a second resonance which is a phenomenon of the thickness ℓ rather than transverse (i.e., t and h) dimensions. Figure 2-11 shows the Smith Chart plot of Z_{eq} for the second, or longitudinal resonance. The heat losses are somewhat lower than for the first resonance since the slot is not so near cutoff. The second resonance is also shown, perhaps more clearly, in Fig. 2-12.

Now that we can calculate the attenuation at resonance for a slot composed of some particular metal with a given conductivity, the natural question arises: How does this loss depend on the conductivity and frequency? To answer the first question let us assume that a wave is entering one end of a slot with attenuation α_1 nepers/meter and consequently the amplitude at the output is given by

$$(2-32) \quad E_1 = E_0 e^{-\alpha_1 \ell}$$

where

ℓ is the thickness of the slot and
 E_0 = amplitude at the beginning of slot.

If the conductivity is now changed from σ_1 to σ_2 , we obtain a new attenuation α_2 , i.e.,

$$(2-33) \quad E_2 = E_0 e^{-\alpha_2 \ell}$$

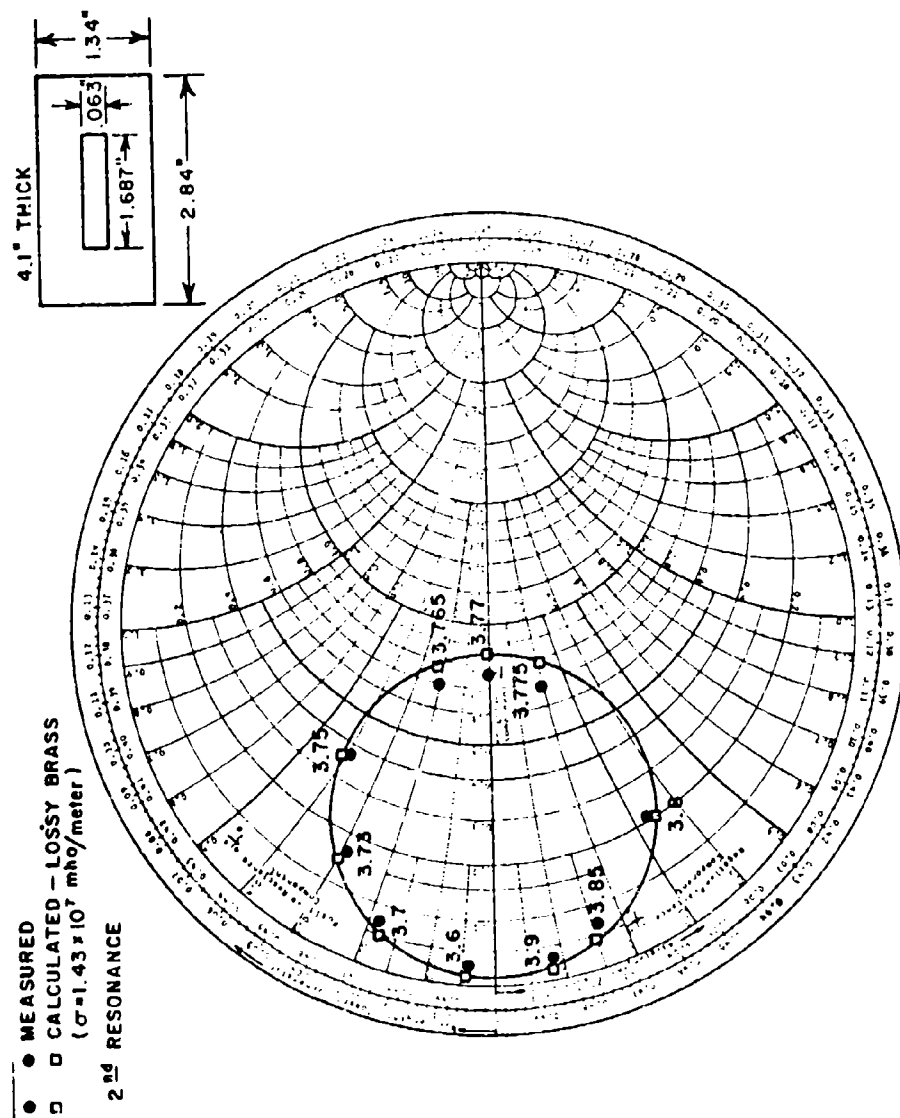


Figure 2-11.--Calculated and measured values of the equivalent impedance Z_{eq} for a 4.1" thick rectangular slot in a waveguide vs. frequency. This is a continuation of Fig. 2-10 and shows the second (longitudinal) resonance.

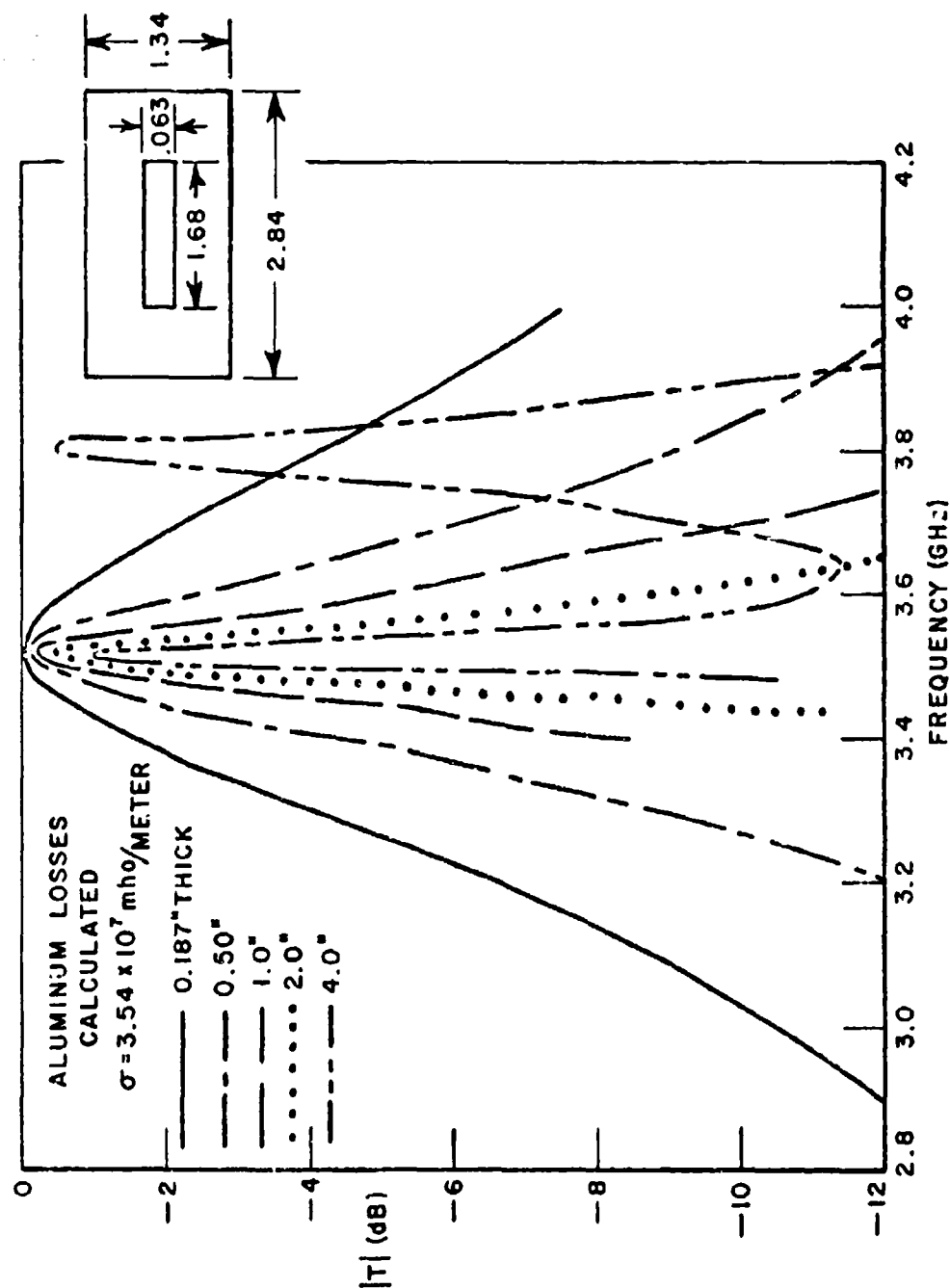


Figure 2-12.--Calculated values of the transmission coefficient for lossy aluminum slots of various thicknesses vs. frequency.

where we have assumed the field at beginning of the slot is unchanged, which is a fairly good approximation. We further know from the perturbational method that

$$(2-34) \quad \alpha_1 = C \sqrt{\frac{\omega\mu}{2\sigma_1}} \quad \alpha_2 = C \sqrt{\frac{\omega\mu}{2\sigma_2}}$$

is a good approximation, with C a constant for constant frequency.

Application of Eqs. (2-34) above readily yields

$$\begin{aligned} \alpha_2 l &= l C \sqrt{\frac{\omega\mu}{2\sigma_2}} = l C \sqrt{\frac{\omega\mu}{2\sigma_1}} \sqrt{\frac{\sigma_1}{\sigma_2}} \\ &= l \alpha_1 \sqrt{\frac{\sigma_1}{\sigma_2}} \end{aligned}$$

or

$$(2-35) \quad \alpha_2 l = \alpha_1 l \sqrt{\frac{\sigma_1}{\sigma_2}}$$

Most of the calculations and measurements of loss in the present Chapter have been performed in the S-band frequency range for practical reasons. However, periodic arrays of slots find important applications at higher as well as lower frequencies and it is therefore pertinent to establish a law which yields the transmission loss when a slot array is scaled to operate at a different frequency. Let us again assume that the attenuation through the slots at frequency f_1 is given by

$$(2-32) \quad E_1 = E_0 e^{-\alpha_1 l}$$

where

l = thickness of slot (plate thickness)

and from Eqs. (2-26) and (2-29)

$$(2-36) \quad \alpha_1 = \frac{\sqrt{\frac{\omega_1 \mu}{2\sigma}}}{h n \sqrt{1 - \left(\frac{f_c}{f}\right)^2}} \left[1 + \frac{2h}{t} \left(\frac{f_c}{f}\right)^2 \right] .$$

If we further assume that all dimensions of the slot array except the thickness λ are scaled with a certain factor N defined by

$$(2-37) \quad N = \frac{f_2}{f_1} ,$$

we know that all frequency ratios $\frac{f}{f_c}$ are unchanged such that the new attenuation constant α_2 is by application of Eq. (2-36) given by

$$(2-38) \quad \alpha_2 = \frac{\sqrt{\frac{\omega_2 \mu}{2\sigma}}}{\frac{h}{n} \eta \sqrt{1 - \left(\frac{f_c}{f}\right)^2}} \left[1 + \frac{2h}{t} \frac{N}{N} \left(\frac{f_c}{f}\right)^2 \right]$$

or

$$(2-39) \quad \alpha_2 \lambda = \alpha_1 \lambda N^{3/2} .$$

In words, Eq. (2-39) says that if a slot array at frequency f_1 is scaled to a new frequency f_2 such that all dimensions except the thickness are divided by $N = \frac{f_2}{f_1}$, the new loss in dB is equal to the old loss multiplied by $N^{3/2}$. If, however, the thickness λ is also reduced with the factor N , we see from Eq. (2-39) that the loss is now only proportional to $N^{1/2}$.

We will now present some calculated data concerning transmission properties of rectangular slots of various sizes and thicknesses with finite conductivity. Figure 2-12 shows the transmission coefficients for smooth, aluminum slots of varying thicknesses and dimensions of $t=1.68"$, $h=.0625"$. It is evident that the bandwidth decreases as the slot becomes thicker. Also evident is the longitudinal resonance for the 4" thick slot which was discussed earlier. For the thin slots the losses are too small to be seen in Fig. 2-12, so they are tabulated in Table 1 for both aluminum and brass. Note that the loss at resonance is approximately proportional to the thickness λ of the slot, which agrees with Eq. (2-35) and Eq. (2-39).

TABLE 1
CALCULATED LOSSES AT RESONANCE
1.68 x 0.0625 x λ SLOT IN S-BAND W.G.

	λ inches	$ T $ dB
Aluminum LOSSES $\sigma = 3.54 \times 10^7$ mho/meter	.0625	-.017
	.125	-.041
	.1875	-.0651
	.5	-.128
	1	-.2526
	2.0	-.497
	4.0	-.966
BRASS LOSSES $\sigma = 1.43 \times 10^7$ mho/meter	.0625	-.026
	.125	-.06
	.1875	-.094
	2.0	-.77
	4.0	-1.49 dB

It is evident from Table 1 that the loss at resonance is dependent on the conductivity of the metal composing the slot. The dependence is illustrated in the curve of Fig. 2-13 which shows an actual computed example (mode theory) of the transmission loss. Also shown in Fig. 2-13 is a curve derived from Eq. (2-35) (infinitely long guide solution). As a reference point we have chosen $\alpha_1 = 0.2$ dB and $\sigma_1 = 1.43 \times 10^7$ mho/meter (corresponding to brass). As can be seen the approximate formula as given by Eq. (2-35) agrees very well with the modal solution loss for values of conductivity σ within practical limits. A computed example (using modal analysis) of the dependence of loss on frequency is shown in Fig. 2-14 for a .25" thick aluminum slot. Also shown is a curve calculated using Eq. (2-39) normalized at $N=4$ with $\alpha_1 \lambda = 0.18$ dB. As can be seen the agreement between the two approaches is very good over the entire range.

As shown in Eq. (2-38) the loss is inversely proportional to the width h of the slot, so that the loss at resonance may be decreased by widening the slot. Resonance curves for somewhat wider slots are shown in Figs. 2-15 and 2-16. Note that widening the slots does not greatly affect the resonant frequency but does result in a wider bandwidth. If the slots are made even wider the resonant properties of the slots may change drastically, as shown in Figs. 2-17 and 2-18. The data in these figures was calculated using the modal analysis method, but with fewer modes in the waveguide since the discontinuity is not as abrupt.

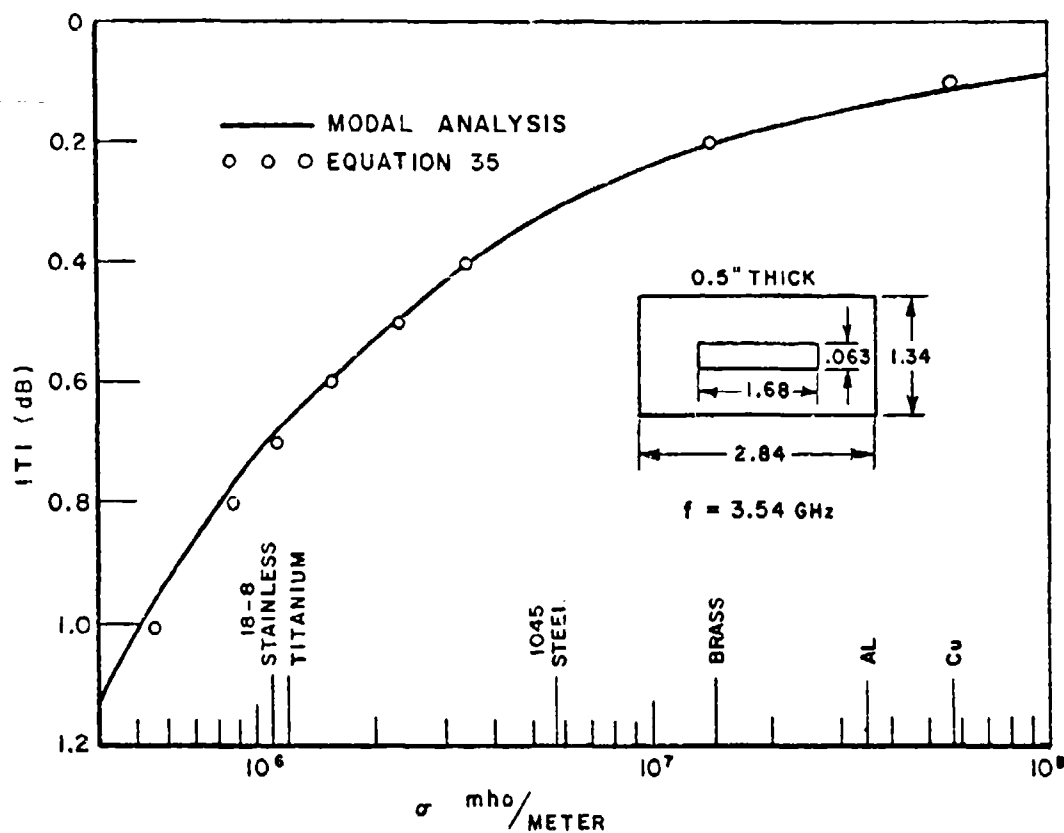


Figure 2-13.--Calculated loss at resonance (3.5 GHz) vs. conductivity for a 0.5" thick rectangular slot in a waveguide.

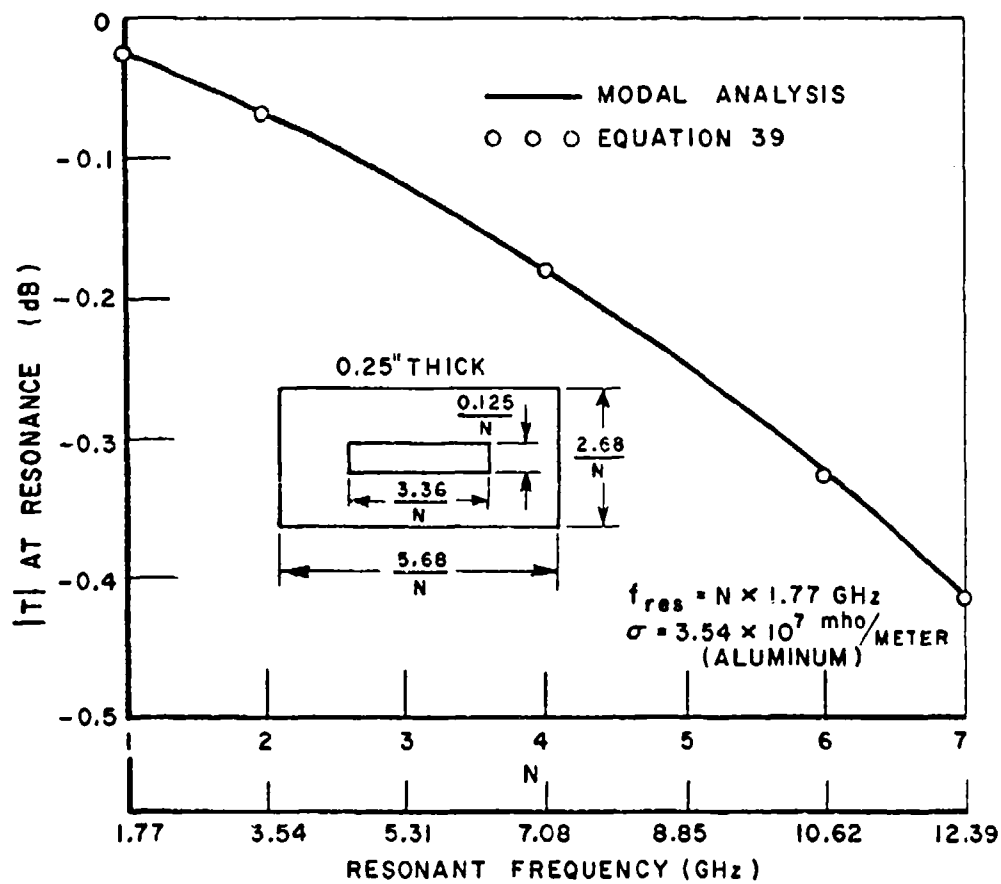


Figure 2-14.--Calculated loss at resonance vs. resonance frequency for a 0.25" thick slot in a waveguide.

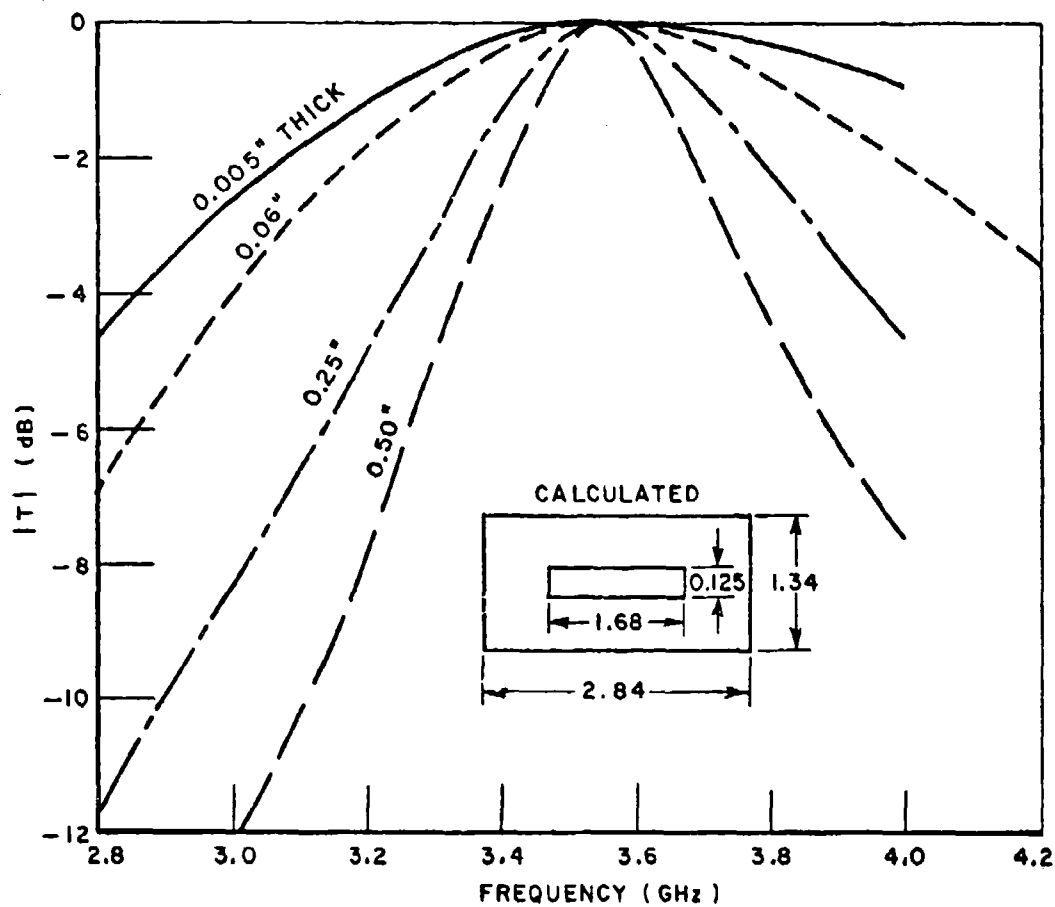


Figure 2-15.--Calculated values of the transmission coefficient vs. frequency for 0.125" wide rectangular slots of various thicknesses in a waveguide.

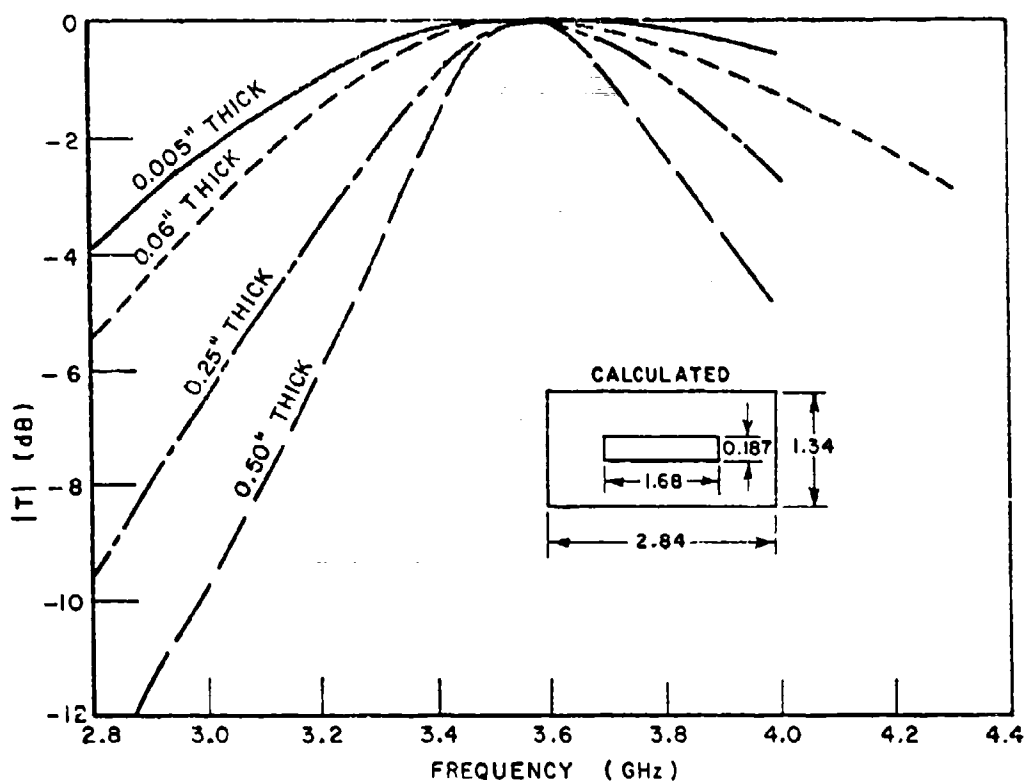


Figure 2-16.--Calculated values of the transmission coefficient vs. frequency for 0.87" wide rectangular slots of various thicknesses in a waveguide.

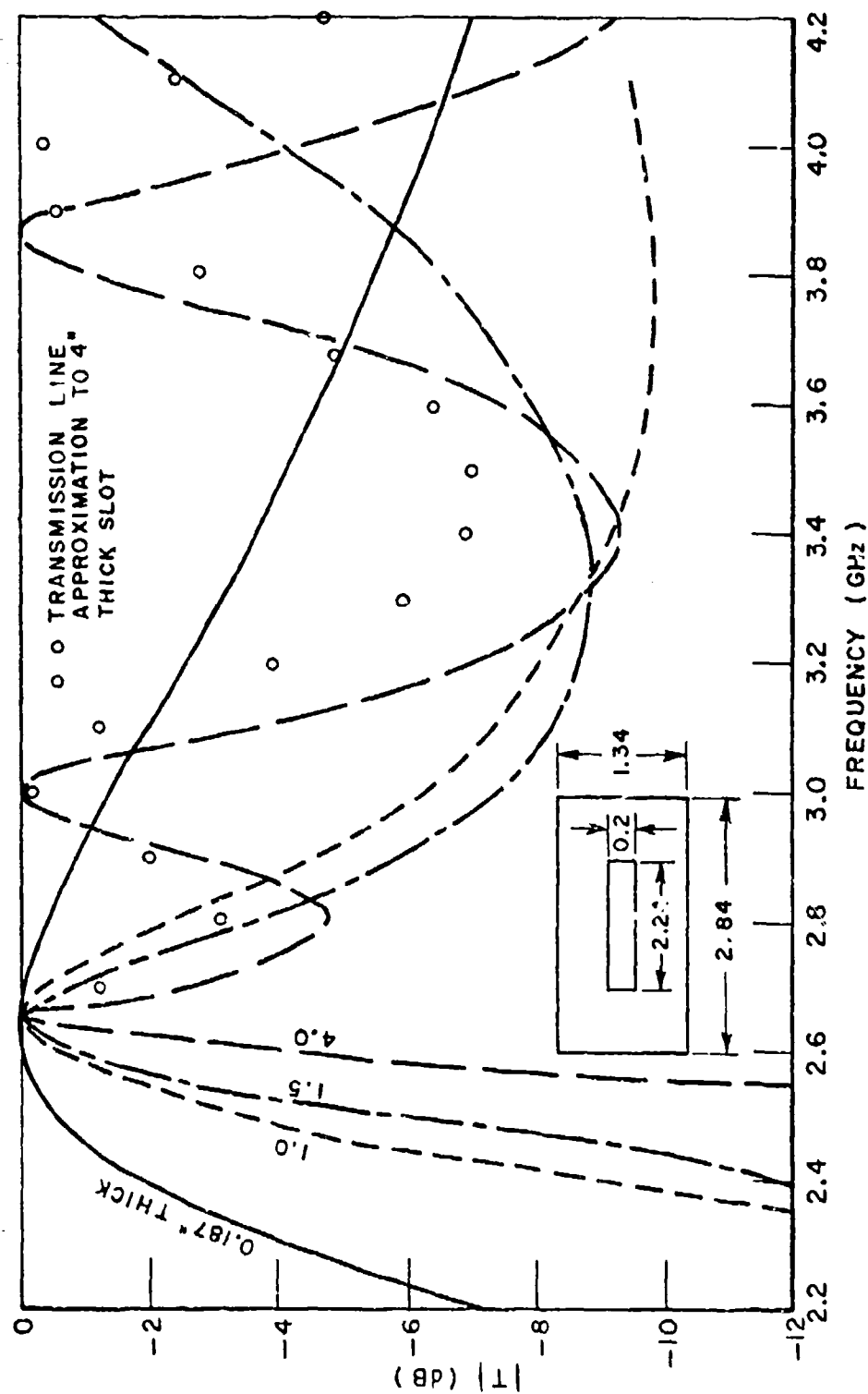


Figure 2-17.--Calculated values of the transmission coefficient vs. frequency for 0.2" wide rectangular slots of various thicknesses in a waveguide.

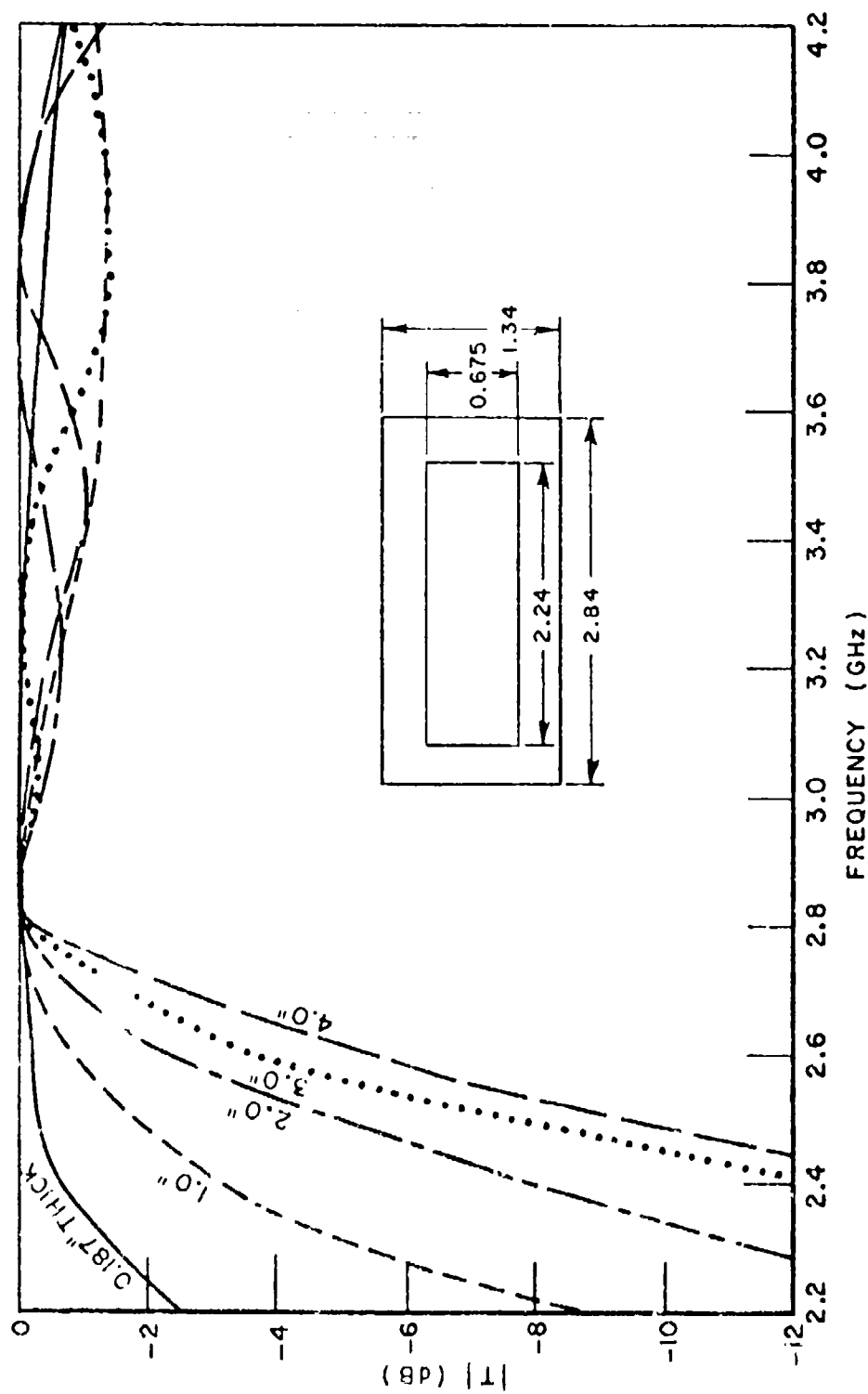


Figure 2-18.--Calculated values of the transmission coefficient vs. frequency for 0.675" wide rectangular slots of various thicknesses in a waveguide.

The previously noted longitudinal resonances are shown clearly in Fig. 2-17. Also shown are approximate results for the 4.0" thick slot, obtained by using transmission line theory without including the effects of the higher order modes excited at the waveguide-slot interfaces. Since this approximation agrees qualitatively with the modal analysis result we may conclude that the second and third resonances shown here are indeed dependent on longitudinal rather than transverse dimensions.

In Fig. 2-18 the resonant nature of the slot is almost completely gone. The slot in Fig. 2-18, if loaded with dielectric to lower its cutoff frequency, would correspond to a waveguide pressure window. It is evident from Figs. 2-17 and 2-18 that when widening the resonant slots in order to reduce losses one must not widen them so much that the resonant properties of the slot are destroyed.

C. The Effect of Plate Thickness on Babinet's Principle

As the panel is made thinner and thinner one expects to approach more and more closely the limiting case of an infinitesimally thin panel, where Babinet's principle applies exactly. That this is the case is illustrated in Fig. 2-19, where we have again plotted the

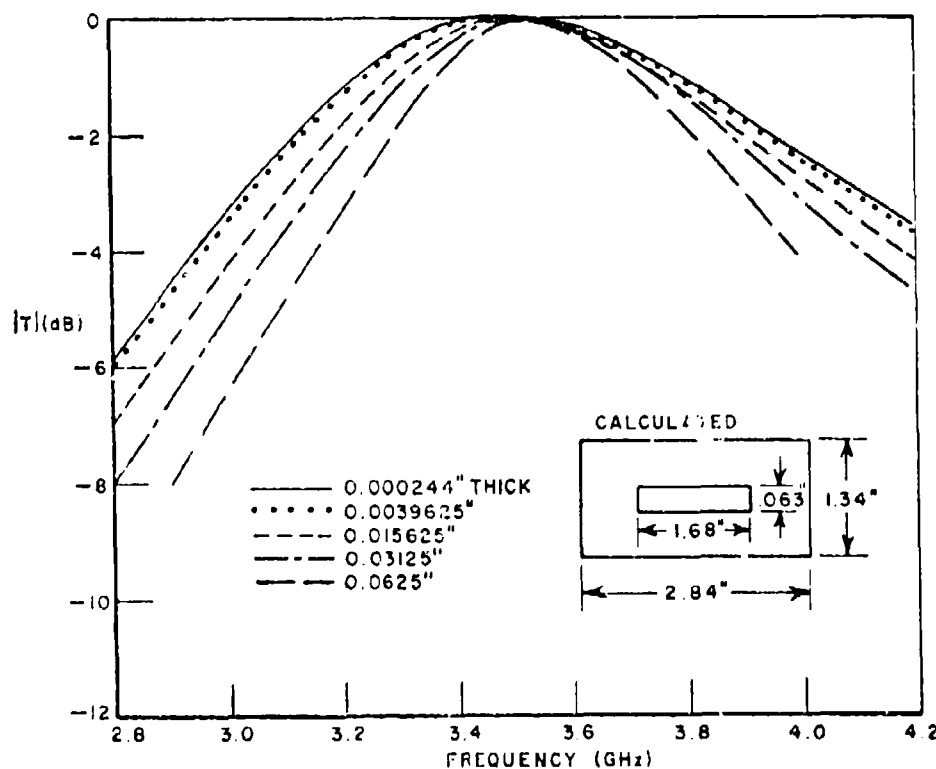


Figure 2-19.--Calculated values of the transmission coefficient vs. frequency for very thin rectangular slots in a waveguide.

transmission coefficient for a narrow rectangular slot in a waveguide as a function of thickness. It is evident that as the slot panel is made thinner a limiting case is being approached. This is further illustrated by combining the data of Figs. 2-12 and 2-19 in order to plot the curve of bandwidth vs thickness shown in Fig. 2-20. To generalize even further, the curve in Fig. 2-20 is replotted in terms of per cent bandwidth, with the panel thickness normalized to wavelengths (at resonance). From Fig. 2-21 it is clear that for a resonant slot the greatest effects of thickness are in the range from $.001\lambda$ to 2.0λ . For greater thicknesses one is approaching the infinitely thick case, while for lesser thicknesses one is approaching the infinitesimally thin case. Thus, in order to apply Babinet's principle to obtain bandwidth figures accurate to within a few per cent the panel thickness should be less than $.001\lambda$.

D. Conclusions

By generalizing the preceding data on arrays of narrow, resonant rectangular slots to the periodic array geometry one can draw the following conclusions:

- (1) As the array is made thicker, the bandwidth will decrease.
- (2) If the array is made very thick, longitudinal resonances will appear, and will be closer to the first (lowest frequency) resonance.
- (3) No matter how thick the array is made, there can be complete transmission at resonance for a perfectly conducting panel.
- (4) The Joule heating losses due to the finite conductivity of the slot wall for an array of resonant, rectangular slots as described herein will be approximately 1 dB for a 4" thick aluminum slot at S-band, and will decrease to less than .02 dB for a 1/16" thick aluminum slot. At X-band a .25" thick slot will have approximately .3 dB loss. Loss is proportional to thickness, to the square root of the conductivity, and to the $3/2$ power of the frequency scale ratio for constant panel thickness.
- (5) Attempting to decrease the losses by widening the slots will degrade and finally destroy the resonant properties of the slot array if the slots are too wide.
- (6) In order to use Babinet's principle to calculate the bandwidth to within a few per cent, the slot array must be thinner than $.001\lambda$.

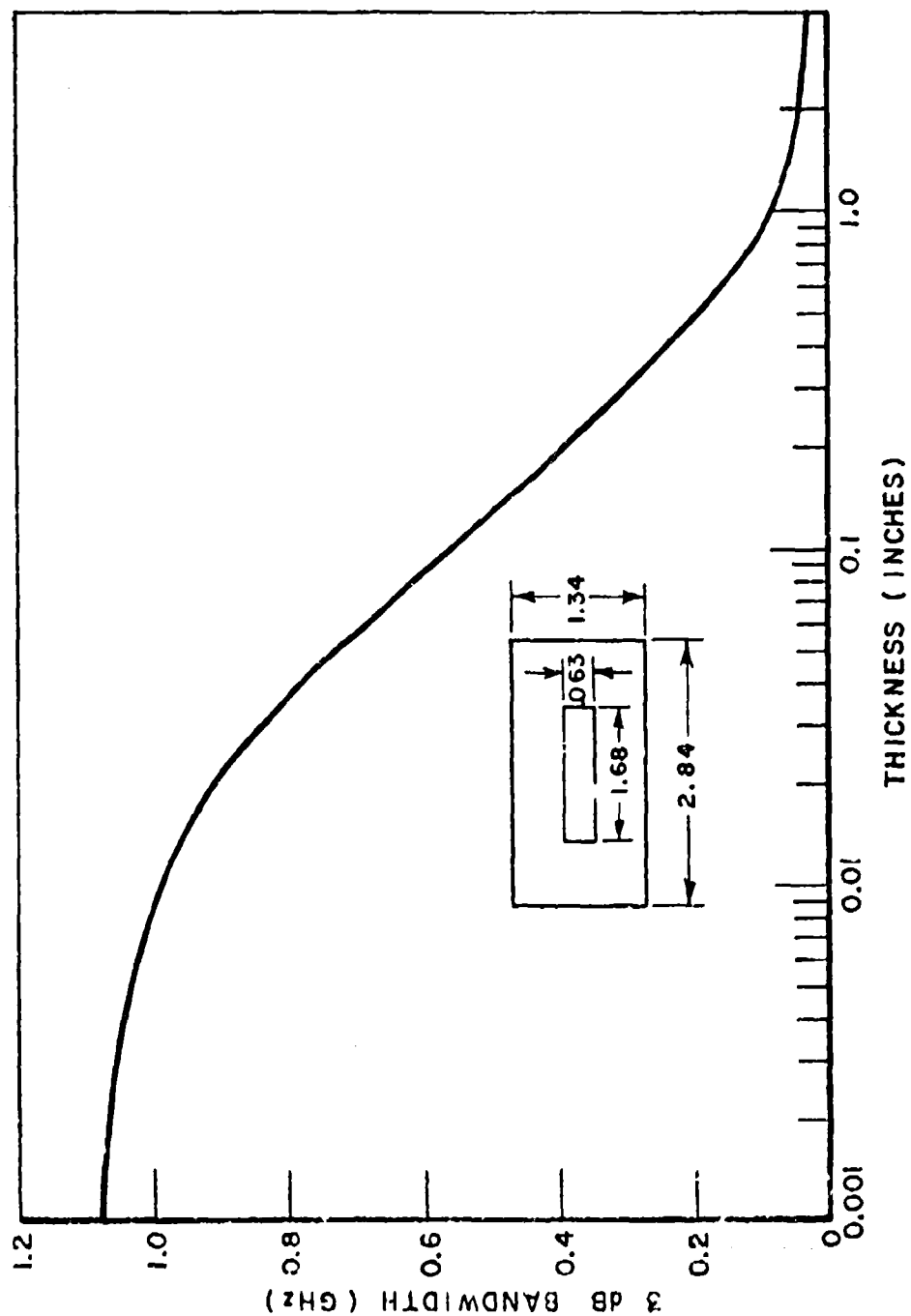


Figure 2-20.--Calculated values of the 3 dB bandwidth vs. slot thickness for a rectangular slot in a waveguide.

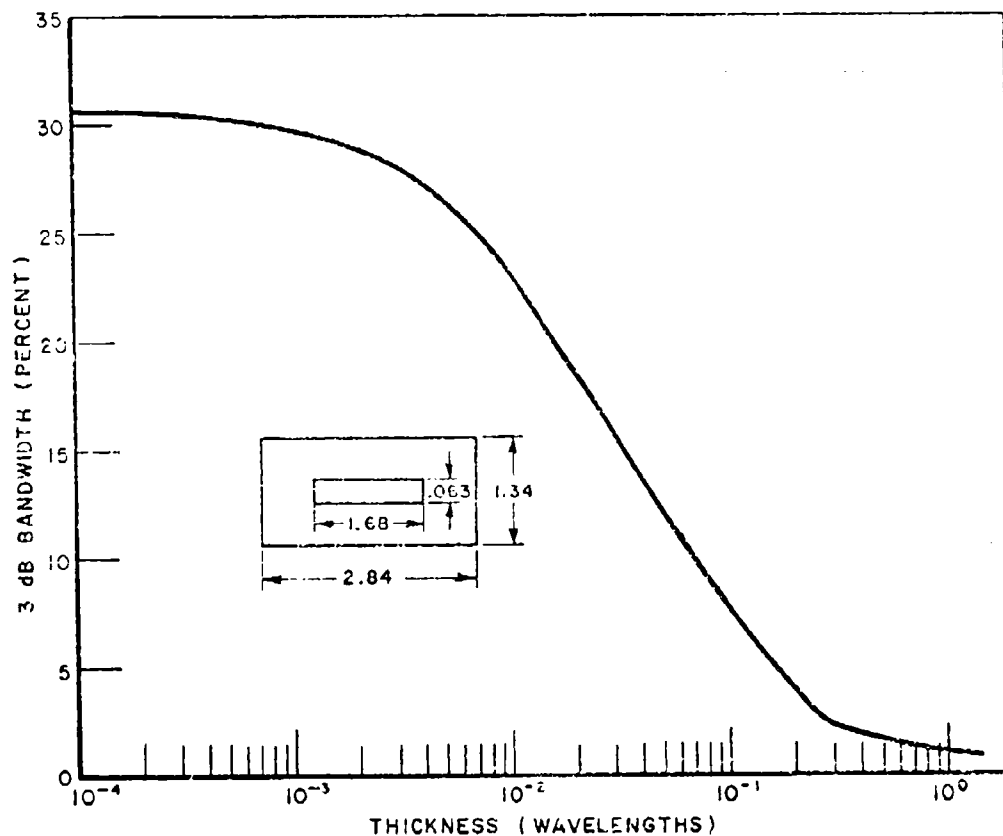


Figure 2-21.--Calculated values of the 3 dB bandwidth in % vs. thickness in wavelengths for a rectangular slot in a waveguide.

Other thickness effects which involve changing incidence angles and dielectric layers will be considered in Chapter IV. However, these basic conclusions reached here for a slot in a waveguide are applicable to slots in a periodic array, and are important in the understanding of the effects of finite thickness on resonant periodic slot arrays.

CHAPTER III MODAL EXPANSIONS

In this chapter we will present the orthogonal mode sets used to describe the fields resulting from a plane wave incident on a periodic slot array. One mode set, the Floquet, is used to describe the fields exterior to the slot array. This mode set will be modified to include the effects of planar dielectric layers adjacent to the array. The fields within the slots will also be expanded in orthogonal modes. Rectangular, single loaded, 4-legged symmetric, and 3-legged symmetric slots will be considered. For the rectangular slot rectangular waveguide modes will be used. This same mode set was also used for the rectangular waveguide problem of Chapter II. For the other slot shapes approximate mode sets will be derived from either the rectangular or coaxial waveguide modes.

A. Floquet Modes

In the exterior region we will use the Floquet mode set developed for the analysis of phased array antennas [28]. The geometry and coordinate system is shown in Fig. 3-1. The direction of the incident plane wave is indicated by the conventional spherical coordinates θ and ϕ , where θ is the angle from the z-axis to the propagation axis of the incident plane wave, and ϕ is the angle from the x-axis to the projection of the propagation axis on the x-y plane.

1. With no dielectric layer

A more general arrangement of the slots is shown in Fig. 3-2. Here the slots are arranged in a periodic grid along the S_1 and S_2 skewed coordinates. Thus we are not limited to a rectangular grid. The spacing between the slots is d_x and e measured along the S_1 and S_2 axes respectively. The central periodic cell is shown in Fig. 3-2. Other identical periodic cells are centered on each slot in the array. If the array is large enough so that Floquet's theorem applies, then the electric and magnetic fields at any point in one of the periodic cells will differ from that at the corresponding point in another of the periodic cells only by a difference of phase. Furthermore, this difference of phase will depend only on the propagation vector direction of the incident plane wave. If we denote the vector propagation constant of the incident plane wave as K_0 , then a complete set of solutions to the scalar wave equation which satisfies the Floquet conditions is [28]

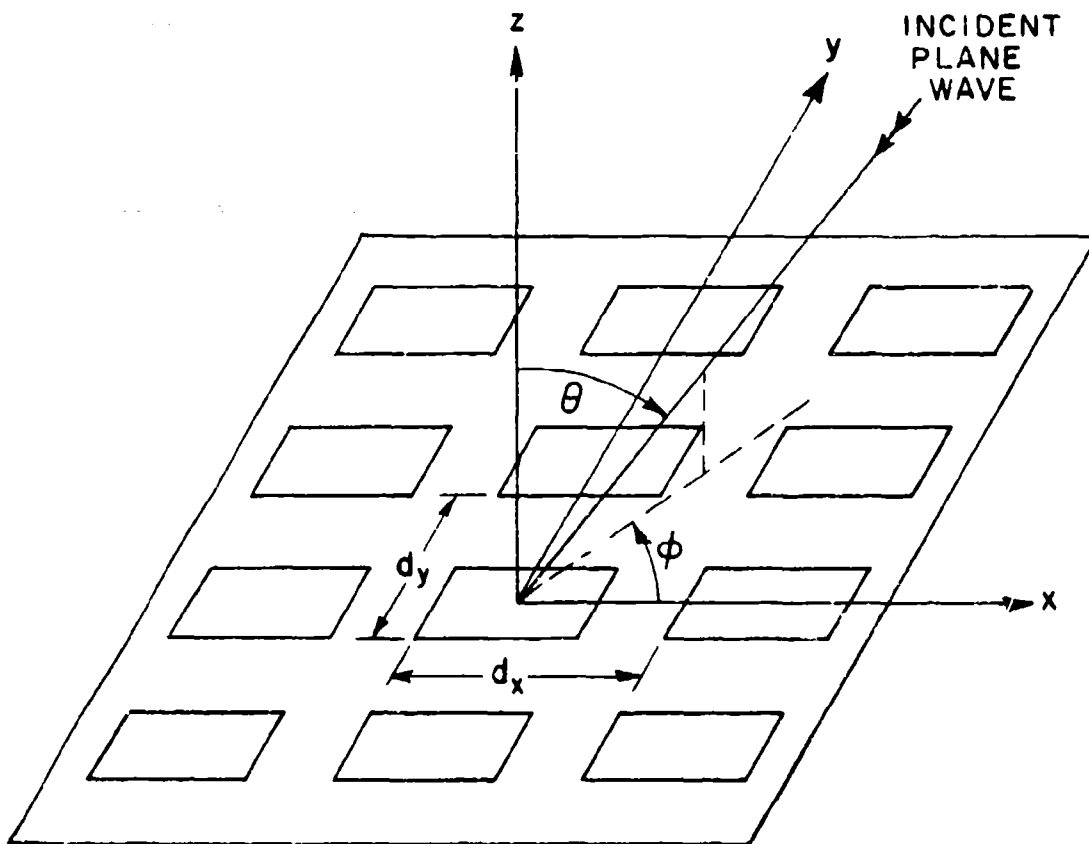


Figure 3-1.--Geometry and coordinate system for a plane wave incident on a periodic slot array.

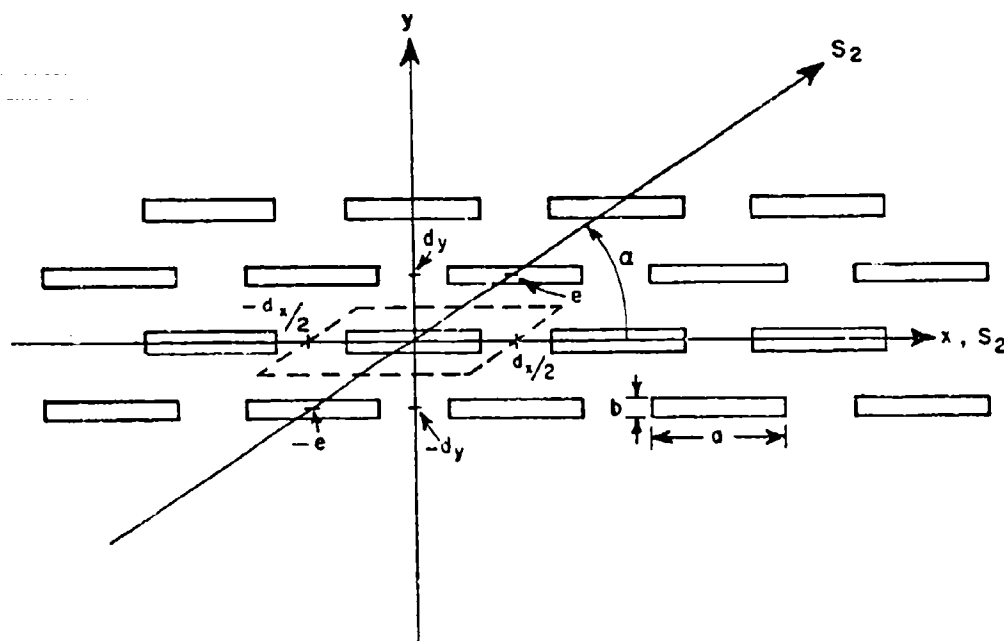


Figure 3-2.--Details of array geometry showing skewed coordinate system and periodic cell.

$$(3-1) \quad S_{pq} = \exp[-j(\bar{K}_0 \cdot \hat{S}_1 + \frac{2\pi p}{d_x})S_1] \exp[-j(\bar{K}_0 \cdot \hat{S}_2 + \frac{2\pi q}{e})S_2] \\ \exp[\pm j \gamma_{pq} z]$$

where p and $q = -\infty, \dots, -1, 0, 1, \dots, +\infty$, and $j = \sqrt{-1}$.

The projection of \bar{K}_0 on the S_1 axis is $\bar{K}_0 \cdot \hat{S}_1$; similarly for the S_2 axis. Note that if in Eq. (3-1) $\bar{K}_0 \cdot \hat{S}_1 = 0$, and S_1 is changed by $\pm m d_x$ (m an integer), then the value of S_{pq} is unchanged. If $\bar{K}_0 \cdot \hat{S}_1$ is not equal to zero and S_1 is changed by $\pm m d_x$, then the phase of S_{pq} is changed in accordance with the Floquet conditions.

Since measuring distances along the skewed axis S_2 is inconvenient, we now proceed to obtain S_{pq} as a function of x and y . From Fig. 3-3, the transformation between the skewed coordinates (S_1, S_2) and the orthogonal coordinates (x, y) of any given point p is

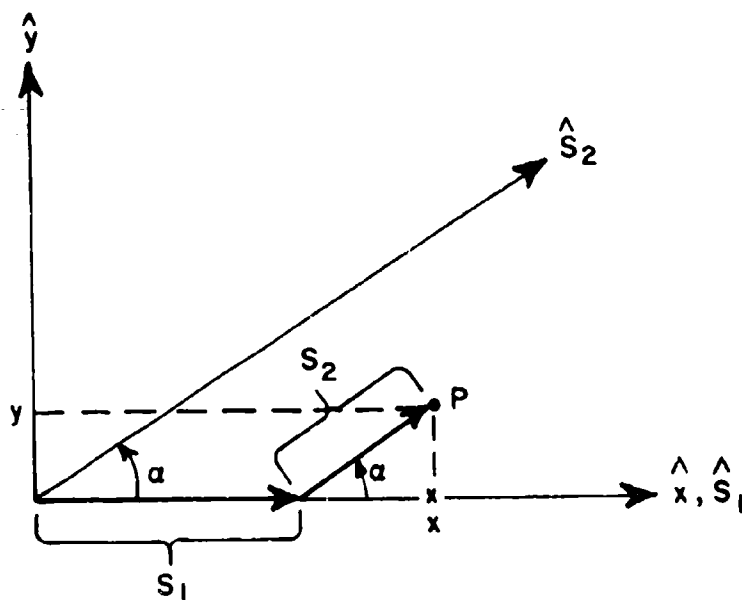


Figure 3-3.--Relationship between skewed coordinate system (S_1, S_2) and orthogonal (x, y) coordinate system.

$$(3-2) \quad S_1 = x - y \cot \alpha$$

$$(3-3) \quad S_2 = y / \sin \alpha$$

$$(3-4) \quad \hat{S}_1 = \hat{x}$$

$$(3-5) \quad \hat{S}_2 = \hat{x} \cos \alpha + \hat{y} \sin \alpha .$$

Substituting Eqs. (3-2) through (3-5) into Eq. (3-1) we obtain, after minor simplification,

$$(3-6) \quad S_{pq} = \exp[-j(\bar{K}_0 \cdot \hat{x} + \frac{2\pi p}{d_x} x)] \cdot \exp[-j(\bar{K}_0 \cdot \hat{y} + \frac{2\pi q}{e \sin \alpha} - \frac{2\pi p}{d_x \tan \alpha}) y] \\ \exp(\pm j \gamma_{pq} z).$$

If we now define

$$(3-7) \quad U_p = K_0 \sin \theta \cos \phi + \frac{2\pi p}{d_x}$$

$$(3-8) \quad V_{pq} = K_0 \sin \theta \sin \phi + \frac{2\pi q}{d_y} - \frac{2\pi p}{d_x \tan \alpha}$$

where $K_0 = \omega \sqrt{\mu_0 \epsilon_0}$, and where $d_y = e \sin \alpha$,

Eq. (3-6) may be written in the form

$$(3-9) \quad S_{pq} = \exp[-j(U_p x + V_{pq} y \pm \gamma_{pq} z)]$$

where U_p and V_{pq} are the propagation constants in the x and y directions respectively. Since S_{pq} must satisfy the scalar wave equation,

$$(3-10) \quad (\gamma_{pq})^2 + (U_p)^2 + (V_{pq})^2 = (K_0)^2$$

so that

$$(3-11) \quad \gamma_{pq} = \begin{cases} \sqrt{(K_0)^2 - (U_p)^2 - (V_{pq})^2} \\ \pm j \sqrt{(U_p)^2 + (V_{pq})^2 - (K_0)^2} \end{cases}$$

where the positive radical is chosen.

It is now a simple matter to construct a complete Floquet mode set as a combination of TE_z and TM_z modes. The electric and magnetic fields expressed in terms of these modes are

$$(3-12) \quad \vec{e}_{ai}^{(1)} = \frac{1}{T_{pq} \sqrt{d_x d_y}} (V_{pq} \hat{x} - U_p \hat{y}) \psi_{pq} \quad TE$$

$$(3-13) \quad \vec{e}_{ai}^{(2)} = \frac{1}{T_{pq} \sqrt{d_x d_y}} (U_p \hat{x} + V_{pq} \hat{y}) \psi_{pq} \quad TM$$

$$(3-14) \quad \vec{h}_{ai}^{(1)} = \frac{1}{T_{pq} \gamma_{pq} \sqrt{d_x d_y}} (U_p \hat{x} + V_{pq} \hat{y}) \psi_{pq} \quad TE$$

$$(3-15) \quad \bar{h}_{ai}^{(2)} = \frac{1}{T_{pq} \eta_{pq}^{(2)} \sqrt{d_x d_y}} (-V_{pq} \hat{x} + U_p \hat{y}) \psi_{pq} \quad \text{TM}$$

where the modal impedance η_{pq}^r is given by

$$(3-16) \quad \eta_{pq}^{(1)} = \frac{k_0}{\gamma_{pq}} \sqrt{\frac{\mu_0}{\epsilon_0}} \quad \text{TE}$$

$$(3-17) \quad \eta_{pq}^{(2)} = \frac{\gamma_{pq}}{k_0} \sqrt{\frac{\mu_0}{\epsilon_0}} \quad \text{TM}$$

with

$$(3-18) \quad \psi_{pq} = \exp(-j(U_p x + V_{pq} y \pm \gamma_{pq} z))$$

$$(3-19) \quad T_{pq}^2 = U_p^2 + V_{pq}^2$$

The superscript (1) or (2) denotes a TE or TM mode, the subscript "a" denotes that this mode expansion is for the region external to the slots, and the subscript i denotes the mode number. The mode $i=1$ corresponds to $p=q=0$, with other i values designed to other combinations of p and q values.

The $i=1$ modes are plane waves. In combination they can represent an incident, reflected, or transmitted plane wave from an arbitrary direction and with arbitrary polarization. The modal impedance η_{00}^r and the Z direction propagation constant γ_{00}^r are positive real numbers since these modes are always propagating modes. The modes for $i>1$ represent either evanescent modes or propagating grating lobes, depending upon whether γ_{pq} is imaginary or real, respectively.

For most applications the presence of propagating grating lobes is undesirable. By utilizing the above property of γ_{pq} a grating lobe diagram can be constructed which quickly shows whether or not propagating grating lobes can exist, and if so, for what scan angles [28]. Referring to Eq. (3-11) it is evident that when γ_{pq} changes from an imaginary to a real number it passes through zero. Setting $\gamma_{pq}=0$ in Eq. (3-11) and substituting for U_p and V_{pq} from Eqs. (3-7) and (3-8) we obtain

$$(3-20) \quad 0 = \left(\frac{2\pi}{\lambda}\right)^2 - \left(\frac{2\pi}{\lambda} T_x + \frac{2\pi p}{d_x}\right)^2 - \left(\frac{2\pi}{\lambda} T_y + \frac{2\pi q}{d_y} - \frac{2\pi p}{d_x \tan \alpha}\right)^2$$

where T_x and T_y are the direction cosines defined as $T_x = \sin\theta\cos\phi$, $T_y = \sin\theta\sin\phi$. Simple manipulation of Eq. (3-20) results in the equation

$$(3-21) \quad 1 = \left(T_x + \frac{p\lambda}{d_x}\right)^2 + \left(T_y + \frac{q\lambda}{d_y} - \frac{p\lambda}{d_x \tan\alpha}\right)^2.$$

Equation (3-21) is a family of circles with unit radius whose centers depend on p , q , and the array geometry.

For an example of the usefulness of Eq. (3-21) let us determine whether any propagating grating lobes can exist for the array of Fig. 3-2 when $d_x = \lambda$. For the array of Fig. 3-2 we then have $d_y = \lambda/3$, $\tan\alpha = 2/3$, and $d_x \tan\alpha = 2\lambda/3$. Substituting these values into Eq. (3-21) we obtain the grating lobe diagram of Fig. 3-4. For real space incidence angles T_x and T_y will be less than 1. Thus any circle which intersects the central circle indicates a possible propagating grating lobe. Four such possibilities are indicated in Fig. 3-4. For values of T_x and T_y which lie in one of the shaded areas the indicated Floquet mode will have a real value of γ_{pq} . Additionally, the $p=2, q=1$ and $p=-2, q=-1$ circles are just touching the center circle. Thus for these modes $\gamma_{pq}=0$, and these modes are just on the verge of becoming propagating grating lobes.

Let us now investigate the orthogonality properties of the above modes. Figure 3-5 shows a detailed drawing of the unit periodic cell of Fig. 3-2, here labeled ABCD. Also shown is a deformed cell, GHIJ, with the same height as the original cell but with acute angle β . We shall now proceed to show that

$$(3-22) \quad \int_{GHIJ} \vec{e}_{ai}^r \times \vec{h}_{aj}^{s*} \cdot \hat{z} \, ds = 0 \quad \begin{cases} i \neq j \\ \text{and/or} \\ r \neq s \end{cases}.$$

We shall first investigate the case where $i \neq j$. Referring to Eqs. (3-12) to (3-15) we have:

$$(3-23) \quad \int_{GHIJ} \vec{e}_{ai}^r \times \vec{h}_{aj}^{s*} \cdot \hat{z} \, ds = \int_{-\frac{d_y}{2}}^{\frac{d_y}{2}} \int_{-\frac{d_x}{2} + \frac{y}{\tan\beta}}^{\frac{d_x}{2} + \frac{y}{\tan\beta}} A \exp(-j U_p x - j V_{pq} y) \exp(j U_m x + j V_{mn} y) dx dy$$

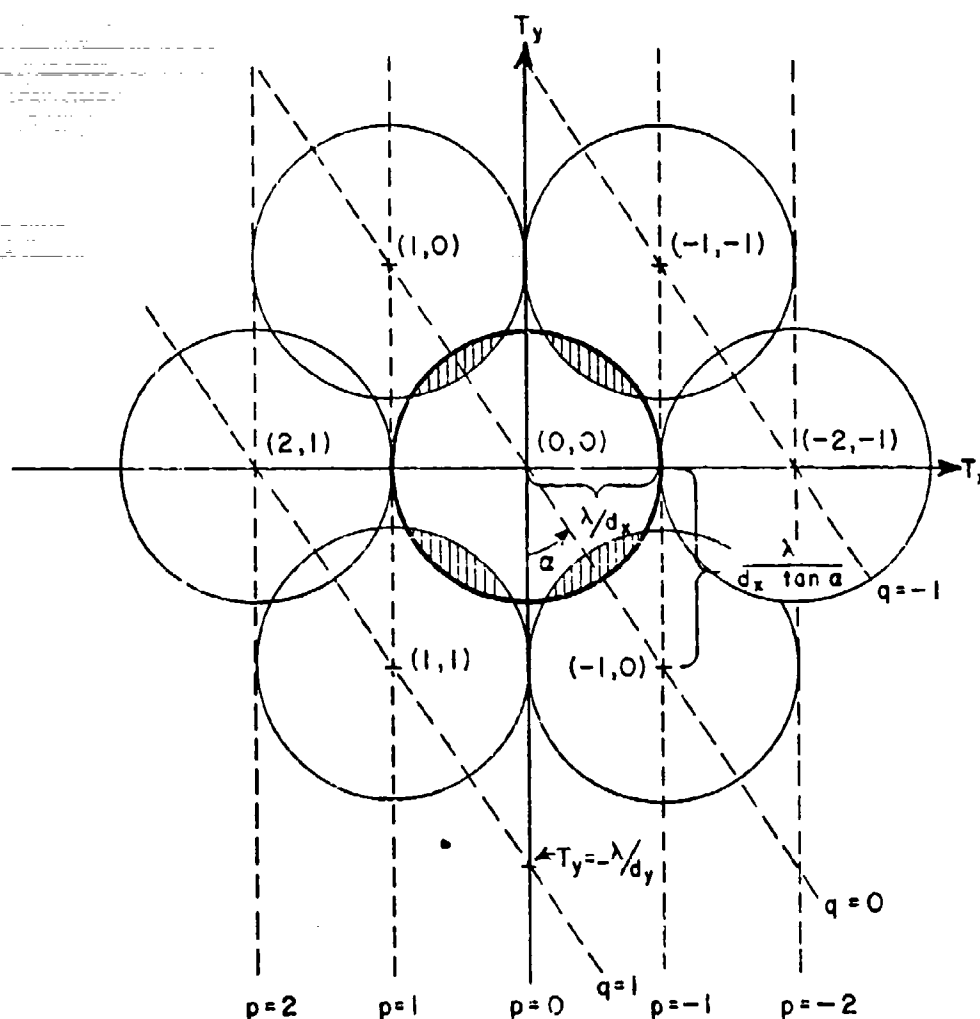


Figure 3-4.--Grating lobe diagram for the array of Fig. 3-2 with $d_x = \lambda$. $T_x = \sin \theta \cos \phi$, $T_y = \sin \theta \sin \phi$.

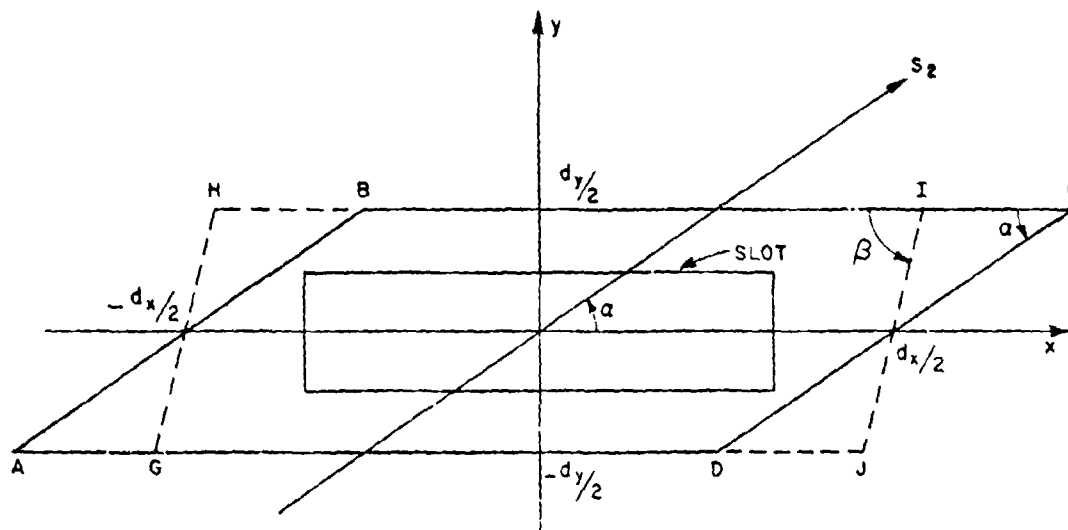


Figure 3-5.--The unit periodic cell ABCD of Fig. 3-2 can be deformed to the shape GHIJ without affecting the orthogonality of the Floquet modes.

where A denotes constant terms. Substituting from Eqs. (3-7) and (3-8) into Eq. (3-23) and simplifying we obtain

$$(3-24) \quad \int_{GHIJ} \vec{e}_{ai} \times \vec{h}_{aj}^* \cdot \hat{z} \, ds =$$

$$A \int_{-\frac{d_y}{2}}^{\frac{d_y}{2}} \exp[-j2\pi y(\frac{q-n}{d_y} - \frac{p-m}{d_x \tan \alpha})] \int_{-\frac{d_x}{2} + \frac{y}{\tan \beta}}^{\frac{d_x}{2} + \frac{y}{\tan \beta}} \exp[-j2\pi x(\frac{p-m}{d_x})] dx dy.$$

Performing the x integration in Eq. (3-24), we have

$$\begin{aligned}
 (3-25) \quad & \int_{-\frac{d_x}{2} + \frac{y}{\tan \theta}}^{\frac{d_x}{2} + \frac{y}{\tan \theta}} \exp[-j2\pi x(\frac{p-m}{d_x})] dx = \\
 & + \frac{d_x}{2j(p-m)} e^{-j \frac{2\pi y(p-m)}{d_x \tan \theta}} \cdot 2j \sin(\pi(p-m)) \\
 & = \begin{cases} 0, & p \neq m \\ d_x, & p = m \end{cases} .
 \end{aligned}$$

Thus if $p \neq m$, Eq. (3-22) is true. Now, if $i=j$, then $p=m$ and $q=n$. However, $i \neq j$ does not necessarily mean $p \neq m$; but if $p=m$ with $i \neq j$ then $q \neq n$. We therefore substitute the results for $p=m$ from Eq. (3-25) into Eq. (3-23) to obtain

$$\begin{aligned}
 (3-26) \quad & \int_{GHJ} \bar{e}_{ai}^r \times \bar{h}_{aj}^{s*} \cdot \hat{z} \, ds \Big|_{p=m} = \\
 & A d_x \int_{-\frac{d_y}{2}}^{\frac{d_y}{2}} \exp(-j2\pi y \frac{q-n}{d_y}) dy \\
 & = A \cdot \frac{d_y}{\pi(q-n)} \sin(\pi(q-n)) \\
 & = 0, \quad q \neq n .
 \end{aligned}$$

Thus Eq. (3-22) is shown to be true for $i \neq j$. We now proceed to examine the case where $i=j$, but $r \neq s$. From Eqs. (3-12) through (3-15) and (3-22) we have

$$(3-27) \quad \int_{GHIJ} \vec{e}_{ai}^r \times h_{ai}^{s*} \cdot \hat{z} \, ds =$$

$$\int_{GHIJ} \frac{1}{d_x d_y} \frac{1}{\eta_s} \left[\frac{U_{pq}}{T_{pq}^2} - \frac{U_{pq}}{T_{pq}^2} \right] \psi_{pq} \psi_{pq}^* \, ds = 0, \quad r \neq s.$$

Thus Eq. (3-22) is shown to be true. Note that this proof of Eq. (3-22) did not depend on the value of β in Fig. 3-5. This is important for two reasons. First, for large slots in a non-rectangular lattice ($\alpha \neq 90^\circ$) it is possible that the slots may not be contained within the original periodic cells. This is illustrated in Fig. 3-6.

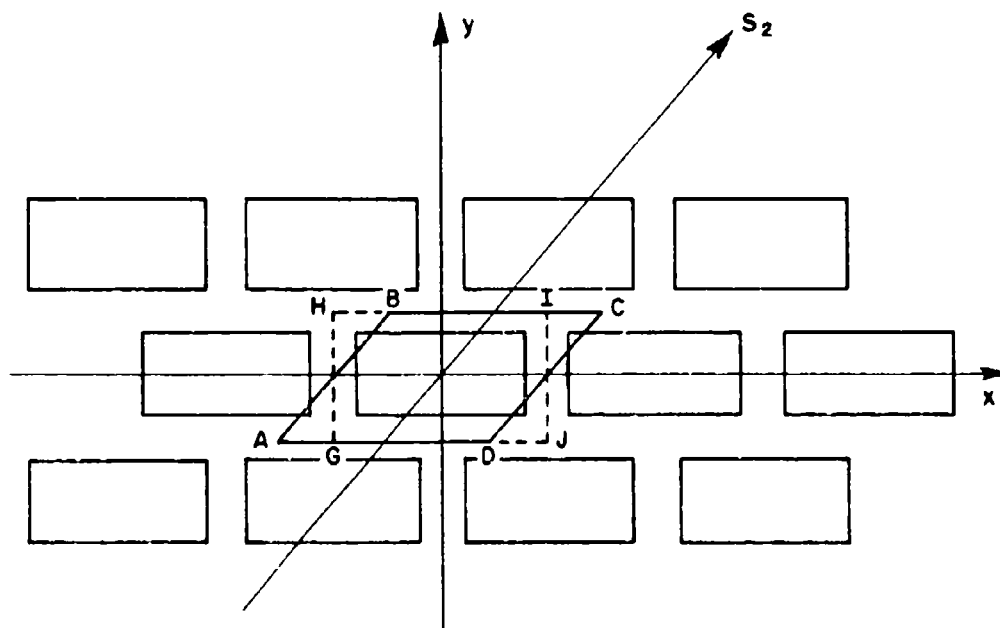


Figure 3-6.--Deformation of original periodic cell ABCD to the periodic cell GHIJ which includes only one slot.

It would be easier to evaluate the integrals required in the mode matching procedure if we could use the deformed periodic cell GHIJ, and we can do this because we have just shown that the orthogonality relationships of the Floquet modes will still be valid. Secondly,

even if the slots are contained within the original periodic cells, the evaluation of the mode matching integrals is simplified if the matching cells are rectangular.

We thus have a complete, orthogonal set of Floquet modes valid in the region exterior to the slot array. We now proceed to modify these modes so as to include the effect of a dielectric layer.

2. Effects of a Dielectric Layer on the Floquet Modes

In the previous section we obtained the Floquet mode set valid for the region external to the slotted panel. In this section we shall see how these modes may easily be modified so as to include the effects of dielectric layers situated next to the metal panel as shown in Fig. 3-7. The most general case of two different layers will be considered, even though for some of the solutions derived in later chapters the two layers must be identical. A plane wave is incident on the panel, and through interaction with the slotted surface a reflected plane wave, a transmitted plane wave, evanescent waves, and possibly grating lobes are excited, as indicated in the figure. Of course, fields will be excited in the slots as well. These will be dealt with in the next sections. We now merely wish to obtain a Floquet mode set valid in the dielectric layer.

Consider the incident and reflected plane waves. These plane waves are a combination of the TE and TM modes of Eqs. (3-12) through (3-15) where $i=1$ ($p=q=0$). While these modes differ in polarization and modal impedance they have the same spatial dependence. Thus we can express each tangential component of the incident and reflected plane wave in the free space region in the following form (easily understood):

$$(3-28) \quad E_{in}^r = A^r \frac{1}{\sqrt{d_x d_y}} f^r(U_0, V_{00}, T_{00}) \exp(-jU_0 x) \exp(-jV_{00} y) \exp(+j\gamma_{00} z)$$

$$(3-29) \quad H_{in}^r = \frac{A^r}{n_{00}} \cdot \frac{1}{\sqrt{d_x d_y}} g^r(U_0, V_{00}, T_{00}) \exp(-jU_0 x) \exp(-jV_{00} y) \exp(+j\gamma_{00} z)$$

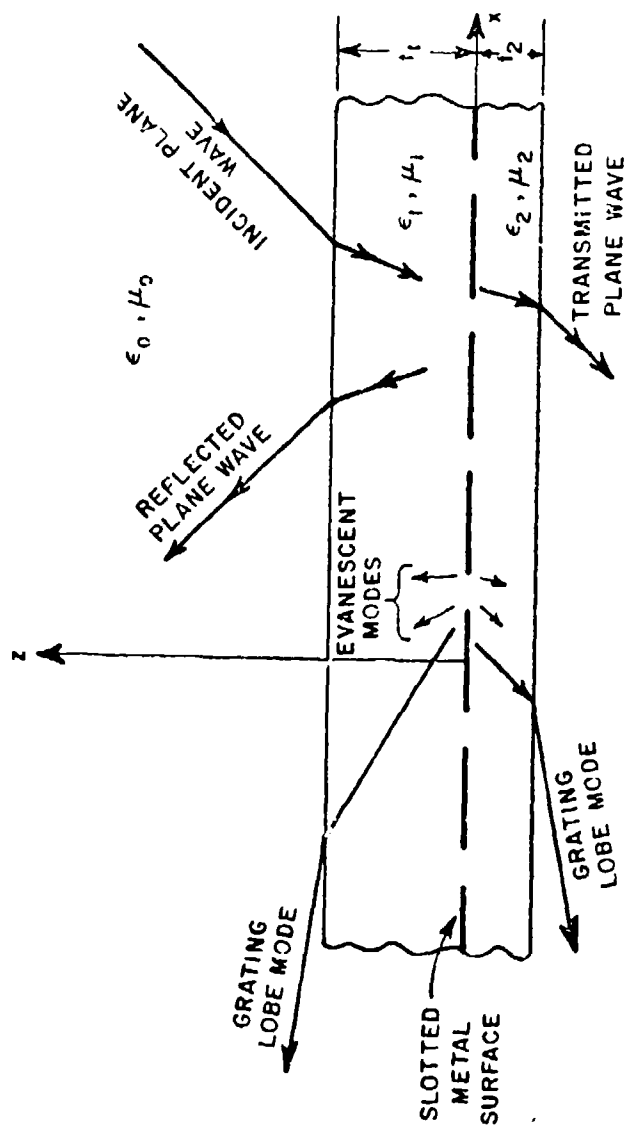


Figure 3-7.--Slotted metal panel covered by dielectric with a plane wave incident. The different modes which may exist on the panel are illustrated schematically.

$$(3-30) \quad E_{re}^r = R^r \frac{1}{\sqrt{d_x d_y}} f^r(U_0, V_{00}, T_{00}) \exp(-jU_0 x) \exp(-jV_{00} y) \exp(-j\gamma_{00} z)$$

$$(3-31) \quad H_{re}^r = \frac{-R^r}{\eta_{00}^r} \frac{1}{\sqrt{d_x d_y}} g^r(U_0, V_{00}, T_{00}) \exp(-jU_0 x) \exp(-jV_{00} y) \exp(-j\gamma_{00} z)$$

where the modes are as defined in Eqs. (3-7) through (3-19). The functions f^r and g^r depend on the polarization and on the value of r ($r=1$ for TE and 2 for TM) but not on the spatial coordinates and will cancel in the final result. The known modal coefficients of the incident wave are denoted by A^r , and the unknown coefficients for the reflected modes are the R^r . Since the TE and TM modes are orthogonal the A^r and R^r , $r=1,2$, can be considered separately.

Now referring to Fig. 3-8, we can express the incident and reflected plane waves in the dielectric region as:

$$(3-32) \quad E_{in}^{rd} = a_1^r \frac{1}{\sqrt{d_x d_y}} f^r(U_0^d, V_{00}^d, T_{00}^d) \exp(-jU_0^d x) \exp(-jV_{00}^d y) \exp(+j\gamma_{00}^{(1)} z)$$

$$(3-33) \quad H_{in}^{rd} = \frac{a_1^r}{\eta_{00}^{r(1)}} \frac{1}{\sqrt{d_x d_y}} g^r(U_0^d, V_{00}^d, T_{00}^d) \exp(-jU_0^d x) \exp(-jV_{00}^d y) \exp(+j\gamma_{00}^{(1)} z)$$

$$(3-34) \quad E_{re}^{rd} = \rho^r \frac{1}{\sqrt{d_x d_y}} f^r(U_0^d, V_{00}^d, T_{00}^d) \exp(-jU_0^d x) \exp(-jV_{00}^d y) \exp(-j\gamma_{00}^{(1)} z)$$

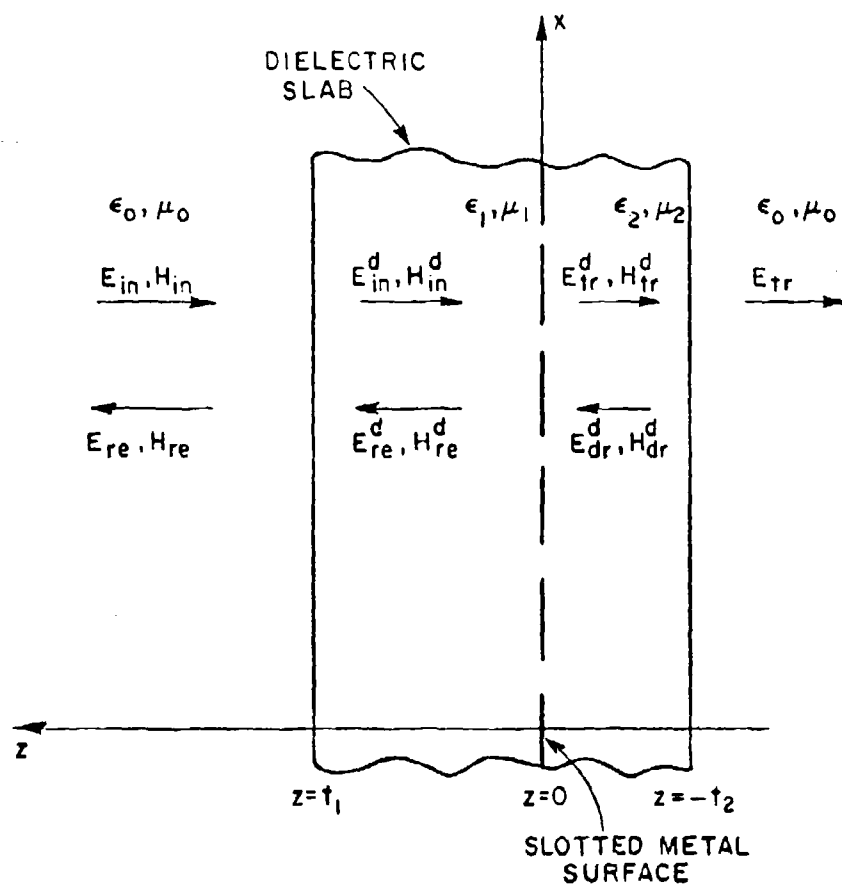


Figure 3-8.--Incident, reflected, and transmitted waves in the free space and dielectric regions.

$$(3-35) \quad H_{re}^{rd} = \frac{-\epsilon^r}{\eta_{00}^r(1)} \frac{1}{\sqrt{\epsilon_x^d \epsilon_y^d}} g^r(U_0^d, V_{00}^d, T_{00}^d) \exp(-jU_0^d x) \exp(-jV_{00}^d y) \exp(-j\gamma_{00}^{(1)} z)$$

where the superscript "d" denotes that these quantities describe conditions in the dielectric region. The parameters $\eta_{00}^{r(1)}$ and $\gamma_{00}^{(1)}$ are evaluated in the same manner as the free space parameters η_{00}^r and γ_{00} except that ϵ_1 and μ_1 are substituted for ϵ_0 and μ_0 in Eqs. (3-11), (3-16), and (3-17) with $K_1 = \omega \mu_1 \epsilon_1$ replacing K_0 .

We wish to express our incident and reflected plane waves in terms of the free space modes of Eqs. (3-28) through (3-31). However, the mode matching integrations will be evaluated at $z=0$, and thus these calculations will be performed on the dielectric modes of Eqs. (3-32) through (3-35). By enforcing boundary conditions at the dielectric interface $z=t_1$, we will establish relationships which will enable us to evaluate R^r and a_1^r in terms of A^r and ρ^r .

Continuity of tangential E and H at the dielectric interface requires that for $z=t_1$

$$(3-36) \quad E_{in}^r + E_{re}^r = E_{in}^{rd} + E_{re}^{rd}$$

$$(3-37) \quad H_{in}^r + H_{re}^r = H_{in}^{rd} + H_{re}^{rd} \quad \Big|_{z=t_1}$$

The first consequence of Eqs. (3-36) and (3-37) is that the phases of Eqs. (3-28) to (3-35) match at $z=t_1$ for all values of x or y , which requires that

$$(3-38) \quad U_0^d = U_0$$

$$(3-39) \quad V_{00}^d = V_{00}$$

and from Eq. (3-19),

$$(3-40) \quad T_{00}^d = T_{00}$$

Use is made of Eqs. (3-38) to (3-40) in the evaluation of $\gamma_{00}^{(1)}$ in Eq. (3-11). While K_0 is now replaced by $K_1 = \omega \sqrt{\mu_1 \epsilon_1}$, U_0 and V_{00} are not changed from their free space values (Snell's Law) when determining $\gamma_{00}^{(1)}$.

We now substitute from Eqs. (3-28)-(3-35) into Eqs. (3-36), (3-37), apply Eqs. (3-38), (3-40), and cancel common factors, obtaining:

$$(3-41) \quad A^r \exp(j\gamma_{00} t_1) + R^r \exp(-j\gamma_{00} t_1) = a_1^r \exp(j\gamma_{00}^{(1)} t_1) + \rho^r \exp(-j\gamma_{00}^{(1)} t_1)$$

$$(3-42) \quad \frac{A^r}{\eta_{00}^r} \exp(j\gamma_{00} t_1) - \frac{R^r}{\eta_{00}^r} \exp(-j\gamma_{00} t_1) = \frac{a_1^r}{\eta_{00}^{(1)r}} \exp(+j\gamma_{00}^{(1)} t_1) - \frac{\rho^r}{\eta_{00}^{(1)r}} \exp(-j\gamma_{00}^{(1)} t_1).$$

Solving Eqs. (3-41) and (3-42) for a_1^r and R^r we obtain

$$(3-43) \quad a_1^r = 2A^r \frac{\eta_{00}^{(1)r}}{\eta_{00}^{(1)r} + \eta_{00}^r} \exp(-j(\gamma_{00}^{(1)} - \gamma_{00}) t_1) - \rho^r \cdot \frac{\eta_{00}^{(1)r} - \eta_{00}^r}{\eta_{00}^{(1)r} + \eta_{00}^r} \exp(-2j\gamma_{00}^{(1)} t_1)$$

$$(3-44) \quad R^r = A^r \frac{\eta_{00}^{(1)r} - \eta_{00}^r}{\eta_{00}^{(1)r} + \eta_{00}^r} \exp(2j\gamma_{00} t_1) + 2\rho^r \frac{\eta_{00}^r}{\eta_{00}^{(1)r} + \eta_{00}^r} \exp(-j(\gamma_{00}^{(1)} - \gamma_{00}) t_1).$$

Equation (3-43) allows us to express the incident mode amplitude a_i^r in the dielectric region in terms of the free space incident mode amplitude A^r . Equation (3-44) allows us to find the free space reflected mode amplitude R^r once the reflected mode amplitude in the dielectric region ρ^r is computed. Thus the solutions presented in later chapters for ρ^r can proceed directly to a field match at the panel surface, since the dielectric layer effects in the incident wave are included in the above expressions.

We now consider the problem of determining the effect of the $z > 0$ dielectric layer on the Floquet mode with $i > 1$, i.e., those which represent either evanescent fields or propagating grating lobes. This problem is considerably simplified as compared to that for the $i=1$ plane wave modes since there are no incident modes in the free space region for $i=1$. In addition, we are primarily interested in evaluating the $i=1$ modes at the surface of the panel so that we can perform our field matching operations.

For the region within the dielectric layer in front of the metal surface ($z > 0$) the Floquet modes are given by Eqs. (3-7) through (3-19) with ϵ_0 and μ_0 replaced by ϵ_1 and μ_1 . Referring to Fig. 3-8, it is a simple matter to use transmission line theory to obtain $Z_{pq}^{r(1)}$, the modal impedance of the i -th Floquet mode evaluated at the front ($z=0^+$) surface of the panel:

$$(3-45) \quad Z_{pq}^{r(1)} = \eta_{pq}^{r(1)} \cdot \frac{\eta_{pq}^{r(1)} + j \eta_{pq}^{r(1)} \tan(\gamma_{pq}^{(1)} l_1)}{\eta_{pq}^{r(1)} + j \eta_{pq}^{r(1)} \tan(\gamma_{pq}^{(1)} l_1)} \quad .$$

When evaluating the Floquet modes in the dielectric regions one must keep in mind that the incidence angle in the dielectric region will not be the same as that in the free space region (Snell's Law). One can easily account for this by using the relationships

$$(3-46) \quad U_p^d = U_p$$

$$(3-47) \quad V_{pq}^d = V_{pq}$$

$$(3-48) \quad T_{pq}^d = T_{pq}$$

when evaluating the Floquet modes in the dielectric region. These relationships correspond to Eqs. (3-38) through (3-40) which were shown true for the plane wave ($i=1$) Floquet Modes.

We can thus express the transverse components of the Floquet modes at the front surface of the panel ($z=0^+$) with a dielectric layer present as:

$$(3-49) \quad \bar{e}_{ai}^{(1)} = \bar{e}_{ai}^r \Big|_{z=0}$$

$$(3-50) \quad \bar{h}_{ai}^{(1)} = \begin{cases} \frac{1}{\eta_{00}^{(1)}} (\hat{z} \times \bar{e}_{ai}^{(1)}) = \frac{1}{\eta_{00}^{(1)}} \bar{r}_{00}^r, & i=1 \\ \frac{1}{Z_{pq}^{(1)}} (\hat{z} \times \bar{e}_{ai}^{(1)}) = \frac{1}{Z_{pq}^{(1)}} \bar{r}_{pq}^r, & i>1 \end{cases}$$

The vector function \bar{r}_{pq}^r has been defined here, and will be used in later sections to simplify certain integral equations.

The Floquet modes for the dielectric region behind the metal panel ($z<0$), are obtained in a similar manner. For the back side, however, there is no incident plane wave to be considered, and this simplifies the problem somewhat. The modal impedance $Z_{pq}^{(2)}$ of the i -th Floquet mode at the back surface of the panel is given by Eq. (3-45) with the superscript (1) replaced by (2) and evaluated for the dielectric thickness t_2 , and parameters ϵ_2 and μ_2 . As indicated by Eq. (3-49) the transverse components of the electric field mode function at the surface of the panel are not affected by the dielectric layer; thus

$$(3-51) \quad \bar{e}_{ai}^{(2)} = \bar{e}_{ai}^{(1)} = \bar{e}_{ai}^r \Big|_{z=0}$$

Since there is no incident wave for $z<0$,

$$(3-52) \quad \bar{h}_{ai}^{(2)} = \frac{1}{Z_{pq}^{(2)}} \bar{r}_{pq}^r$$

for all values of i . Using Eqs. (3-51) and (3-52) we can express the electric and magnetic fields at $z=0^-$. However, the free space transmission coefficients T^r are desired. Referring to Fig. 3-8 we have for the transverse (to z) components of the dominant mode ($i=1$) plane wave:

$$(3-53) \quad E_{tr}^{rd} = \tau^r \frac{1}{\sqrt{d_x d_y}} f^r(U_o, V_{oo}, T_{oo}) \exp(-jU_o x) \exp(-jV_{oo} y) \\ \exp(+j\gamma_{oo}^{(2)} z)$$

$$(3-54) \quad H_{tr}^{rd} = \frac{\tau^r}{n_{oo}^{r(2)}} \frac{1}{\sqrt{d_x d_y}} g^r(U_o, V_{oo}, T_{oo}) \exp(-jU_o x) \exp(-jV_{oo} y) \\ \exp(+j\gamma_{oo}^{(2)} z)$$

$$(3-55) \quad E_{dr}^{rd} = \tau^r \frac{1}{\sqrt{d_x d_y}} f^r(U_o, V_{oo}, T_{oo}) \exp(-jU_o x) \exp(-jV_{oo} y) \\ \exp(-j\gamma_{oo}^{(2)} z)$$

$$(3-56) \quad H_{dr}^{rd} = - \frac{\tau^r}{n_{oo}^{r(2)}} \frac{1}{\sqrt{d_x d_y}} g^r(U_o, V_{oo}, T_{oo}) \exp(-jU_o x) \exp(-jV_{oo} y) \\ \exp(-j\gamma_{oo}^{(2)} z)$$

$$(3-57) \quad E_{tr}^r = T^r \frac{1}{\sqrt{d_x d_y}} f^r(U_{oo}, V_{oo}, T_{oo}) \exp(-jU_o x) \exp(-jV_{oo} y) \\ \exp(j\gamma_{oo} z)$$

$$(3-58) \quad H_{tr}^r = T^r \frac{1}{n_{oo}^r} \frac{1}{\sqrt{d_x d_y}} g^r(U_{oo}, V_{oo}, T_{oo}) \exp(-jU_o x) \exp(-jV_{oo} y) \\ \exp(j\gamma_{oo} z)$$

where the various terms are discussed following Eq. (3-35). Note especially that the superscript (2) of $\gamma_{oo}^{(2)}$ is not an exponent, but rather indicates that $\gamma_{oo}^{(2)}$ is to be evaluated for the ϵ_2 and μ_2

dielectric region. Boundary conditions require that the transverse components of E and H be continuous. Thus, following the procedure used previously to obtain R^r and a_1^r , we have at $z=-t_2$:

$$(3-59) \quad T^r \exp(-j\gamma_{00} t_2) = \tau^r \exp(-j\gamma_{00}^{(2)} t_2) + \psi^r \exp(j\gamma_{00}^{(2)} t_2)$$

$$(3-60) \quad \frac{T^r}{r_{00}} \exp(-j\gamma_{00} t_2) = \frac{\tau^r}{r_{00}^{(2)}} \exp(-j\gamma_{00}^{(2)} t_2) - \frac{\psi^r}{r_{00}^{(2)}} \exp(j\gamma_{00}^{(2)} t_2)$$

We could now go ahead and solve for T^r in terms of τ^r and ψ^r . However, we realize that the modal matching solution will not yield the values of τ^r and ψ^r but instead gives the value of total dominant mode field at $z=0^-$, expressed as

$$(3-61) \quad E_{tr}^{rd} \Big|_{z=0^-} + E_{dr}^{rd} \Big|_{z=0^-} = b_1^r \frac{1}{\sqrt{d_x d_y}} f^r(U_0, V_{00}, T_{00}) \exp(-jU_0 x) \exp(-jV_{00} y)$$

$$(3-62) \quad H_{tr}^{rd} \Big|_{z=0^-} + H_{dr}^{rd} \Big|_{z=0^-} = b_1^r \frac{1}{Z_{pq}^{r(2)}} \frac{1}{\sqrt{d_x d_y}} g^r(U_0, V_{00}, T_{00}) \exp(-jU_{00} y) \exp(-jV_{00} y).$$

where it is evident that

$$(3-63) \quad b_1^r = \tau^r + \psi^r.$$

Using Eq. (3-63) we can proceed to solve Eqs. (3-59) and (3-60) for T^r in terms of b_1^r as follows. Substituting $b_1^r - \psi^r$ for τ^r in Eq. (3-59) and rearranging terms we obtain

$$(3-64) \quad T^r = b_1^r \exp[-j(\gamma_{00}^{(2)} - \gamma_{00}) t_2] + 2j\psi^r \sin(\gamma_{00}^{(2)} t_2) \cdot \exp[j\gamma_{00} t_2].$$

Making the same substitution in Eq. (3-60) we obtain

$$(3-65) \quad \psi^r = [b_1^r \exp(-j\gamma_{00}^{(2)} t_2) - \frac{n_{00}^{r(2)}}{r_{00}} T^r \exp(-j\gamma_{00} t_2)] / [2 \cos(\gamma_{00}^{(2)} t_2)].$$

Finally, we substitute for ψ^r from Eq. (3-65) into Eq. (3-64) to obtain:

$$(3-66) \quad T^r = b_1^r \exp[-j(\gamma_{00}^{(2)} - \gamma_{00}) t_2] \cdot \frac{1 + j \tan(\gamma_{00}^{(2)} t_2)}{1 + j \frac{n_{00}^{r(2)}}{r_{00}} \tan(\gamma_{00}^{(2)} t_2)}.$$

Thus we can solve for the fields at the back surface of the panel ($z=0^-$) with a dielectric layer present by expressing the fields as indicated by Eqs. (3-51) and (3-52), and then by using Eq. (3-66) obtain the free space plane wave transmission coefficients T^r .

B. Internal Slot Modes

The preceding section of this chapter dealt with the Floquet mode set used to express the fields in the region external to the slots. In this section of the chapter the modes used to describe the fields inside the slot will be developed. Mode sets for the rectangular, single loaded, 4-legged symmetric and 3-legged symmetric slots will be presented. The mode sets for all of these slot shapes will be adequate for describing the fields in the slot regardless of the slot (panel) thickness. However, we will in later chapters present actual calculated data for thick slot arrays only for the rectangular slot case. This is due to the difficulty of fabricating thick metallic panels perforated with the more complicated loaded slot shapes which would be required for experimental confirmation of the theory.

1. Rectangular Slot Modes

The electric and magnetic fields for a rectangular slot with coordinate system as shown for the center slot of Fig. 3-2 can be expressed as a combination of rectangular waveguide modes. This mode set is similar to that used in Chapter II to describe the fields in the rectangular waveguide problem. A more thorough discussion will be given here.

The slots are assumed to be narrow, i.e., $b \ll \lambda$, and $b \ll a$, so that to a good approximation the fields in the slot will be TE_x . This assumption is not necessary, but it enables us to use a more efficient mode set.

The mode set which is TE_x is obtained from the wave function [44]

$$(3-67) \quad \psi^{TE_x} = \sin\left(\frac{f\pi x}{a} - \frac{f\pi}{2}\right) \cos\left(\frac{g\pi y}{b} - \frac{g\pi}{2}\right) \exp(\pm j\Gamma_{fg} z)$$

where

$$(3-68) \quad \Gamma_{fg} = \begin{cases} \sqrt{k_3^2 - \left(\frac{f\pi}{a}\right)^2 - \left(\frac{g\pi}{b}\right)^2} \\ \pm j\sqrt{\left(\frac{f\pi}{a}\right)^2 + \left(\frac{g\pi}{b}\right)^2 - k_3^2} \end{cases}$$

In Eq. (3-68) the expression which has a positive radical is chosen. The integers f and g denote the mode number, and $k_3 = \omega \sqrt{\mu_3 \epsilon_3}$, where ϵ_3 and μ_3 are the parameters of the slot medium. The relative permittivity and permeability of the material in the slot may thus differ from that surrounding the panel. The transverse (to z) components of the modes in the slot are obtained from

$$E_x = 0 \quad H_x = \frac{1}{j\omega\mu_3} \left(\frac{\partial^2}{\partial x^2} + k_3^2 \right) \psi$$

$$E_y = \frac{\partial \psi}{\partial z} \quad H_y = \frac{1}{j\omega\mu_3} \frac{\partial^2 \psi}{\partial x \partial y}$$

with some slight simplification as:

$$(3-69) \quad \bar{e}_{bj} = \hat{y} \sin\left(\frac{f\pi x}{a} - \frac{f\pi}{2}\right) \cos\left(\frac{g\pi y}{b} - \frac{g\pi}{2}\right) e^{\pm j\Gamma_{fg} z}$$

$$(3-70) \quad \bar{h}_{bj} = -\hat{x} \gamma_{bj} \sin\left(\frac{f\pi x}{a} - \frac{f\pi}{2}\right) \cos\left(\frac{g\pi y}{b} - \frac{g\pi}{2}\right) e^{\pm j\Gamma_{fg} z} \\ + \hat{y} \frac{\gamma_{bj}}{ab} \cdot \frac{fg\pi^2}{(k_3)^2 - \left(\frac{f\pi}{a}\right)^2} \cos\left(\frac{f\pi x}{a} - \frac{f\pi}{2}\right) \sin\left(\frac{g\pi y}{b} - \frac{g\pi}{2}\right) e^{\pm j\Gamma_{fg} z}$$

The subscript b denotes that these modes are valid within the slot. The subscript j is a mode number running from 0 to infinity; for each j there is a corresponding value for f and g, with j=0 corresponding to f=1, g=0, etc. Also

$$(3-71) \quad Y_{bj} = \sqrt{\frac{\epsilon_3}{\mu_3}} \cdot \frac{1}{k_3} \cdot \frac{(K_3)^2 - \left(\frac{f\pi}{a}\right)^2}{r_{fg}}$$

These modes are linear combinations of the more usual TE_z and TM_z modes, except that the TE_{xf0} modes are identical to the TE_{zf0} modes. If the slots are wide enough so that E_x in the slot is not negligible, one could form a complete mode set by adding to the above set the TM_x modes. In this case, however, it would be just as efficient to use the TE_z and TM_z mode set. For the narrow slots which are being considered here, $E_x \approx 0$, and thus the fields in the slots can be described most efficiently with just the TE_x mode set.

It is easy to show that the above modes satisfy the orthogonality relationship

$$(3-72) \quad \int_b \vec{e}_{bn} \times \vec{h}_{bj} \cdot \hat{z} \, ds = 0, \quad n \neq j$$

where $\int_b ds$ denotes integration over the slot cross section.

2. Single Loaded Slot Modes

The mode matching method has heretofore been applied only to arrays of slots which were circular or rectangular, so that the usual waveguide modes could be used as a basis for the tangential fields in the slots. Transmission line loaded slot arrays (see Fig. 1-7), however, have better performance for many applications than arrays of circular or rectangular slots, and it is therefore desirable to extend the modal method to arrays of loaded slots. In this section we will deal with the single loaded slot, and in the next section with 3-legged and 4-legged loaded slots.

One possible approach would be to solve for the modes of a cylindrical waveguide with a cross section identical to the shape of the desired loaded slot. This procedure would involve considerable difficulty in terms of the effort involved and the numerical problems encountered. Actually, it is not necessary or perhaps even desirable to expand in terms of waveguide modes.

In order to provide an efficient basis for the transverse (to z) fields of the single loaded slot of Fig. 3-9 we will again make the

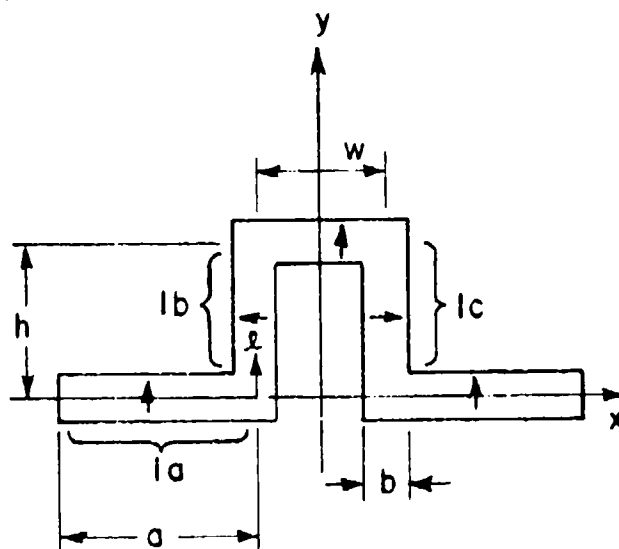


Figure 3-9.--Coordinates and dimensions used to express the single loaded slot modes.

approximation that the slots are narrow enough so that the component of the E-field which is parallel with the long edge of the slot may be neglected. For example, in region 1a of Fig. 3-9 only the E_y component is significant, while in region 1b only the E_x component. This approximation will be very good for most narrow band loaded slots, where b is usually $\ll \lambda$. To further simplify the representation we will make the approximation that the variation of the fields across the narrow dimension of the slot is negligible. This would correspond in a narrow rectangular slot to approximating the fields using only the TE_{n0} modes. If we now visualize "bending" these TE_{n0} rectangular guide modes into the single loaded slot shape we obtain the approximate mode set which will be used to describe the transverse fields in the single loaded slot. Making use of the coordinate ℓ , which is the distance measured from the point $x=-a-\frac{w}{2}$, $y=0$ along the center of the slot in Fig. 3-9, we can express this approximate mode set as

$$(3-73) \quad \vec{e}_{bn} = \sin\left(\frac{n\pi\ell}{T}\right) \vec{F}(\ell) e^{\pm j\Gamma_{n0}z}$$

$$(3-74) \quad \vec{h}_{bn} = Y_{bn} \sin\left(\frac{n\pi\ell}{T}\right) (\hat{z} \times \vec{F}(\ell)) e^{\pm j\Gamma_{n0}z}$$

where T is the total length of the slot, and

where $F(x)$ is equal to $-\hat{x}$ in region 1b, $+\hat{x}$ in region 1c and $+\hat{y}$ elsewhere, as indicated by the arrows which represent the tangential E-field across the slot.

The value of Γ_{n0} is given by Eq. (3-68), with Y_{bn} given by Eq. (3-71) with $f=n$ and $g=0$. The orthogonality relation of Eq. (3-72) can easily be shown true for this mode set.

The given mode set is a reasonable approximation to the transverse fields in the single loaded slot except where the vector function $F(x)$ changes direction (i.e., at $x=0, y=-w; y=0, y=w; x=h, y=w; x=h, y=-w$). In these areas the mode fields change abruptly and do not approximate the actual fields very well. However, for $b \ll a$ these corner regions form a very small percentage of the total slot aperture. Also, in practical slots the corners are actually rounded slightly. We are content to let the validity of this approximation be judged by the accuracy of the results which can be obtained with this mode set.

3. Symmetrical Loaded Slot Modes

In this section approximate mode sets will be derived for the 4-legged and 3-legged symmetric slots. The mode sets for these two loaded slot types will be nearly identical, and thus they will both be considered in this section.

The modes are derived from an approximate mode set for the fields in a coaxial waveguide with $a-b \ll 1/2(a+b) \equiv r_0$, where r_0 is the average radius of the coaxial waveguide. The coordinate system for the coaxial waveguide is shown in Fig 3-10. With the above restriction on a and b the dominant modes are the TE_{n0} modes. Johnson [45] gives the following approximate expressions for the TE_{n0} coaxial waveguide modes:

$$(3-73) \quad \bar{e}_n = \frac{1}{r} e^{jn\theta} e^{-j\Gamma_n z} \hat{r}$$

$$(3-74) \quad \bar{h}_n = \sqrt{\frac{\epsilon_3}{\mu_3}} \frac{\Gamma_n}{K_3} \frac{1}{r} e^{jn\theta} e^{-j\Gamma_n z} \hat{\theta}$$

with

$$(3-75) \quad \Gamma_n = \begin{cases} \sqrt{(K_3)^2 - \left(\frac{n}{r_0}\right)^2} \\ \pm j \sqrt{\left(\frac{n}{r_0}\right)^2 - (K_3)^2} \end{cases} \quad (\text{choose positive radical})$$

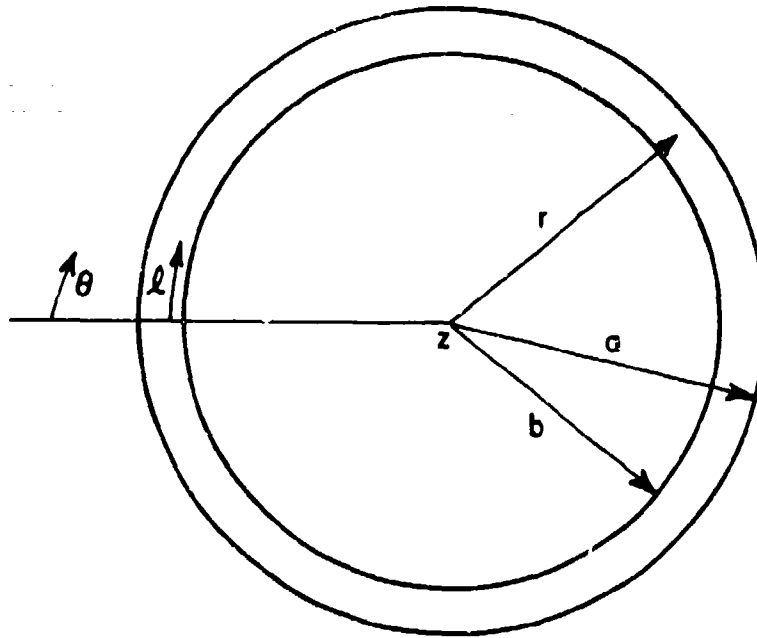


Figure 3-10.--Coordinate system for expressing the approximate mode set for a narrow coaxial waveguide.

and ϵ_3 and μ_3 the constitutive parameters for the region inside the coaxial waveguide. If we now make the additional restriction that $a-b \ll \lambda$ we can simplify the above modes even more by noting that $1/r$ will be nearly constant over the small region $b < r < a$. If in Eqs. (3-73) through (3-75) we assume $1/r$ is constant, define the average circumference $S=2\pi r_0$, and separate the angular exponential term into sine and cosine modes, we arrive at the following approximate mode set for the narrow coaxial waveguide:

$$(3-76) \quad \bar{e}_{bj} = \begin{cases} \sin\left(\frac{2n\pi\ell}{S}\right) e^{-j\Gamma_n z} \bar{G}(\ell) & j=1,3,5; \quad n = \frac{j+1}{2} \\ \cos\left(\frac{2n\pi\ell}{S}\right) e^{-j\Gamma_n z} \bar{G}(\ell) & j=2,4,6,8; \quad n = \frac{j}{2} \end{cases}$$

$$(3-77) \quad \bar{h}_{bj} = \begin{cases} \sqrt{\frac{\mu_3}{\epsilon_3}} \frac{\Gamma_n}{K_3} \sin\left(\frac{2n\pi\ell}{S}\right) e^{-j\Gamma_n z} (\hat{z} \times \bar{G}(\ell)) & j=1,3,5; \quad h = \frac{j+1}{2} \\ \sqrt{\frac{\mu_3}{\epsilon_3}} \frac{\Gamma_n}{K_3} \cos\left(\frac{2n\pi\ell}{S}\right) e^{-j\Gamma_n z} (\hat{z} \times \bar{G}(\ell)) & j=2,4,6; \quad n = \frac{j}{2} \end{cases}$$

where

$$(3-78) \quad r_n = \begin{cases} \sqrt{(k_3)^2 - \left(\frac{2n\pi}{S}\right)^2} \\ + j \sqrt{\left(\frac{2n\pi}{S}\right)^2 - (k_3)^2} \end{cases} \quad (\text{choose positive radical})$$

and where λ is measured as shown in Fig. 3-10, from $\theta=0$ along the center of the coaxial opening. The vector function $\vec{G}(\lambda)$ is merely equal to \hat{r} for the coaxial waveguide. The subscript j uniquely determines the mode, i.e., $j=1$ is the $n=1$ sine mode, $j=2$ is the $n=1$ cosine mode, etc. The subscript b again denotes that the mode is valid in the slot region rather than in the free space (Floquet mode) region.

We can now quite simply adapt this mode set to the 4-legged and 3-legged loaded slots by "bending" the approximate coaxial modes into the proper shape, just as the rectangular slot modes were "bent" into the loaded slot shape.

The 4-legged slot geometry is shown in Fig. 3-11. In order to apply the approximate mode set of Eqs. (3-76), (3-77), and 3-78), the 4-legged slot must have $b \ll \lambda$ and $b \ll S$, where the average perimeter S is now given by $S=4d+8c$. The coordinate λ of Fig. 3-11 is measured from the point $x=-c-d/2$, $y=0$ along the center of the slot. Finally, we define $\vec{G}(\lambda)$ as a unit vector whose direction in each straight segment of the slot is indicated by the arrows drawn in the slot, as was done for the function $\vec{F}(\lambda)$ defined for the single loaded slot modes. With these quantities thus defined, Eqs. (3-76), (3-77), and (3-78) express the approximate mode set used to describe the modes in the 4-legged symmetric slot.

The approximate mode set for the 3-legged loaded slot of Fig. 3-12 can be expressed similarly. The average circumference S is now given by $S=3d+6c$. By redefining the unit vector $\vec{G}(\lambda)$ in Eqs. (3-76) and (3-77) to agree with the directions indicated by the arrows of Fig. 3-12, the equations will now serve to describe the modes for the 3-legged slot as well.

Although the \vec{H}_{bj} modes have been given for completeness, only the \vec{E}_{bj} modes will be needed in later chapters for these two types of slots. This is because calculated data for thick panels perforated with slots of these shapes will not be given in this work. The reason is that the unconnected, central piece of conductor makes this type of slot difficult to fabricate in a thick panel. (Normally, these slot types are etched in thin copper laminated to a dielectric, with the dielectric substrate serving to support the central metal piece.)

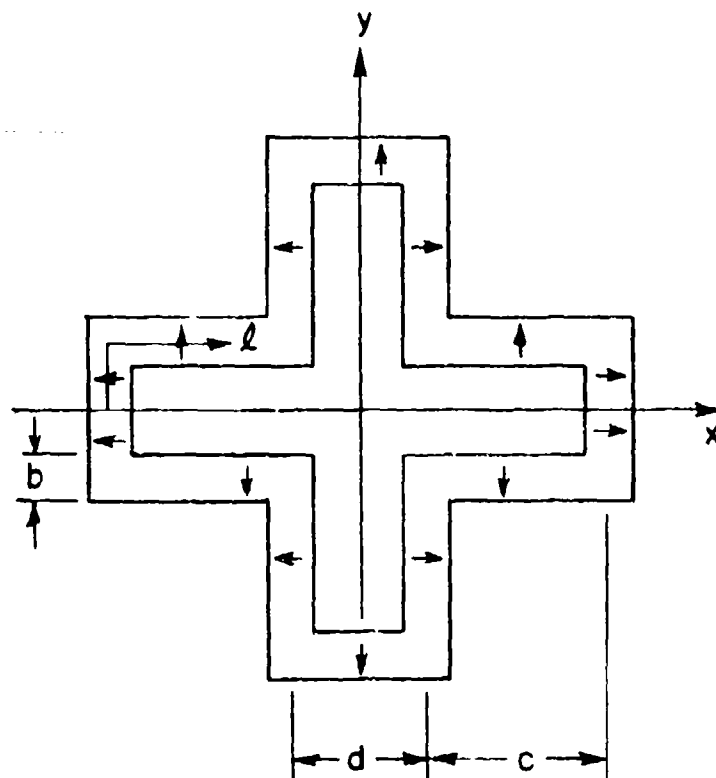


Figure 3-11.--Coordinates and dimensions for expressing the approximate mode set for the 4-legged symmetric loaded slot.

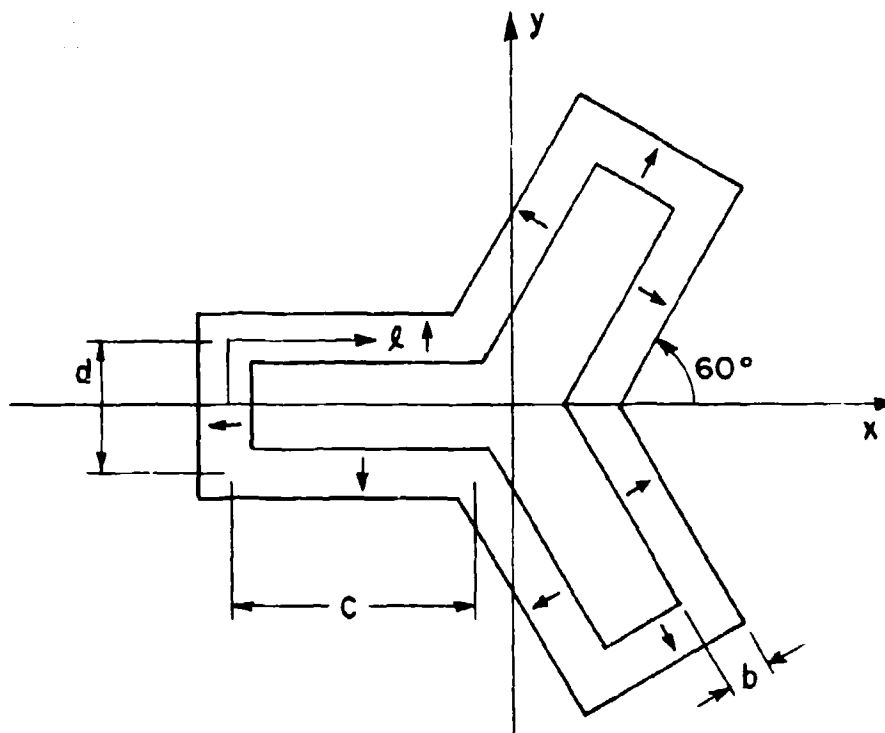


Figure 3-12.--Coordinates and dimensions for expressing the approximate mode set for the 3-legged loaded slot.

It is interesting to note that if a moment method solution for the current on the complementary 4-legged loaded loop were formulated, one choice of basis functions for the currents on the wire would be an entire domain Fourier Series basis. This basis would be mathematically equivalent to the \bar{e}_{bj} modes given in Eq. (3-76) with $z=0$.

CHAPTER IV THICKNESS AND DIELECTRIC EFFECTS

In the previous chapter the mode sets used to describe the fields resulting from plane wave scattering by a periodic slot array were derived. In this chapter moment methods will be used to solve for the unknown modal coefficients and thus obtain the scattered fields. The geometry of the problem is illustrated in Fig. 4-1. Although an

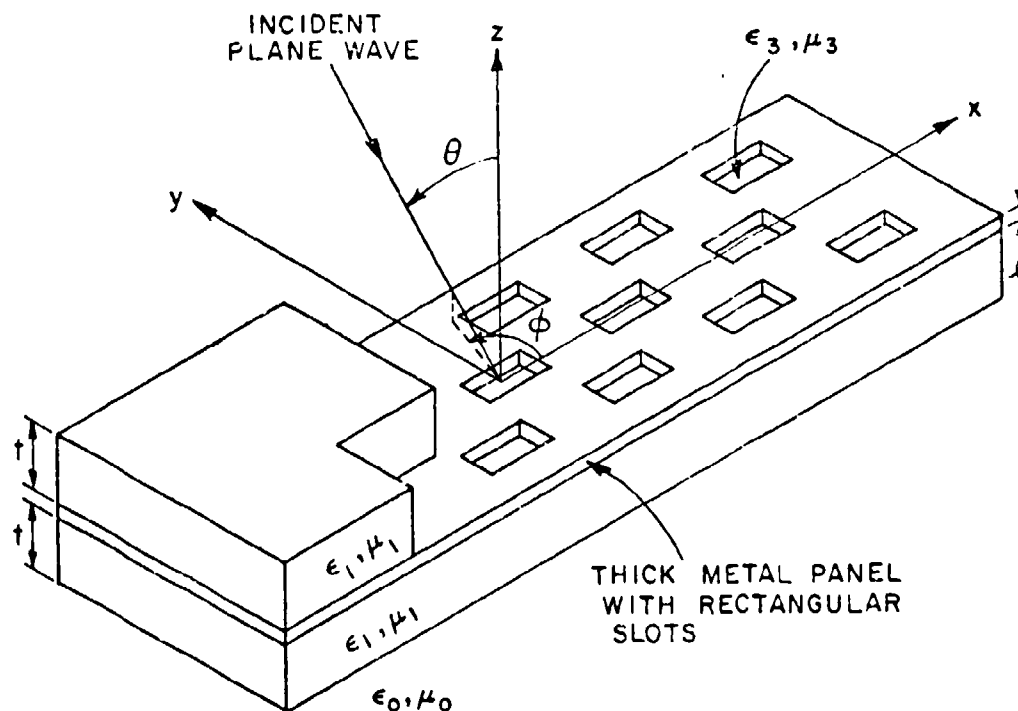


Figure 4-1.--Coordinates and dimensions for an array of slots in thick metal panel covered with dielectric layers.

interlaced grid is shown, the Floquet mode set can accommodate other grids (see Chapter III). The dielectric layers may be of arbitrary thickness and permittivity but must be identical. (The basic method of solution can be applied when the dielectric layers are different, but the procedure will be more involved.) This is not a major shortcoming for practical geometries since Munk [4] has shown that general lossless transmission will be obtained with identical dielectric layers. The slots themselves may be filled with a

dielectric of different permittivity and permeability than that of the external dielectric layers, and are cut in a perfectly conductive panel of finite thickness λ .

Mathematically, the problem is quite similar to the thick waveguide window problem treated in Chapter II. The main differences are that the Floquet mode set rather than the waveguide mode set is used to describe the fields external to the slot, and that the presence of dielectric layers is included in the theory. This mathematical similarity is due to the fact that, because of the periodicity of the Floquet modes, the boundary conditions for tangential E and H need to be enforced only over one periodic cell of the infinite array. Thus the modal analysis method of Wexler [38] can be used for the thick slot array just as it was used in the waveguide window problem of Chapter II.

Chen outlined an equivalent method of solution for thick slot arrays [33], and, although he did not actually give the solution, he did present some calculated results for rectangular and circular slots in thick panels. His results all showed large shifts of resonance frequency with incidence angle. The final sentence of his paper states that "Shifts of resonance frequency and changes in bandwidth in the opposite sense for the perpendicular and parallel polarizations as functions of incident angle limit many useful applications of this perforated plate". We shall show that with proper use of dielectric loading, arrays of rectangular slots can be designed with negligible frequency shift and greatly reduced changes in bandwidth with changing incidence angles. This result is of practical importance since rectangular slots are somewhat easier to fabricate than the more complicated loaded slot shapes, especially for thicker panels.

A. Thick Panel Solution

Referring to Fig. 4-1, we have a plane wave incident on the panel from the +z direction. For $z > t$, i.e., in the free space region, this plane wave can be expressed as

$$(4-1) \quad \vec{E}_{in} = \sum_{r=1}^{\infty} A^r \vec{e}_{ar}^r$$

$$(4-2) \quad \vec{H}_{in} = \sum_{r=1}^{\infty} A^r \vec{h}_{ar}^r$$

Similarly, the specularly reflected plane wave can be expressed as

$$(4-3) \quad \vec{E}_{re} = \sum_{r=1}^{\infty} R^r \vec{e}_{ar}^r$$

$$(4-4) \quad \vec{H}_{re} = \sum_{r=1}^2 -R^r \vec{h}_{ar}^r$$

The modal coefficients A^r are known, i.e., are determined by the polarization of the incident wave. We wish to determine the R^r . From the results of the previous chapter (Eqs. (3-32) through (3-35) and Eq. (3-43)) we can express the tangential fields at the surface of the panel ($z=0^+$) as:

$$(4-5) \quad \vec{E}|_{z=0^+} = \sum_{r=1}^2 [a_1^{rd} + \rho^r(1-DF^r)] \vec{e}_{ar}^{r(1)} + \sum_{r=1}^2 \sum_{i=2}^{\infty} a_i^r \vec{e}_{ai}^{r(1)}$$

$$(4-6) \quad \vec{H}|_{z=0^+} = \sum_{r=1}^2 [a_1^{rd} - \rho^r(1+DF^r)] \vec{h}_{ar}^{r(1)} - \sum_{r=1}^2 \sum_{i=2}^{\infty} a_i^r \vec{h}_{ai}^{r(1)}$$

where the ρ^r and a_i^r are unknown modal coefficients and we define

$$(4-7) \quad a_1^{rd} = 2 A^r \frac{\eta_{00}^{r(1)}}{\eta_{00}^{r(1)} + \eta_{00}^r} \exp[-j(\gamma_{00}^{r(1)} - \gamma_{00}^r)t_1]$$

$$(4-8) \quad DF^r = \frac{\eta_{00}^{r(1)} - \eta_{00}^r}{\eta_{00}^{r(1)} + \eta_{00}^r} \exp[-2j\gamma_{00}^{r(1)}t_1]$$

In order to express the fields in the slots we must first consider the effects of the finite thickness on the slot fields. This problem was also considered in Chapter II. We will use the same approach here, but will explain the technique from a somewhat different point of view.

Since we are treating the metal panel as perfectly conducting, the tangential electric field will be zero except in the slots. In the slots at $z=0$ the tangential fields will have to include the reflections from the other end of the slot. As illustrated in Fig. 4-2, a mode i is excited in the slot and propagates in the $-z$ direction. When it strikes the end of the slot at $z=-\lambda$ not only is mode i reflected, but also modes j, k , etc. Thus in order to evaluate the modes at $z=0$ one would need to evaluate the scattering matrix S_{ij} for the discontinuity at $z=-\lambda$, where S_{ij} represented the

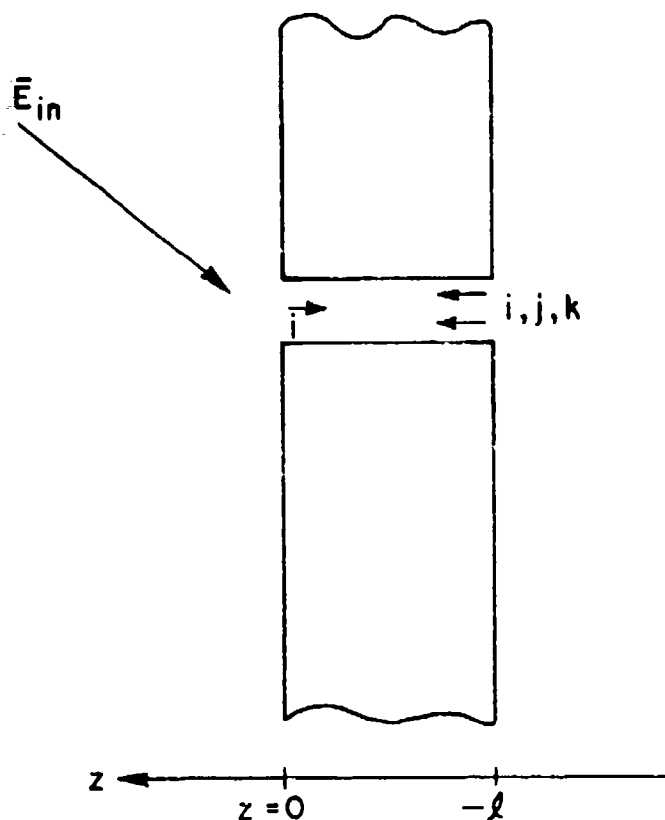


Figure 4-2.--A slot mode i excited when the incoming plane wave hits the panel at $z=0$ will excite other modes, j, k, \dots , as well as mode i itself when it is reflected by the end of the slot at $z=-\ell$.

reflected amplitude of mode j due to mode i . This scattering matrix would be difficult and time-consuming to evaluate. We can skirt this problem, however, by considering the situation in Fig. 4-3. In Fig. 4-3a is illustrated symmetric excitation. Identical plane waves are incident on the array and phased so that at $z=-\ell/2$ the E fields add and the H fields cancel producing an open circuit. Similarly, Fig. 4-3b illustrates antisymmetric excitation which effectively produces a short circuit at $z=-\ell/2$. Thus, if the panels are covered with dielectric, the dielectric layers on each side must be identical. If we should solve for the fields in the half-space $z > -\ell/2$ with both symmetric and antisymmetric excitation and add them, the reflection coefficient obtained would be that for a single incident plane wave, as illustrated in Fig. 4-3c. If on the other hand we subtract the fields, then the reflection coefficient obtained for the half space $z > -\ell/2$ would actually be equal to the transmission coefficient for the panel, as illustrated in Fig. 4-3d.

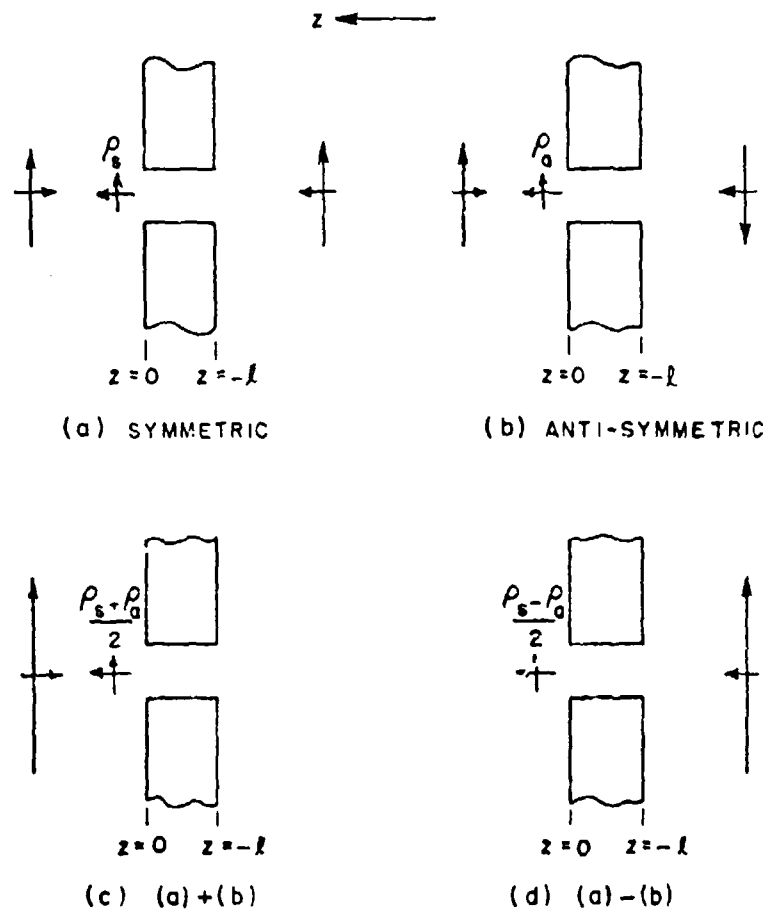


Figure 4-3.--Symmetric and anti-symmetric excitation of a slot in the array.

The symmetric and antisymmetric excitations also diagonalize the scattering matrix S_{ij} , enabling us to expand the tangential fields in the central slot at $z=0^-$ as

$$(4-9) \quad \bar{E}|_{z=0^-} = \sum_{j=1}^{\infty} b_j \bar{e}_{bj}(1+S_{jj})$$

$$(4-10) \quad \bar{H}|_{z=0^-} = \sum_{j=1}^{\infty} b_j \bar{h}_{bj}(1-S_{jj})$$

where

$$(4-11) \quad S_{jj} = \pm \exp(-j\tau_{fg})$$

With the positive and negative signs corresponding to symmetric and antisymmetric excitation respectively. The \bar{e}_{bj} and \bar{h}_{bj} modes are given in the previous chapter for various slot shapes.

We can now proceed to satisfy the boundary conditions. Tangential E and H must be continuous at the slot aperture, while tangential E must vanish elsewhere. If we equate Eq. (4-5) with Eq. (4-9), take a cross product with $\bar{h}_{am}^{r(1)*}$, and integrate over a periodic cell, we obtain

$$(4-12) \quad [a_1^{rd} + \rho^r(1-DF^r)] \int_a \bar{e}_{a1}^{r(1)} \times \bar{h}_{a1}^{r(1)*} \cdot \hat{z} \, ds = \\ \sum_{j=1}^{\infty} b_j(1+S_{jj}) \int_b \bar{e}_{bj} \times \bar{h}_{a1}^{r(1)*} \cdot \hat{z} \, ds \quad r=1,2$$

for $m=1$, $r=1$ or 2 , and

$$(4-13) \quad a_m^r \int_a \bar{e}_{am}^{r(1)} \times \bar{h}_{am}^{r(1)*} \cdot \hat{z} \, ds = \\ \sum_{j=1}^{\infty} b_j(1+S_{jj}) \int_b \bar{e}_{bj} \times \bar{h}_{am}^{r(1)*} \cdot \hat{z} \, ds$$

for $m=2,3,\dots,\infty$ and $r=1,2$. The notation $\int_a ds$ denotes an integration over the central periodic cell (see Fig. 3-2). Equations (4-12) and (4-13) enforce continuity of tangential E across the slot aperture and, since the integrations containing \bar{e}_{bj} are zero except over the slot aperture ($\int_b ds$), also enforce tangential E=0 at the metallic surface. The orthogonality relation of Eq. (3-22) was used in obtaining Eqs. (4-12) and (4-13). To enforce continuity of tangential H across the aperture we equate Eq. (4-6) with Eq. (4-10), take a cross product with \bar{e}_{bn} , integrate over the slot aperture, and apply the orthogonality relationship of Eq. (3-22), obtaining

$$(4-14) \quad \sum_{r=1}^2 [a_1^{rd} - \rho^r(1+DF^r)] \int_b \bar{e}_{bn} \times \bar{h}_{a1}^{r(1)} \cdot \hat{z} \, ds \\ - \sum_{r=1}^2 \sum_{i=2}^{\infty} a_i^{rd} \int_b \bar{e}_{bn} \times \bar{h}_{ai}^{r(i)} \cdot \hat{z} \, ds = b_n(1-S_{nn}) \int_b \bar{e}_{bn} \times \bar{h}_{bn} \cdot \hat{z} \, ds$$

for $n=1,2,\dots,\infty$. Equations (4-12) through (4-14) actually represent a doubly infinite set of equations. We must therefore truncate the mode sets, retaining enough modes to obtain a good approximation to the true solution. We will leave the discussion of how many modes are required to a later section. For now we will include $2M$ Floquet modes and N waveguide modes in our solution.

It should be noted that Eqs. (4-12) through (4-14) are nearly identical to Eqs. (2-16), (2-17), and (2-19) obtained for the waveguide iris problem of Chapter II. The differences are that in this chapter the Floquet mode set rather than the waveguide modes are used to describe the fields outside the slot and that dielectric layers are now included in the analysis. This similarity is due to the fact that we are matching the tangential fields over only one periodic cell in the array.

Equations (4-13) and (4-14) form a coupled system of equations. If we solve Eq. (4-13) for the a_m^r , change index m to i , and substitute into Eq. (4-14), we obtain,

$$\begin{aligned}
 (4-15) \quad & \sum_{r=1}^2 \rho^r (1 + DF^r) \int_b \bar{e}_{bn} x \bar{h}_{a1}^{r(1)} \cdot \hat{z} ds + b_n (1 - S_{nn}) \int_b \bar{e}_{bn} x \bar{h}_{bn} \cdot \hat{z} ds \\
 & + \sum_{j=1}^N b_j (1 + S_{jj}) \sum_{r=1}^2 \frac{\int_b \bar{e}_{bj} x \bar{h}_{ai}^{r(1)*} \cdot \hat{z} ds}{\int_a \bar{e}_{ai}^{rd} x \bar{h}_{ai}^{r(1)*} \cdot \hat{z} ds} \cdot \int_b \bar{e}_{bn} x \bar{h}_{ai}^{r(1)} \cdot \hat{z} ds \\
 & = \sum_{r=1}^2 a_1^{rd} \int_b \bar{e}_{bn} x \bar{h}_{a1}^{r(1)} \cdot \hat{z} ds, \quad n=1,2,\dots,N
 \end{aligned}$$

which is actually N equations but with $N+2$ unknowns, namely the b_j and the ρ^r . However, if we rearrange Eq. (4-12) we obtain

$$\begin{aligned}
 (4-16) \quad & \rho^r (1 - DF^r) \int_a \bar{e}_{a1}^{r(1)} x \bar{h}_{a1}^{r(1)*} \cdot \hat{z} ds - \sum_{j=1}^N b_j (1 + S_{jj}) \int_b \bar{e}_{bj} x \bar{h}_{a1}^{r(1)*} \cdot \hat{z} ds \\
 & = - a_1^{rd} \int_a \bar{e}_{a1}^{r(1)} x \bar{h}_{a1}^{r(1)*} \cdot \hat{z} ds, \quad r=1,2
 \end{aligned}$$

which together with Eq. (4-15) forms a system of $N+2$ equations with $N+2$ unknowns.

In order to simplify Eqs. (4-15) and (4-16) we shall evaluate the integral $\int_a \bar{e}_{ai}^{r(1)} \times \bar{h}_{ai}^{r(1)*} \cdot \hat{z} ds$. From Eqs. (3-12) to (3-15), (3-18), (3-19), and (3-49), (4-50), we obtain

$$(4-17) \quad \int_a \bar{e}_{ai}^{r(1)} \times \bar{h}_{ai}^{r(1)*} \cdot \hat{z} ds = \frac{1}{\eta_{00} r(T)^*} \cdot \frac{1}{\sqrt{d_x d_y}} \int_a \left(\frac{U_p^2 + V_{pq}^2}{T_{pq}^2} \right) \exp(-j(U_p x + V_{pq} y)) \\ \cdot \exp(+j(U_p x + V_{pq} y)) ds = \frac{1}{\eta_{00} r(T)^*}$$

for $i=1$, and similarly

$$(4-18) \quad \int_a \bar{e}_{ai}^{r(1)} \times \bar{h}_{ai}^{r(1)*} \cdot \hat{z} ds = \frac{1}{z r(T)^*} \cdot \frac{1}{\sqrt{d_x d_y}} \int_a \left(\frac{U_p^2 + V_{pq}^2}{T_{pq}^2} \right) \exp(-j(U_p x + V_{pq} y)) \\ \exp(+j(U_p x + V_{pq} y)) ds = \frac{1}{z r(T)^*}$$

for $i \neq 1$. By applying Eqs. (4-17) and (4-18), and using the $\bar{\phi}_{pq}^r$ function defined in Eq. (3-50), we can rewrite Eq. (4-15) and Eq. (4-16) as

$$(4-19) \quad \sum_{r=1}^2 \rho^r (1 + DF^r) \frac{1}{\eta_{00} r(T)} \int_b \bar{e}_{bn} \times \bar{\phi}_{00}^r \cdot \hat{z} ds + b_n (1 - S_{nn}) \int_b \bar{e}_{bn} \times \bar{h}_{bn} \cdot \hat{z} ds \\ + \sum_{j=1}^N b_j (1 + S_{jj}) \sum_{r=1}^2 \int_{i=2}^M \int_b \bar{e}_{bj} \times \bar{\phi}_{pq}^{r*} \cdot \hat{z} ds \cdot \frac{1}{z r(T)} \int_b \bar{e}_{bn} \times \bar{\phi}_{pq}^r \cdot \hat{z} ds \\ = \sum_{r=1}^2 a_1^r d \frac{1}{\eta_{00} r(T)} \int_b \bar{e}_{bn} \times \bar{\phi}_{00}^r \cdot \hat{z} ds \quad n=1, 2, \dots, N$$

$$(4-20) \quad \rho^r (1 - DF^r) - \sum_{j=1}^N b_j (1 + S_{jj}) \int_b \bar{e}_{bj} \times \bar{\phi}_{00}^r \cdot \hat{z} ds = -a_1^r \quad r=1, 2.$$

The system of equations given by Eq. (4-19), and (4-20) must actually be solved twice, once for symmetric excitation and once for antisymmetric excitation. If we denote the reflection coefficients in the dielectric region as ρ_s^r and ρ_a^r for symmetric and antisymmetric excitation respectively, we can find the corresponding free space reflection coefficients R_s^r and R_a^r from Eq. (3-44). Recalling the properties of symmetric and antisymmetric excitation it is evident that the free space reflection coefficients R^r and the free space transmission coefficients T^r are given by

$$(4-21) \quad R^r = 1/2 (R_s^r + R_a^r)$$

$$(4-22) \quad T^r = 1/2 (R_s^r - R_a^r).$$

Due to the difficulty of machining complex slot shapes in thick panels, we will be primarily concerned with rectangular slot arrays. For rectangular slots we have, from Eqs. (3-69) and (3-70),

$$(4-23) \quad \int_b \bar{e}_{bj} \times \bar{h}_{bj} \cdot \hat{z} \, ds =$$

$$Y_{bj} \int_{-b/2}^{b/2} \int_{-a/2}^{a/2} \sin^2\left(\frac{f\pi x}{a} - \frac{f\pi}{2}\right) \cos^2\left(\frac{g\pi x}{b} - \frac{g\pi}{2}\right) dx dy$$

$$= \begin{cases} .25 \, ab \, Y_{bj} & \text{for } g \neq 0 \\ .50 \, ab \, Y_{bj} & \text{for } g = 0 \end{cases}$$

where the integral is evaluated at the front surface of the panel ($z=0$). The $\int_b \bar{e}_{bj} \times \bar{h}_{pq}^r \cdot \hat{z} \, ds$ integrals are evaluated in closed form, with the results given in Appendix B.

The solution was then programmed in Fortran IV for computer solution. The convergence and accuracy of this solution will be investigated in Section B. Then in following sections of this chapter various results obtained from the above solution will be presented. In Section C we will illustrate how the undesired shift of resonance with incidence angle which limits the applications of rectangular slot arrays can be eliminated by sandwiching the array between dielectric layers of the proper thickness and dielectric constant. These dielectric layers also have the effect of greatly reducing the change of bandwidth with incidence angle. In Section D we will

discuss how the presence of these dielectric layers will cause the Wood's anomaly transmission null to move downwards in frequency. Section E shows how a similar downward shift of the Wood's anomaly null frequency can be caused by certain slot arrangements. In section F we will show how the undesired resonance shift can be eliminated for thicker panels (0.1") by filling the rectangular slots with dielectric. Finally, in Section G some general comments on the interaction of thickness and dielectric effects will be made and supported by calculations.

B. Convergence Properties of the Modal Solution

In this section we shall first show a comparison between calculated and measured data, and then investigate the convergence properties of the modal solution.

In Fig. 4-4 are shown measured points and calculated curves given by Munk [3] for the reflection from a periodic array of rectangular strip dipoles. The Wood's anomalies are shown quite clearly in these curves, and the shift of resonance frequency with incidence angle is quite severe. Note that the reflection curves do not reach 0 dB for frequencies above the Wood's anomaly. This is because some of the incident energy is being radiated in the grating lobe directions.

Transmission curves for the complementary slot array calculated using the modal analysis solution of the previous section are shown in Fig. 4-5. The panel thickness is 0.0175 cm. The number of Floquet modes used was 242, with the maximum absolute values of p and q equal to 5. Four modes were used to describe the fields in the slots, with $f=1,3,5$, and 7, and $g=0$. For these incidence angles the even ordered modes are not excited. The agreement between the two solutions is quite good. Note that for the frequencies above the Wood's anomalies the modal solution agrees better with the measured points than the mutual impedance solution curves of Fig. 4-4. The main discrepancy between the two solutions is that the resonance curves given by the modal solution are more narrow banded. This is as it should be, however, since finite thickness causes the bandwidth of a slot array to become more narrow, while a thick dipole array will have a wider bandwidth than a thin one.

In the next three figures we shall illustrate some of the convergence properties of the modal solution. In Fig. 4-6 are resonance curves for the same panel geometry as Fig. 4-5 for (near) normal incidence. Since p and q will have negative values the total number of Floquet modes is given by $2 \cdot (2 \cdot p_{\max} + 1)(2 \cdot q_{\max} + 1)$, where p_{\max} and q_{\max} represent the absolute maximum values of p and q respectively. For this case $p_{\max}=q_{\max}=5$, thus the number of Floquet modes is at 242. The number of slot modes is varied from 1 to 4 (only the odd modes ($f=1,3,5,\dots$) are excited). It is evident that for this geometry and incidence angle the solution converges quite rapidly in terms of the slot modes, with good results obtained even with just 1 mode in the slot.

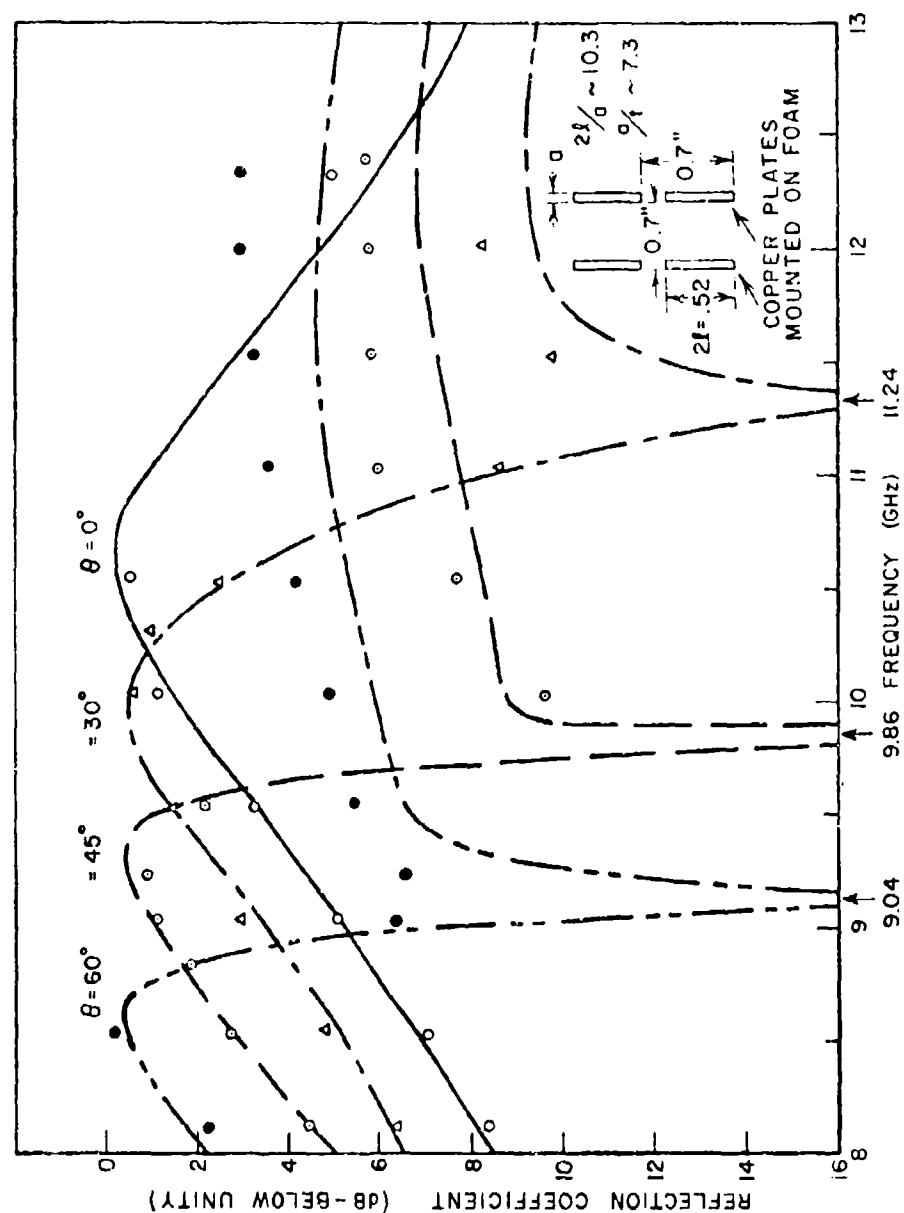


Figure 4-4.--Calculated curves (mutual impedance method) and measured points (from Munk, [3]) for the bistatic reflection coefficient for an array of dipoles; t is the thickness of the copper plates.

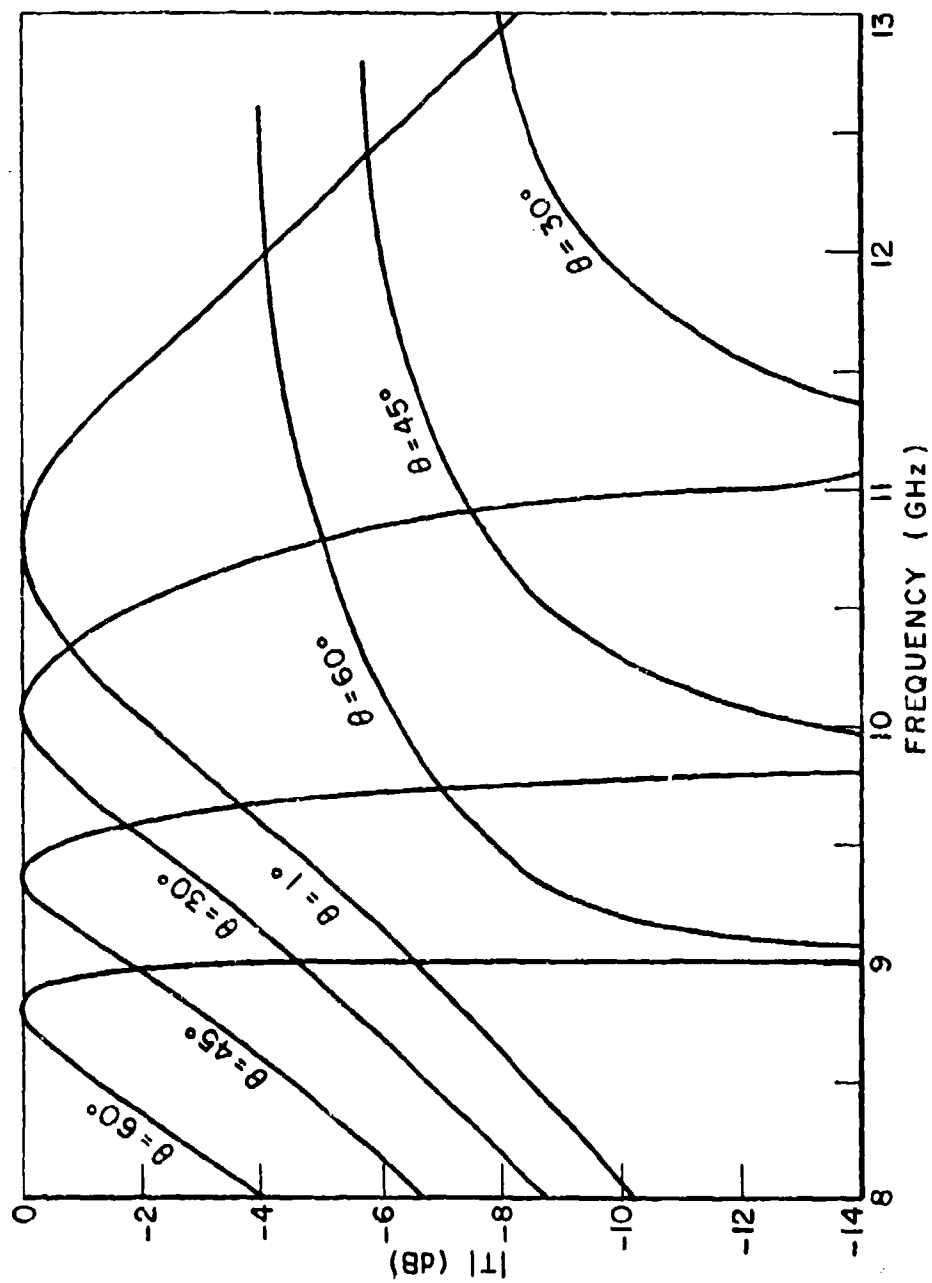


Figure 4-5.--Transmission curves for the slot array which is the complement of the dipole array of Fig. 4-5 calculated using the modal analysis solution.

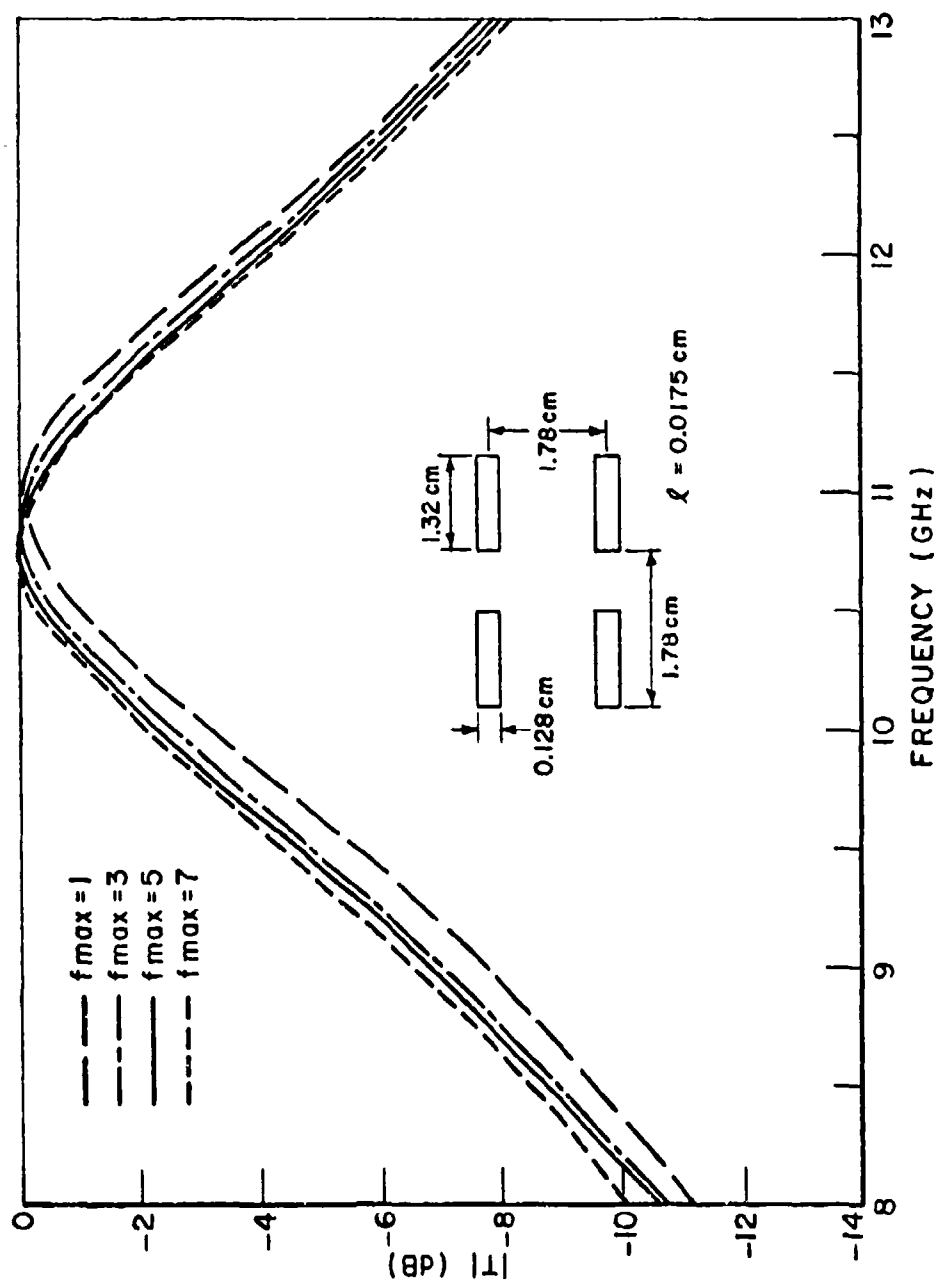


Figure 4-6.--Convergence data consisting of calculated transmission curves for an array of slots in a 0.0175 cm thick panel for near normal (1° E-plane) incidence vs. frequency. The slot mode index f has maximum values of 1, 3, 5, and 7 for the various curves. The number of Floquet modes is kept constant at 242.

In Figs. 4-7 and 4-8 we show more general convergence data for the modal solution. The panel geometry is again the same as in Fig. 4-4, except that now the panel is sandwiched between two dielectric layers .3175 cm thick with $\epsilon_r=4.0$. The frequency is held constant at 5 GHz, while both the number of Floquet modes and slot modes are varied. Figure 4-7 is for 80° H-plane incidence ($\theta=80^\circ$, $\phi=0^\circ$) while Fig. 4-8 is for 80° E-plane ($\theta=80^\circ$, $\phi=90^\circ$). There are several points which should be made concerning the two figures. The first is that the convergence rate is dependent on the incidence angle. The E-plane solution is converging faster than the H-plane, even when considered on a percent error basis. This is also true for the mutual impedance solution, i.e., more terms in the impedance summation are required for H-plane (slot panels) convergence than for E-plane.

The second point is that a very high ratio of Floquet modes to slot modes is needed for convergence. This agrees qualitatively with results for other modal type solutions, where it was found that for optimum results the ratio of modes in the two regions should be in proportion to the relative size of the two regions [40]. However, these results were for much simpler, two dimensional problems and do not apply precisely to the geometry being considered here. Note that the size of the matrix required to solve for the modal coefficients does not depend on the number of Floquet modes, but depends only on the number of slot modes. Thus the integral equation formulation of the previous section is quite efficient in terms of computer storage space required for this geometry.

The third point is that for a given number of slot modes there is a minimal number of Floquet modes, below which number the solution will not have converged, and above which number very little change occurs in the result. One method for detecting that the required minimal number of Floquet modes has been included in the solution is to observe the calculated modal coefficients. Normally, the modal coefficients will decrease in magnitude roughly as the attenuation constant increases. If instead they increase exponentially one can conclude that more Floquet modes should be included in the solution [46]. This minimum required number of Floquet modes is evident in Fig. 4-8, where for $f_{\max}=5$ the solution has converged at $p_{\max}=q_{\max}=4$, while for $f_{\max}=7$ the solution does not converge until $p_{\max}=q_{\max}=5$. Note that this minimal number of Floquet modes increased with the increase in the number of slot modes, which agrees with the statement of point two that for a given geometry there is an optimum ratio of Floquet modes to slot modes.

In general, for three dimensional mode matching problems of the type being considered here there seems to be no simple way to arrive at the optimum number of modes required for convergence, and one is forced to run convergence tests of the type shown. These convergence tests are complicated by the fact that there are two mode sets to be considered.

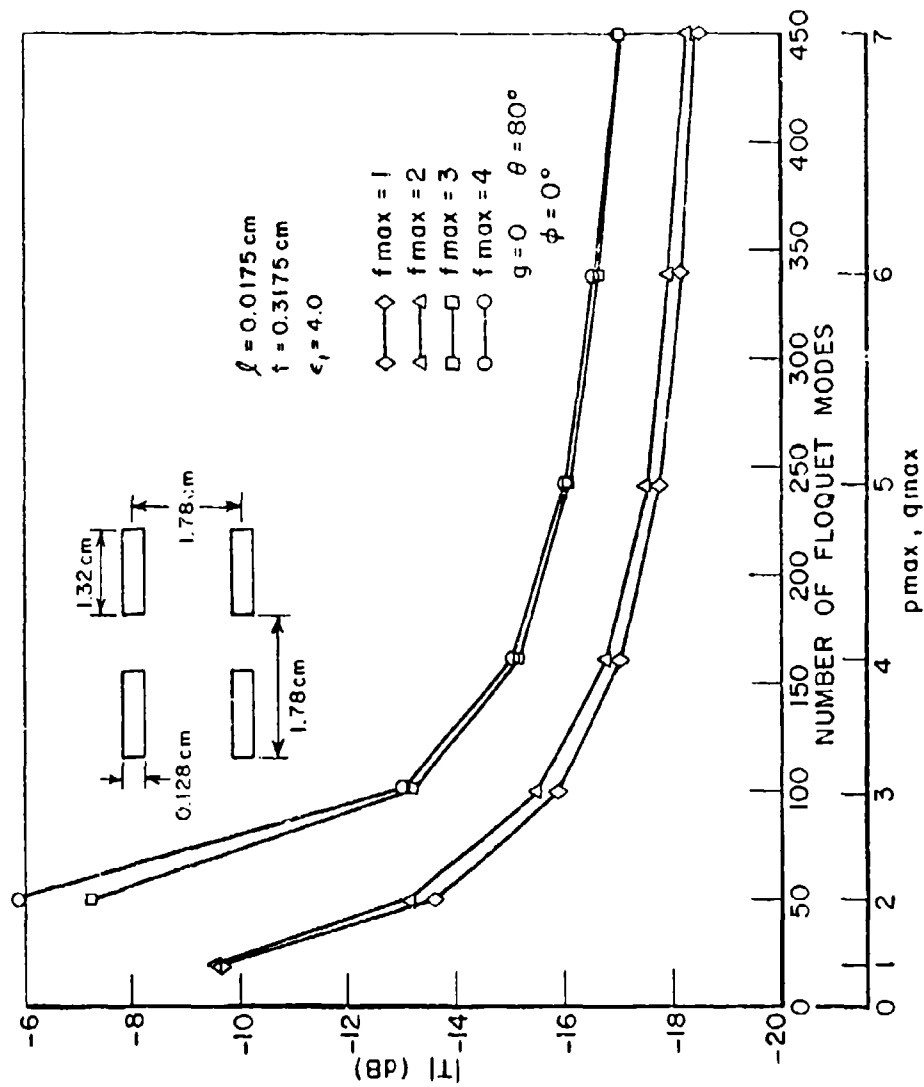


Figure 4-7.--Convergence data consisting of the transmission coefficient at 5 GHz for the array shown for various numbers of slot modes (f_{\max}) vs. the number of Floquet modes; 80° H-plane incidence.

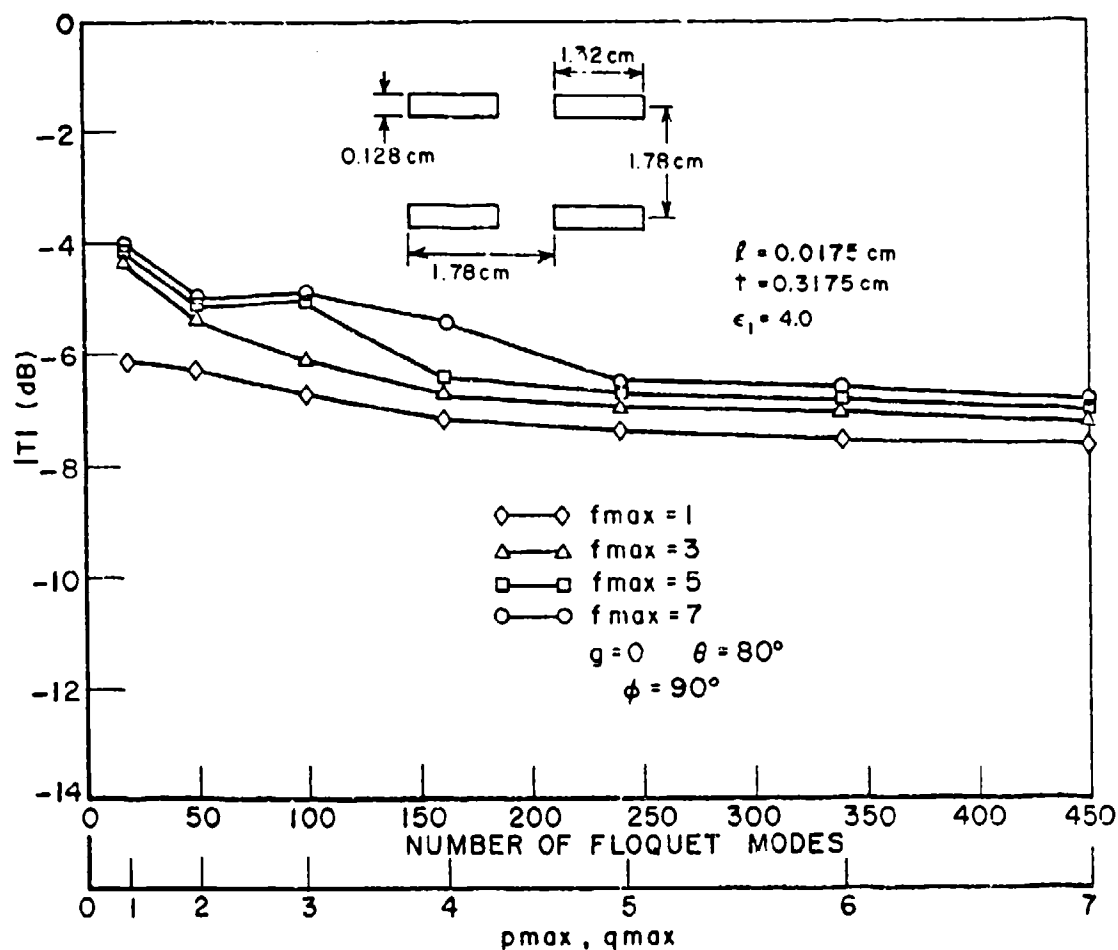


Figure 4-8.--Convergence data consisting of the transmission coefficient at 5 GHz for the array shown for various numbers of slot modes (only the odd modes are excited) vs. the number of Floquet Modes; 80° E-plane incidence.

Now that our discussion of the convergence properties of this solution has been completed, let us proceed to show some of the results obtained using this solution.

C. Thin Arrays Covered with Dielectric Slabs

In this section we are concerned with investigating the effects of cladding resonant slot arrays in dielectric slabs. While the calculated curves are for thin ($k < .01\lambda$) arrays of rectangular slots, many of the results obtained will apply to arrays of loaded slots as well. This is true of the results obtained concerning the effects of the dielectric slabs on the Wood's anomaly, which will be discussed more fully in the next section. Also, the effect which the dielectric slabs have of stabilizing the bandwidth of slot arrays as a function of incidence angle has application to loaded slot arrays as well.

It will be shown here that arrays of rectangular slots covered with dielectric slabs can be designed to overcome the undesirable shift of resonance frequency with incidence angle normally found in such arrays. This development is of practical interest since rectangular slots may be more easily fabricated than loaded slots, especially in thick panels where chemical milling does not give good results.

In Fig. 4-9 we show an interesting series of calculated curves which illustrates the effects of dielectric layers of various thicknesses on the resonance frequency of a slot array. The panel geometry is the same as that of Fig. 4-5, and the curves shown are all for near normal incidence ($\theta=1^\circ$, $\phi=90^\circ$). The dielectric material is lossless with $\epsilon_r=4.0$. The number of modes used is the same as in Fig. 4-5. The curve marked NO DIELECTRIC is the same as the corresponding $\theta=1^\circ$ curve of Fig. 4-5, and is calculated with the perforated metal panel in free space. If the slots themselves are filled with a lossless dielectric material with $\epsilon_r=4$ (referring to Fig. 4-1, we have $\epsilon_3=4.0$, $\epsilon_1=1.0$) the resonance frequency is reduced slightly. For a thicker panel the reduction will be greater, as will be illustrated in a later section of this chapter.

If we leave the dielectric in the slot ($\epsilon_3=4.0$) and also coat the array on both sides with dielectric layers of various thicknesses ($\epsilon_1=4.0$) we obtain the remaining curves. Note that even for the 0.079 cm thick coating, with a thickness of only $.017\lambda$ at 6.5 GHz, the reduction in resonance frequency is quite marked. Note also that the shift in resonance frequency with dielectric thickness is not monotonically downward, but that the panel with the thickest dielectric layer ($t=0.7$ cm) actually resonates at a higher frequency than several of the panels with thinner dielectric layers. Munk et.al. [4] have shown that this resonance frequency vs thickness oscillation is a transmission line effect which is superimposed on the usual monotonic decrease in resonant frequency vs dielectric thickness, and which tends to cause relative minima in resonance frequency for dielectric thicknesses $\beta t = \pi/4 + n\pi$, and relative maxima for $\beta t = 3\pi/4 + n\pi$, where $\beta = \omega\sqrt{\epsilon\mu}$, i.e., is the propagation constant in the dielectric. The shoulders on the curves for $t=0.317$ cm and $t=0.5$ cm are due to the same transmission line effects.

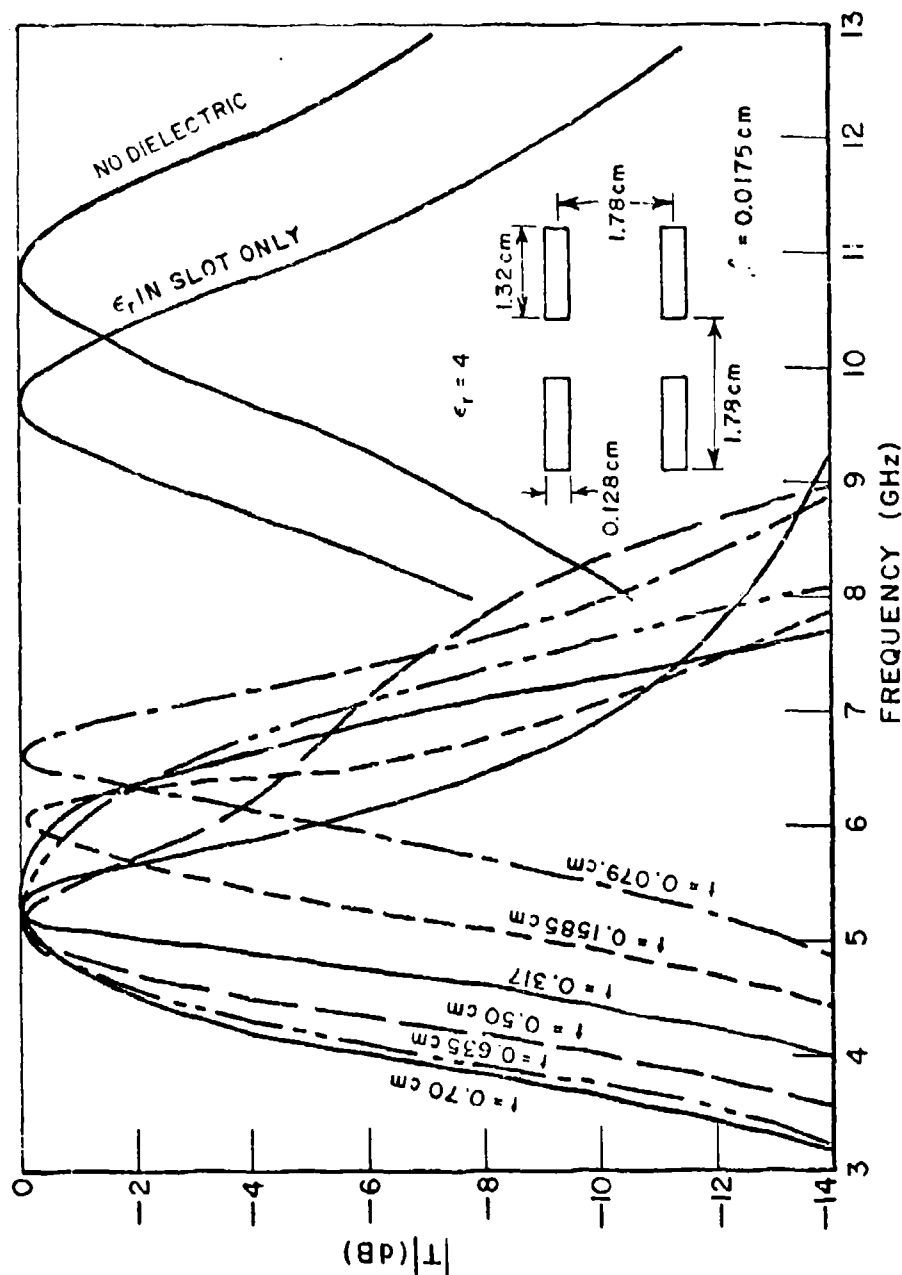


Figure 4-9.--Transmission coefficient vs. frequency for a slot array covered with varying thicknesses of dielectric material. Near normal ($\theta=1^\circ$, $\phi=90^\circ$) incidence.

The next three figures show the effects of coating a resonant slot array with dielectric layers of the same thickness (0.7 cm) but varying dielectric constants (1.5, 2.6, 4.0). Again the actual panel geometry is the same as in Fig. 4-5. Various incidence angles are shown for both E- and H-plane incidence (i.e., $\phi=90^\circ$ and 0°).

Comparing Fig. 4-10 with Fig. 4-5 it is evident that the shift of the resonance frequency with incidence angle has been reduced somewhat over the free space case even though the dielectric constant is only 1.5. The frequency of the Wood's anomaly null, i.e., the null in the transmission coefficient which, for the non-dielectric case, is associated with the onset of a propagating grating lobe, has been shifted downward slightly in frequency due to the presence of the dielectric layer. This downward shift is a function of the dielectric thickness and permittivity and will be discussed more fully in the next section, where the null will be referred to as a "surface wave null". The frequency at which the free space grating lobe begins to propagate is not changed by the presence of the dielectric layer. This is evident from inspection of the 60° and 30° H-plane curves and the 30° E-plane curves which have an abrupt change in slope at the onset of the free space grating lobes. The frequencies at which these changes in slope occur are approximately 9.04, 11.24, and 11.24 Hz respectively, which agree with the free space values evident in Figs. 4-4 and 4-5. The 30° E-plane resonance curve has a second resonance at 11.1 GHz which is "forced" by the effect of the dielectric layer on the Floquet modal impedance. This forced resonance does not result in lossless transmission due to the propagating free space grating lobe.

Moving on now to Fig. 4-11, we can see that increasing the dielectric constant from 1.5 to 2.6 has caused both the resonance frequencies and the Wood's anomaly (surface wave) null frequencies to move downward for the various incidence angles. The resonance frequencies are almost aligned now, with better alignment prevented by the shoulder on the 60° E-plane resonance curve. Both the 30° and 60° E-plane resonance curves have a nearly lossless forced resonance. Note the abrupt change in slope of the 60° E-plane curve at 9.04 GHz (the onset of the propagating grating lobe). The increase in the dielectric constant has allowed the formation of an incipient forced resonance in the 60° H-plane curve at 9.05 GHz. This forced resonance right at the grating lobe onset can exist for this incidence plane because the element pattern prevents the grating lobe from being strongly excited at its onset. The 12.1 GHz resonance for 60° H-plane incidence is again due to the effect of the dielectric layer on a Floquet modal impedance, and not to a higher order slot mode resonance.

It is instructive to examine the bandwidths of the various resonance curves. Compared with Fig. 4-10, it is evident that the bandwidth of the 60° H-plane curve has been increased considerably with the increase in the dielectric constant. This increase is quite

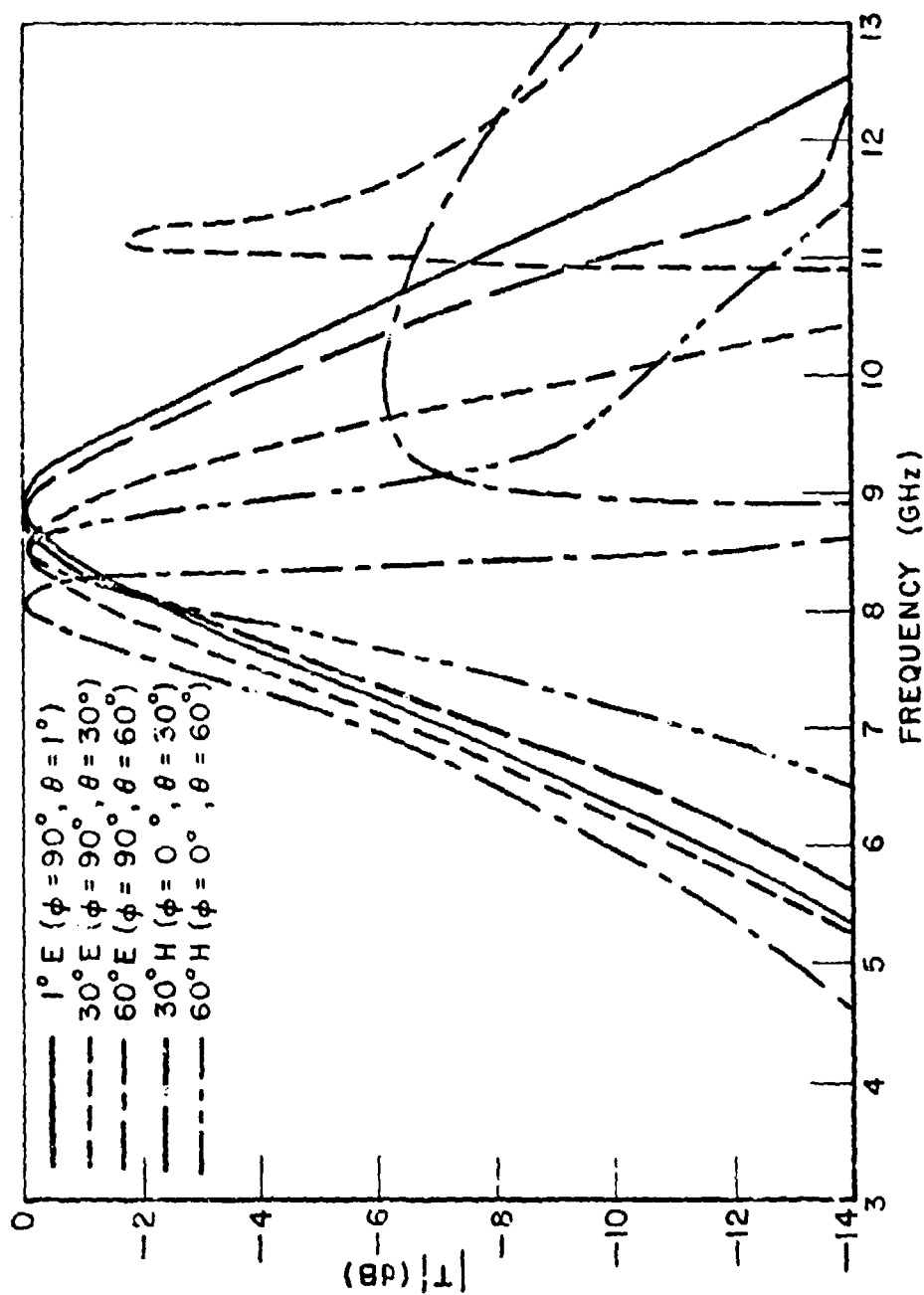


Figure 4-10.--Calculated transmission coefficient curves for the slotted panel of Fig. 4-5 ($d_x=d_y=1.78$ cm, $a=1.32$ cm, $b=0.128$ cm, $\alpha=90^\circ$) covered on both sides by a dielectric layer 0.7 cm thick with $\epsilon_r=1.5$ in the dielectric layer and in the slot.

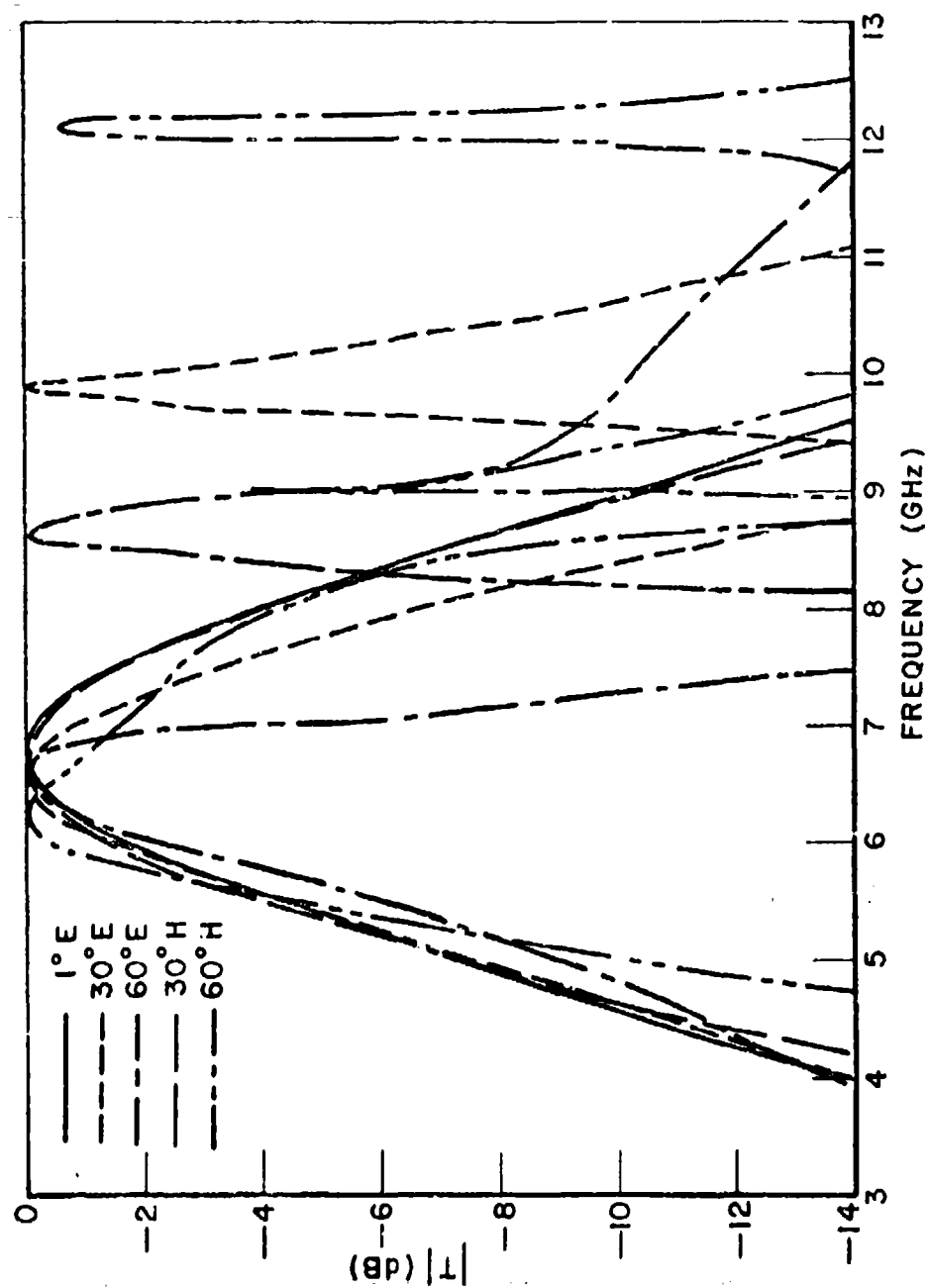


Figure 4-11.--Calculated transmission coefficient curves for the slotted panel of Fig. 4-5 ($d_x=d_y=1.78$ cm, $a=1.32$ cm, $b=0.128$ cm, $\alpha=90^\circ$) covered on both sides by a dielectric layer 0.7 cm thick with $\epsilon_r=2.6$ in the dielectric layer and in the slot.

significant, for it tends to confirm previous predictions [4] that the E- and H-plane bandwidths of a resonant slot array could be made nearly independent of incidence angle by coating the array on both sides with dielectric slabs of the proper thickness and dielectric constant. The ratio between the 60° E-plane and 60° H-plane resonance curve bandwidths would normally be approximately 4:1, while in Fig. 4-11 this ratio is reduced to 2:1. This example is not conclusive, however, since the Wood's anomaly (surface wave) null just above resonance for the 60° E-plane curve tends to narrow the bandwidth of this curve. If this null were removed, the 60° E-plane bandwidth would increase. But note that this increase would tend to decrease the ratio between the E- and H-plane bandwidths even more, provided it was limited to approximately a factor of two. Much further work has been performed on this subject, and the interested reader is referred to the work by Munk et.al., reported in reference [5].

The resonance curves obtained by increasing the dielectric constant to 4.0 are shown in Fig. 4-12. The lower, primary resonance frequencies are now aligned quite well at 5.5 GHz, although the dip in the resonance curve for 60° H-plane incidence shows a calculated loss of 0.6 dB. The 60° H-plane curve now shows a dielectric forced resonance at 8.3 GHz, as does the 30° H-plane curve at 11.4 GHz. The maximum ratio of the 4 dB bandwidths is again approximately 2:1. Measured transmission curves for the geometry corresponding to Fig. 4-12 are shown in Fig. 4-13. The agreement is good. The stable resonance frequency is confirmed, as is the reduction in the variation of bandwidth with incidence angle. The measured dielectric forced resonances are lossy due to the finite size of the measured panel (approximately $8'' \times 10''$). An important point is that the lowering of the frequency of the Wood's anomaly (surface wave) null, which was predicted by the theory to take place when the panel was coated with dielectric, has been confirmed by the measurements. This phenomenon will be discussed in more detail in the next section.

Figure 4-14 shows calculated transmission curves for the same slot geometry with ϵ_r still 4.0 but with the dielectric only half as thick. Note that the 60° H-plane bandwidth has narrowed considerably compared with the results of Fig. 4-12. The thinner dielectric is not able to cause the increase of the H-plane bandwidth, which seems to indicate that the thicker layer is required in order to obtain the bandwidths nearly independent of incidence angle which were evident in Fig. 4-12. Measured curves corresponding to the calculated curves of Fig. 4-14 are shown in Fig. 4-15. Again the agreement is good. The stable fundamental resonance frequencies are confirmed, as are the frequencies and general shapes of the dielectric forced resonances. The measured loss at the fundamental resonance is primarily due to imperfections in the array and to experimental error.

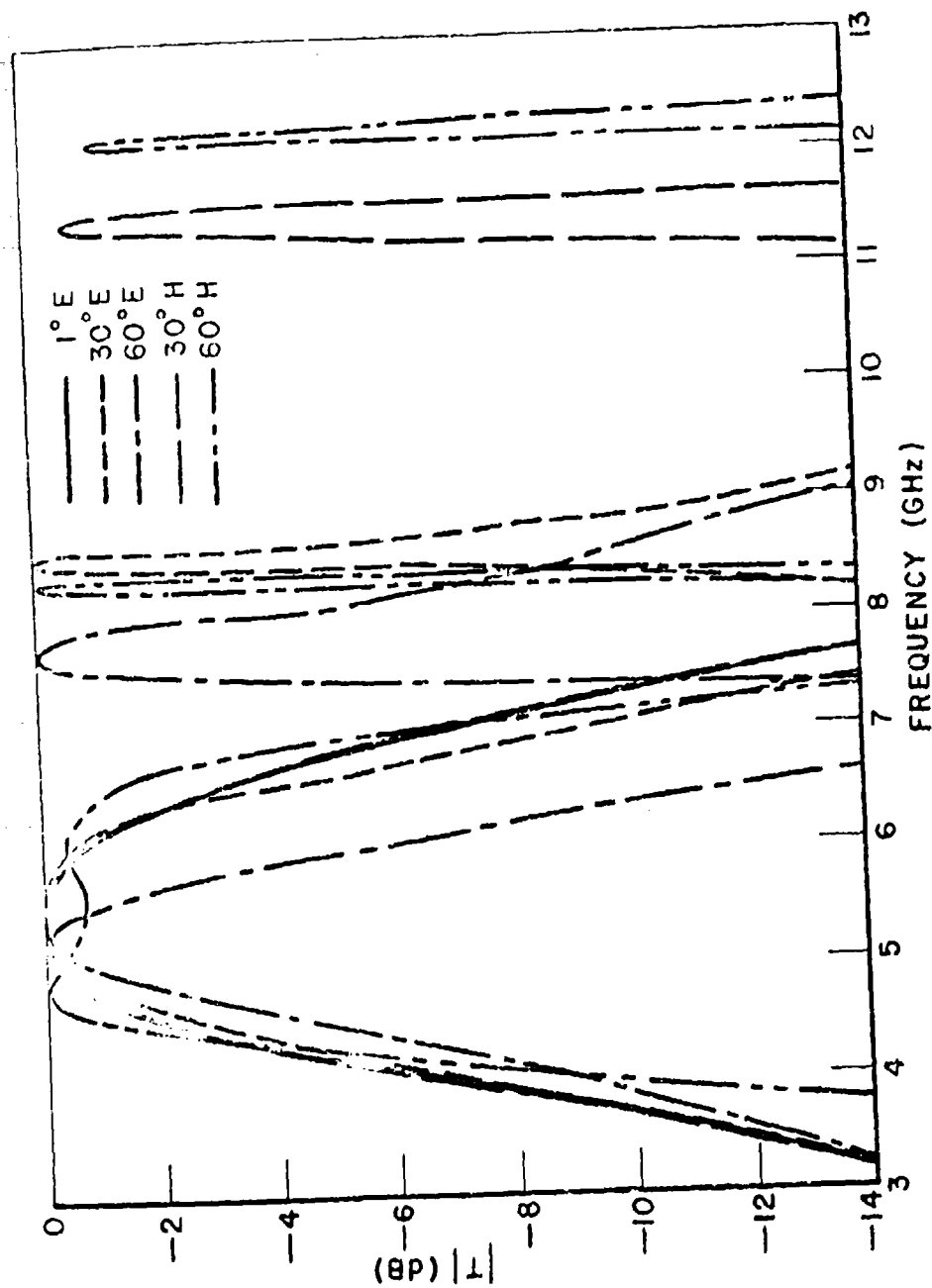


Figure 4-12.--Calculated transmission coefficient curves for the slotted panel of Fig. 4-5 ($d_x = d_y = 1.78$ cm, $a = 1.32$ cm, $b = 0.128$ cm, $\alpha = 90^\circ$) covered on both sides by a dielectric layer 0.7 cm thick with $\epsilon_r = 4.0$ in the dielectric layer and in the slot.

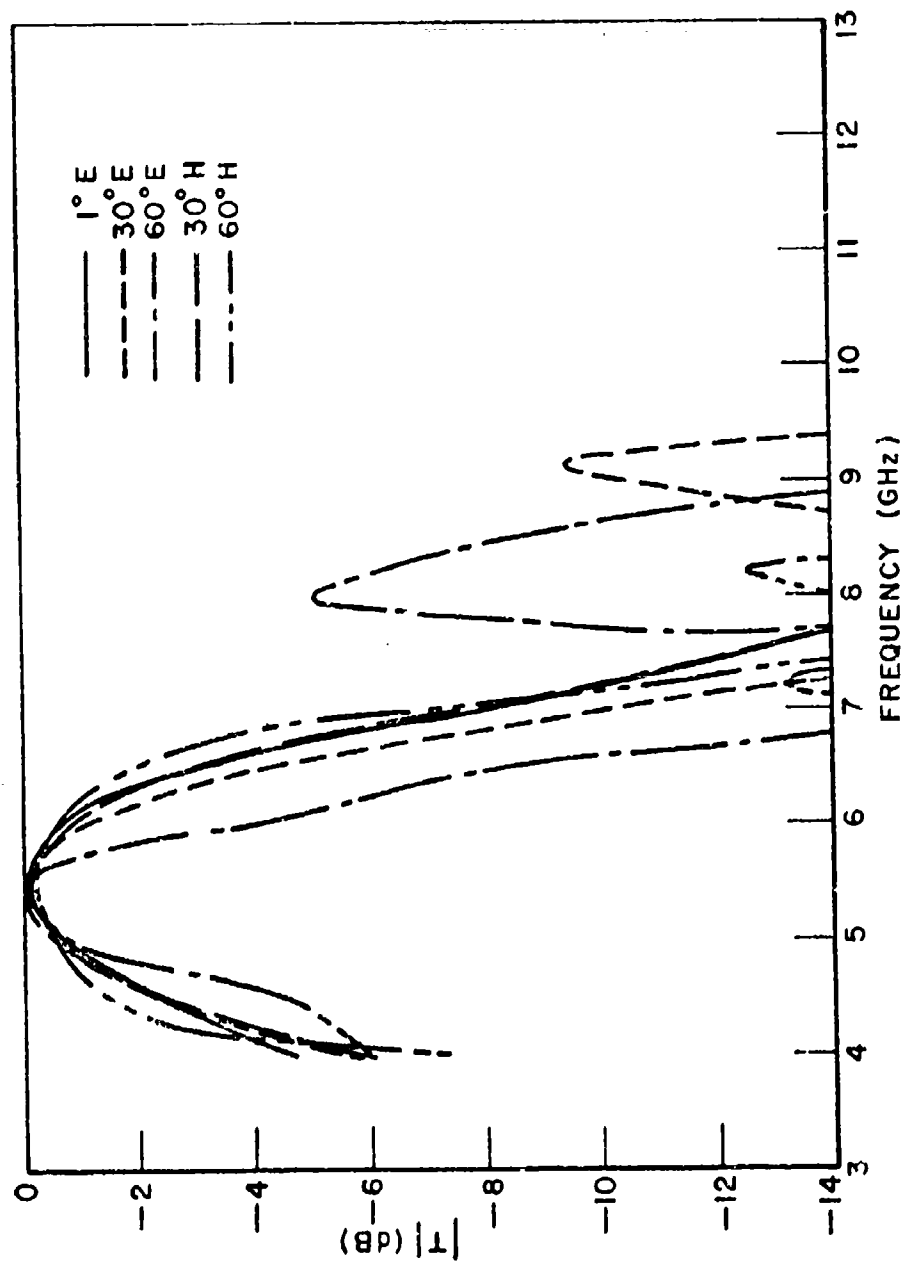


Figure 4-13.--Measured transmission curves for the dielectric coated array of Fig. 4-12.

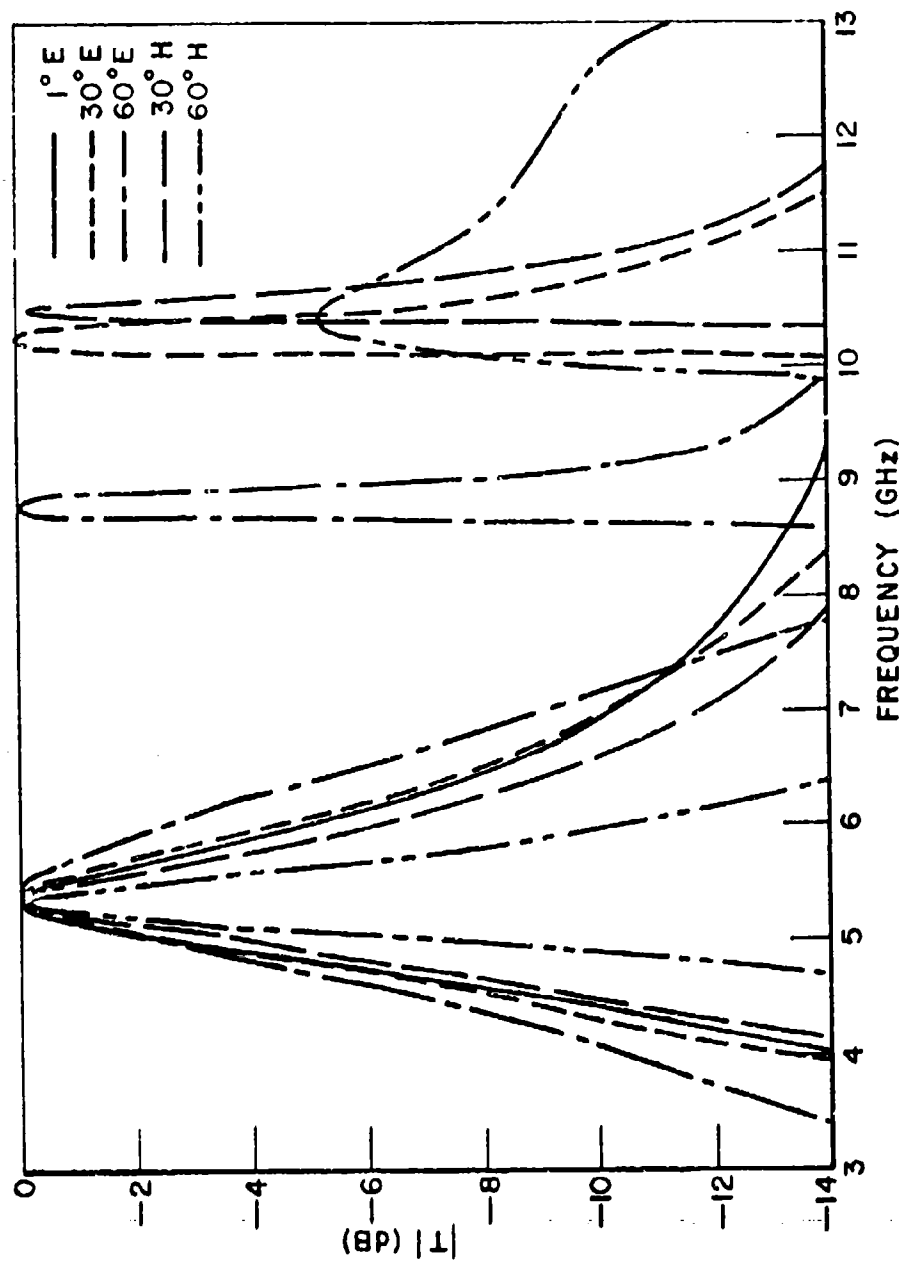


Figure 4-14. ---Calculated transmission coefficient curves for the slotted panel of Fig. 4-5 ($d_x = d_y = 1.78$ cm, $a = 1.32$ cm, $b = 0.128$ cm, $\alpha = 90^\circ$) covered on both sides by a dielectric layer 0.35 cm thick with $\epsilon_r = 4.0$ in the dielectric layer and in the slot.

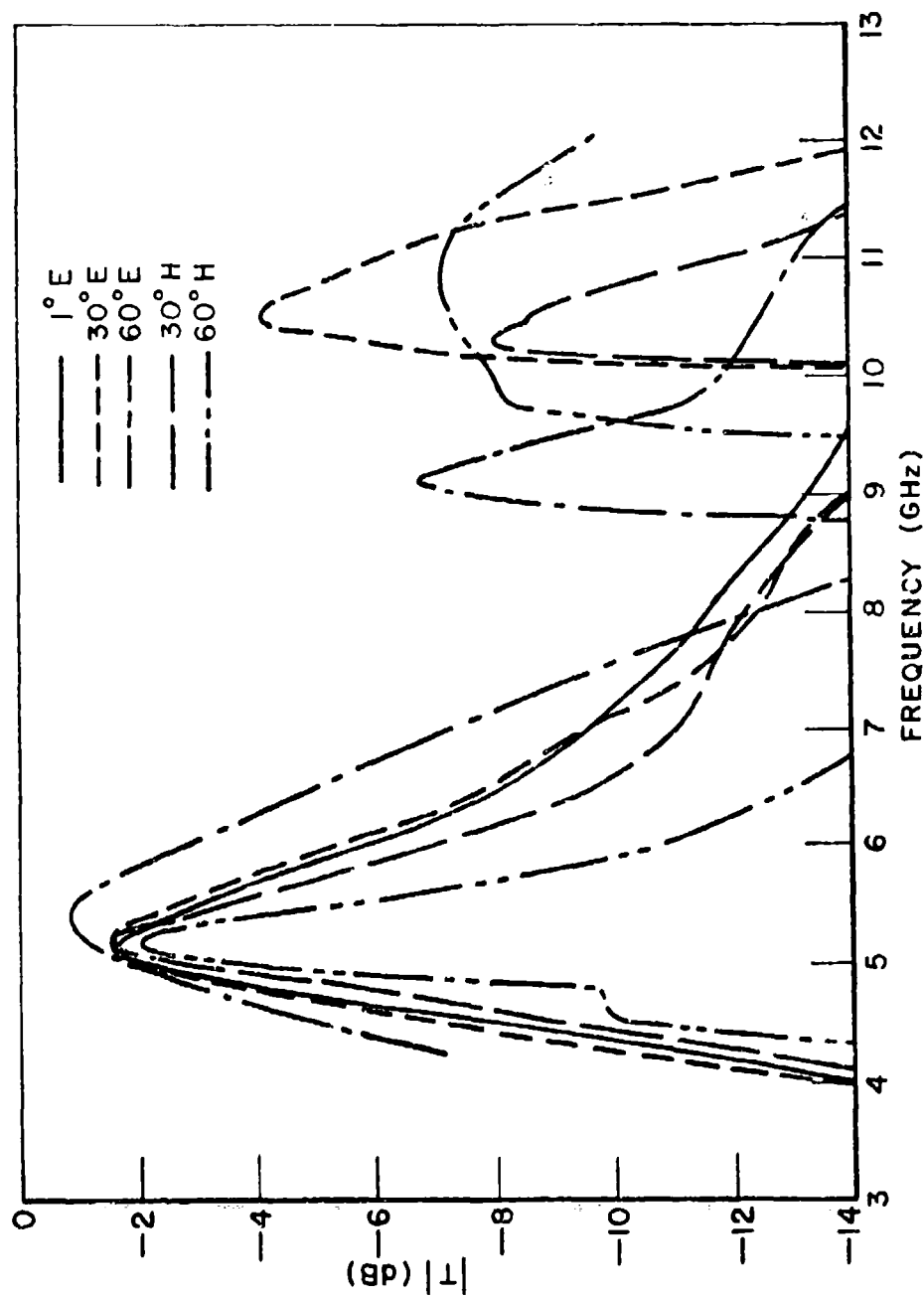


Figure 4-15.--Measured transmission curves for the dielectric coated array of Fig. 4-14.

D. Dielectric Layers and Wood's Anomaly

In the previous section of this chapter calculated and measured transmission coefficient curves were presented which showed that the frequency of the Wood's anomaly transmission null was decreased with the increase in the thickness of the dielectric layers surrounding the resonant slot array. In this section we will show how this frequency reduction can be quite simply determined without recourse to the computer. Also an explanation of how the dielectric layer affects the Wood's anomaly nulls, the grating lobe onset, and the forced resonances will be presented.

The term Wood's anomaly has been used here to denote a null in the transmission coefficient of a slot array which, for the free space case, is associated with the onset of one or more propagating grating lobes. Several of these nulls are indicated in Fig. 4-4. For an array of small slots in free space the Wood's anomaly will occur just below the frequency at which the grating lobe starts to propagate in real space, which for normal incidence on a rectangular grid array will first occur when the separation between adjacent slots is one wavelength. The phenomenon was investigated by R.W. Wood [47] who was concerned with explaining certain anomalous dark bands in spectra produced by optical gratings. He found that these transmission nulls were due to destructive interference along the plane of the grating which occurred when the spacing between adjacent lines was an integral multiple of one wavelength (normal incidence). We are concerned here with the same phenomenon.

Much research into this phenomenon has been done in the analysis of phased arrays. In the phased array literature the phenomenon is known by the name of blind angle, although the same term is also used to denote transmission nulls due to other causes. We will hereafter denote the Wood's anomaly phenomenon by the term "surface wave null", since, as we shall show, the null is caused by the presence of a surface wave field on the surface of the panel.

While the presence of a dielectric layer will lower the frequency of this surface wave null it will not affect the frequency at which the grating lobes come into real space, i.e., become propagating. This can be seen quite easily by examining the Floquet modes of Chapter III. However, a more physical explanation of this fact can be made. In Fig. 4-16 the geometry for a plane wave incident on an array of thin slots covered with dielectric is shown. The plane wave is incident at an angle θ_i . Due to refraction the incidence angle inside the dielectric becomes θ_r , and from Snell's law we have

$$(4-24) \quad \frac{\sin \theta_i}{\sin \theta_r} = \sqrt{\epsilon_1 / \epsilon_0}.$$

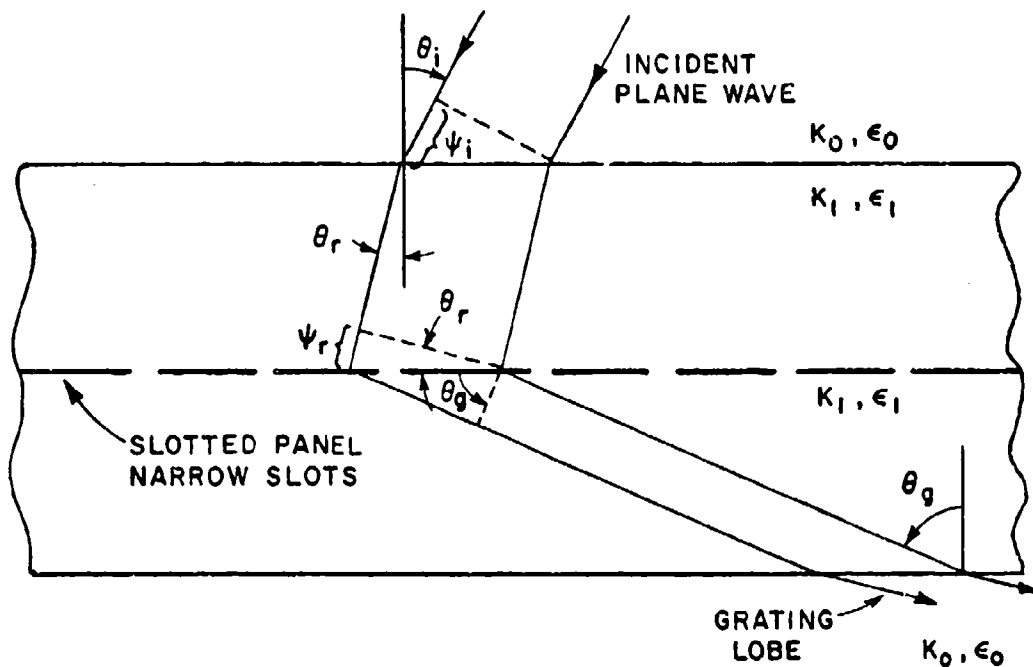


Figure 4-16.--Section of a dielectric covered slot array with a propagating grating lobe.

In free space the grating would start to propagate as soon as the electrical spacing between adjacent elements became 2π radians. However, with the dielectric layer present the grating lobe will not be able to propagate until θ_g , the angle of the grating lobe direction in the dielectric media, is less than θ_c , the critical angle for the dielectric material. The critical angle θ_c is given by

$$(4-25) \quad \sin \theta_c = 1/\sqrt{\epsilon_1}.$$

Thus at the onset of the propagating grating lobe $\theta_c = \theta_g$, and

$$(4-26) \quad K_1 d_x \sin \theta_r + K_1 d_x \sin \theta_c = 2\pi.$$

Now if we apply Eqs. (4-24) and (4-25) and note that $K_1 = K_0 \sqrt{\epsilon_1/\epsilon_0}$, Eq. (4-26) readily reduces to

$$(4-27) \quad K_0 d_x (1 + \sin \theta_i) = 2\pi$$

which is the same equation which is obtained for the free space case.

Thus the presence of the dielectric layer does not alter the frequency at which the grating lobes begin to propagate.

By use of Snell's law it is quite easy to show that the relative phase of the incident wave at adjacent slots is not affected by the presence of the dielectric, i.e., that $\psi_i = \psi_r$. The presence of the dielectric will, however, affect the propagation between the slots. We denote the propagation constant between the slots as K_w . It is evident that the surface wave null will occur when the electrical spacing between adjacent slots is 2π radians, so that for the Wood's anomaly condition we have

$$(4-28) \quad K_1 d_x \sin \epsilon_r + K_w d_x = 2\pi$$

or, again applying Eq. (4-24)

$$(4-29) \quad K_0 d_x (\sin \epsilon_i + K_w/K_0) = 2\pi$$

For $K_w=K_0$ we have the free space Wood's anomaly null condition. As the dielectric layer increases in thickness, K_w will increase towards its limiting factor of K_1 . This is illustrated by the curve shown in Fig. 4-17. The points were calculated using the modal analysis method. The panel geometry is the same as for Fig. 4-5, and again 242 Floquet modes and 4 slot modes ($f=1,3,5,7$; $g=0$) were used. The K_w/K_0 values were obtained by calculating the $\theta=60^\circ$ transmission curve for the various dielectric thicknesses, and determining the Wood's anomaly frequency for that thickness. Once this frequency is known the value of K_w/K_0 is easily determined from Eq. (4-29).

These same K_w/K_0 values, and thus the surface wave null frequency, can also be obtained by using only one Floquet mode. The method is based on the fact that, for the free space case, the Wood's anomaly null occurs when the Floquet modal impedance η_{pq}^r of the mode describing the incipient grating lobe is equal to zero. The grating lobe will become propagating when the modal impedance changes from an imaginary to a real number. For the η_{pq}^r modal impedance (free space) these two phenomena happen at almost the same frequency since η_{pq}^r passes through zero as it changes from an imaginary to a real quantity.

Now with a dielectric layer present, the modal impedance $Z_{pq}^{r(1)}$ of any Floquet mode evaluated at the panel surface is given by transmission line theory as

$$(3-45) \quad Z_{pq}^{r(1)} = \eta_{pq}^{r(1)} \cdot \frac{\eta_{pq}^r + j\eta_{pq}^{r(1)} \tan(\gamma_{pq}^{(1)} t_1)}{\eta_{pq}^{r(1)} + j\eta_{pq}^r \tan(\gamma_{pq}^{(1)} t_1)}$$

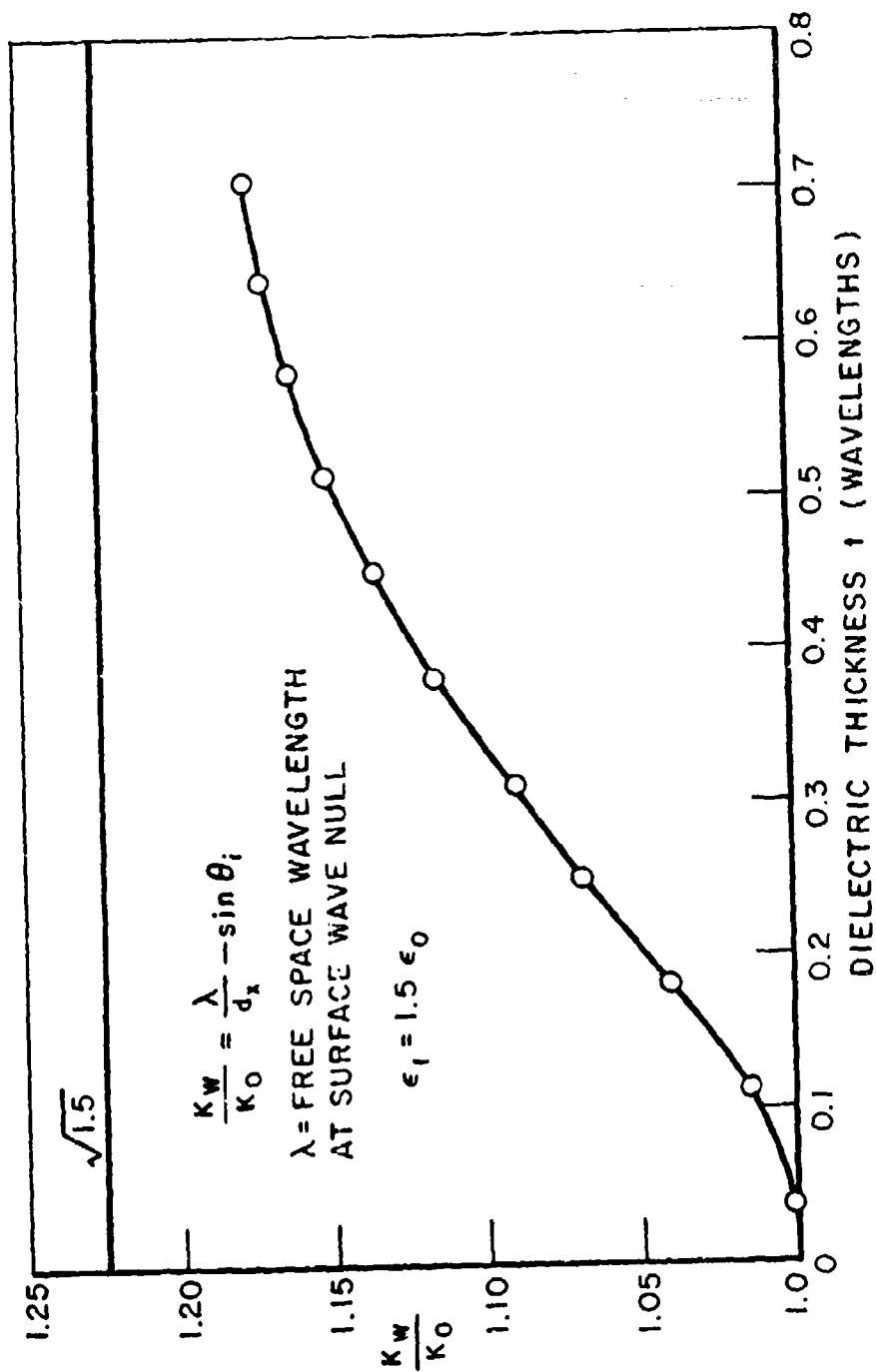


Figure 4-17.--The normalized surface wave null propagation constant vs. the dielectric thickness as calculated using 2 different methods; 1) full modal solution, 2) one Floquet mode. The dielectric thickness is measured in wavelengths (in the dielectric).

If we evaluate this $Z_{pq}^{r(1)}$ modal impedance for the Floquet mode describing the incipient grating lobe (for the case illustrated in Fig. 4-17 this is the $p=0, q=-1, r=2$ mode) we find that the frequency at which $Z_{pq}^{r(1)}$ is equal to zero corresponds to the frequency of the surface wave null as calculated using the modal solution. The curve of k_w/k_0 vs. dielectric thickness shown in Fig. 4-17 can be obtained by setting the left side of Eq. (3-45), i.e., $Z_{pq}^{r(1)}$, equal to zero and solving the resulting transcendental equation to obtain the surface wave null frequency. Thus a very simple calculation can determine the surface wave null frequency in the presence of a dielectric layer. If several dielectric layers of different thicknesses and permittivities were present the expression for $Z_{pq}^{r(1)}$ of Eq. (3-45) could be extended quite easily to include their effects.

Now a frequency where some particular $Z_{pq}^{r(1)}$ is equal to zero will not necessarily be a frequency where a surface wave null occurs. For example, the element pattern may be such that the Floquet mode with the zero value of $Z_{pq}^{r(1)}$ is not excited. Referring back to Eq. (4-19), consider the factors

$$\int_b \bar{e}_{bj} \times \bar{\phi}_{pq}^{r*} \cdot \hat{z} ds \cdot \frac{1}{Z_{pq}^{r(1)}} \cdot \int_b \bar{e}_{bn} \times \bar{\phi}_{pq}^r \cdot \hat{z} ds.$$

Now at a particular frequency where $Z_{pq}^{r(1)}$ is zero, this will be the dominating term in the system of equations unless one of the integrals is also equal to zero for all \bar{e}_{bj} modes. This would occur if the element pattern of the slot is such that the pqr Floquet mode is not excited, i.e., there is a null in the element pattern in the direction of propagation of that Floquet mode.

Since this $Z_{pq}^{r(1)}$ modal impedance is so important, let us briefly discuss its behavior as a function of frequency and dielectric thickness. We will here be speaking of the $r=2$ Floquet modes in particular, but the behavior we describe will apply to all of the $Z_{pq}^{r(1)}$ impedances with suitable changes in sign.

First, if there is no dielectric layer present $Z_{pq}^{r(1)} = \eta_{pq}^r$, the free space modal impedance. For frequencies well below the onset of the propagating free space grating lobe η_{pq}^r will be a large negative imaginary quantity. As the frequency is increased the value of η_{pq}^r (and thus $Z_{pq}^{r(1)}$ for no dielectric) moves monotonically upward along the imaginary axis toward zero. When it reaches zero the free space Wood's anomaly null occurs, and for higher frequencies η_{pq}^r moves slowly outward along the positive real axis and the pqr Floquet mode now describes a propagating grating lobe.

Let us now examine the behavior of $Z_{pq}^{r(1)}$ (Eq. (3-45)) with a thin dielectric layer present. For frequencies well below the frequencies where η_{pq}^r and $\eta_{pq}^{r(1)}$ become real $Z_{pq}^{r(1)}$ is negative imaginary. As the frequency is increased $Z_{pq}^{r(1)}$ moves slowly up along the imaginary axis toward zero, but without reaching zero, until the frequency where $\eta_{pq}^{r(1)}$ (the Floquet mode impedance in the dielectric layer) becomes real is reached. $Z_{pq}^{r(1)}$ then moves more rapidly up along the imaginary axis, passes through zero, and keeps increasing along the positive imaginary axis until η_{pq}^r changes to a real quantity, at which point $Z_{pq}^{r(1)}$ becomes complex with a positive real part and the grating lobe now propagates in real space. As the frequency is further increased the real part of Z_{pq}^r increases while the imaginary part slowly decreases to an insignificant value.

Now for a thick dielectric layer the behavior of $Z_{pq}^{r(1)}$ in the range of frequencies where $\eta_{pq}^{r(1)}$ is real while η_{pq}^r is still imaginary deserves further discussion. $Z_{pq}^{r(1)}$ moves more rapidly up the imaginary axis, and continues upward until η_{pq}^r becomes real. However, if the dielectric layer is thick enough $Z_{pq}^{r(1)}$ may, as the frequency is increased, move upward along the imaginary axis, pass through zero, continue to move upward along the imaginary axis high enough to cause a forced dielectric resonance (i.e., a max in the transmission coefficient), continue upward through $+j\infty$, start upward again from $-j\infty$, pass through zero again causing another surface wave null etc.,

until n_{pq}^r finally becomes real. Thus between two closely spaced frequencies, i.e., between where $n_{pq}^{r(1)}$ and n_{pq}^r become real, respectively, the transmission coefficient may rapidly change from null to peak to null again due to the rapid changes in the $z_{pq}^{r(1)}$ modal impedance for that particular Floquet mode.

The nature of the fields which exist on the panel surface at the surface wave null frequency will now be investigated. Previous investigations of nulls which occurred in the transmission coefficient for waveguide simulations of resonant slot arrays had been shown to be surface waves by Munk and Luebbers [4]. Also, research into phased array blind angles have led to the conclusion that there are driven surface wave fields at the frequency where the blind angle occurs. Munk has suggested [48] that at the surface wave null frequency (where $z_{pq}^{r(1)}$ of Eq. (3-45) is zero) Eq. (3-45) is equivalent to the characteristic equation for a surface guided wave [49]. We shall now show that this is indeed the case, and thus justify our nomenclature of "surface wave" null.

Let us reconsider the specific case just investigated, the $p=0$, $q=-1$, $r=2$ Floquet mode with E-plane incidence ($\phi=90^\circ$). Referring to Eqs. (3-7), (3-11), (3-13), and (3-15) we see that this mode is TM to the y axis, and that at the onset of the grating lobe the propagation is in the y direction. We now suggest that at the surface wave null frequency this free space mode together with its counterpart inside the dielectric describe a TM_y surface guided wave propagating in the y direction.

Referring to Harrington [49] we find that if we adjust his coordinate system and dimensions so that they agree with our own, his characteristic equation for the K_y propagation constant for the odd TM surface guided wave mode traveling in the y direction [Eq. (4-56) of Harrington] can be written as

$$(4-30) \quad t_1 \sqrt{k_1^2 - (k_y)^2} \tan(\sqrt{k_1^2 - (k_y)^2} t_1) = \frac{\epsilon_1}{\epsilon_0} t_1 \sqrt{(k_y)^2 - k_0^2}.$$

Now we note that this surface wave cannot exist on our structure unless it satisfies the Floquet conditions. However, this can be quite simply enforced for this case ($p=0$, $q=-1$, $\phi=90^\circ$) by letting $k_y = V_{pq}$, where V_{pq} has been defined in Eq. (3-8). Eq. (4-30) now becomes

$$(4-31) \quad \sqrt{k_1^2 - V_{pq}^2} \tan(\sqrt{k_1^2 - V_{pq}^2} t_1) = \frac{\epsilon_1}{\epsilon_0} \sqrt{V_{pq}^2 - k_0^2}$$

where the common factor t_1 has been eliminated. Referring to Eq. (3-11), we recognize that Eq. (4-31) can be written as

$$(4-32) \quad \gamma_{pq}^{(1)} \tan(\gamma_{pq}^{(1)} t_1) = \frac{\epsilon_1}{\epsilon_0} j \gamma_{pq}.$$

If we now substitute for γ_{pq} and $\gamma_{pq}^{(1)}$ using Eq. (3-17), we readily obtain

$$(4-33) \quad \eta_{pq}^{r(1)} k_1 \sqrt{\frac{\epsilon_1}{\mu_1}} \tan(\gamma_{pq}^{(1)} t_1) = \frac{\epsilon_1}{\epsilon_0} \eta_{pq}^r k_0 \sqrt{\frac{\epsilon_0}{\mu_0}}$$

which, with slight simplification, can be written as

$$(4-34) \quad \eta_{pq}^r + j \eta_{pq}^{r(1)} \tan(\gamma_{pq}^{(1)} t) = 0.$$

Comparing Eq. (4-34) with Eq. (3-45) we see that if the characteristic equation for the surface wave is satisfied then $Z_{pq}^{r(1)}$ for the Floquet mode corresponding to that surface wave will be zero. Thus a propagating surface wave which satisfies the Floquet condition coincides in frequency with a null in the transmission coefficient, justifying our term "surface wave null". In addition, the curve of Fig. 4-17 can be obtained by imposing the Floquet conditions on the characteristic equation for a surface wave and then solving for the frequency which satisfies the equation.

E. The Brick Array and Wood's Anomaly

As mentioned previously, the behavior and field structure of resonant slot arrays and phased array antennas are quite similar in many respects. Thus the discoveries made in one area may be applicable to the other. Some unusual properties of the "brick array" phased array antenna are here shown to carry over to the corresponding resonant slot array. While this type of slot array does not have the narrow band properties desirable from many applications, a knowledge of the phenomenon that it illustrates would be important to the design of wide bandwidth resonant slot arrays.

The term brick array denotes an interlaced array of large rectangular slots spaced closely together. The appearance of such an array brings to mind a brick wall, as is evident from the insert in Fig. 4-18. Farrel and Kuhn [50] reported some interesting results for a phased array antenna of this type. Their antenna was not covered with a dielectric layer, so that the grating lobe diagram of Chapter III should have quite accurately predicted the Wood's anomaly null frequency (i.e., the blind angle) for the array. Yet they presented both calculated and measured data which clearly showed the blind angle occurring at a scan angle well inside that predicted by the grating lobe diagram. This would correspond in a resonant slot array to a reduction in the frequency of the Wood's anomaly null. In the previous sections of this chapter we have shown that such a reduction could be caused by the presence of a dielectric layer. However, a reduction of the Wood's anomaly (i.e., transmission null) frequency for a periodic slot array due to the slot shape or lattice arrangement had not to our knowledge been reported.

In order to investigate this phenomenon several sets of plane wave transmission curves were calculated for a slot array corresponding to the phased array geometry of Farrel and Kuhn. In order to eliminate possible thickness effects the modal solution for an infinitesimally thin panel, which is given in the following chapter, was used to calculate the curves in this section. All of the curves were calculated using 50 Floquet modes (p and q range from -2 to +2, $r=1,2$). The curves shown in Fig. 4-18 were calculated using only 1 slot mode ($f=1, g=0$). The curves are for various incidence angles in the H-plane, and show the usual reduction with incidence angle for the resonance frequency and the frequency of the Wood's anomaly transmission null. The grating lobe diagram yields the following frequencies at which grating lobes become propagating: $\theta=1^\circ$, 13.86 and 14.21 GHz; $\theta=30^\circ$, 10.88 GHz; $\theta=60^\circ$, 10.01 GHz. It is evident from the curves of Fig. 4-18 that the Wood's anomaly transmission nulls occur at the frequencies of grating lobe onsets for the various incidence angles. This is what is expected for a periodic array with no dielectric present.

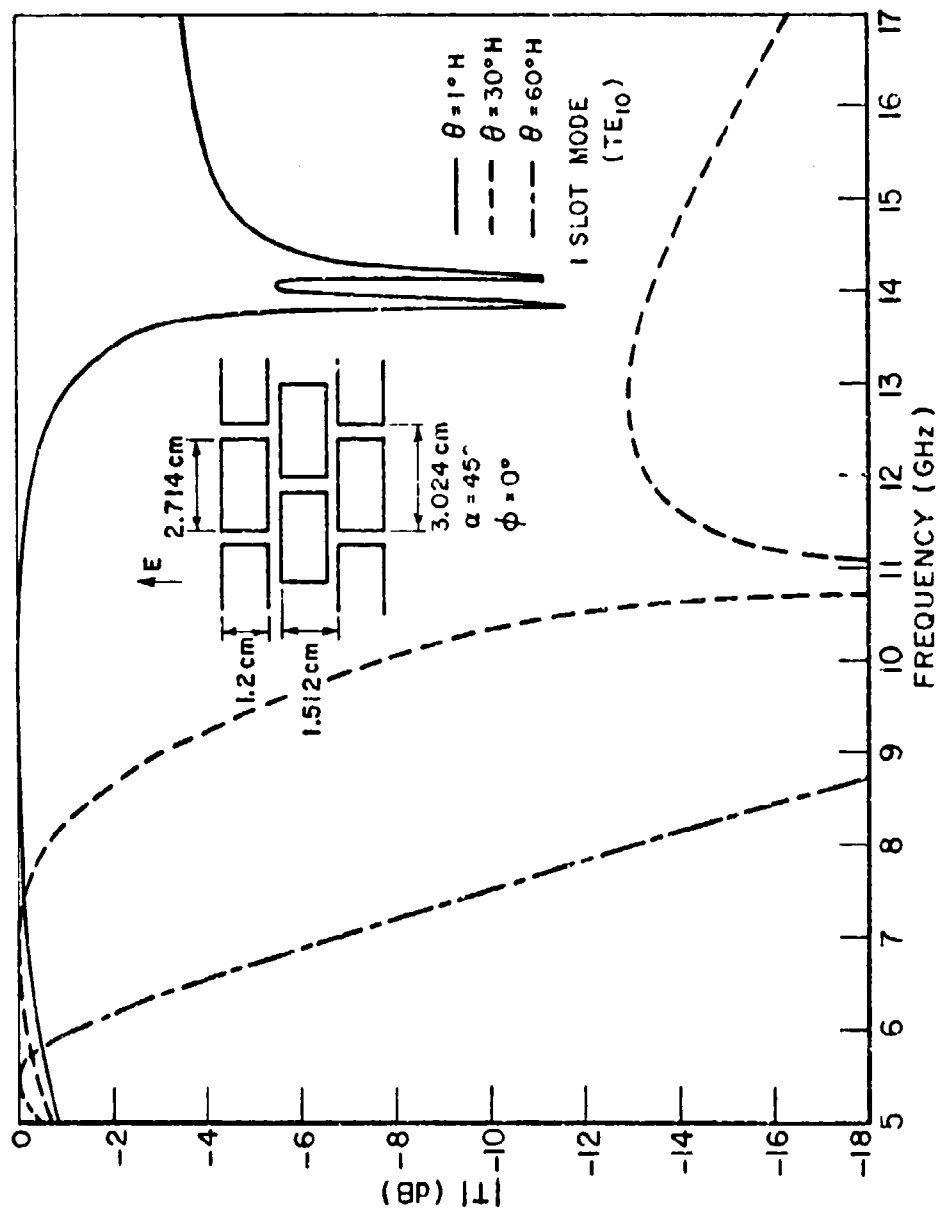


Figure 4-18.--Calculated transmission curves for the slot array shown using only the TE_{10} slot mode.

Now let us observe the curves of Fig. 4-19. These transmission curves were calculated under the same conditions as those in Fig. 4-18 except that 3 modes ($f=1,2,3$; $g=0$) instead of one were used to describe the fields in the slots. Note that for all three incidence angles the transmission null has been moved downward in frequency. This shift is similar to that observed for the dielectric coated slot arrays in the previous sections of this chapter. There is no dielectric present in this case, so that this shift is due to some other phenomenon, which requires higher order modes in the slot.

Stark, in a paper [51] which is partly concerned with explaining the previously noted results of Farrel and Kuhn, concludes that two slot modes are required to calculate the correct blind angle value for the "brick array". This agrees with our results and strongly suggests that the phased array and the resonant slot array nulls are due to the same phenomenon. Stark investigated several geometries and found that the shift of the null was strongly dependent on the lattice spacing. He also found that the shift was not observed for arrays of slots arranged in a rectangular grid rather than an interlaced grid and scanned in the H-plane. We performed calculations for an array identical to that of Figs. 4-18 and 4-19 except that the slot width b was reduced from 1.2 cm to 0.3 cm. No change in the null frequency was observed.

The physical explanation of why the transmission null shifts downward in frequency may be as follows [48]: It is known that if the slots in an array are such that two different slot modes are present which resonate at separate but closely spaced frequencies the result will be a null in the array transmission coefficient. This null will be at a frequency between the two frequencies where the individual modes resonate [16]. Examining the calculated data for the 60° H-plane curves of Fig. 4-19 we find that indeed two slot modes are strongly excited, the $f=1$ $g=0$ mode (TE_{10}) at approximately 5 GHz, and the $f=2$ $g=0$ mode (TE_{20}) at approximately 10 GHz. Thus the 7 GHz null in the 60° H-plane curve of Fig. 4-19 can be explained as due to the destructive interference of the two resonant slot modes, while the absence of the Wood's anomaly null at 10 GHz is then due to a zero in the 2-mode element pattern in a direction such as to prevent the sudden excitation of the grating lobe. The grating lobe does begin to propagate at this frequency, however, causing the slope discontinuity evident at 10 GHz.

Before leaving this topic there is another interesting phenomenon evident in the transmission curves of Fig. 4-19 which deserves explanation. This is the presence of the abrupt changes in slope which occur at approximately 13.2 GHz for $\theta=30^\circ$, and at 10.6 GHz for $\theta=60^\circ$. These discontinuities are due to the onset of a different grating lobe than is responsible for the Wood's anomaly nulls. The grating lobe responsible for these discontinuities begins to propagate in the $\theta=90^\circ$, $\phi=0^\circ$ direction. Thus the element pattern prevents the onset

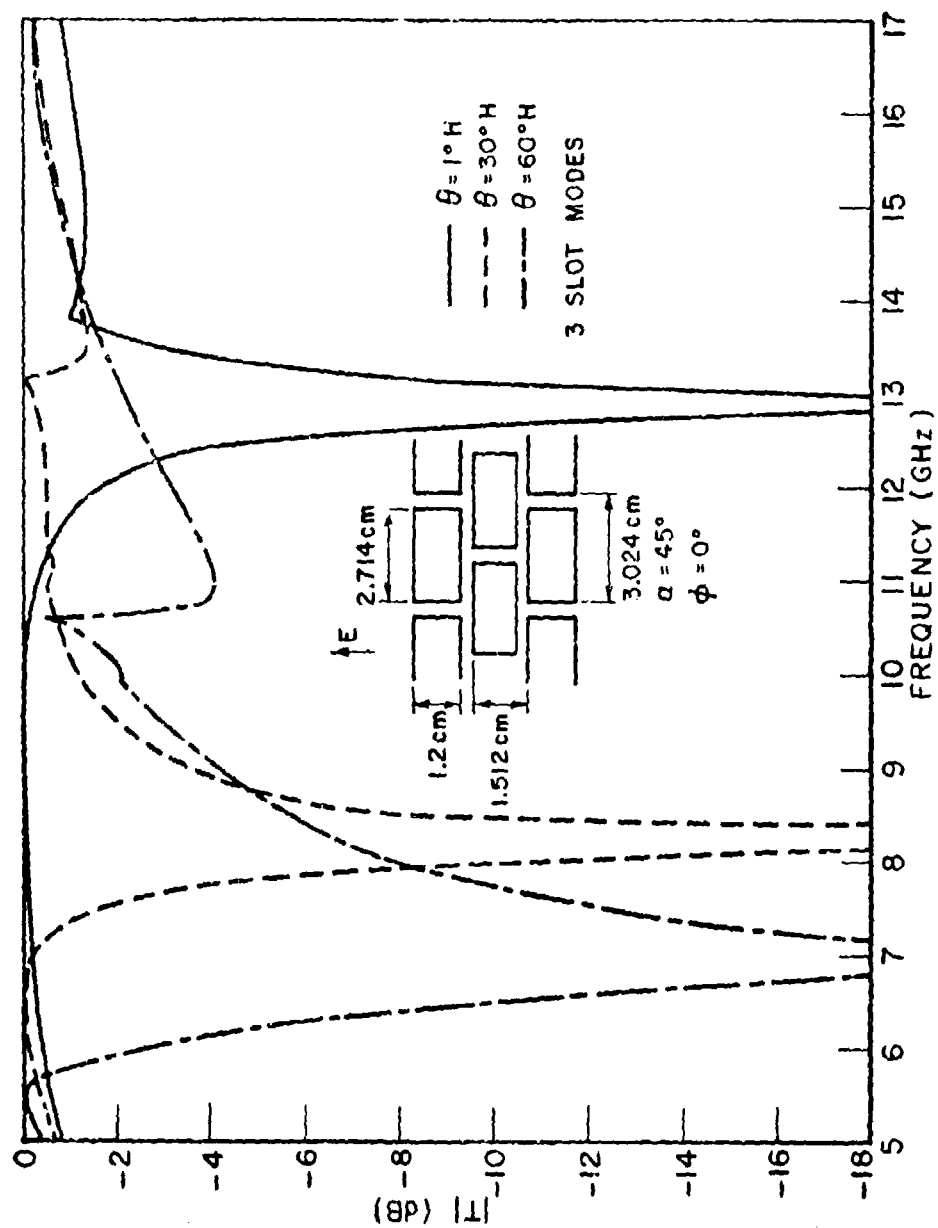


Figure 4-19.--Calculated transmission curves for the slot array of Fig. 4-18 but with 3 slot modes (TE_{10} , TE_{20} , TE_{30}).

of this grating lobe from causing a Wood's anomaly null. Its sudden emergence into real space does, however, cause these discontinuities in the transmission coefficient which are evident in Fig. 4-19.

The discontinuity in the $\theta=1^\circ$ curve at 13.9 GHz is caused by the same process but the grating lobe in this case is not one which propagates in the $\theta=90^\circ$, $\phi=0^\circ$ direction. In this case the grating lobe in question is associated with one of the nulls evident in the $\theta=1^\circ$ curve of Fig. 4-18.

F. Thick Slots Filled With Dielectric

Most of the work done on resonant slot arrays has been performed on thin arrays where the panel thickness t is approximately 0.01 inches or less. This is due to several reasons. One reason is that, as discussed in Chapter II, Babinet's principle does not give good results for arrays much thicker than .001 λ . (You will recall that in order to use the mutual impedance method to calculate transmission through a slot array one must apply Babinet's Principle.) Another reason is that thick arrays of slots are difficult to make, and this difficulty is increased when loaded slots rather than rectangular slots are used. Thick slot arrays are desirable, however, for applications where mechanical strength is required. Thus it seemed desirable, in order to simplify the construction problems as much as possible, to design a thick array of rectangular slots which would have both mechanical strength and good electrical properties.

As mentioned several times previously, the usual shortcoming of arrays of rectangular slots is that their resonance frequency shifts with incidence angle. This shortcoming can be eliminated by using slots loaded with the Babinet complement of a short circuited transmission line. As an alternative to this, it was felt that perhaps the same good qualities of the transmission line loaded slot could be obtained from a thick rectangular slot if it were filled with a high permittivity dielectric. This should load the slot much as a transmission line does, in that the resonance frequency of the slot would be reduced and its bandwidth would narrow.

After investigating many different geometries and dielectric constants using the modal solution computer program, the geometry shown in the insert of Fig. 4-20 was found to have a stable resonance frequency with incidence angle, as shown by the transmission curves. Note that the incidence angles range to 80° in both the E- and H-planes, which represents a very severe stability test. In a previous section of this chapter another technique for stabilizing the resonant frequency of an array of rectangular slots was shown. This method required the array to be covered on both sides with a layer of dielectric, which eliminates it from applications which require the metallic panel surface to be exposed. The present technique does not require these external dielectric layers in order to achieve frequency stability with incidence angle.

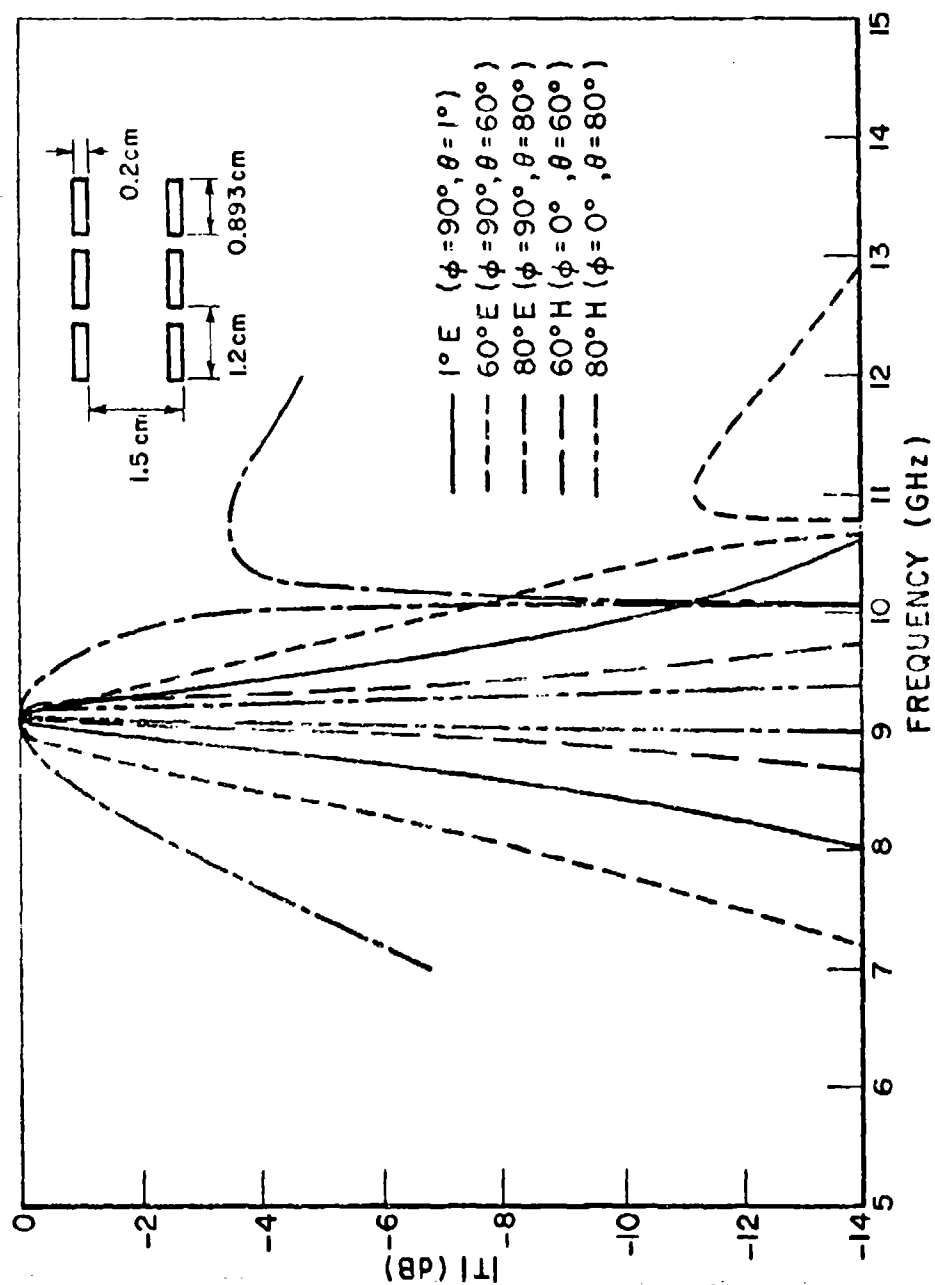


Figure 4-20.--Calculated transmission curves for an array of rectangular slots in a 0.1" thick metal panel ($l=0.254$ cm). The slots are filled with dielectric of $\epsilon_r=5.0$ ($\epsilon_3=5\epsilon_0$).

Several attempts were made to fabricate a panel with the dimensions of Fig. 4-20 by means of chemical etching. The slots were then filled with Emerson and Cumming Stycast 35DA, a casting resin with $\epsilon_r=5.0$. These panels showed good angle of incidence stability but considerable loss at resonance. A typical set of measured transmission curves for such a panel is shown in Fig. 4-21. Examination of these thick, chemically milled panels showed considerably nonuniformity in the size and shape of slots. Another panel was made using the electrical discharge machining process. This panel appeared to be much more uniform than the ones made using chemical milling. The slots in this panel were also filled with the Emerson and Cumming Stycast 35DA, and the resulting measured transmission curves are shown in Fig. 4-22. Note that the transmission loss at resonance has been drastically reduced, but that the resonance frequencies still shift slightly with incidence angle in the E-plane. This shift is related to the fact that the measured panel resonates at 10.2 GHz whereas the calculations show the resonance at 9.2 GHz. Since the E-plane Wood's anomaly occurs at 10.7 GHz and 10.1 GHz for 60° E- and 80° E-plane incidence, respectively, it is evident that the E-plane shift is caused by the nearness of Wood's anomaly to the resonant frequency. Thus if the measured panel had resonated at the design frequency of 9.1 GHz the resonance frequencies would have been stable with incidence angle for E-plane as well as H-plane incidence.

The most likely explanation for measured resonance being at 10.2 GHz rather than at 9.2 GHz is that the relative dielectric constant of the casting resin was less than 5.0. This would not be too surprising, since 10 GHz is the upper limit of the applicability of this material.

Thus, the measured curves obtained, although not in perfect agreement with the calculations, indicate that the concept of obtaining a stable resonance frequency by filling thick rectangular slots with a dielectric material is sound. The resonance frequencies were perfectly aligned for H-plane scan angles, and the shift for the E-plane scan angles was due to the nearness of the Wood's anomaly null to the resonance frequency.

If the metallic surface was not required to be exposed, this design could be further improved by coating the array on both sides with a dielectric layer to reduce the change of bandwidth with incidence angle, as discussed in Section C of this chapter. An example of this is shown in Fig. 4-23, where the thick array of Figs. 4-20 to 4-22 has been coated on both sides with a dielectric of $\epsilon_r=1.5$, .635 cm thick. The change of bandwidth with incidence angle is considerably less than for the uncoated array of Fig. 4-20.

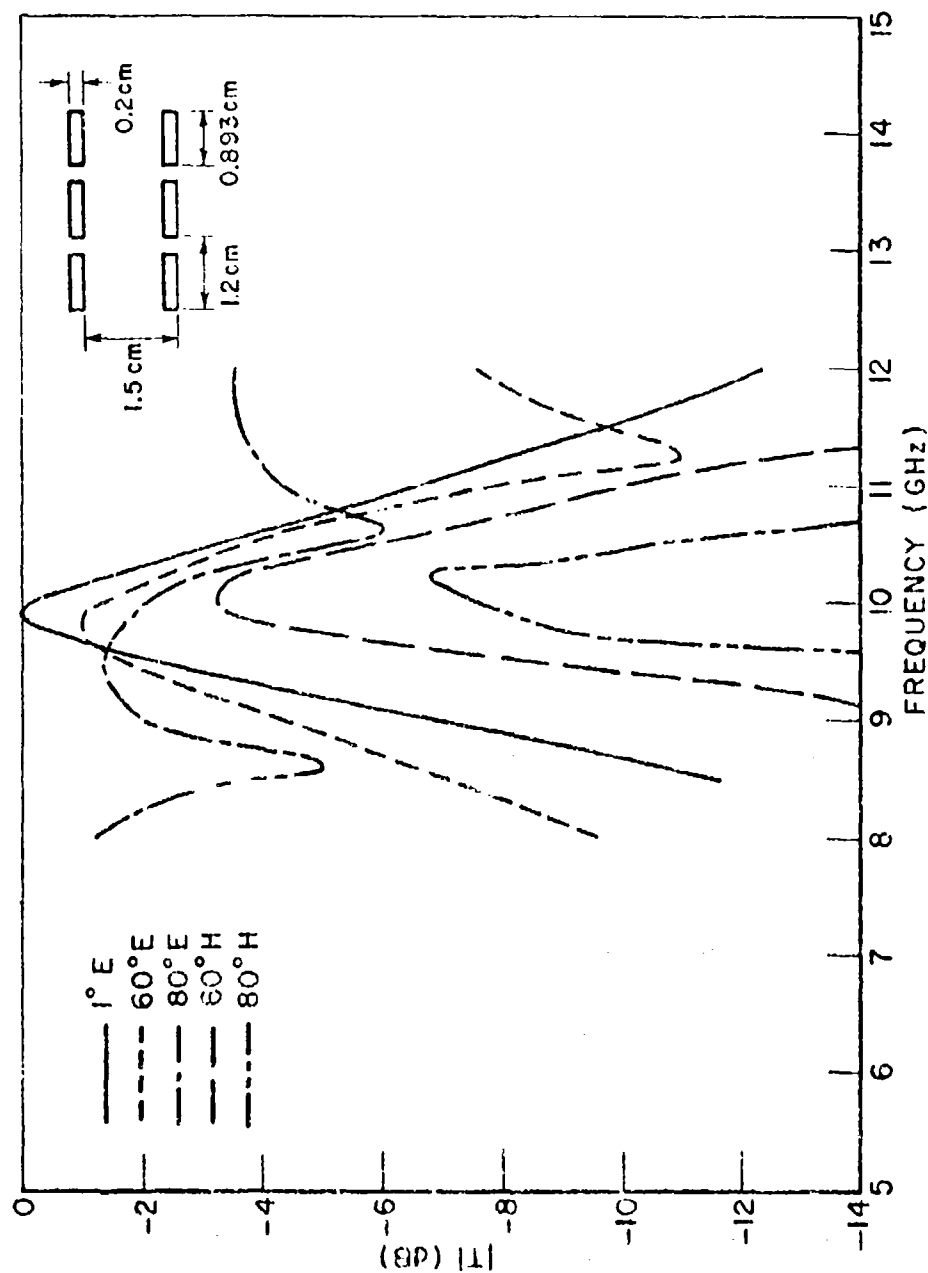


Figure 4-21.--Measured transmission curves for a slot array chemically etched to approximate the design of Fig. 4-20. The slots were etched in a 0.1" thick aluminum panel and filled with Emerson and Cumming Stycast 35DA ($\epsilon_r=5$).

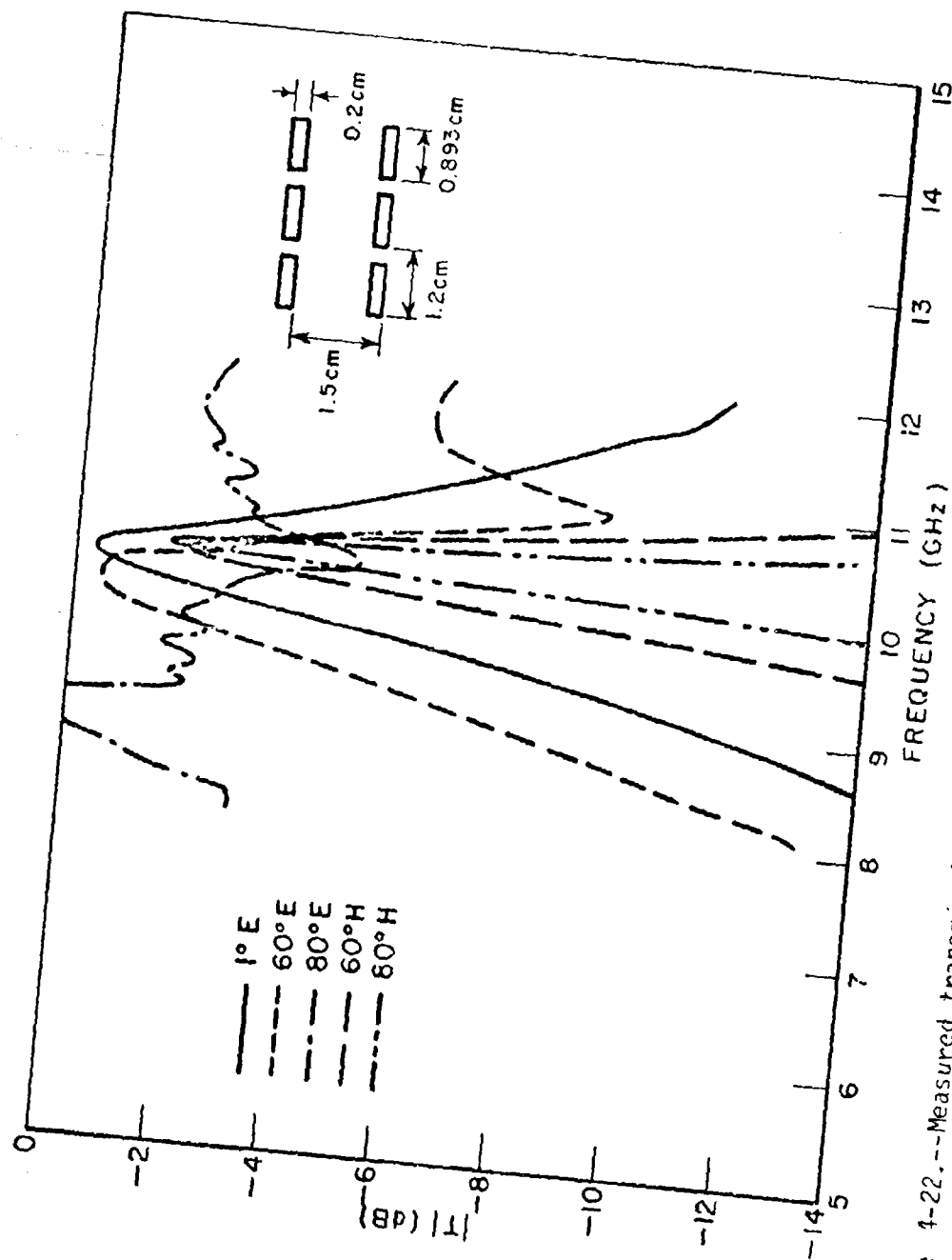


Figure 4-22.--Measured transmission curves for a slot array of the design used in Figs. 4-20 and 4-21 made using electrical discharge machining on a 0.1" thick aluminum panel. The slots are again filled with Emerson and Cuming Stycast 350A ($\epsilon_r=5$)

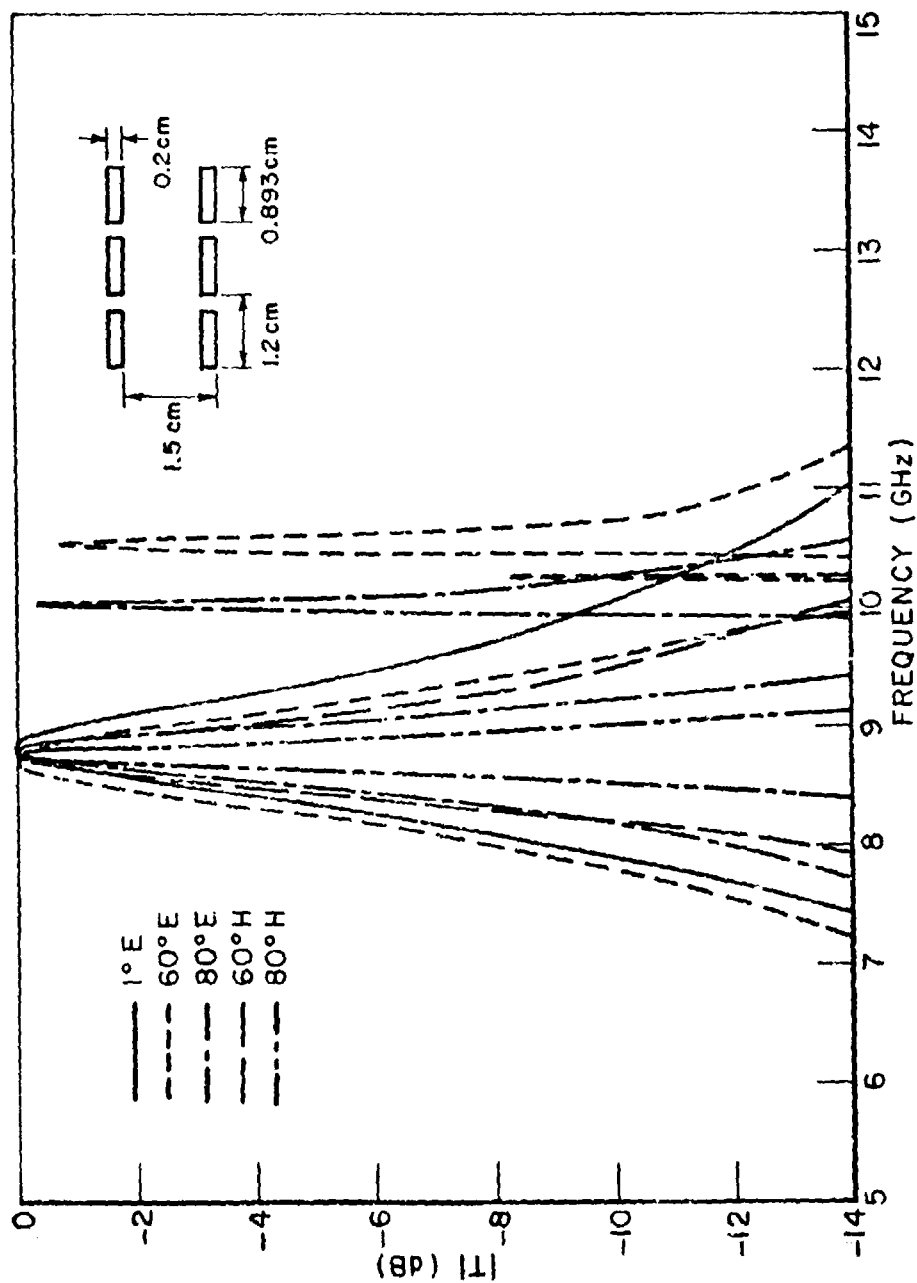


Figure 4-23.--Calculated transmission curves for the array of Figs. 4-20 and 4-21 coated on both sides with a 0.635 cm thick dielectric layer with $\epsilon_r=1.5$ ($t=0.635$ cm, $\epsilon_1=1.5\epsilon_0$). The metal panel is 0.1" thick ($\lambda=0.254$ cm) and the slots are filled with dielectric of $\epsilon_r=5$ ($\epsilon_3=5\epsilon_0$).

G. Thickness - Dielectric Interactions

In the previous section measured and calculated results for a particular thick panel design were presented. In this section we shall present calculated transmission curves which illustrate the effects of panel thickness on various panel and dielectric geometries. We are concerned primarily with the bandwidth and resonance frequency of the transmission curve, so that only the normal incidence results will be shown.

The basic geometry of the panels considered will be the same as for the panel of Fig. 4-5. However, the thickness λ of the panel will now be varied from .015 cm to .254 cm. For these various thicknesses three different dielectric configurations will be studied for their effects: 1) no dielectric, 2) dielectric in slot only, and 3) dielectric in slot and in a .159 cm (1/16") layer on each side of the panel. The dielectric is lossless with $\epsilon_r=4.0$. In all of the following calculated curves 242 Floquet modes ($p_{\max}=q_{\max}=5$) and four rectangular slot modes (the modes $f=1,3,5,7$; $g=0$) were used. While only rectangular slots are considered, resonant windows with other slot shapes should behave similarly.

In Fig. 4-24 we show calculated transmission coefficient curves for a resonant window with no dielectric present and with the thickness λ varying from .015 cm to .254 cm. Despite the wide range of thickness, the resonance frequency has increased by less than 4%. This agrees with the observation made in Chapter II that the resonance frequency of a waveguide window is relatively unaffected by changes in thickness. The more prominent effect of the changing thickness is the change in the transmission curve bandwidth. Increasing the thickness λ will in general decrease the bandwidth of the resonant surface. This also agrees with the observations made in Chapter II concerning waveguide windows.

Let us now consider Fig. 4-25. For these calculations the slot is filled with a lossless dielectric of relative permeability 4.0. For this configuration the resonance frequency as well as the bandwidth changes with thickness, as shown by the various transmission curves in the figure. This decrease in resonance frequency with thickness can be explained by considering the case of an infinitesimally thin panel. For the infinitesimally thin panel the resonance frequency will not be effected at all by filling the slots with dielectric. One way of seeing this is to realize that this dielectric layer will itself be infinitesimally thin and thus can not affect the electric fields of the panel. Mathematically, this statement can be justified by noting that the integral equation expressions for the fields of the thin panel formulated in the following chapter do not depend on the parameters of the material filling the slot (except, of course, for the special case where this material is a perfect conductor). As the panel is made thicker the material in the slot

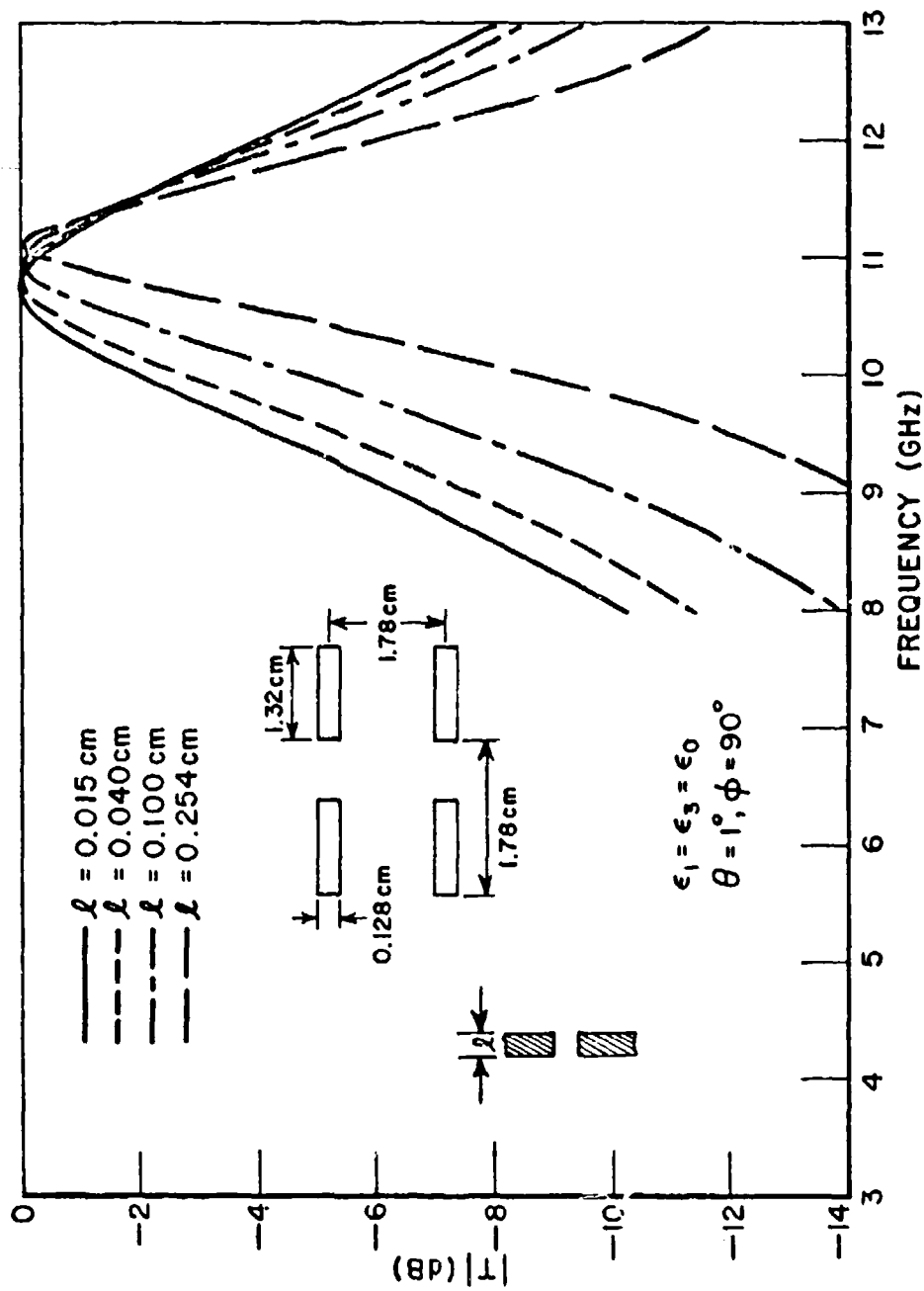


Figure 4-24.--Calculated transmission curves for an array of rectangular slots in metallic panels of various thicknesses with no dielectric present.

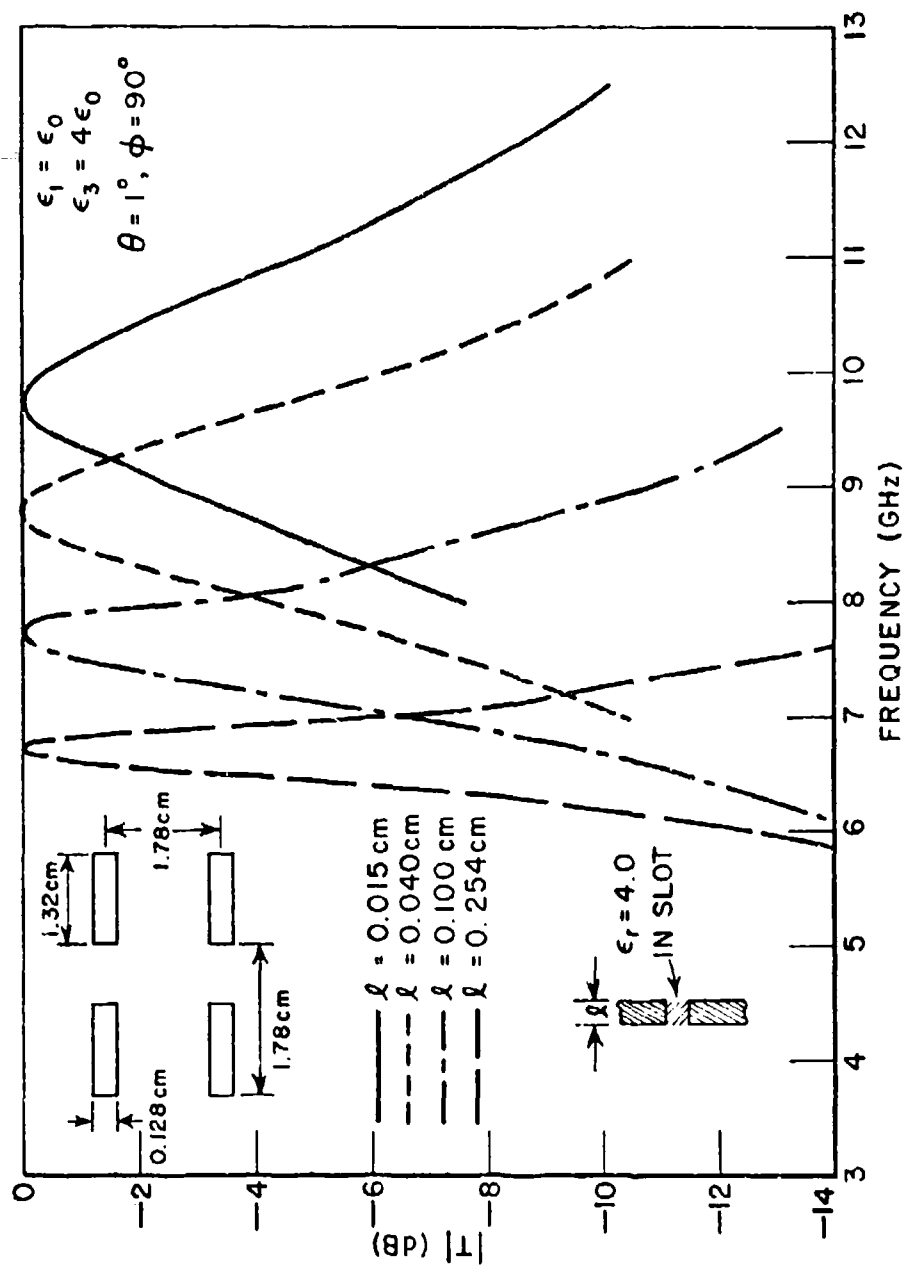


Figure 4-25.--Calculated transmission curves for the same slot arrays of Fig. 4-25 but with the slots filled with dielectric ($\epsilon_3=4\epsilon_0$).

becomes finitely thick, and thus can affect the fields of the thicker panels. Further, the interior of the slots is a region of relatively high field strengths, and thus the dielectric material of the slot will have a considerable effect on the resonant frequency even for quite thin panels. Comparing Figs. 4-24 and 4-25 we see that even for the thinnest panel considered the resonance frequency is reduced by about 10% when the slot is filled with dielectric of $\epsilon_r=4$. As the panel is made thicker a greater portion of the panel fields are within the slot, and thus the resonance frequency will continue to decrease. A lower bound for this decrease is the original resonance frequency divided by the square root of the relative dielectric constant of the material filling the slot. This lower bound can never be reached, however, since this would require that all the space around the panel have $\epsilon_r=4$. This lower bound can, however, be approached quite closely by a thick panel. The thickest panel considered in Fig. 4-25 is only 0.1" thick and yet is only 1 GHz away from the lower bound, which for the panel and dielectric considered here is about 5.6 GHz.

The decrease in bandwidth with increasing thickness is greater than that for the previous, non-dielectric case due to the loading effects of the dielectric. The relatively greater decrease in bandwidth is partially compensated by the decrease in the electrical spacing between the slots, which is a consequence of the decrease in the resonance frequency. (You will recall from Chapter I that decreasing the slot spacing increases the transmission bandwidth.)

Finally, the transmission curves of Fig. 4-26 are for slotted panels coated on both sides with a 1/16" thick dielectric layer, with the slots being filled with the same dielectric material. As shown in Reference [4] and in Fig. 4-9 a thin layer of dielectric will lower the resonance frequency to nearly the lower bound of $1/\sqrt{\epsilon_r}$ times the free space resonance. Thus we see from the results of Fig. 4-26 that for this configuration the increasing thickness does not affect the resonance frequency, since this has already been lowered by the dielectric layer. The bandwidth, however, continues to decrease with increasing thickness.

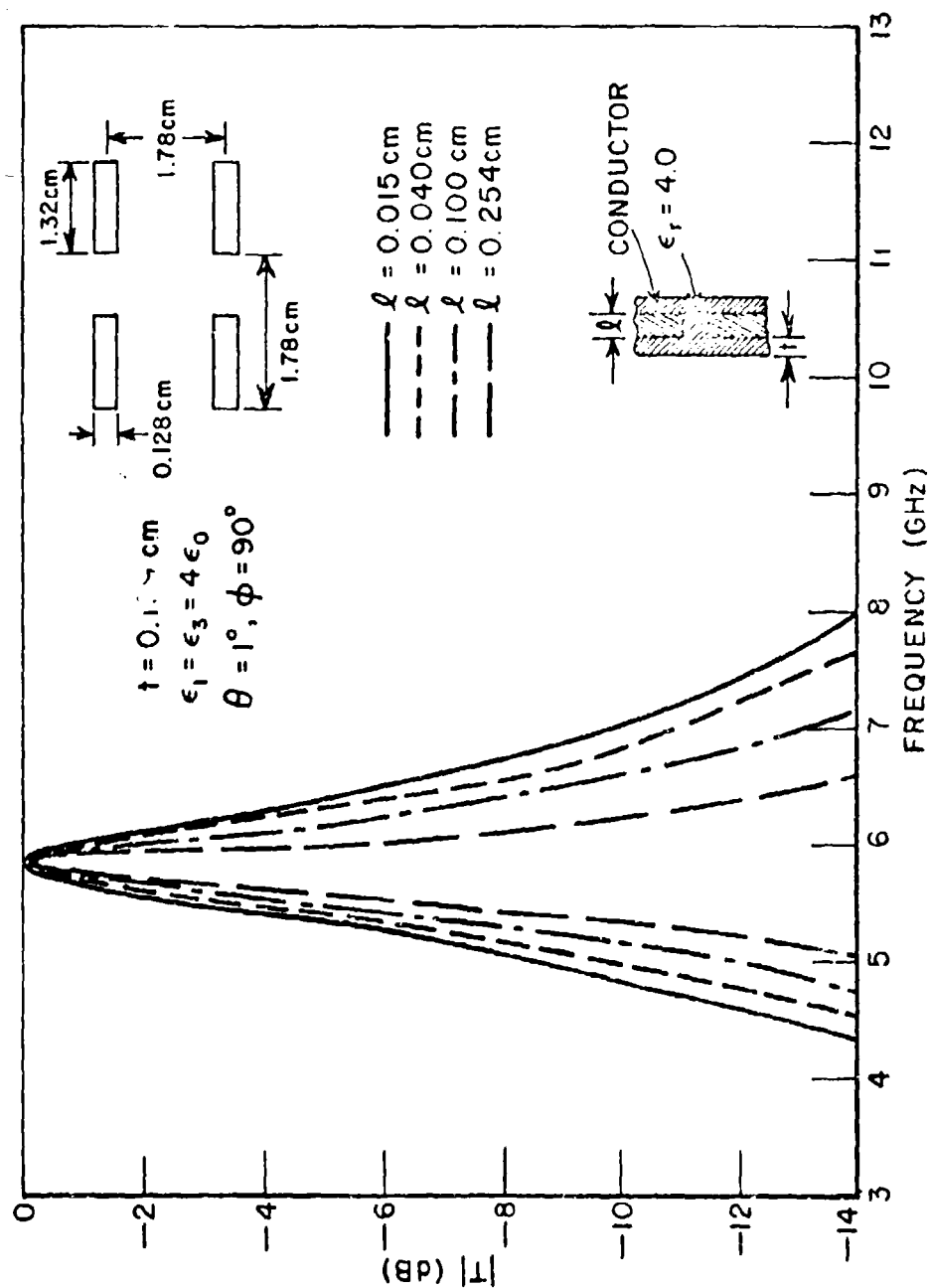


Figure 4-26.--Calculated transmission curves for the slot arrays of Figs. 4-24 and 4-25 but with a .159 cm thick dielectric layer on both sides of the array in addition to the dielectric material in the slots.

CHAPTER V THIN LOADED SLOT ARRAYS

In this chapter a moment method solution for the reflection and transmission coefficients for an infinite, periodic slot array will be derived. The result is similar to that obtained by Chen, who applied it to arrays of rectangular [26] and circular slots [30]. The solution will be extended here to arrays of loaded slots, using the approximate mode sets presented in a previous chapter to describe the electric fields in the loaded slots.

One might question the need for a thin panel solution, thinking that the same results could be obtained by using the thick panel solution presented previously and making the panel very thin. However, the thin panel solution has two advantages over the thick panel solution. The first is that only one system of equations needs to be solved for the thin panel solution, whereas with the thick panel solution two systems (symmetric and antisymmetric) must be solved to obtain a transmission coefficient. The other advantage is that the dielectric layers on either side of the panel need not be identical, as was the case for the thick panel solution given in Chapter IV.

A. Derivation of Moment Method Solution

The geometry for the periodic slot array is again shown in Fig. 5-1. The array may be covered on one or both sides by a dielectric sheet of arbitrary thickness, permittivity, and permeability. The direction of the incident plane wave is determined by θ and ϕ (see Fig. 3-1), and the complex amplitudes of the reflected and transmitted plane waves are desired.

Using the Floquet modes of Eqs. (3-12) to (3-15) the incident fields in the free space region (i.e., external to the dielectric) can be expressed as:

$$(5-1) \quad \vec{E}^i = \sum_{r=1}^2 A^r \vec{e}_{a1}^r$$

$$(5-2) \quad \vec{H}^i = \sum_{r=1}^2 A^r \vec{h}_{a1}^r$$

where the A^r are known coefficients which determine the magnitude and polarization of the incident plane wave. If we now define the quantities

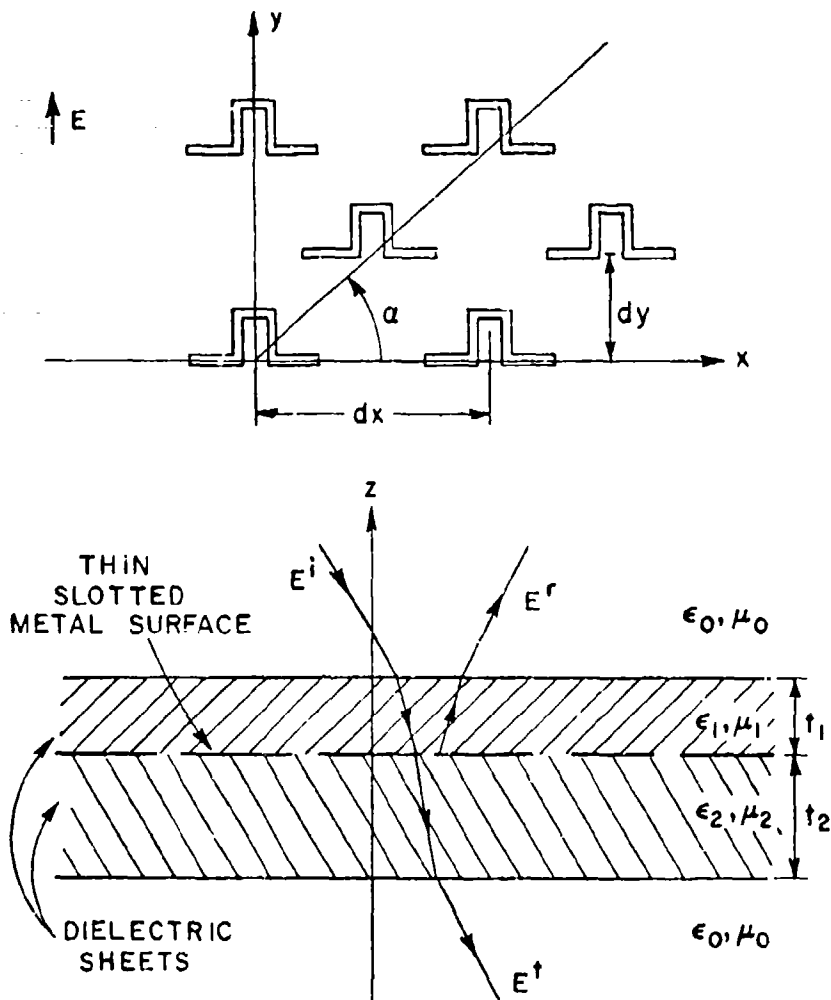


Figure 5-1.--Front and edge views of a periodic array of loaded slots covered by dielectric layers.

$$(5-3) \quad a_1^{rd} = 2 A^r \frac{\eta_{00}^{r(1)}}{\eta_{00}^{r(1)} + \eta_{00}^r} \exp[-j(\gamma_{00}^{r(1)} - \gamma_{00})t_1]$$

$$(5-4) \quad DF^r = \frac{\eta_{00}^{r(1)} - \eta_{00}^r}{\eta_{00}^{r(1)} + \eta_{00}^r} \exp(-2j\gamma_{00}^{r(1)}t_1)$$

we can, by use of Eqs. (3-32) through (3-35), and (3-43), express the tangential fields at the front surface of the panel as:

$$(5-5) \quad \vec{E}|_{z=0^+} = \sum_{r=1}^2 [a_1^{rd} + \rho^r(1-DF^r)] \vec{e}_{a1}^{r(1)} + \sum_{r=1}^2 \sum_{i=2}^{\infty} a_i^r \vec{e}_{ai}^{r(1)}$$

$$(5-6) \quad \vec{H}|_{z=0^+} = \sum_{r=1}^2 [a_1^{rd} - \rho^r(1+DF^r)] \vec{h}_{a1}^{r(1)} - \sum_{r=1}^2 \sum_{i=2}^{\infty} a_i^r \vec{h}_{ai}^{r(1)}$$

where the ρ^r and a_i^r are unknown modal coefficients. The Floquet mode functions $\vec{e}_{a1}^{r(1)}$ and $\vec{h}_{a1}^{r(1)}$ are given in Eqs. (3-49) and (3-50), and were obtained by modifying the free space Floquet mode functions so as to include some of the effects of the dielectric layer. Note that the above equations are identical to those given in Chapter IV, since the geometries are identical for the space external to the panel itself.

The tangential fields at the back surface of the panel can be expressed as:

$$(5-7) \quad \vec{E}|_{z=0^-} = \sum_{\ell=1}^2 \sum_{m=1}^{\infty} b_m^{\ell} \vec{e}_{ai}^{\ell(2)}$$

$$(5-8) \quad \vec{H}|_{z=0^-} = \sum_{\ell=1}^2 \sum_{m=1}^{\infty} b_m^{\ell} \vec{h}_{ai}^{\ell(2)}$$

where the b_m^{ℓ} are unknown modal coefficients, and the Floquet mode functions are given in Eqs. (3-51) and (3-52).

In order to determine the unknown quantities we will enforce the tangential field boundary conditions over the central periodic cell (Fig. 3-2). Due to the periodic nature of the Floquet modes, this will actually enforce the boundary conditions over the entire surface of the array. The required boundary conditions are that the tangential E and H fields must be continuous across the aperture, and that the tangential E field must vanish at the conducting surface.

Enforcing the electric field boundary condition, we equate Eqs. (5-5) and (5-7), obtaining

$$\begin{aligned}
 (5-9) \quad \sum_{r=1}^2 [a_1^{rd} + \rho^r (1-DF^r)] \bar{e}_{a1}^{r(1)} + \sum_{r=1}^2 \sum_{i=2}^{\infty} a_i^r \bar{e}_{ai}^{r(1)} &= \sum_{\ell=1}^2 \sum_{m=1}^{\infty} b_m^{\ell} \bar{e}_{m\ell}^{(2)} = \\
 &= \begin{cases} \bar{E}_b & \text{in slot aperture} \\ 0 & \text{on groundplane} \end{cases}
 \end{aligned}$$

where \bar{E}_b is the unknown tangential electric field in the slot aperture. If we now take a cross product with $\bar{h}_{a1}^{r(2)*}$, take a dot product of this result with \hat{z} , and apply the orthogonality relation of Eq. (3-22), we obtain

$$\begin{aligned}
 (5-10) \quad [a_1^{rd} + \rho^r (1-DF^r)] \int_a \bar{e}_{a1}^{r(1)} \times \bar{h}_{a1}^{r(2)*} \cdot \hat{z} ds &= b_1^r \int_a \bar{e}_{a1}^{r(2)} \times \bar{h}_{a1}^{r(2)*} \cdot \hat{z} ds \\
 &= \int_b \bar{E}_b \times \bar{h}_{a1}^{r(2)*} \cdot \hat{z} ds
 \end{aligned}$$

where $\int_a ds$ denotes an integration over the entire central periodic cell and $\int_b ds$ denotes an integration over the central slot aperture only. The tangential E field boundary condition of zero on the conducting surface is applied by making the rightmost integration in Eq. (5-10) equal to zero except over the slot aperture. Since $\bar{e}_{a1}^{r(1)} = \bar{e}_{a1}^{r(2)}$ (3-51) Eq. (5-10) can be reduced to

$$(5-11) \quad a_1^{rd} + \rho^r (1-DF^r) = b_1^r = \int_b \bar{E}_b \times \bar{h}_{a1}^{r(2)*} \cdot \hat{z} ds / \int_a \bar{e}_{a1}^{r(2)} \times \bar{h}_{a1}^{r(2)*} \cdot \hat{z} ds .$$

If the dielectric layers were absent Eq. (5-11) would simply state that $1+R=T$ for an infinitesimally thin planar scatterer.

Multiplying Eq. (5-9) by $\bar{h}_{ai}^{r(2)*}$ and taking the dot product with \hat{z} we similarly obtain

$$(5-12) \quad a_i^r \int_a \bar{e}_{ai}^{r(1)} \times \bar{h}_{ai}^{r(2)*} \cdot \hat{z} ds = b_i^r \int_a \bar{e}_{ai}^{r(2)} \times \bar{h}_{ai}^{r(2)*} \cdot \hat{z} ds = \int_b \bar{E}_b \times \bar{h}_{ai}^{r(2)*} \cdot \hat{z} ds$$

which can easily be reduced to

$$(5-13) \quad a_i^r = b_i^r = \int_b \bar{E}_b x \bar{h}_{ai}^{r(2)*} \cdot \hat{z} ds / \int_a \bar{e}_{ai}^{r(2)} x \bar{h}_{ai}^{r(2)*} \cdot \hat{z} ds.$$

The continuity of tangential H across the slot aperture is now enforced by equating Eqs. (5-6) and (5-8) over the slot aperture, resulting in

$$(5-14) \quad \sum_{r=1}^2 [a_1^{rd} - \rho^r (1 + DF^r)] \bar{h}_{a1}^{r(1)} - \sum_{r=1}^2 \sum_{i=2}^{\infty} a_i^r \bar{h}_{ai}^{r(1)} = \sum_{k=1}^2 \sum_{m=1}^{\infty} b_m^k \bar{h}_{ai}^{k(2)}.$$

Substituting for a_i^r and b_m^k from Eq. (5-13) and combining terms we obtain:

$$(5-15) \quad \sum_{r=1}^2 \rho^r (1 + DF^r) \bar{h}_{a1}^{r(1)} + \sum_{r=1}^2 b_1^r \bar{h}_{a1}^{r(2)} = \sum_{r=1}^2 a_1^{rd} \bar{h}_{a1}^{r(1)} - \sum_{r=1}^2 \sum_{i=2}^{\infty} (\bar{h}_{ai}^{r(1)} + \bar{h}_{ai}^{r(2)}) \cdot \int_b \bar{E}_b x \bar{h}_{ai}^{r(2)*} \cdot \hat{z} ds / \int_a \bar{e}_{ai}^{r(2)} x \bar{h}_{ai}^{r(2)*} \cdot \hat{z} ds.$$

Substituting for ρ^r and b_1^r from Eq. (5-11), Eq. (5-15) readily becomes

$$(5-16) \quad - \sum_{r=1}^2 \frac{(1 + DF^r)}{(1 - DF^r)} a_1^{rd} \bar{h}_{a1}^{r(1)} + \sum_{r=1}^2 \frac{(1 + DF^r)}{(1 - DF^r)} \bar{h}_{a1}^{r(1)} \cdot \frac{\int_b \bar{E}_b x \bar{h}_{a1}^{r(2)*} \cdot \hat{z} ds}{\int_a \bar{e}_{a1}^{r(2)} x \bar{h}_{a1}^{r(2)*} \cdot \hat{z} ds} + \sum_{r=1}^2 \bar{h}_{a1}^{r(2)} \cdot \frac{\int_b \bar{E}_b x \bar{h}_{a1}^{r(2)*} \cdot \hat{z} ds}{\int_a \bar{e}_{a1}^{r(2)} x \bar{h}_{a1}^{r(2)*} \cdot \hat{z} ds} = \sum_{r=1}^2 a_1^{rd} \bar{h}_{a1}^{r(1)} - \sum_{r=1}^2 \sum_{i=2}^{\infty} (\bar{h}_{ai}^{r(1)} + \bar{h}_{ai}^{r(2)}) \cdot \frac{\int_b \bar{E}_b x \bar{h}_{ai}^{r(2)*} \cdot \hat{z} ds}{\int_a \bar{e}_{ai}^{r(2)} x \bar{h}_{ai}^{r(2)*} \cdot \hat{z} ds}$$

In order to simplify Eq. (5-16) we shall first evaluate the integral $\int_a \bar{e}_{ai}^{r(2)} x \bar{h}_{ai}^{r(2)*} \cdot \hat{z} ds$. From Eqs. (3-12) to (3-15), (3-18), (3-19), (3-51), and (3-52) we can write

$$(5-17) \int_a \bar{e}_{ai}^{r(2)} x \bar{h}_{ai}^{r(2)*} \cdot \hat{z} ds = \frac{1}{z_{pq}^{r(2)*}} \cdot \frac{1}{\sqrt{d_x d_y}} \int_a \frac{U_p^2 + V_{pq}^2}{T_{pq}^2} \exp(-j(U_p x + V_{pq} y)) \cdot \exp(+j(U_p x + V_{pq} y)) ds = \frac{1}{z_{pq}^{r(2)*}}$$

since the area of the central periodic cell is equal to $d_x d_y$ (see Fig. 3-2). In addition, we can combine terms by introducing the $\bar{\Phi}_{pq}^r$ function defined in Eq. (3-50). With these changes Eq. (5-16) becomes

$$(5-18) \sum_{r=1}^2 \left[\frac{1+DF^r}{1-DF^r} \cdot \frac{1}{\eta_{00}^{r(1)}} + \frac{1}{z_{00}^{r(2)}} \right] \bar{\Phi}_{00}^r \cdot \int_b \bar{E}_b \times \bar{\Phi}_{00}^{r*} \cdot \hat{z} ds \\ + \sum_{r=1}^2 \sum_{i=2}^{\infty} \left(\frac{1}{z_{pq}^{r(1)}} + \frac{1}{z_{pq}^{r(2)}} \right) \bar{\Phi}_{pq}^r \cdot \int_b \bar{E}_b \times \bar{\Phi}_{pq}^{r*} \cdot \hat{z} ds \\ = \sum_{r=1}^2 a_1^{rd} \left(1 + \frac{1+DF^r}{1-DF^r} \right) \frac{1}{\eta_{00}^{r(1)}} \bar{\Phi}_{00}^r$$

The unknown quantity in Eq. (5-18) is the slot aperture electric field \bar{E}_b . We can expand this aperture field using the mode sets presented in Chapter III as

$$(5-19) \quad \bar{E}_b = \sum_{j=1}^N c_j \bar{e}_{bj}$$

where we are using N modes to approximate the aperture field distribution. The proper set of \bar{e}_{bj} modes will be chosen from those in Chapter III depending on the shape of the slot aperture, but this will not affect the present derivation. Expanding the unknown aperture field thusly will allow us to use a moment method solution to obtain the unknown aperture fields. Since the fields are expanded in modes,

this type solution is often referred to as modal matching. Applying Galerkin's method, we substitute from Eq. (5-19) for \bar{E}_b , simultaneously cross multiply Eq. (5-19) by \bar{e}_{bn} , and take a dot product with \hat{z} , obtaining

$$\begin{aligned}
 (5-20) \quad & \sum_{r=1}^2 \left[\frac{1+DF^r}{1-DF^r} \cdot \frac{1}{\eta_{00}^r(1)} + \frac{1}{Z_{00}^r(2)} \right] \int_b \bar{e}_{bn} \times \bar{\phi}_{00}^r \cdot \hat{z} ds \cdot \sum_{j=1}^N C_j \int_b \bar{e}_{bj} \times \bar{\phi}_{00}^{r*} \cdot \hat{z} ds \\
 & + \sum_{r=1}^2 \sum_{i=2}^M \left(\frac{1}{Z_{pq}^r(1)} + \frac{1}{Z_{pq}^r(2)} \right) \int_b \bar{e}_{bn} \times \bar{\phi}_{pq}^r \cdot \hat{z} ds \cdot \sum_{j=1}^N C_j \int_b \bar{e}_{bj} \times \bar{\phi}_{pq}^{r*} \cdot \hat{z} ds \\
 & = \sum_{r=1}^2 a_1^{rd} \cdot \frac{2}{1-DF^r} \cdot \frac{1}{\eta_{00}^r(1)} \int_b \bar{e}_{bn} \times \bar{\phi}_{00}^r \cdot \hat{z} ds .
 \end{aligned}$$

Equation (5-20) is really N equations with the N unknowns being the C_j . Note that Eq. (5-20) requires the equality of integrations only over the slot aperture. This agrees with the condition that tangential H need be continuous only in the slot. The Floquet mode set has been truncated at $2M$ terms so as to allow a computer solution for the unknowns. Normally N will be quite small, i.e., usually less than 10 modes are required to approximate the fields in the slot aperture in order to obtain a valid result for the transmission coefficient. However, since the slot makes up only a small part of a periodic cell, many more Floquet modes will be required in order for the solution to converge [40]. But even though $2M$ is quite large compared with N , only an $N \times N$ system of equations (vis. Eq. (5-20)) will need to be solved.

Once the C_j are determined the value of ρ^r can be obtained by combining Eqs. (5-11), (5-17), and (5-19) as

$$(5-21) \quad \rho^r = \frac{1}{1-DF^r} \cdot \sum_{j=1}^N C_j \int_b \bar{e}_{bj} \times \bar{\phi}_{00}^{r*} \cdot \hat{z} ds - \frac{a_1^{rd}}{1-DF^r} .$$

The free space modal reflection coefficient R^r is then obtained from ρ^r by using Eq. (3-44). Similarly, the Floquet mode coefficients for the back side of the panel are given by

$$(5-22) \quad b_i^r = \sum_{j=1}^N C_j \int_b \bar{e}_{bj} \times \bar{\phi}_{pq}^{r*} \cdot \hat{z} ds .$$

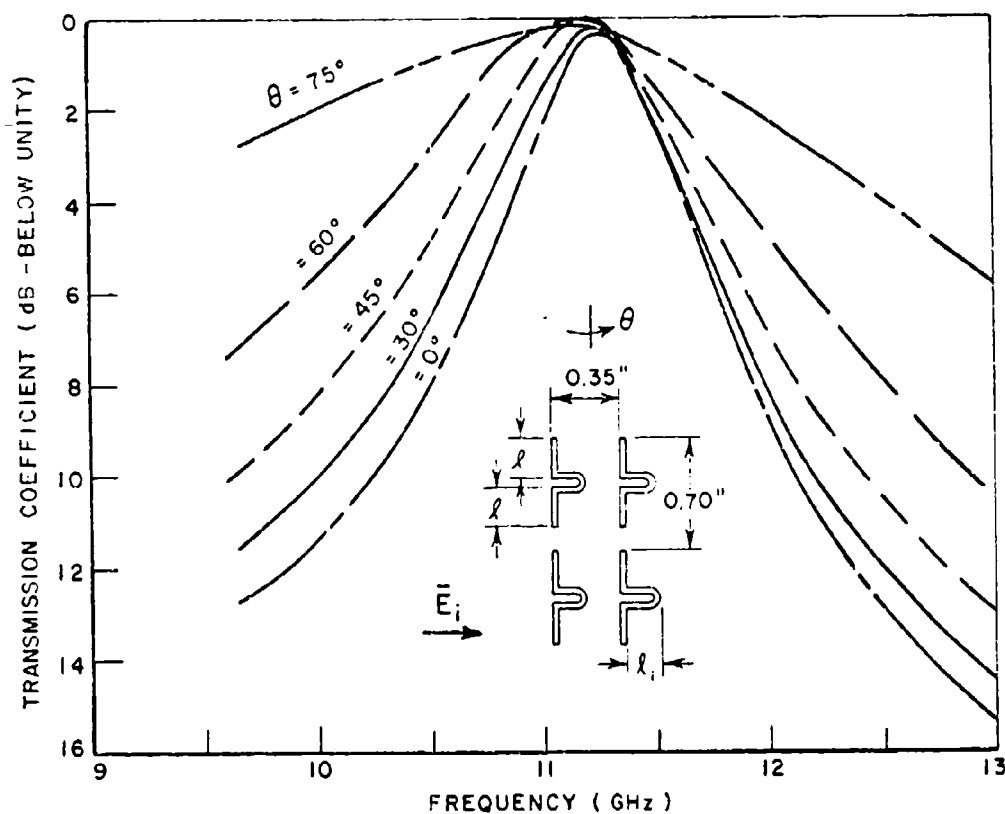


Figure 5-2.--Computed transmission coefficient curves using the mutual impedance method (Munk [3]) for an array of single loaded slots for various incidence angles in the E-plane ($\phi=90^\circ$) $\ell=\ell_1=0.38$ cm.

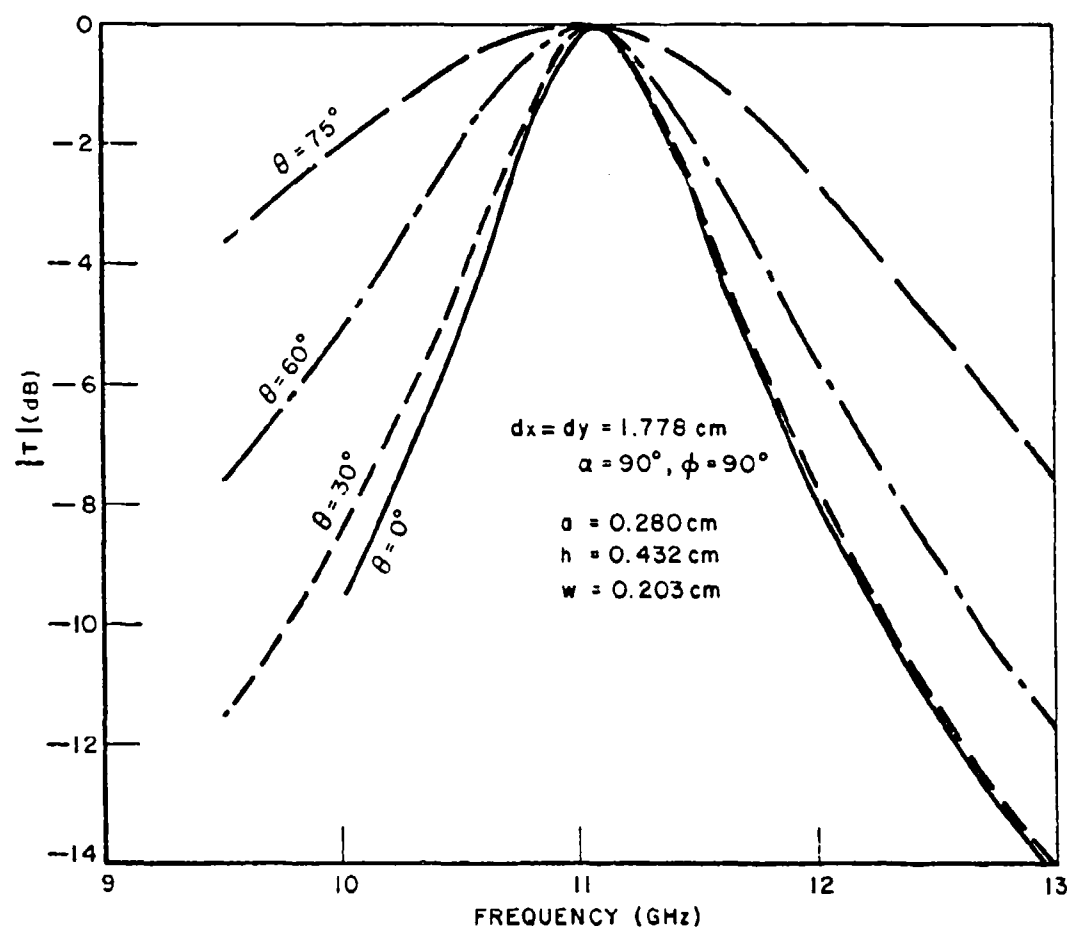


Figure 5-3.--Computed transmission curves using the modal matching solution for the loaded slot array of Fig. 5-2 for various E-plane incidence angles.

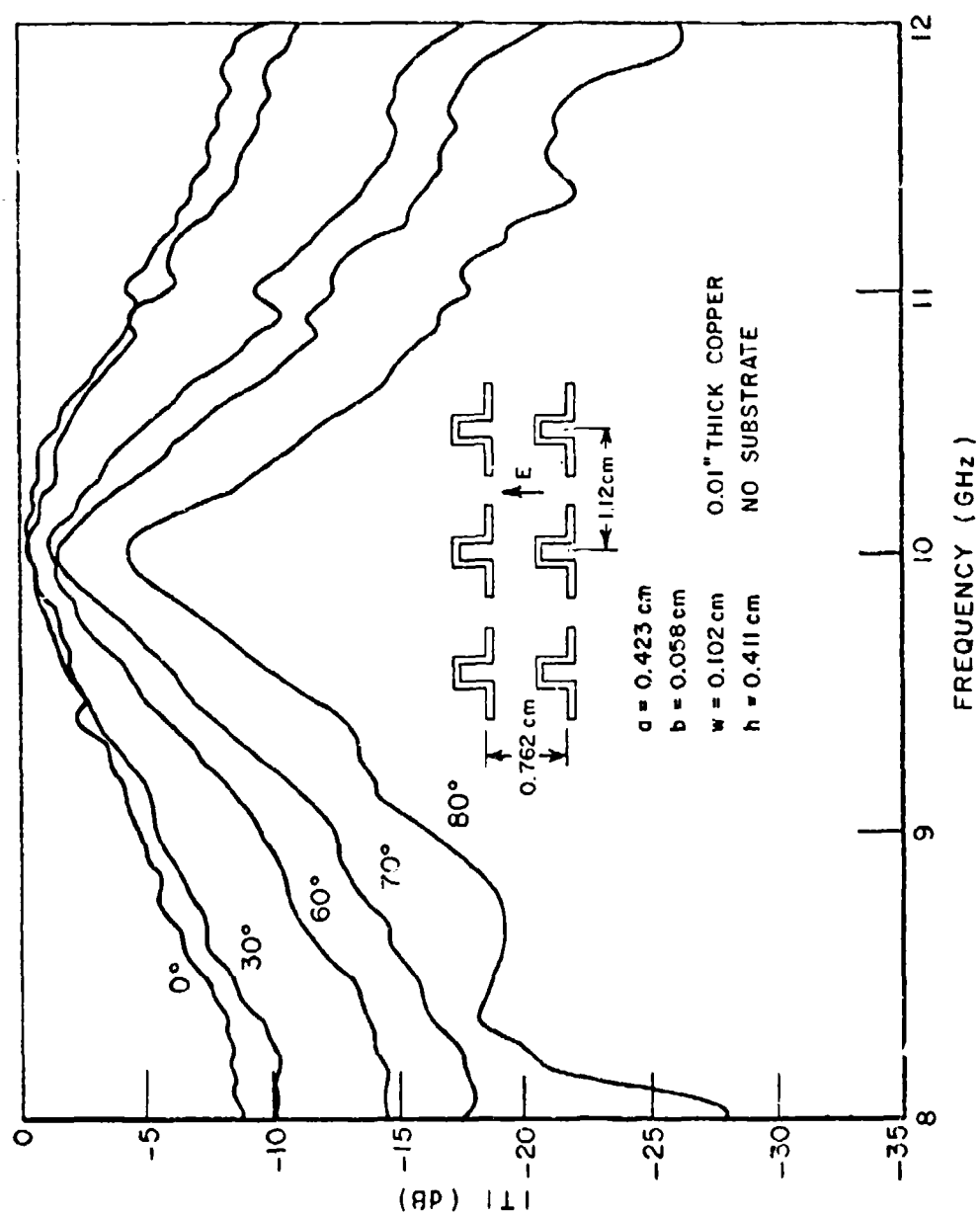


Figure 5-4.--Measured transmission curves showing the transmission loss at resonance for an array of loaded slots with H-plane ($\phi=0^\circ$) incidence.

line load, and can be explained qualitatively as follows: The arrows contained in the slot of Fig. 3-9 illustrate the direction of the electric field vector in the slot for the dominant sinusoidal mode. It is evident that with the incident E field polarized as shown any cross polarized radiation from one side of the transmission line load (i.e., region 1b) would be exactly canceled by radiation from the other side of the transmission line load (i.e., region 1c), providing that ϕ is equal to 90° . However, for angles of incidence with $\phi \neq 90^\circ$ the cross polarized radiation from the opposite sides of the transmission line would not cancel due to the phase difference introduced by the finite width of the transmission line.

Using the modal matching method this loss can be calculated. The transmission curves presented in Fig. 5-5 are calculated for the array measured for Fig. 5-4, and show good agreement with the measured data. The curves were calculated using 374 Floquet modes and 7 modes in the slot, with the even ordered slot modes now included. Convergence tests were made in arriving at these figures, with the required high ratio of Floquet modes to slot modes evidently due to the complex, non-symmetric shape of the slot. Actually, even with 374 modes the solution had not quite yet converged, and this may be partially responsible for the 2.0% error in the calculated resonance frequency. The magnitude of the transmitted cross polarized radiation was also measured and is shown in Fig. 5-6, with the corresponding calculated curves in Fig. 5-7. These curves show that the magnitude of the cross polarized radiation at resonance increases with increasing angle of incidence. This is due to the increasing phase difference between the two arms of the transmission line load.

Note that while the calculations accurately predict the level of the cross polarized radiation, the measured transmission loss is somewhat greater than is calculated (Figs. 5-4 and 5-5). This is probably due to copper losses and to imperfections in the array elements.

The difference in impedance levels between the T_{00}^1 and T_{00}^2 transmission coefficients must be taken into account when calculating the cross polarized transmission coefficients and also when checking for conservation of energy, viz.

$$(5-23) \quad \frac{|A_{00}^1|^2}{\eta_{00}} + \frac{|A_{00}^2|^2}{\eta_{00}^2} = \frac{|R_{00}^1|^2}{\eta_{00}} + \frac{|T_{00}^1|^2}{\eta_{00}} + \frac{|R_{00}^2|^2}{\eta_{00}^2} + \frac{|T_{00}^2|^2}{\eta_{00}^2}$$

providing no grating lobes can propagate. While conservation of energy is not a sufficient condition to assure accuracy, it is a necessary one.

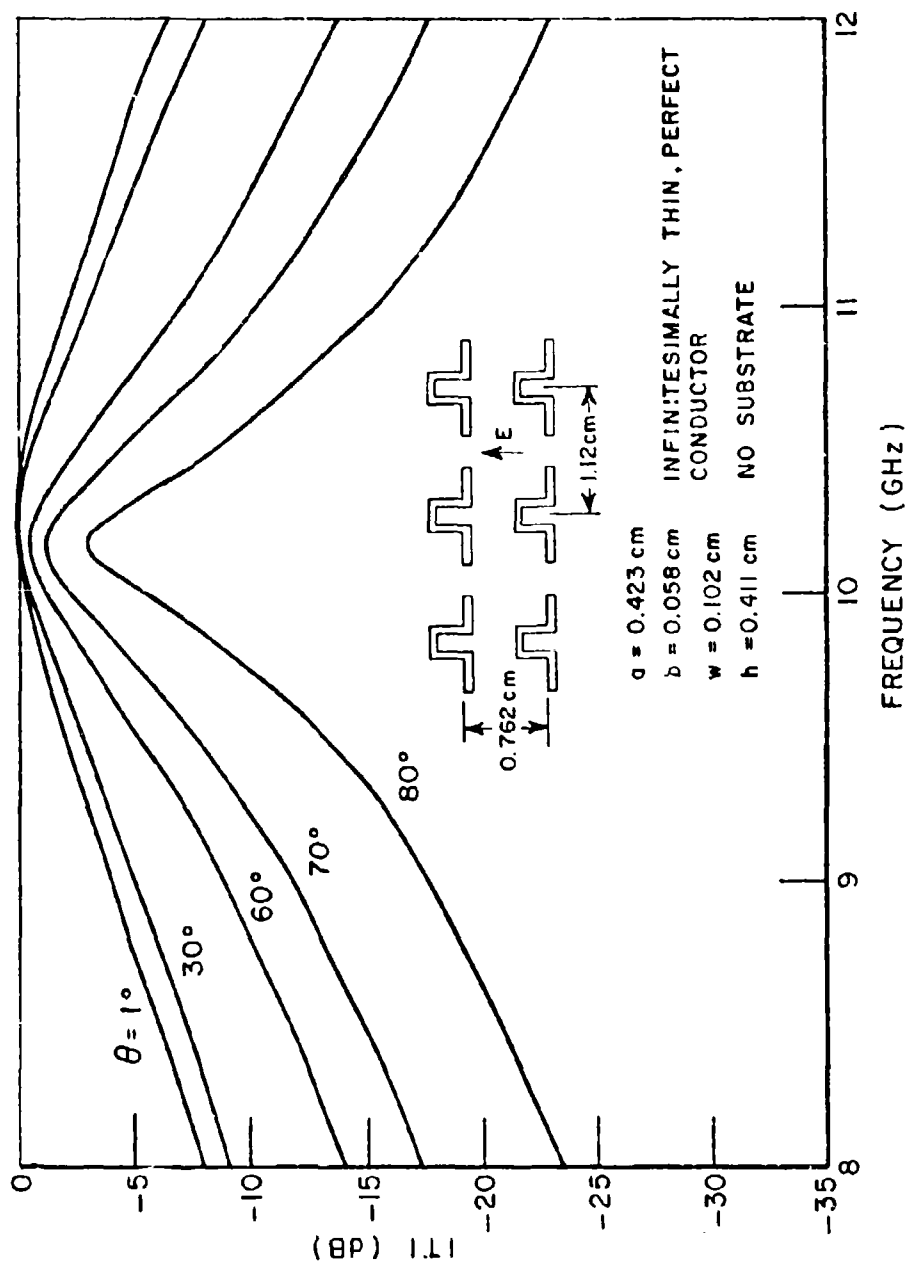


Figure 5-5.--Calculated transmission curves for various incidence angles θ ($\phi=0^\circ$) for the single loaded slot array of Fig. 5-4.

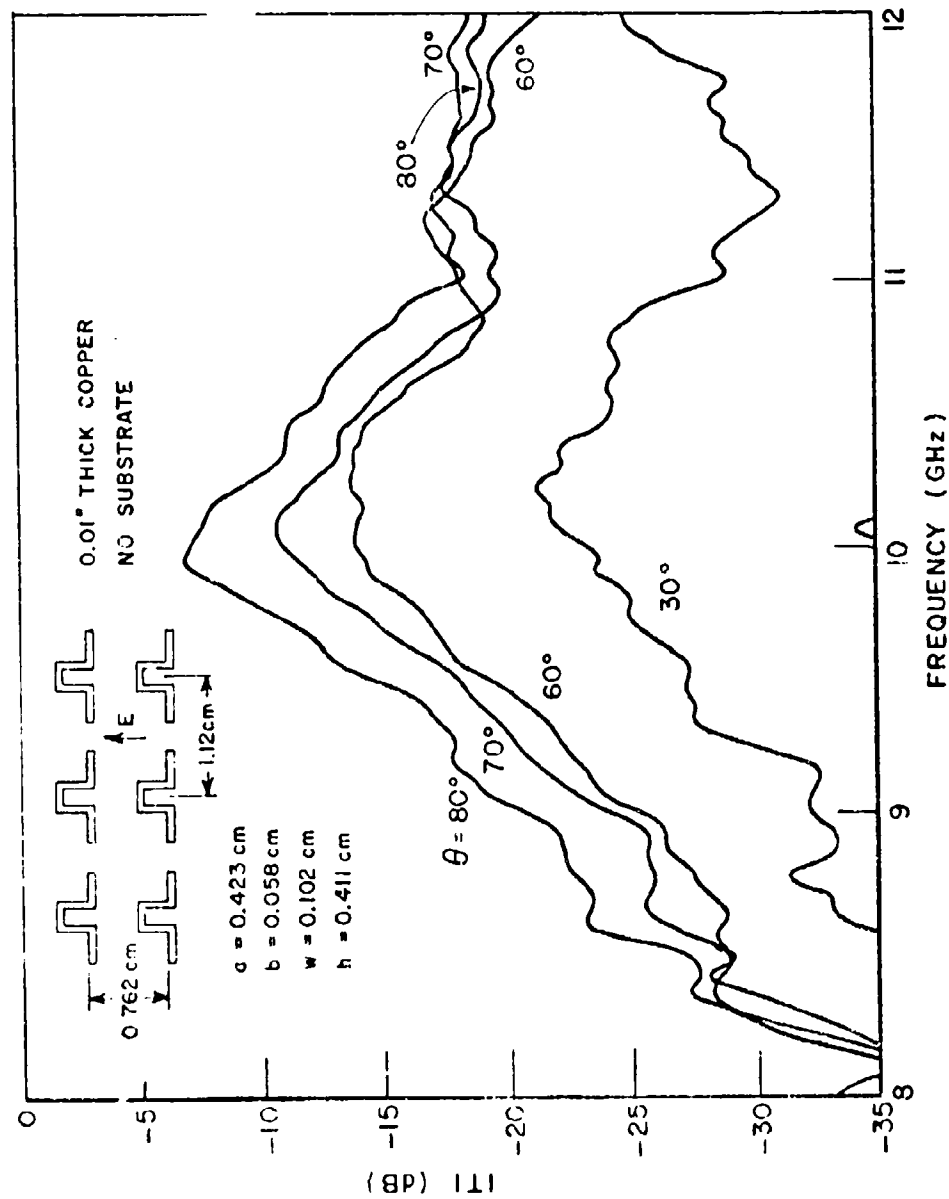


Figure 5-6.--Measured transmission of the cross polarized radiation for the same loaded slot array of Figs. 5-4 and 5-5 for various incidence angles θ in the H-plane ($\phi=0^\circ$).

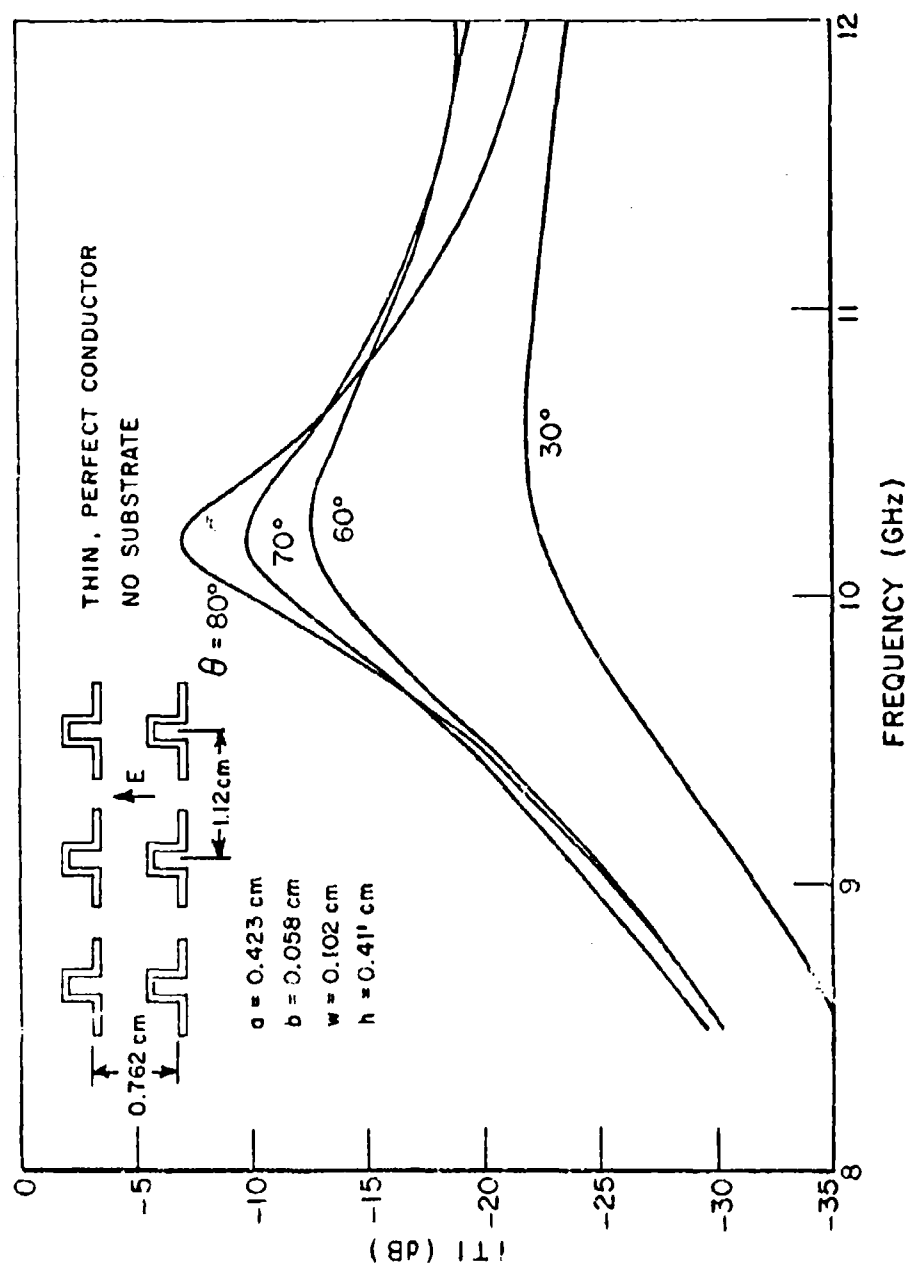


Figure 5-7.--Calculated transmission of the cross polarized radiation which corresponds to the measured curves of Fig. 5-6.

This cross polarized radiation is undesirable for most applications. It can be reduced by arranging singly loaded slots so that the load extends in opposite directions on alternating slots, thus canceling out the cross polarized radiation [14]. Alternatively, loaded slot elements can be designed so that they do not radiate a significant cross polarized component. This method is better for many applications since the resulting surface will transmit waves of arbitrary polarization without the need to interlace two orthogonal arrays of single loaded slots. Two examples of this type of slot element are the 4-legged and 3-legged symmetric loaded slots which will be considered in the remaining sections of this chapter.

C. 4-legged Symmetric Slots

The 4-legged symmetric loaded slot geometry is shown in Fig. 5-8. Due to its symmetry, resonant windows made with this type of

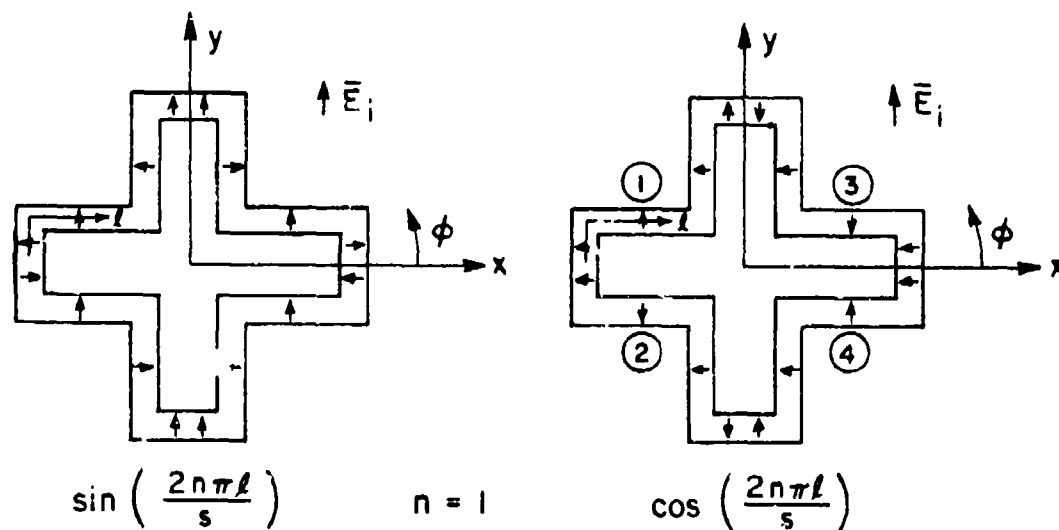


Figure 5-8.--Electric field polarities for the $n=1$ sine and cosine modes for the 4-legged symmetric loaded slot.

slot do not have the large cross polarized transmission losses exhibited by arrays of singly loaded slots. Also, this type slot has the advantage, at least for most applications, of transmitting arbitrarily polarized waves. For a given slot width and shape, the 4-legged element would tend to be more wide banded than the corresponding single loaded element.

The \bar{e}_{bj} modes used to describe the electric field in the 4-legged loaded slot are given by Eq. (3-76) with $z=0$. The polarity distributions of the electric field for the $n=1$ sine and cosine modes are

sketched in Fig. 5-8. With the incident E field polarized as shown the $n=1$ sine mode will be the dominant mode in the slot. At the first resonance the calculations show that the fields in the slot will be almost exactly described by this mode, since its modal coefficient will be several orders of magnitude greater than for any other mode. Contrarily, the $n=1$ cosine mode will not be excited at all for incidence directions in the cardinal planes (i.e., $\phi=0^\circ$ or $\phi=90^\circ$). This can be explained by referring to Fig. 5-8. For incidence angles in the $\phi=0^\circ$ plane the coupling of the incident E field with the $n=1$ cosine mode in region 1 of the slot will be exactly canceled by that from region 2. Similarly, the coupling over regions 3 and 4 will cancel. For incidence angles in the $\phi=90^\circ$ plane, regions 1 and 3 will cancel one another, as will regions 2 and 4. Similar results are obtained for all of the other odd ordered cosine modes. Thus these odd ordered cosine modes need not be included in the computer program for cardinal plane incidence angles, resulting in a considerable time savings. (Naturally, including them will not result in incorrect results; the calculated modal coefficients will equal zero within the limits of round-off error.)

The E field polarities for the $n=2$ sine and cosine modes are illustrated in Fig. 5-9. Using similar arguments as before, it is

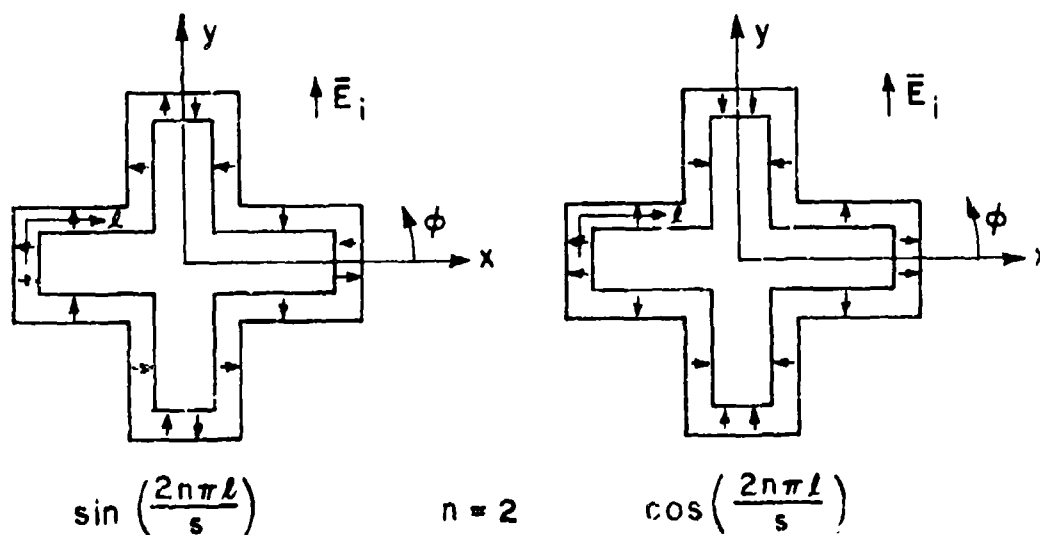


Figure 5-9.---Electric field polarities for the $n=2$ sine and cosine modes for the 4-legged symmetric loaded slot.

evident that the sine mode will not be excited for incidence angles with $\phi=90^\circ$, while the cosine mode will not be excited for incidence angles with $\phi=0^\circ$. These $n=2$ modes describe the fields in the slot at the second resonance. Thus while the same mode (the $n=1$ sine mode)

is strongly excited for the first resonance for both cardinal incidence planes, this is not the case for the second resonance. There, which mode is excited depends on the direction of the incoming plane wave. Some applications for resonant windows require that the second resonance be as far above the first as possible. This knowledge about the electric field distribution in the slots may prove quite helpful in designing new slot shapes which have the required second resonance properties.

Now that the method for eliminating the unexcited slot modes for the various incidence directions has been discussed, we are ready to present some computed curves along with experimental verification of those curves. The first series of curves is for the array of slots with the geometry shown in the inset of Fig. 5-10. The slots are in a square grid arrangement with 1.355 cm spacing. The parameters b , c , and d describe the slots themselves and are defined in Fig. 3-11. The actual panel was made by chemically etching the slots in a 0.002" thick layer of copper on a 0.072 cm thick dielectric substrate with $\epsilon_r=2.38$. The effects of the dielectric layer are included in the mode matching solution. The effects of the finite thickness of the copper are negligible for this thickness and frequency. The number of Floquet modes used to calculate this series of curves was 242, with p and q each ranging from -5 to +5, and r equal to 1 or 2. The number and type of modes used to describe the fields in the slots varies depending on the plane of incidence, and will be given for each case.

In Figs. 5-10 and 5-11 are calculated and measured curves for the 4-legged slot array for various incidence angles θ in the $\phi=0^\circ$ plane (see Fig. 3-1). The frequency range includes the first resonance region. The curves were calculated using the first 7 sine modes in the slot. The agreement between the calculated and measured curves is quite good. Note especially that the calculations predict very accurately the shift of the resonance frequency with incidence angle. This is often the most important parameter of a resonant window.

Figures 5-12 and 5-13 show calculated and measured curves for the same frequency range but for incidence angles with $\phi=90^\circ$. The odd sine modes and even cosine modes were used to describe the fields in the slots, with n ranging from 1 to 7. The agreement is again quite good. The discontinuities in the calculated curves are surface wave nulls associated with the onset of propagating grating lobes. The frequencies at which the grating lobes start to propagate are indicated on the abscissa for the various incidence angles. For a square grid array, (i.e., $d_x=d_y$) for a given incidence angle, the grating lobes will start to propagate at the same frequency for both the $\phi=0^\circ$ and $\phi=90^\circ$ incidence planes. Yet the surface wave nulls were not evident in Figs. 5-10 and 5-11, since the element pattern prevented the grating lobes from being suddenly excited in that plane. The measured nulls are not so deep and pronounced as the calculated

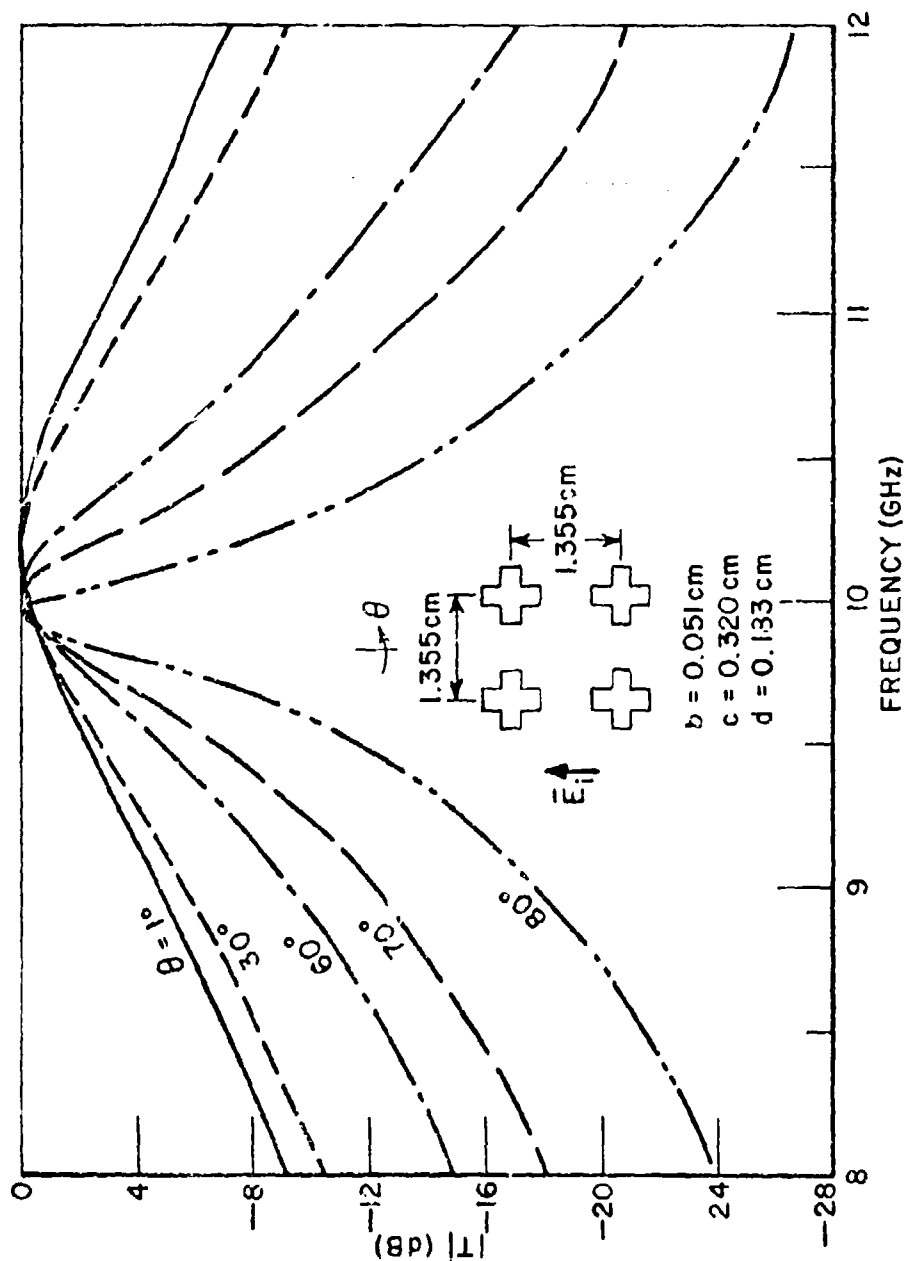


Figure 5-10.--Calculated transmission curves for an array of 4-legged symmetric slots on a thin dielectric substrate ($t_2=0.072 \text{ cm}$, $\epsilon_2=2.38\epsilon_0$; $t_1=0$), H-plane incidence.

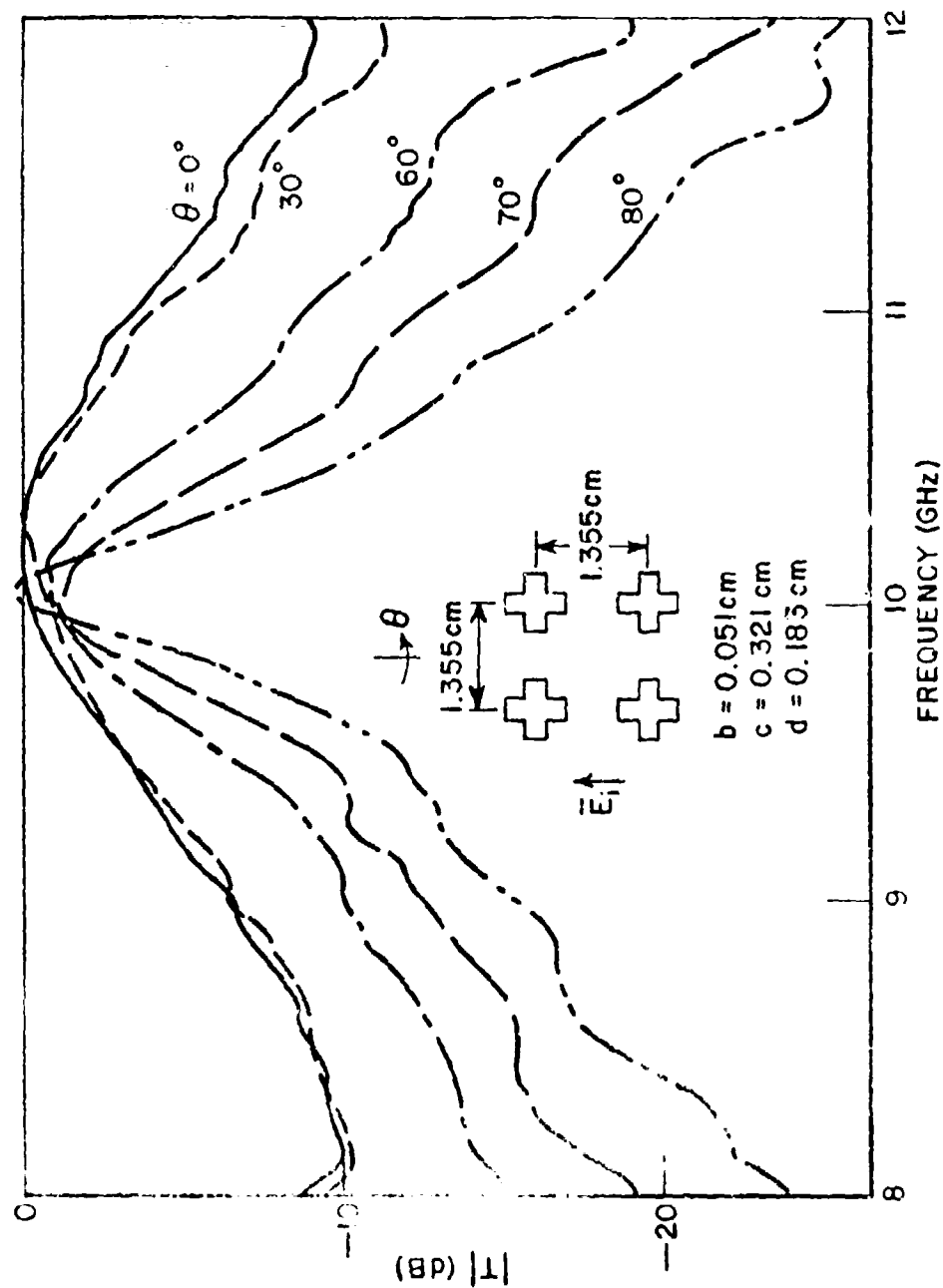


Figure 5-11.--Measured transmission curves corresponding to the calculated curves of Fig. 5-10.

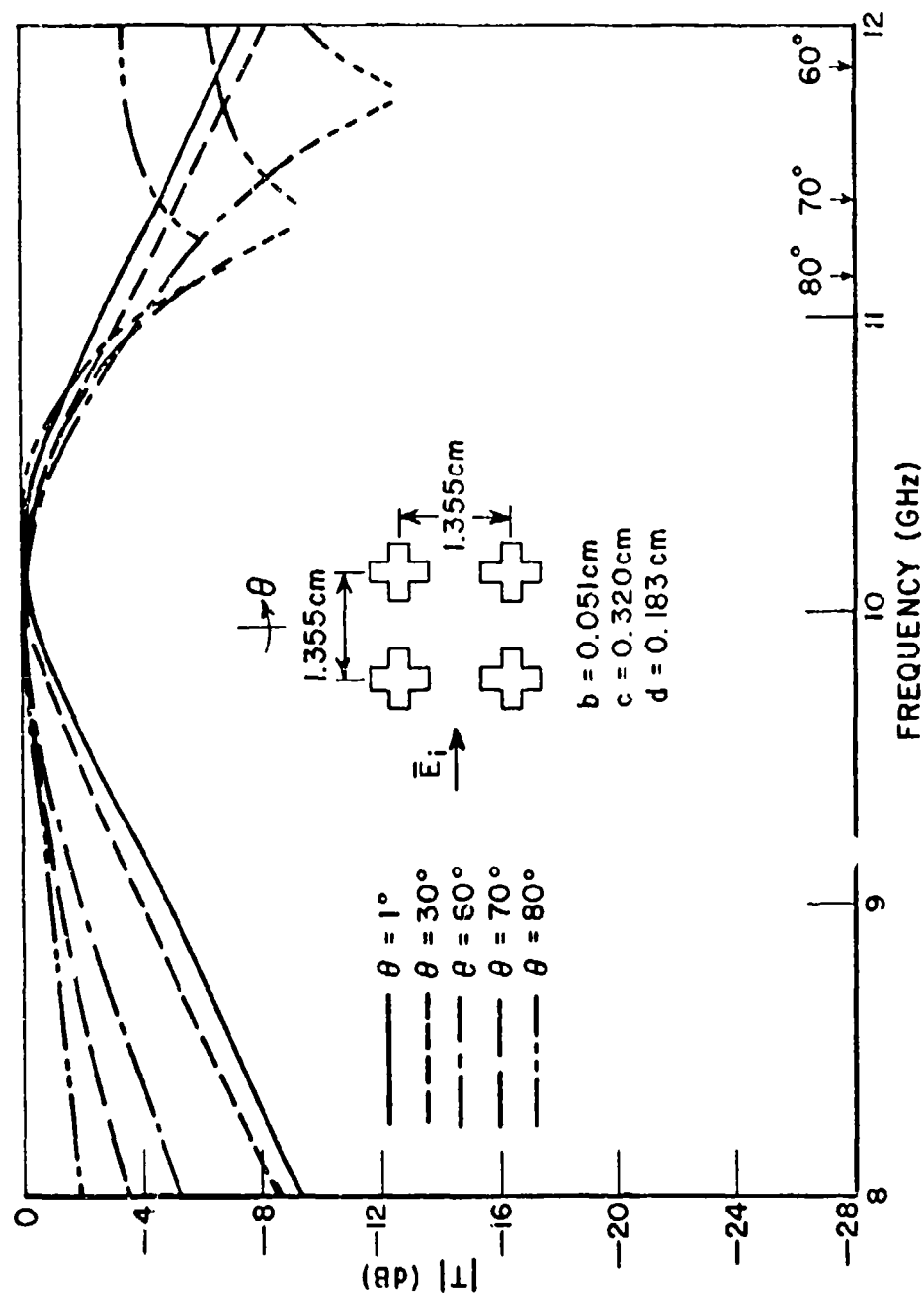


Figure 5-12.--Calculated transmission curves for an array of 4-legged symmetric slots on a thin dielectric substrate ($t_2=0.072$ cm, $\epsilon_2=2.38\epsilon_0$; $t_1=0$), E-plane incidence.

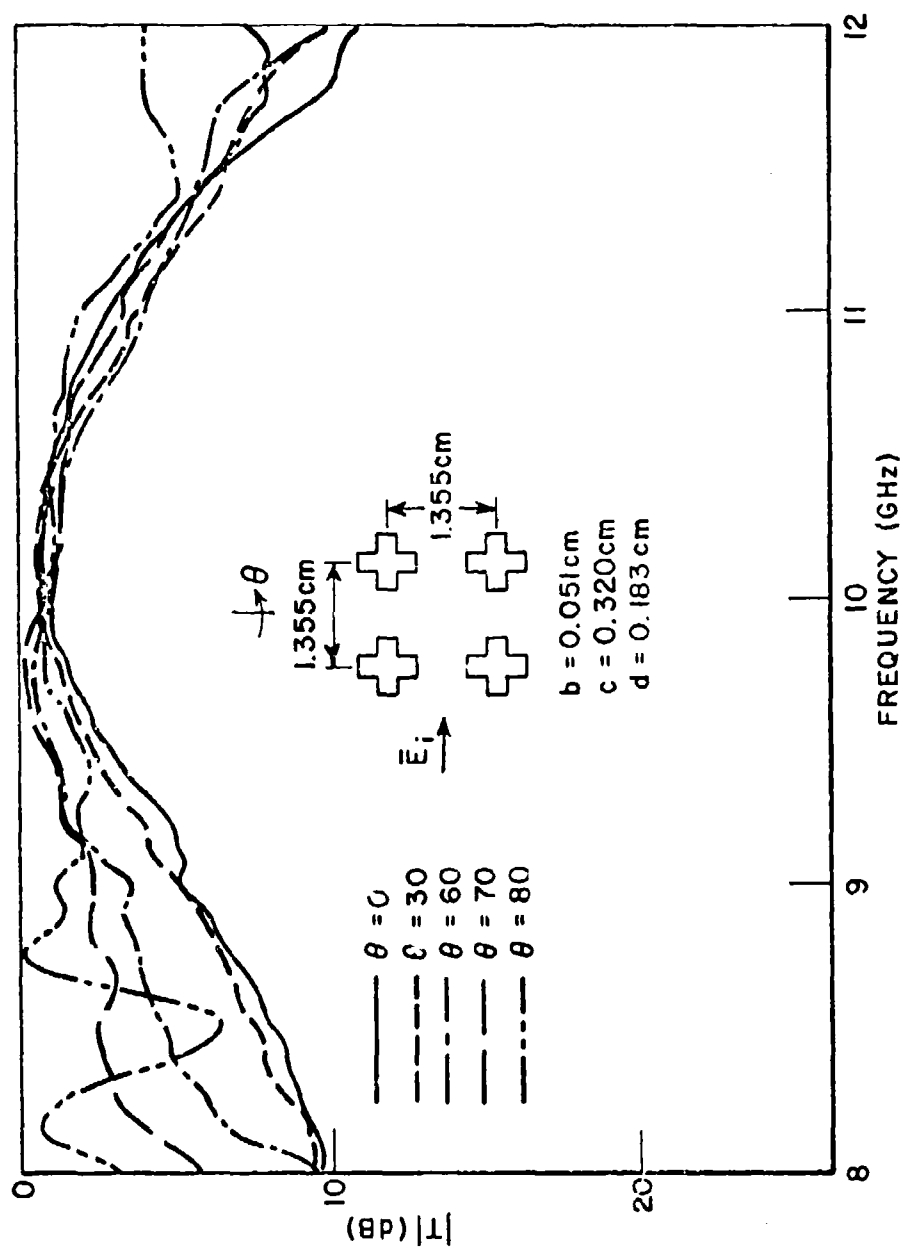


Figure 5-13.--Measured transmission curves corresponding to the calculated curves of Fig. 5-12.

ones due to the finite size of the panels measured (approximately 1 ft. square). The oscillation in the 80° curve near 8.5 GHz is assumed to be due to a measurement error.

These first resonance curves could also have been calculated using the impedance method of Munk [3]. However, the second resonance curves which are about to be presented have not been calculated using the mutual impedance method. This is because higher order modes are needed to describe the slot fields in the second resonance region, and the presence of these modes makes the application of the mutual impedance method somewhat more complex.

Calculated and measured transmission curves showing the second resonance for incidence angles in the $\phi=0^\circ$ plane are presented in Figs. 5-14 and 5-15. The first 7 sine modes are used to describe the slot fields. The general shapes of the calculated and measured curves agree quite well. However, the frequency of the second resonance differs by approximately 1 GHz. There are at least two possible explanations for the disagreement. The most likely explanation is experimental error. The measurements were taken using a sweep generator coupled with a computerized data taking system. Thus a small calibration error would well explain the discrepancy, since 1 GHz is only about a 6% error at the second resonance frequency. The other explanation is that the modal solution is in error in this plane. Despite the error in frequency, the calculations predict the levels of the second resonance peaks quite accurately. The transmission peaks are lossy since there are propagating grating lobes. The lack of a second resonance peak for normal incidence is predicted quite accurately by the calculations. Referring to the modal polarity diagrams in Fig. 5-9, it is evident that neither the second order sine mode nor the second order cosine mode will be excited by a normally incident plane wave. This observation tends to confirm our previous statement that these 2nd order modes describe quite accurately the slot fields at second resonance.

Second resonance transmission curves for incidence directions with $\phi=90^\circ$ are shown in Figs. 5-16 and 5-17. Again, the odd sine modes and even cosine modes with n running from 1 to 7 were used to describe the fields in the slots. For this incidence plane the calculations predict the frequency of the second resonance quite accurately. However, the overall agreement as regards the general shapes of the curves and the peak values at the second resonance is not quite so good as for the $\phi=0^\circ$ curves. The transmission curve behavior in this plane seems to be more complicated. The general trends, i.e., the shoulders on the resonance curves, the relative heights of the resonance peaks for various incidence angles, and the null preceding the resonance peak, are predicted quite accurately. The $\theta=30^\circ$ transmission null just below 15 GHz is evident in both the calculated and measured data. The depth of the measured null is limited by the finite size of the panel. This finite panel size also is an important factor in the discrepancies between the calculated and measured data.

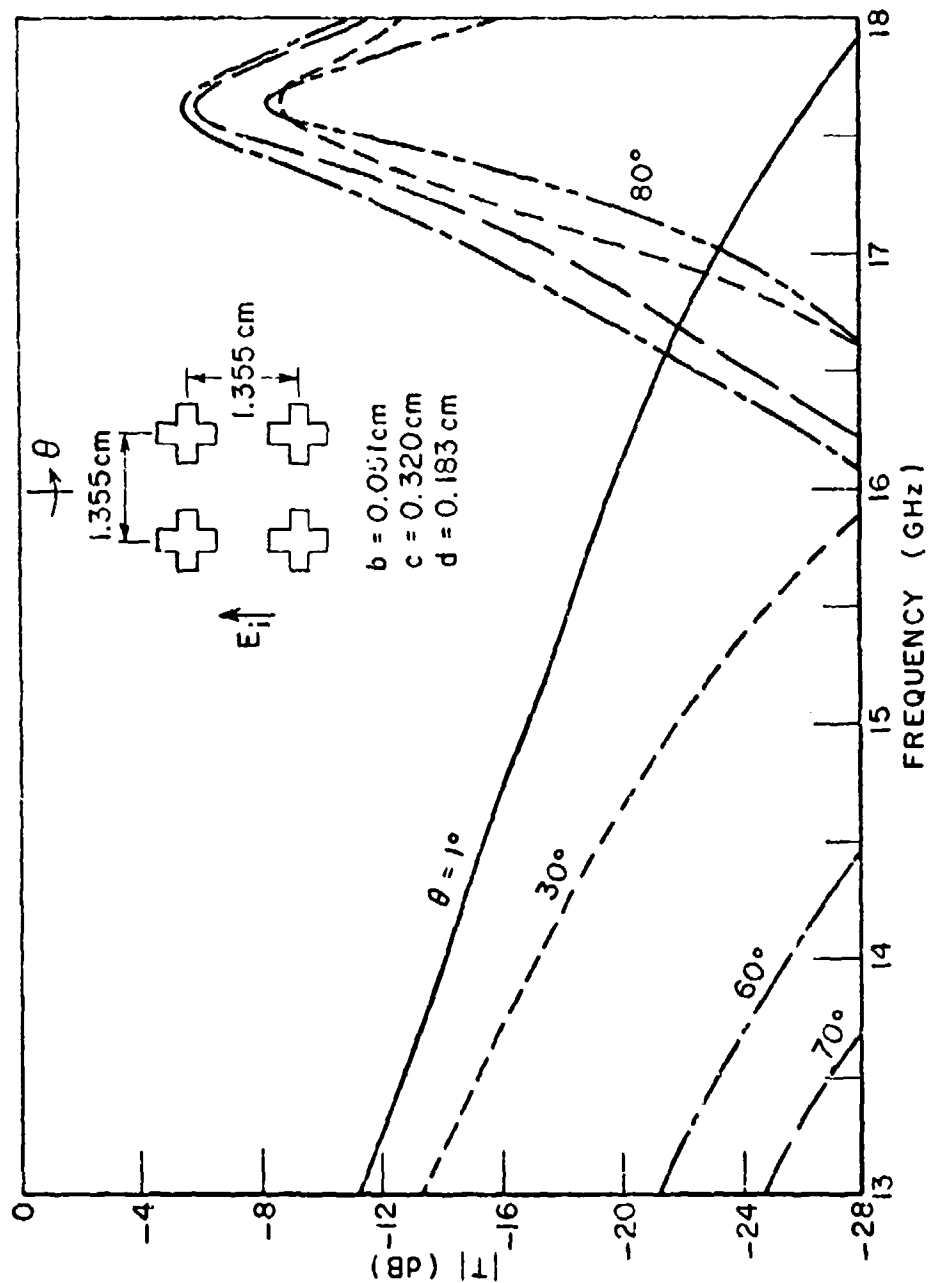


Figure 5-14.--Calculated transmission curves for an array of 4-legged symmetric slots on a thin dielectric substrate ($t_2=0.072 \text{ cm}$, $\epsilon_2=2.38\epsilon_0$; $t_1=0$), H-plane incidence. The frequency range includes the second resonance.

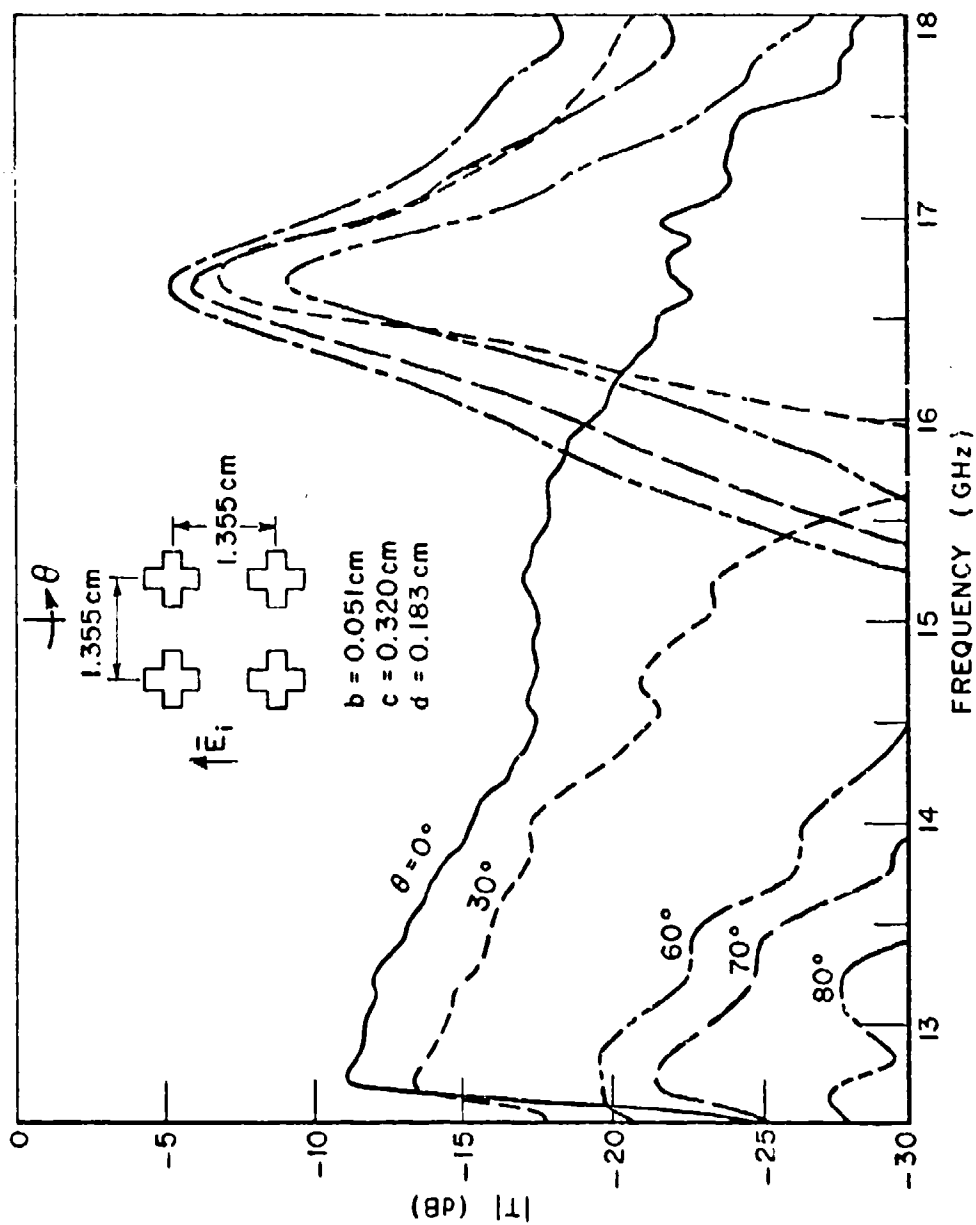


Figure 5-15.--Measured transmission curves corresponding to the calculated curves of Fig. 5-14.

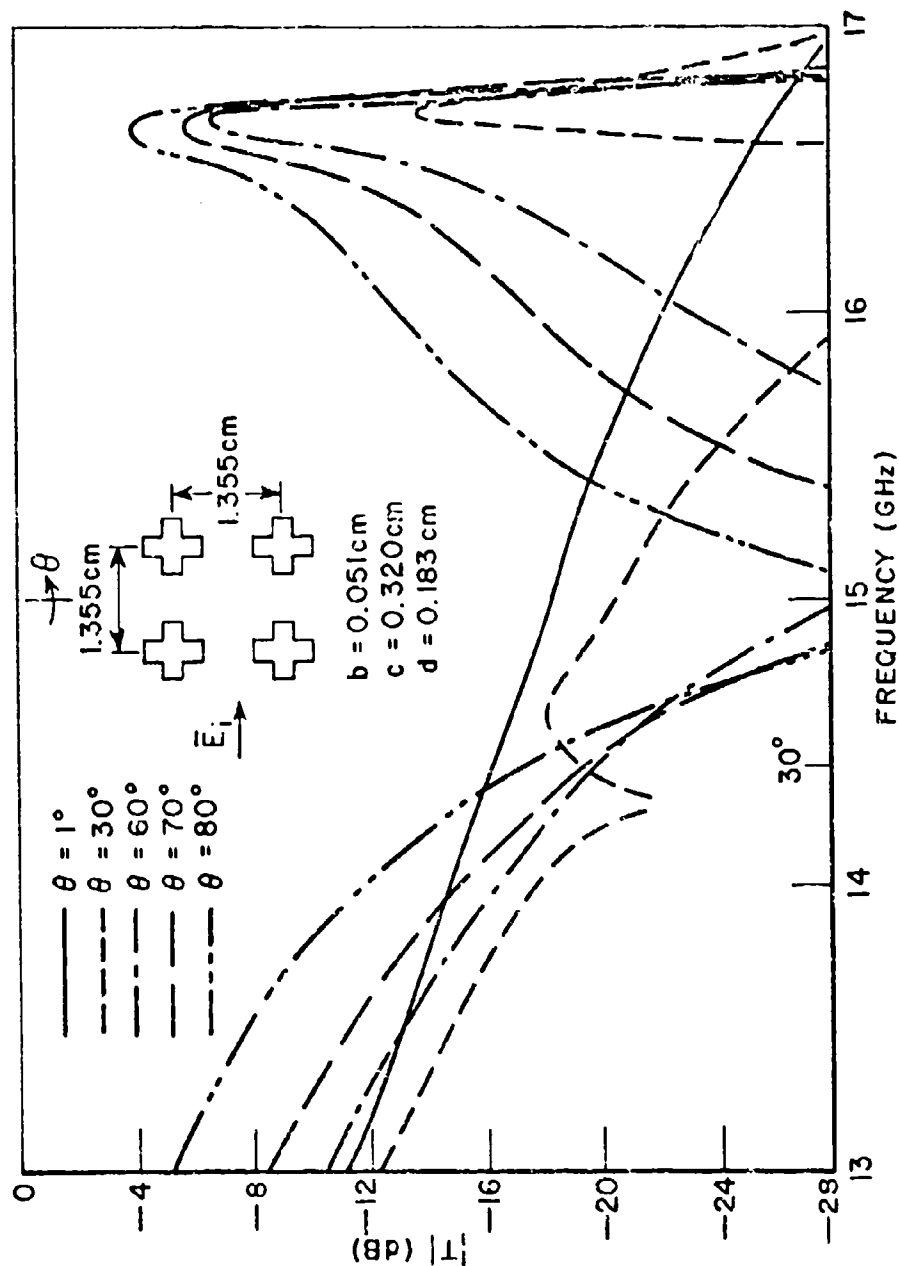


Figure 5-16.--Calculated transmission curves for an array of 4-legged symmetric slots on a thin dielectric substrate ($t_2=0.072\text{ cm}$, $\epsilon_2=2.38\epsilon_0$; $t_1=0$), E-plane incidence. The frequency range includes the second resonance.

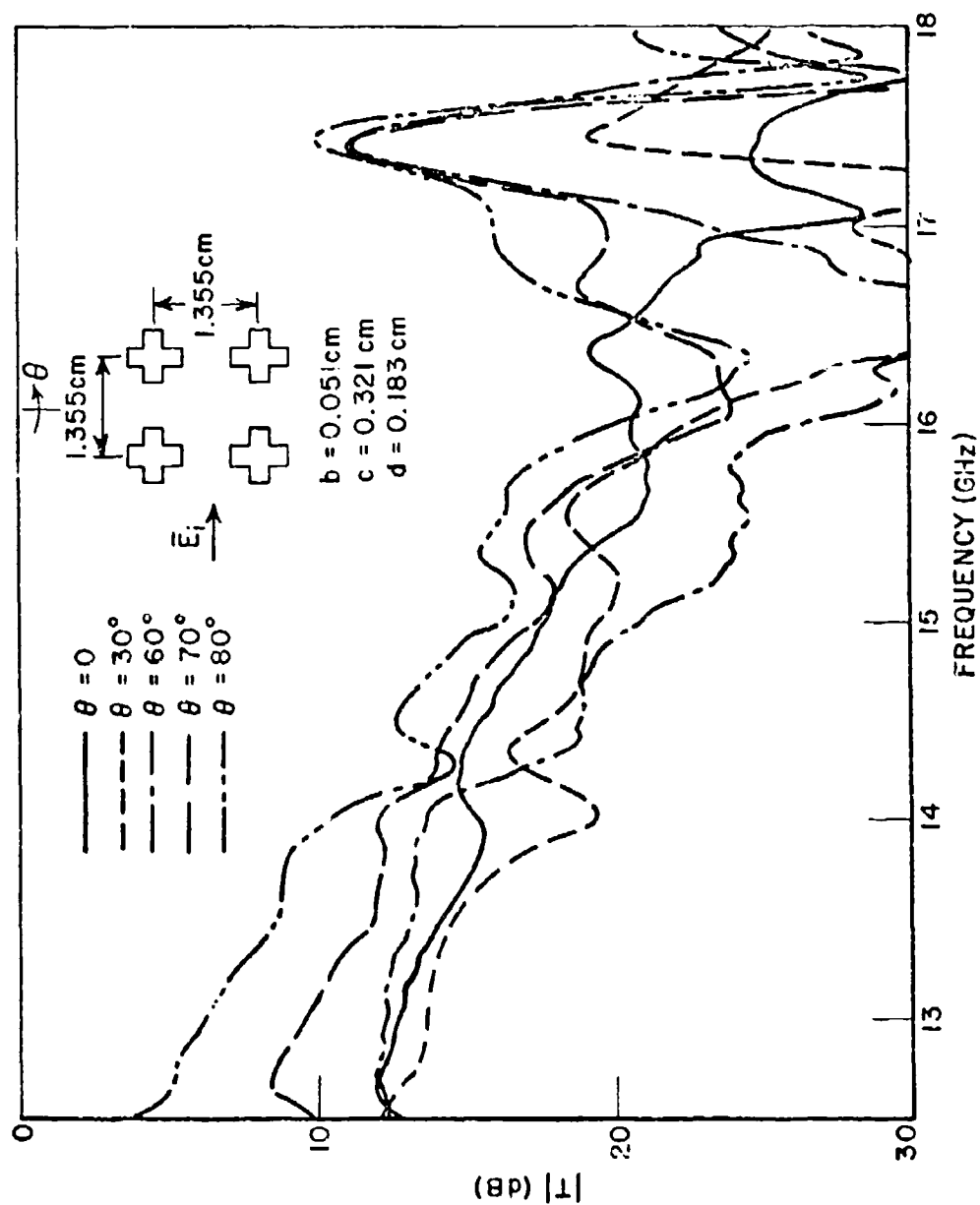


Figure 5-17.--Measured transmission curves corresponding to the calculated curves of Fig. 5-16.

Throughout these calculations, slot modes which are not excited for a particular incidence direction are not included in the solution. However, one must be sure to include all of the excited modes. This is illustrated in Fig. 5-18. These curves were calculated for the same conditions as those in Fig. 5-16 but without the even ordered cosine modes. The $\theta=1^\circ$ curves are nearly identical, since the cosine modes are not excited for normal incidence. But the second resonance peak is missing from the 60° and 80° curves. This comparison also confirms the previous statement that the 2nd order cosine mode is responsible for the second resonance in the $\phi=90^\circ$ incidence plane.

One final point needs to be made regarding 4-legged slot arrays. Referring back to Fig. 5-10, there is a noticeable shift of resonance frequency with incidence angle. This shift can be eliminated by decreasing the interelement spacings d_x and d_y . Calculated transmission curves for such an array are shown in Fig. 5-19, with the confirming measured curves in Fig. 5-20. Again, 7 sine modes were used for the slot fields. This panel has the same frequency stability as the single loaded slot panel of Fig. 5-4 but without the undesired transmission loss.

D. 3-legged Symmetric Slot

The 3-legged symmetric slot element shown in Fig. 3-12 was developed by Pelton [1,2] for application in a high aspect ratio radome design. The 3-legged slots have the desirable properties of the 4-legged slots. They can transmit arbitrarily polarized waves without significant cross polarization losses when arranged in a triangular grid. Pelton has shown that the triangular grid arrangement tends to yield a more stable resonance frequency (with varying incidence angle) than the rectangular grid, especially for incidence angles not in the principal planes (i.e., $\phi=45^\circ$ rather than 0° or 90°). To our knowledge calculated transmission curves for arrays of this type have not yet appeared in the literature, although Pelton is presently engaged in the analysis of these slots using the mutual impedance method [53].

The modal analysis method can be used to calculate transmission through an array of 3-legged slots. The e_{bj} modes used to describe the fields in the 3-legged loaded slot are given by Eq. (3-76) with $z=0$ and the proper definition for $G(k)$. The electric field polarities for the $n=1$ sine and cosine modes are shown in Fig. 5-21. The 3-legged slot does not have symmetry in the cardinal ($\phi=0^\circ, 90^\circ$) planes as does the 4-legged slot. Thus both x polarized and y polarized E fields must be considered. For y polarized E fields the sine mode will be strongly excited by the incident wave, while for x polarized E fields the cosine mode will be. These two modes are the dominant modes in the first resonance region. The calculated transmission curves for 3-legged slot panels presented in this section were made using 98 Floquet modes (p and q running from -3 to $+3$,

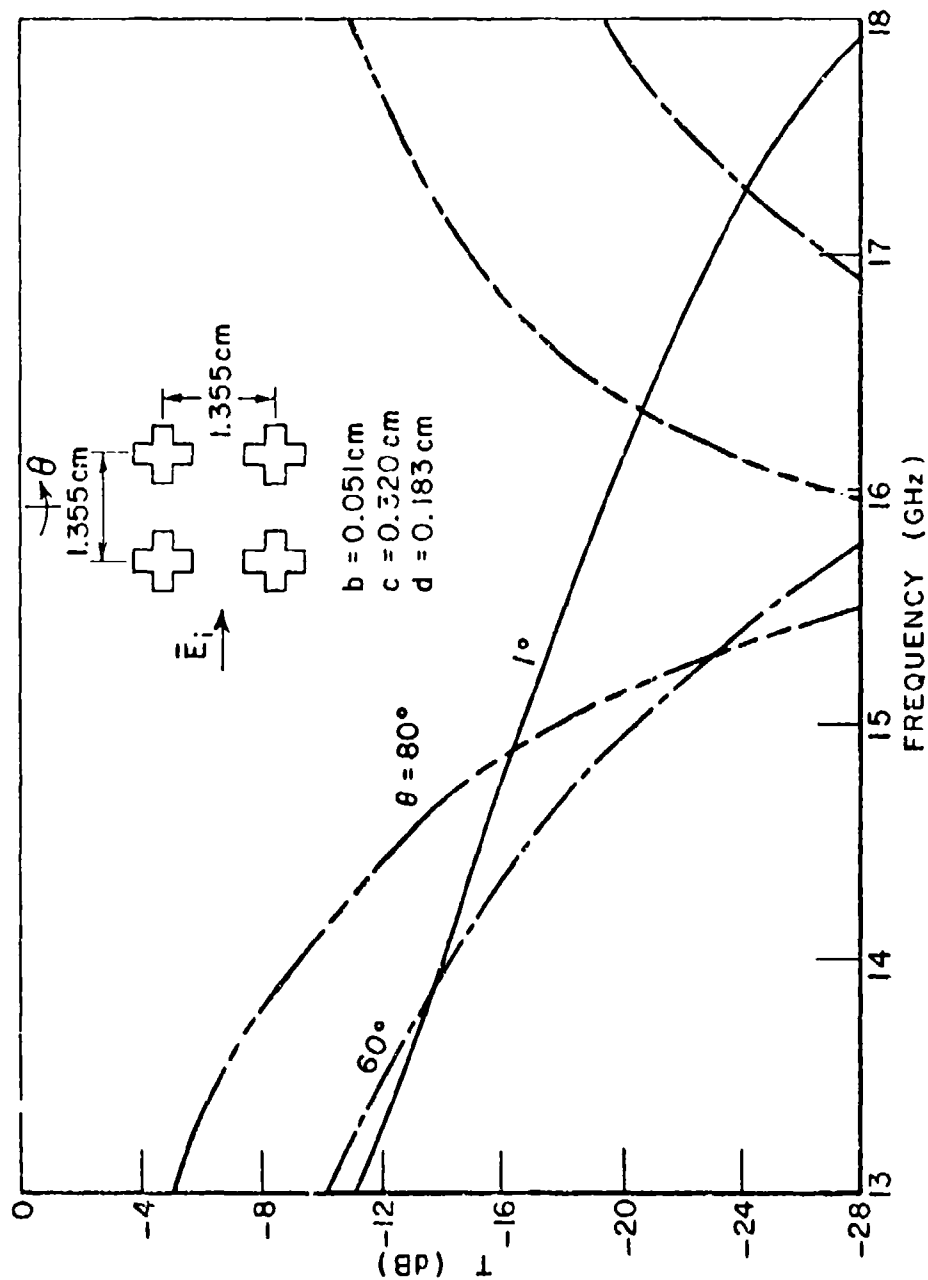


Figure 5-18.--Calculated transmission curves for the array of Fig. 5-16 but with the even ordered cosine modes omitted.

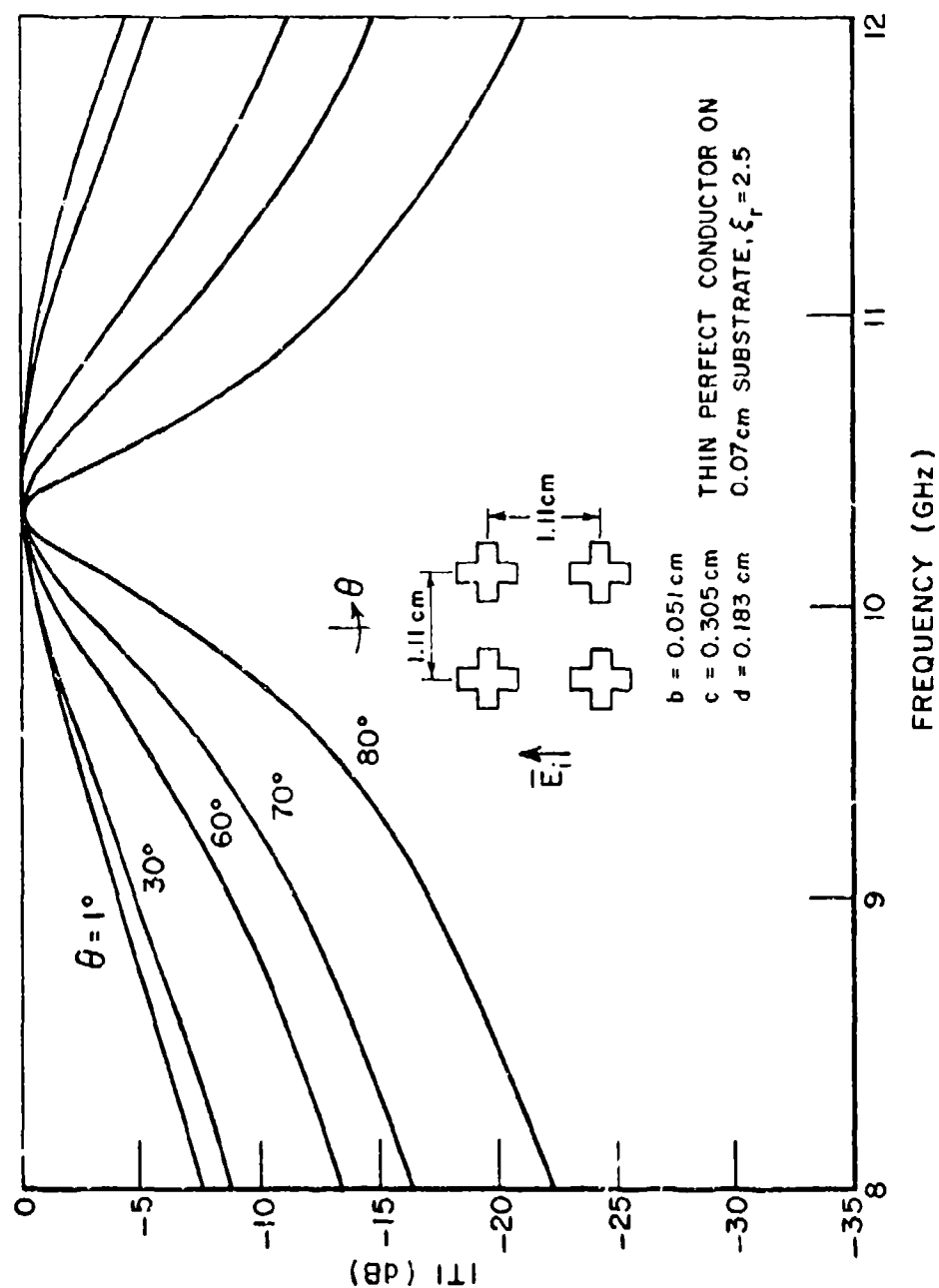


Figure 5-19.--Calculated transmission curves for an array of 4-legged symmetric slots on a thin dielectric substrate, H-plane incidence.

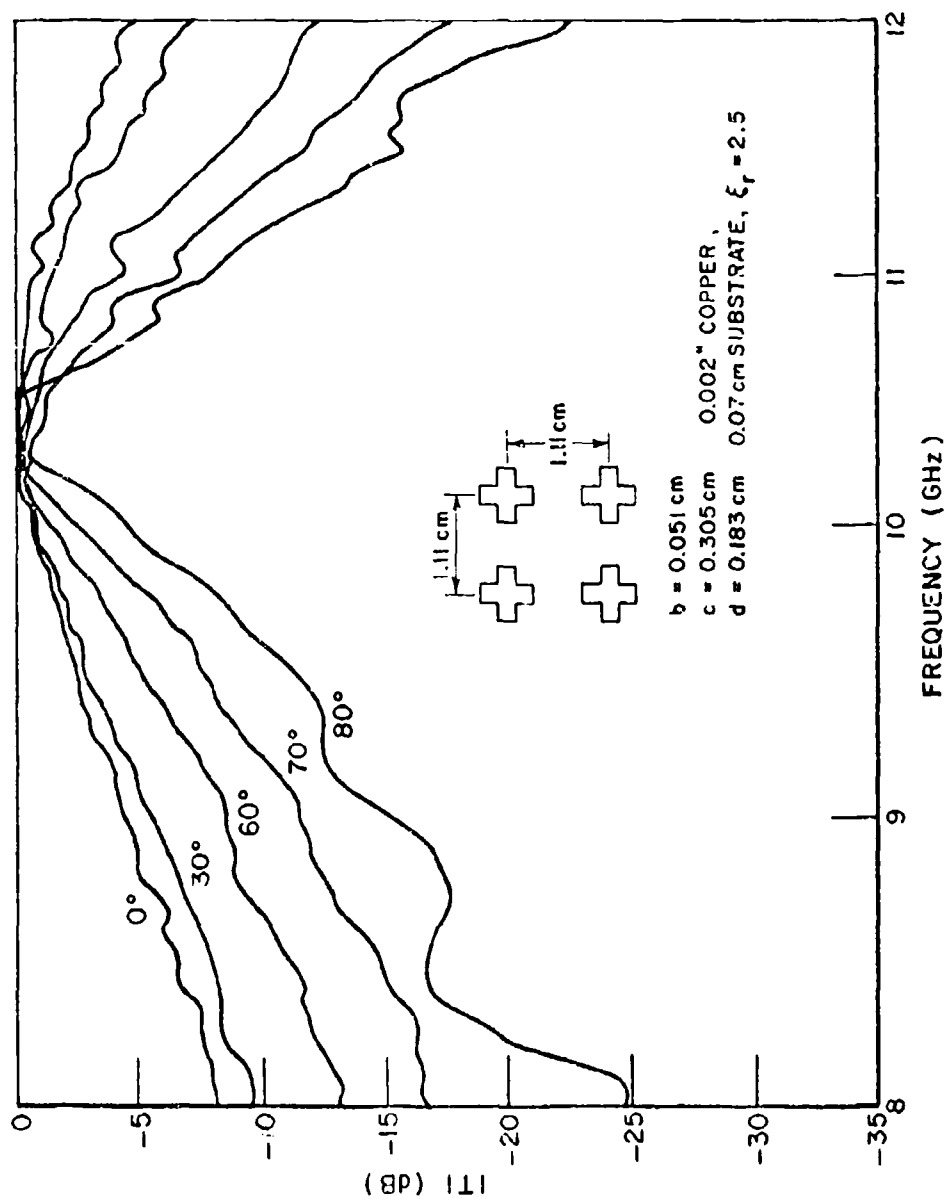


Figure 5-20.--Measured transmission curves corresponding to the calculated curves of Fig. 5-19.

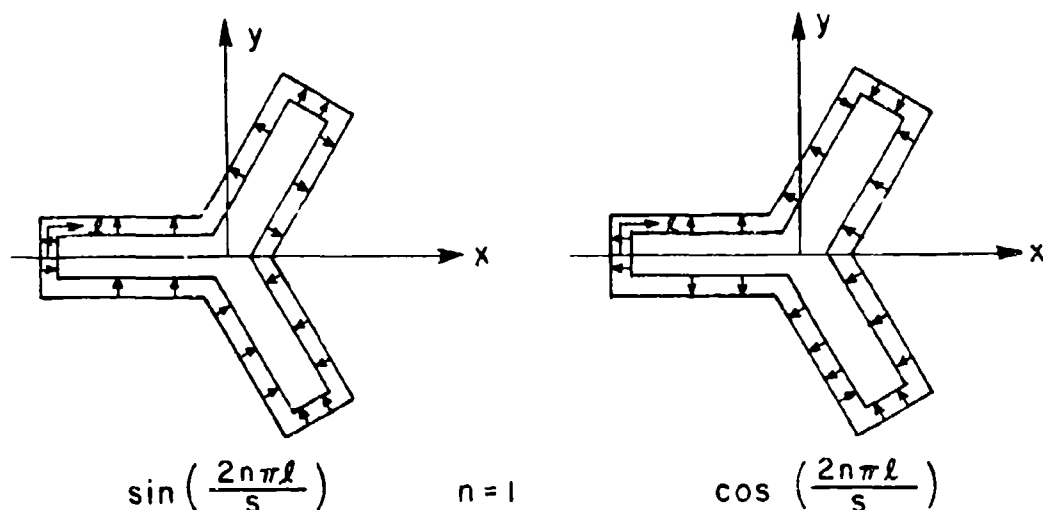


Figure 5-21.--Electric field polarities for the $n=1$ sine and cosine modes for the 3-legged symmetric loaded slot.

$r=1,2$) and 6 slot modes, the sine and cosine modes up to $n=3$. Relatively fewer Floquet modes are needed for convergence than for the previously considered 4-legged slot panels. The 3-legged slots are packed more tightly and thus the array has a smaller ratio of periodic cell size to slot size.

In Figs. 5-22 and 5-23 are calculated and measured transmission curves for a 3-legged slot array with polarization and incidence angle as shown in the inserts. (The dimensions b , c , and d are defined in Fig. 3-12.) The measured panel was chemically etched in .002" thick copper bonded to a 1/32" dielectric substrate with $\epsilon_r=2.5$. The measurements are taken from Pelton [2]. The electric field is x directed and the incidence angles are in the $\phi=90^\circ$ plane. The agreement between the calculated and measured curves is quite good. Figures 5-24 and 5-25 show calculated and measured curves for the same polarization but with the incidence angles in the $\phi=0^\circ$ plane. Again, the agreement is quite good.

For this polarization the $n=1$ cosine mode is the dominant slot mode (viz. Fig. 5-21). If we change to a y polarized incident plane wave the $n=1$ sine mode will be the dominant mode. Calculated transmission curves for this polarization with $\phi=0^\circ$ incidence angles are shown in Fig. 5-26, with the corresponding measured curves given in Fig. 5-27. The two sets of data agree quite well in general shape, but the calculated curves show a resonance frequency shift of approximately 0.4 GHz (when compared with Figs. 5-22 and 5-23) which is not

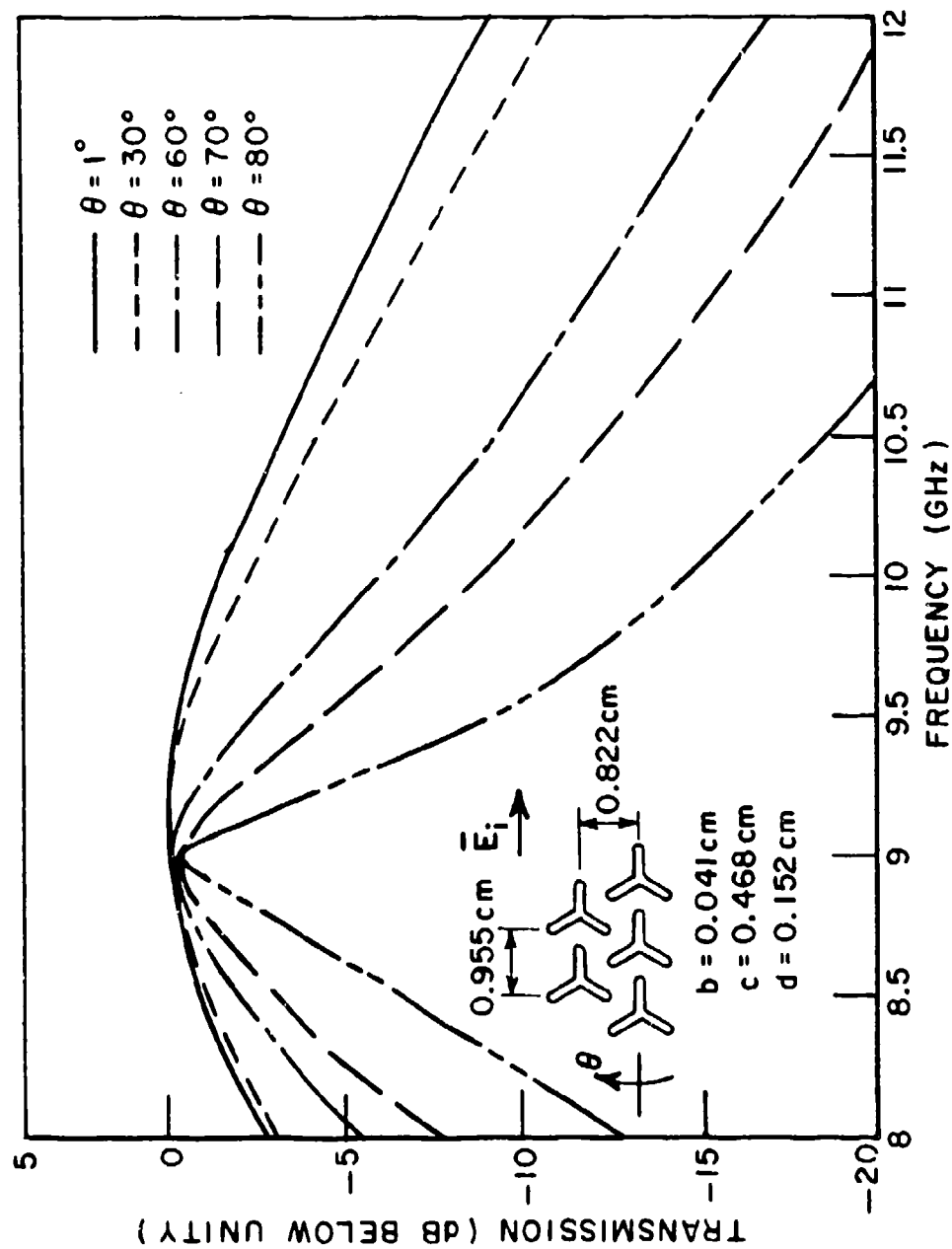


Figure 5-22.--Calculated transmission curves for an array of 3-legged symmetric slots on a thin dielectric substrate ($t_2=0.08 \text{ cm}$, $\epsilon_2=2.50\epsilon_0$; $t_1=0$), H-plane incidence ($\phi=90^\circ$).

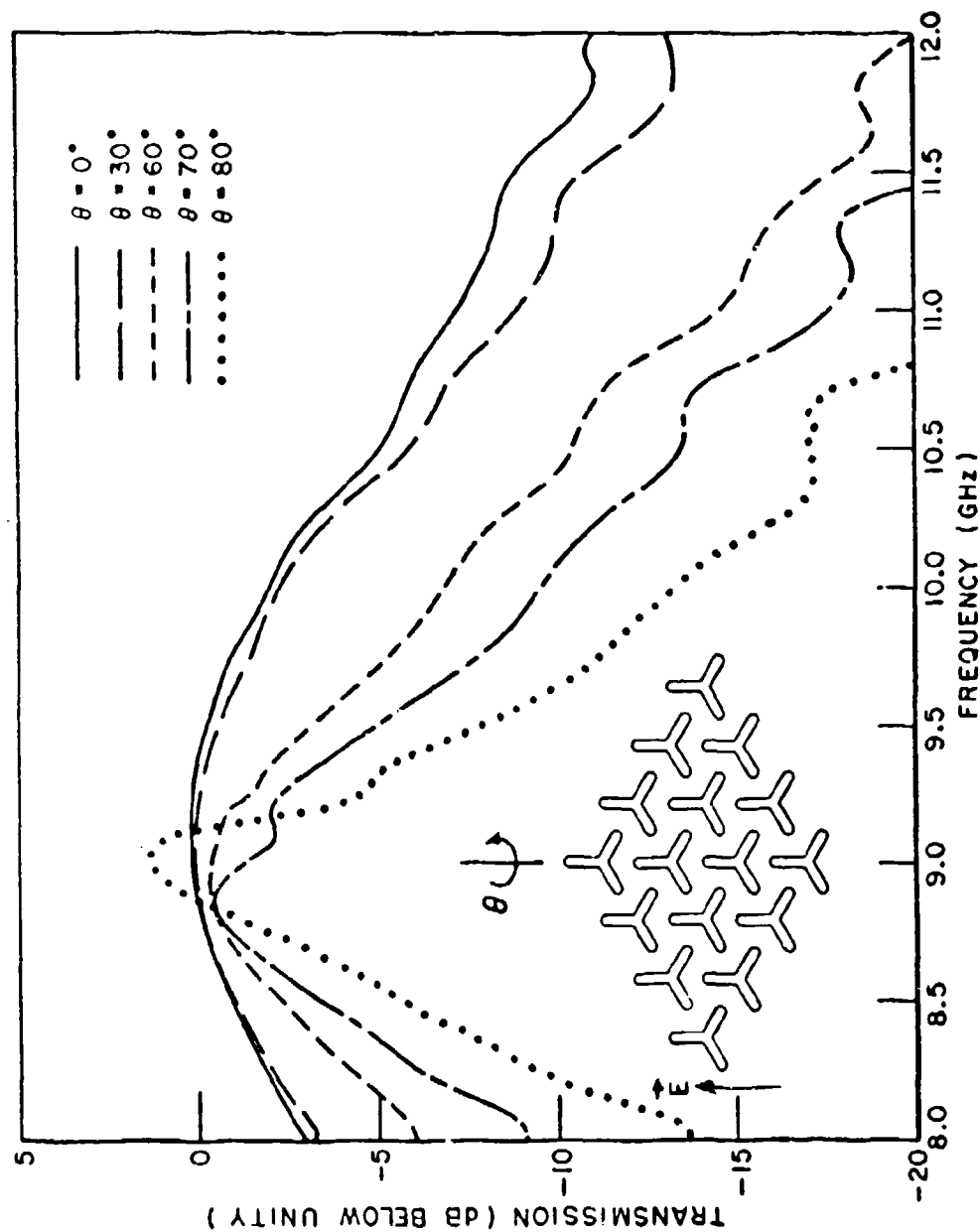


Figure 5-23.--Measured transmission curves corresponding to the calculated curves of Fig. 5-22.

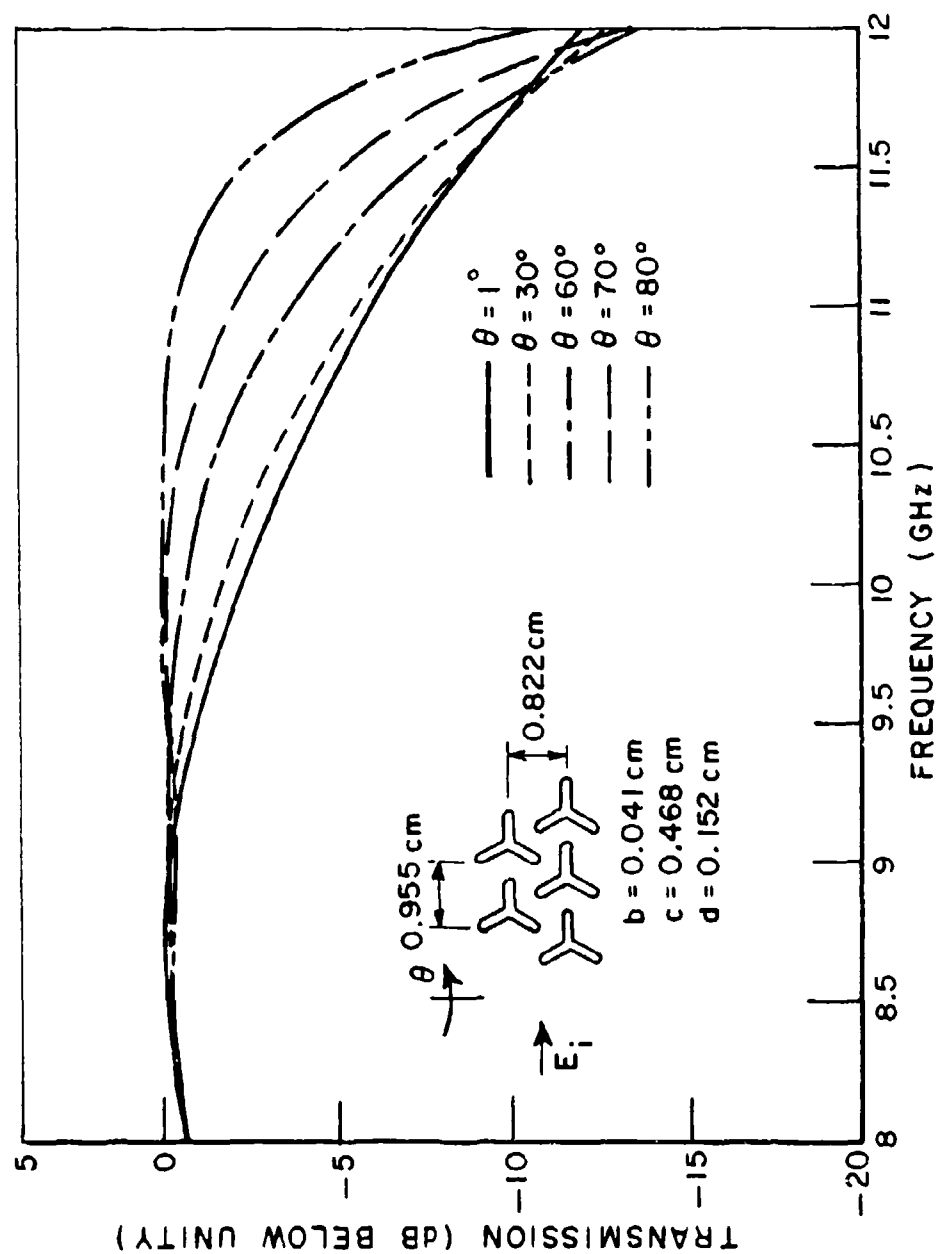


Figure 5-24. --Calculated transmission curves for an array of 3-legged symmetric slots on a thin dielectric substrate ($t_2=0.08$ cm, $\epsilon_2=2.5\epsilon_0$; $t_1=0$), E-plane incidence ($\phi=0^\circ$).

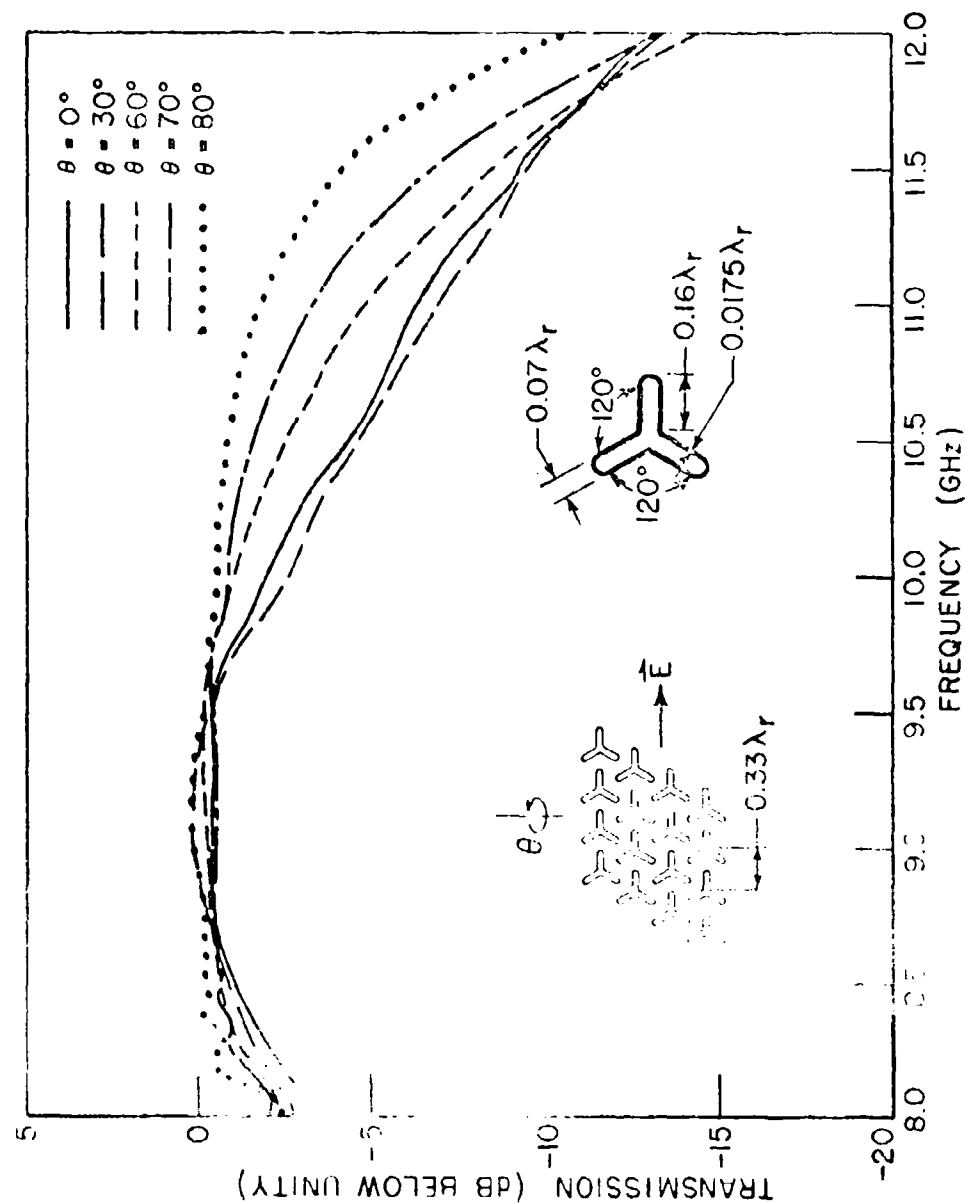


Figure 5-25.--Measured transmission curves corresponding to the calculated curves of Fig. 5-24.

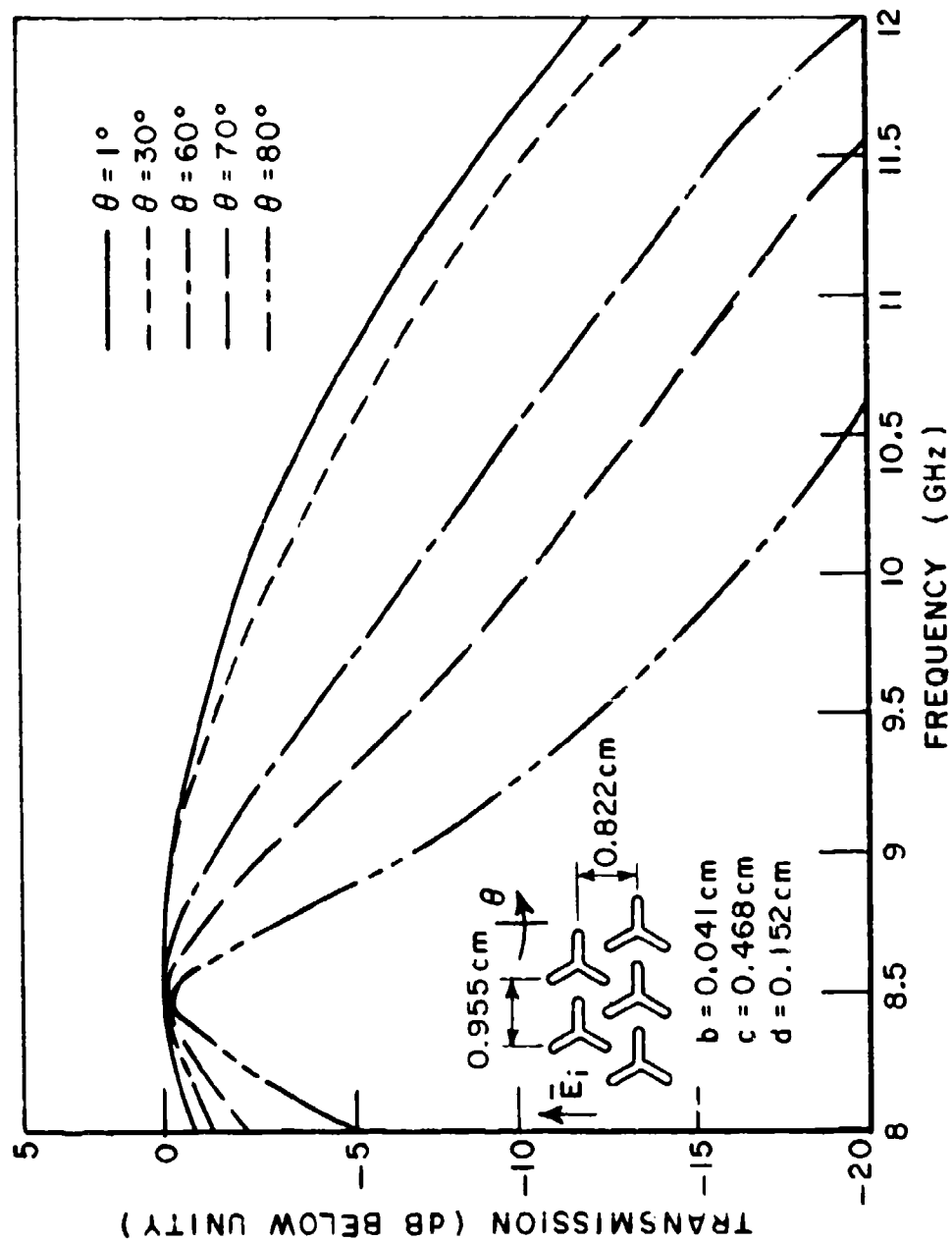


Figure 5-26.--Calculated transmission curves for an array of 3-legged symmetric slots on a thin dielectric substrate ($t_2=0.03 \text{ cm}$, $\epsilon_2=2.5\epsilon_0$; $t_1=0$), H-plane incidence ($\phi=0^\circ$).

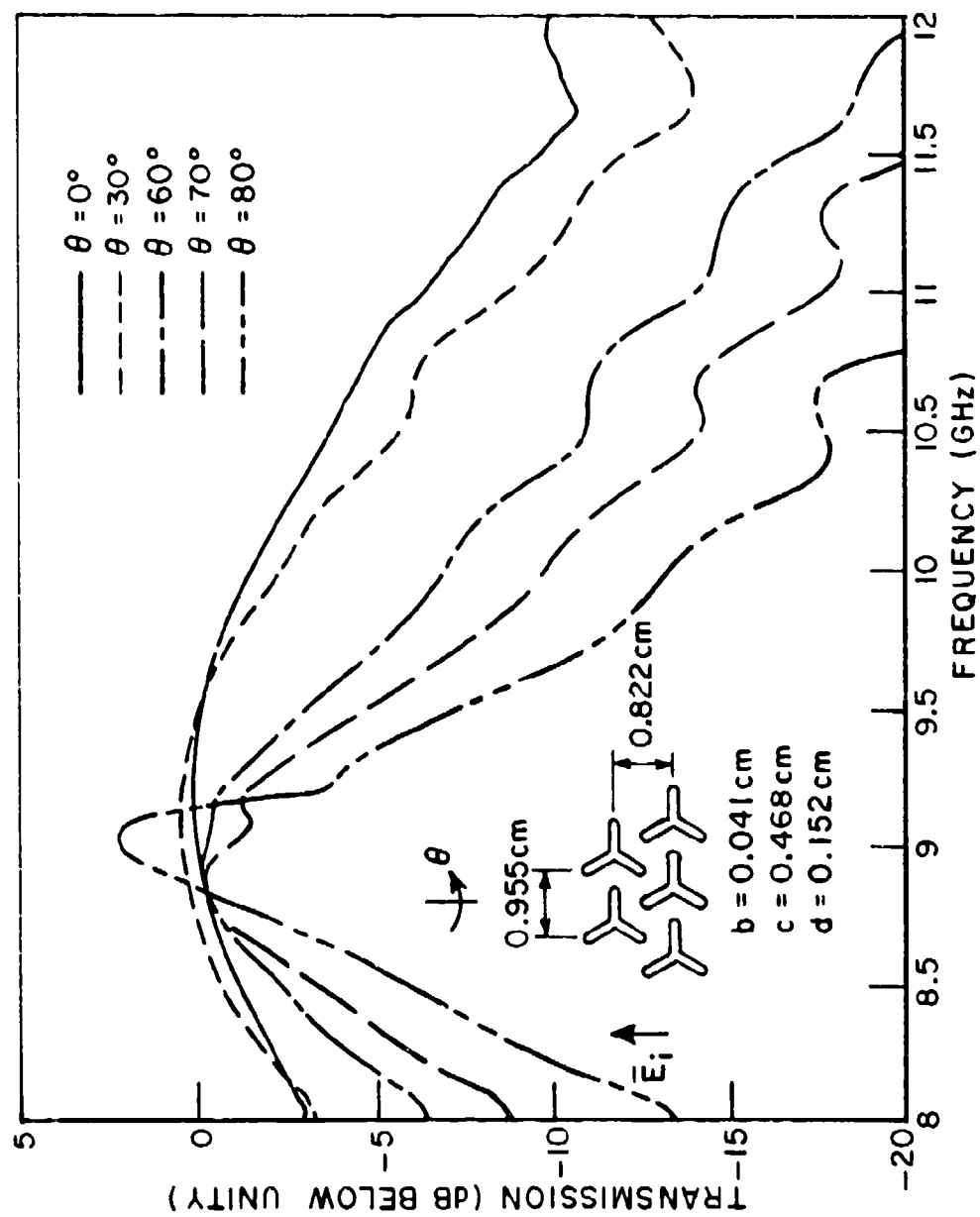


Figure 5-27.--Measured transmission curves corresponding to the calculated curves of Fig. 5-26.

confirmed by the measured data. This discrepancy may be due to numerical problems associated with changing the polarization of the E field. This change of polarity completely changes the field structure in the slot and in the periodic cell. Thus the equations to be solved and the resulting set of modal coefficients are entirely different for the two cases. Theoretically this should not matter, but practically speaking one of the slot field distributions may be more difficult to match with the truncated Floquet mode set than the other. One would not expect that the discrepancy is due to a fundamental shortcoming in the theory since such good agreement is obtained for the other polarization.

By making allowances for this resonant shift much additional useful information on transmission through 3-legged loaded slot arrays can be obtained using the modal solution. This would be especially true for the higher resonances, where the mutual impedance type solutions have not yet been applied successfully.

CHAPTER VI BIPLANAR SLOT ARRAYS

For many applications a two layer slot array may be more desirable than a single layer slot array since a wider passband and sharper skirts can be obtained. The geometry of the biplanar slot array is illustrated in Fig. 6-1. The structure is composed of two thin slot arrays of the type considered in the previous chapter which are parallel to one another and separated a perpendicular distance $2t_2+t_3$. The space between the two arrays is filled with dielectric layers with parameters μ_2, ϵ_2 and μ_3, ϵ_3 as shown. The two outer surfaces of the array are covered with a dielectric layer of thickness t_1 with parameters ϵ_1 and μ_1 . The possibility of improving the performance of biplanar slot arrays by coating them with dielectric was suggested by Munk [4]. The method of solution which we will employ requires that the structure be symmetric about the plane $z=-t_2-.5t_3$. Thus the two slotted panels and the outer dielectric layers must be identical.

We desire to obtain the plane wave transmission coefficient for this structure. To our knowledge this problem has not previously been solved using the modal analysis method. Munk et. al. have previously solved the biplanar problem illustrated using the mutual impedance method with the condition that $\epsilon_1=\epsilon_2=\epsilon_3=\epsilon_0$, and $\mu_1=\mu_2=\mu_3=\mu_0$, i.e., the two arrays are in free space [19,20]. The modal analysis solution presented here was the first to include the effects of the various dielectric layers. However, Munk has since modified the mutual impedance solution to include dielectric layers [5].

A. Derivation of Solution

The modal solution which we are about to derive for the biplanar array is a combination of the techniques used to obtain the solutions of the two previous chapters. Since the structure is thick, the technique of using symmetric and antisymmetric excitations, which simplified the solutions reached in Chapters II and IV for the thick structures, will again be used. Since the slotted panels themselves are thin, the field matching method and the expansion of the fields in the slots will be quite similar to those used in Chapter V for thin slot arrays.

The modal expansion for the region $z>0$ is the same as for the two previous configurations. Again, the Floquet modes of Chapter III are used. The direction of the incident plane wave is determined by θ and ϕ (see Fig. 3-1). Using the free space Floquet modes of Eqs. (3-12) to (3-15) the x and y components of the incident fields in the free space region ($z>t_1$) can be expressed as

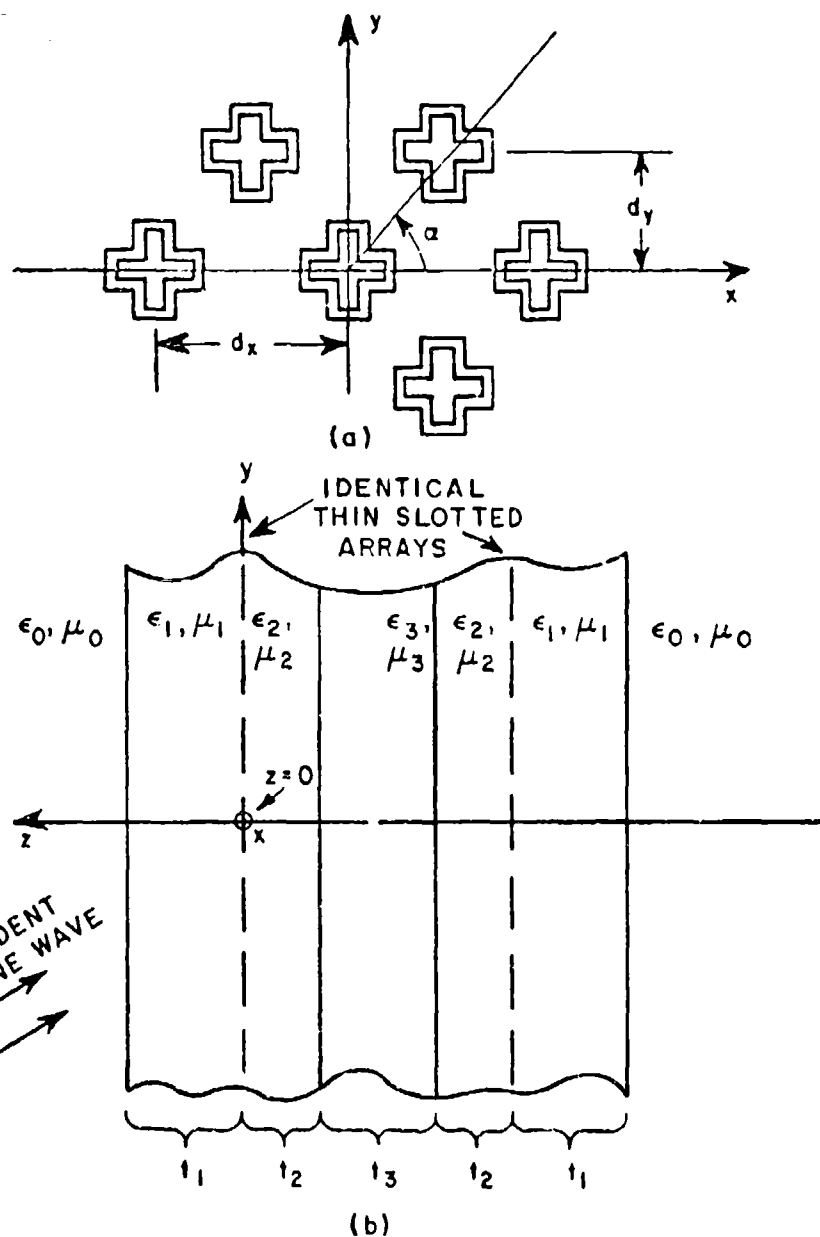


Figure 6-1.--Geometry and coordinates for a biplanar slot array:

- a) Typical geometry of one of the two thin slot arrays.
- b) Arrangement of the two slot arrays to form a biplanar slot array.

$$(6-1) \quad \vec{E}^i = \sum_{r=1}^2 A^r \vec{e}_{a1}^r$$

$$(6-2) \quad \vec{H}^i = \sum_{r=1}^2 A^r \vec{h}_{a1}^r$$

where the A_r are known coefficients which are determined by the direction and polarization of the incident plane wave. To express the fields at the front surface of the first panel (at $z=0^+$) we first define the quantities

$$(6-3) \quad a_1^{rd} = 2 A^r \frac{\eta_{00}^{r(1)}}{\eta_{00}^{r(1)} + \eta_{00}^r} \exp[-j(\gamma_{00}^{r(1)} - \gamma_{00})t_1]$$

$$(6-4) \quad DF^r = \frac{\eta_{00}^{r(1)} - \eta_{00}^r}{\eta_{00}^{r(1)} + \eta_{00}^r} \exp(-2j\gamma_{00}^{r(1)}t_1)$$

which are needed to account for the dielectric discontinuity at $z=t_1$. The superscript (1) denotes quantities which are evaluated in the dielectric region with parameters ϵ_1 and μ_1 . By applying the results of Chapter III expressed in Eqs. (3-32) through (3-35) and (3-43), the tangential fields at the front surface of the first slotted panel can be expressed as

$$(6-5) \quad \vec{E}|_{z=0^+} = \sum_{r=1}^2 [a_1^{rd} + \rho^r(1-DF^r)] \vec{e}_{a1}^{r(1)} + \sum_{r=1}^2 \sum_{i=2}^{\infty} a_i^r \vec{e}_{ai}^{r(1)}$$

$$(6-6) \quad \vec{H}|_{z=0^+} = \sum_{r=1}^2 [a_1^{rd} - \rho^r(1+DF^r)] \vec{h}_{a1}^{r(1)} - \sum_{r=1}^2 \sum_{i=2}^{\infty} a_i^r \vec{h}_{ai}^{r(1)} .$$

The ρ^r and a_i^r are unknown modal coefficients. The Floquet mode functions $\vec{e}_{a1}^{r(1)}$ and $\vec{h}_{a1}^{r(1)}$ are defined in Eqs. (3-49), (3-50), and are simply the free space Floquet mode functions modified so as to include the effects of the dielectric layer on their modal impedance.

We now desire to expand the tangential fields on the back side of the first panel, i.e., at $z=0^-$, in some orthogonal mode set. We can use the Floquet electric field mode functions \bar{e}_{ai}^r to expand the electric fields, since for $z=0$ they are not affected by the presence of the dielectric, (by Eq. (3-51), $\bar{e}_{ai}^{r(1)} = \bar{e}_{ai}^{r(2)} = \bar{e}_{ai}^{r(3)} = \bar{e}_{ai}^r$). The Floquet magnetic field mode functions at $z=0^-$ are then given by

$$(6-7) \quad \bar{h}_{ai}^{r(2)} = \frac{1}{Z_{pq}^{r(2)}} (\hat{z} \times \bar{e}_{ai}^{r(2)}) = \frac{1}{Z_{pq}^{r(2)}} \bar{\Phi}_{pq}^r$$

where we now have to determine the modal impedance $Z_{pq}^{r(2)}$. Equation (6-7) can be written only because we are using symmetric and anti-symmetric excitations in solving this problem. Otherwise, the mode coupling at the surface of the second panel would have to be taken into account, and Eq. (6-7) would be a matrix equation involving a scattering matrix. This scattering matrix S_{ij} would give the amplitude of a mode j reflected from the second panel due to a unit amplitude mode i striking the panel. As explained in Chapter IV, this scattering matrix can be diagonalized by using symmetric and antisymmetric excitation (see the discussion preceeding Eq. (4-9)). Rather than repeat this discussion, let us merely state that symmetric excitation produces an open circuit at the center of the structure (i.e., at $z=-t_2-0.5t_3$), while antisymmetric excitation produces a short circuit. Thus Eq. (6-7) can be written for symmetric and antisymmetric excitations since there will be no mode coupling at a short or open circuit.

The determination of the modal impedance $Z_{pq}^{r(2)}$ at $z=0^-$ is now quite straightforward. Consider the transmission line model shown in Fig. 6-2. The modal impedance Z_c at the center of the structure will be ∞ or 0 for symmetric or antisymmetric excitation, respectively. The modal impedance $Z_{pq}^{r(3)}$ at $z=-t_2$ will be given by

$$(6-8) \quad Z_{pq}^{r(3)} = \begin{cases} \eta_{pq}^{r(3)} \coth(j\gamma_{pq}^{r(3)} t_3/2), & Z_c = \infty \\ \eta_{pq}^{r(3)} \tanh(j\gamma_{pq}^{r(3)} t_3/2), & Z_c = 0 \end{cases}$$

where $\gamma_{pq}^{r(3)}$ and $\eta_{pq}^{r(3)}$ are the propagation constant and modal impedance of the pq th mode evaluated with parameters ϵ_3, μ_3 (see Chapter III).

The desired modal impedance at $z=0^-$, $Z_{pq}^{r(2)}$, is now given by

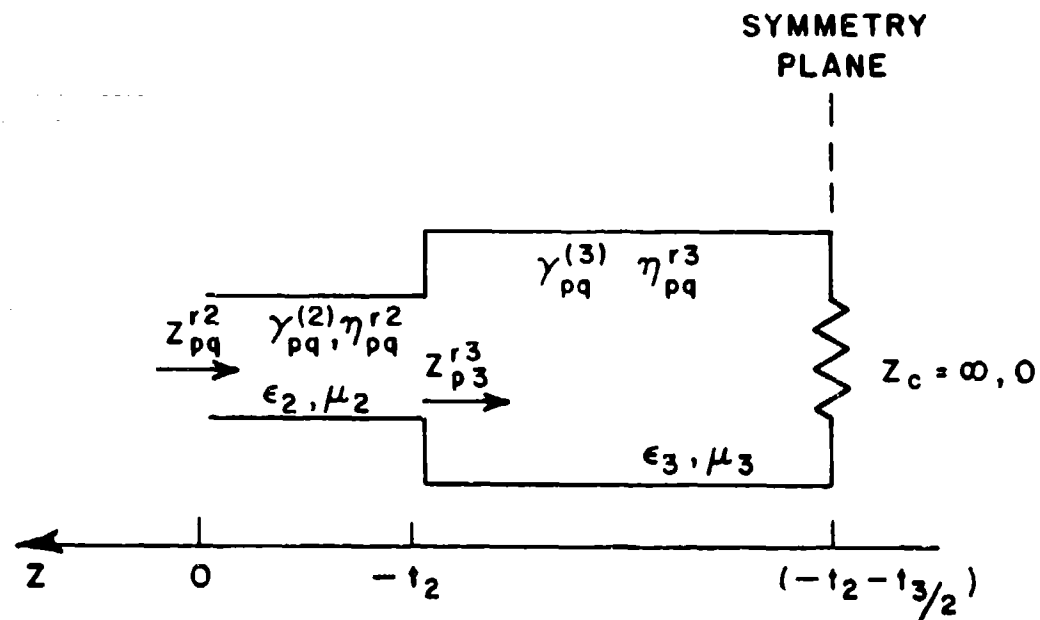


Figure 6-2.--Transmission line model of the dielectric layers between the two slotted panels used to determine the modal impedance $Z_{pq}^{r(2)}$ at the $z=0^-$ surface of the front panel.

$$(6-9) \quad Z_{pq}^{r(2)} = \eta_{pq}^{r(2)} \cdot \frac{Z_{pq}^{r(3)} + \eta_{pq}^{r(2)} \tanh(j\gamma_{pq}^{r(2)} t_2)}{\eta_{pq}^{r(2)} + Z_{pq}^{r(3)} \tanh(j\gamma_{pq}^{r(2)} t_2)}.$$

Note that if $t_2=0$, $Z_{pq}^{r(2)} = Z_{pq}^{r(3)}$.

We now expand the fields at $z=0^-$ as follows:

$$(6-10) \quad E|_{z=0^-} = \sum_{r=1}^2 \sum_{i=1}^{\infty} B_i^r \bar{e}_{ai}^{r(2)}$$

$$(6-11) \quad H|_{z=0^-} = \sum_{r=1}^2 \sum_{i=1}^{\infty} B_i^r \bar{h}_{ai}^{r(2)}.$$

The B_i^r are unknown modal coefficients.

We can now proceed to solve for the unknown modal coefficients by applying the boundary conditions. Tangential E must be continuous in the slot aperture and zero on the ground plane. Thus we can equate Eqs. (6-5) and (6-10) and obtain

$$(6-12) \quad \sum_{r=1}^2 [a_1^{rd} + \rho^r(1-DF^r)] \bar{e}_{a1}^{r(1)} + \sum_{r=1}^2 \sum_{i=2}^{\infty} a_i^r \bar{e}_{ai}^{r(1)} \\ = \sum_{r=1}^2 \sum_{i=1}^{\infty} B_i^r \bar{e}_{ai}^{r(2)} = \begin{cases} \bar{E}_t & \text{in slot} \\ 0 & \text{elsewhere} \end{cases}$$

where \bar{E}_t is the unknown tangential electric field in the slot aperture. To simplify Eq. (6-12) we take the cross product with $\bar{h}_{a1}^{r(2)*}$, dot the result with \hat{z} , integrate over a unit cell, and apply the orthogonality relation of Eq. (3-22), obtaining

$$(6-13) \quad [a_1^{rd} + \rho^r(1-DF^r)] \int_a \bar{e}_{a1}^{r(1)} \times \bar{h}_{a1}^{r(2)*} \cdot \hat{z} ds \\ = B_1^r \int_a \bar{e}_{a1}^{r(2)} \times \bar{h}_{a1}^{r(2)*} \cdot \hat{z} ds = \int_b \bar{E}_t \times \bar{h}_{a1}^{r(2)*} \cdot \hat{z} ds$$

where $\int_a ds$ denotes an integration over one unit cell and $\int_b ds$ denotes an integration over one slot aperture. Since $\bar{e}_{ai}^{r(1)} = \bar{e}_{ai}^{r(2)}$, Eq. (6-13) can be reduced to

$$(6-14) \quad a_1^{rd} + \rho^r(1-DF^r) = B_1^r = \int_b \bar{E}_t \times \bar{h}_{a1}^{r(2)*} \cdot \hat{z} ds / \int_a \bar{e}_{a1}^{r(2)} \times \bar{h}_{a1}^{r(2)*} \cdot \hat{z} ds.$$

If we now multiply Eq. (6-12) by $\bar{h}_{ai}^{r(2)*}$, dot the result with \hat{z} , and integrate over a unit cell, we obtain

$$(6-15) \quad a_i^r \int_a \bar{e}_{ai}^{r(1)} \times \bar{h}_{ai}^{r(2)*} \cdot \hat{z} ds = B_i^r \int_a \bar{e}_{ai}^{r(2)} \times \bar{h}_{ai}^{r(2)*} \cdot \hat{z} ds \\ = \int_b \bar{E}_t \times \bar{h}_{ai}^{r(2)*} \cdot \hat{z} ds, \quad i \neq 1$$

or, simplifying,

$$(6-16) \quad a_i^r = B_i^r = \int_b E_t x \bar{h}_{ai}^{r(2)*} \cdot \hat{z} ds / \int_a \bar{e}_{ai}^{r(2)} x \bar{h}_{ai}^{r(2)*} \cdot \hat{z} ds \quad i \neq 1.$$

The other boundary condition which we must enforce is continuity of the tangential magnetic field across the slot aperture. We thus equate Eq. (6-6) and (6-11), so that in the slot aperture

$$(6-17) \quad \sum_{r=1}^2 [a_1^{rd} - \rho^r (1 + DF^r)] \bar{h}_{a1}^{r(1)} - \sum_{r=1}^2 \sum_{i=2}^{\infty} a_i^r \bar{h}_{ai}^{r(1)} = \sum_{r=1}^2 \sum_{i=1}^{\infty} B_i^r \bar{h}_{ai}^{r(2)}.$$

If we now substitute for a_i^r and B_i^r from Eq. (6-16), Eq. (6-17) is reduced to

$$(6-18) \quad \sum_{r=1}^2 [a_1^{rd} - \rho^r (1 + DF^r)] \bar{h}_{a1}^{r(1)} - \sum_{r=1}^2 \sum_{i=2}^{\infty} \bar{h}_{ai}^{r(1)} \cdot \int_b E_t x \bar{h}_{ai}^{r(2)*} \cdot \hat{z} ds / \int_a \bar{e}_{ai}^{r(2)} x \bar{h}_{ai}^{r(2)*} \cdot \hat{z} ds \\ = \sum_{r=1}^2 B_1^r \bar{h}_{a1}^{r(2)} + \sum_{r=1}^2 \sum_{i=2}^{\infty} \bar{h}_{ai}^{r(2)} \cdot \int_b E_t x \bar{h}_{ai}^{r(2)*} \cdot \hat{z} ds / \int_a \bar{e}_{ai}^{r(2)} x \bar{h}_{ai}^{r(2)*} \cdot \hat{z} ds.$$

From Eq. (6-14) we readily obtain

$$(6-19) \quad \rho^r = - \frac{a_1^{rd}}{1 - DF^r} + \frac{1}{1 - DF^r} \cdot \int_b E_t x \bar{h}_{a1}^{r(2)*} \cdot \hat{z} ds / \int_a \bar{e}_{a1}^{r(2)} x \bar{h}_{a1}^{r(2)*} \cdot \hat{z} ds.$$

Substituting for B_1^r from Eq. (6-14) and for ρ^r from Eq. (6-19), Eq. (6-18) can be written, with some minor simplification, as

$$(6-20) \quad \sum_{r=1}^2 a_1^{rd} \bar{h}_{a1}^{r(1)} \left[1 + \frac{1+DF^r}{1-DF^r} \right] = \sum_{r=1}^2 \left[\frac{1+DF^r}{1-DF^r} \bar{h}_{a1}^{r(1)} + \bar{h}_{a1}^{r(2)} \right].$$

$$\int_b \bar{E}_t x \bar{h}_{a1}^{r(2)*} \cdot \hat{z} ds / \int_a \bar{e}_{a1}^{r(2)} x \bar{h}_{a1}^{r(2)*} \cdot \hat{z} ds + \sum_{r=1}^2 \sum_{i=2}^{\infty} [\bar{h}_{ai}^{r(1)} + \bar{h}_{ai}^{r(2)}].$$

$$\int_b \bar{E}_t x \bar{h}_{ai}^{r(2)*} \cdot \hat{z} ds / \int_a \bar{e}_{ai}^{r(2)} x \bar{h}_{ai}^{r(2)*} \cdot \hat{z} ds.$$

In order to further simplify Eq. (6-20) we shall evaluate the integral

$$\int_a \bar{e}_{ai}^{r(2)} x \bar{h}_{ai}^{r(2)*} \cdot \hat{z} ds$$

at the surface of the front panel ($z=0$). From Eqs. (3-12) to (3-15), (3-18), (3-19), (3-51) and (6-7), we can write

$$(6-21) \quad \int_a \bar{e}_{ai}^{r(2)} x \bar{h}_{ai}^{r(2)*} \cdot \hat{z} ds = \frac{1}{z_{pq}^{r(2)*}} \cdot \frac{1}{\sqrt{d_x d_y}} \int_a \left(\frac{U_p^2 + V_{pq}^2}{T_{pq}^2} \right) \exp(-j(U_p x + V_{pq} y)) \exp(+j(U_p x + V_{pq} y)) ds$$

$$= \frac{1}{z_{pq}^{r(2)*}}$$

since the area of the central periodic cell is equal to $d_x d_y$ (see Fig. 3-2). By using the results of Eq. (6-21), and by introducing the $\bar{\phi}_{pq}^r$ function of Eqs. (3-50) and (6-7), Eq. (6-20) can be written as

$$(6-22) \quad \sum_{r=1}^2 a_1^{rd} \cdot \frac{2}{1-DF^r} \frac{1}{n_{oo}^{r(1)}} \bar{\phi}_{oo}^r = \sum_{r=1}^2 \left[\frac{1+DF^r}{1-DF^r} \cdot \frac{1}{n_{oo}^{r(1)}} + \frac{1}{z_{oo}^{r(2)}} \right] \bar{\phi}_{oo}^r$$

$$\cdot \int_b \bar{E}_t x \bar{\phi}_{oo}^{r*} \cdot \hat{z} ds + \sum_{r=1}^2 \sum_{i=2}^{\infty} \left[\frac{1}{z_{pq}^{r(1)}} + \frac{1}{z_{pq}^{r(2)}} \right] \bar{\phi}_{pq}^r \cdot \int_b \bar{E}_t x \bar{\phi}_{pq}^{r*} \cdot \hat{z} ds.$$

All of the quantities in Eq. (6-22) are known quantities with the exception of \bar{E}_t , the transverse field in the slot aperture. Using the modes presented in Chapter III to describe the aperture fields in the various slots, we can express \bar{E}_t approximately as

$$(6-23) \quad \bar{E}_t = \sum_{j=1}^N C_j \bar{e}_{bj}$$

where our modal summation is truncated at N terms. We now proceed to apply the method of moments to obtain the unknown aperture field \bar{E}_t . Using Galerkin's method, we substitute the expression of Eq. (6-23) for the aperture field \bar{E}_t in Eq. (6-22), and simultaneously multiply by \bar{e}_{bn} , obtaining

$$(6-24) \quad \sum_{r=1}^2 a_1^{rd} \frac{2}{1-DF^r} \frac{1}{n_{oo}^{r(1)}} \int_b \bar{e}_{bn} x_{\bar{\Phi}}^{r_{oo}} \cdot \hat{z} ds =$$

$$\sum_{r=1}^2 \left[\frac{1+DF^r}{1-DF^r} \frac{1}{n_{oo}^{r(1)}} + \frac{1}{z_{oo}^{r(2)}} \right] \int_b \bar{e}_{bn} x_{\bar{\Phi}}^{r_{oo}} \cdot \hat{z} ds \cdot \sum_{j=1}^N C_j \int_b \bar{e}_{bj} x_{\bar{\Phi}}^{r_{oo}} \cdot \hat{z} ds$$

$$+ \sum_{r=1}^2 \sum_{i=2}^M \left[\frac{1}{z_{pq}^{r(1)}} + \frac{1}{z_{pq}^{r(2)}} \right] \int_b \bar{e}_{bn} x_{\bar{\Phi}}^{r_{pq}} \cdot \hat{z} ds \cdot \sum_{j=1}^N C_j \int_b \bar{e}_{bj} x_{\bar{\Phi}}^{r_{pq}} \cdot \hat{z} ds.$$

Since n can range from 1 to N , Eq. (6-24) is actually N equations, with the N unknowns being the C_j modal coefficients. The Floquet mode set has been truncated at $2M$ terms to allow a computer solution. Normally N will be quite small, i.e., less than 10, while M will be quite large, 121 being a typical number. But note that even with M being quite large, only an $N \times N$ system of equations needs to be solved.

The system of equations given by Eq. (6-24) must be solved twice, once for symmetric excitation and once for antisymmetric excitation. If we denote the resulting modal coefficients as C_j^s for symmetric excitation and C_j^a for antisymmetric excitation, then from Eqs. (6-7), (6-19), (6-21), and (6-23), and the properties of symmetric and antisymmetric excitations, we have

$$(6-25) \quad \rho^r = \frac{1}{1-DF^r} \sum_{j=1}^N \left(\frac{C_j^s + C_j^a}{2} \right) \int_b \bar{e}_{bj} x_{\bar{\Phi}}^{r_{oo}} \cdot \hat{z} ds - \frac{a_1^{rd}}{1-DF^r}$$

The free space modal reflection coefficients R^r are then determined by Eq. (3-44).

We can find the free space modal transmission coefficients T^r by a similar process. Let b_j^r be given by

$$(6-26) \quad b_j^r = \sum_{j=1}^N \left(\frac{C_j^s - C_j^a}{2} \right) \int_b \bar{e}_{bj} \times \bar{\phi}_{00}^r \cdot \hat{z} ds.$$

Equation (3-66) cannot be applied directly since the biplanar structure has a finite thickness. However, if we multiply Eq. (3-66) by the factor $-\exp(j\gamma_{00}(2t_2+t_3))$ which corrects for the phase delay caused by the finite thickness of the biplanar slot array and for the change in propagation direction which takes place when the symmetric and antisymmetric excitations are subtracted, we obtain for the modal transmission coefficients T^r

$$(6-27) \quad T^r = -b_1^r \exp(+j\gamma_{00}(2t_2+t_3)) \frac{\exp[-j(\gamma_{00}^{(1)} - \gamma_{00})t_1] \frac{1+j\tan(\gamma_{00}^{(1)}t_1)}{r^{(1)}}}{1+j\frac{n_{00}}{r^{(1)}}\tan(\gamma_{00}^{(1)}t_1)}.$$

The reflected and transmitted fields are now given by Eqs. (6-1) and (6-2) with R^r ($-R^r$ for reflected H field) or T^r substituted for A^r .

The calculated results presented in the remaining sections of this chapter were obtained from a Fortran IV computer coding of the above solution. The $\int_b \bar{e}_{bj} \times \bar{\phi}_{pq}^r \cdot \hat{z} ds$ integrals can be evaluated in closed form for the slot shapes considered in this chapter. The results are given in Appendix B. The coefficient matrix is not Hermitian. However, the factor $\int_b \bar{e}_{bn} \times \bar{\phi}_{pq}^r \cdot \hat{z} ds \cdot \int_b \bar{e}_{bj} \times \bar{\phi}_{pq}^r \cdot \hat{z} ds$, because of its symmetry in j and n , need only be evaluated over the upper triangular portion of the matrix, with its conjugate value being used in the lower triangular portion. This symmetry results in a considerable time saving, since for this solution much more time is required to evaluate the coefficient matrix than to solve the resulting system of equations. This is because the ratio of M to N required for convergence is usually quite high for the geometries we are considering. The computed curves were checked for convergence. Results for various biplanar geometries, both with and without dielectric layers, will be presented in the remaining sections of this chapter.

B. Biplanar Arrays Without Dielectric Layers

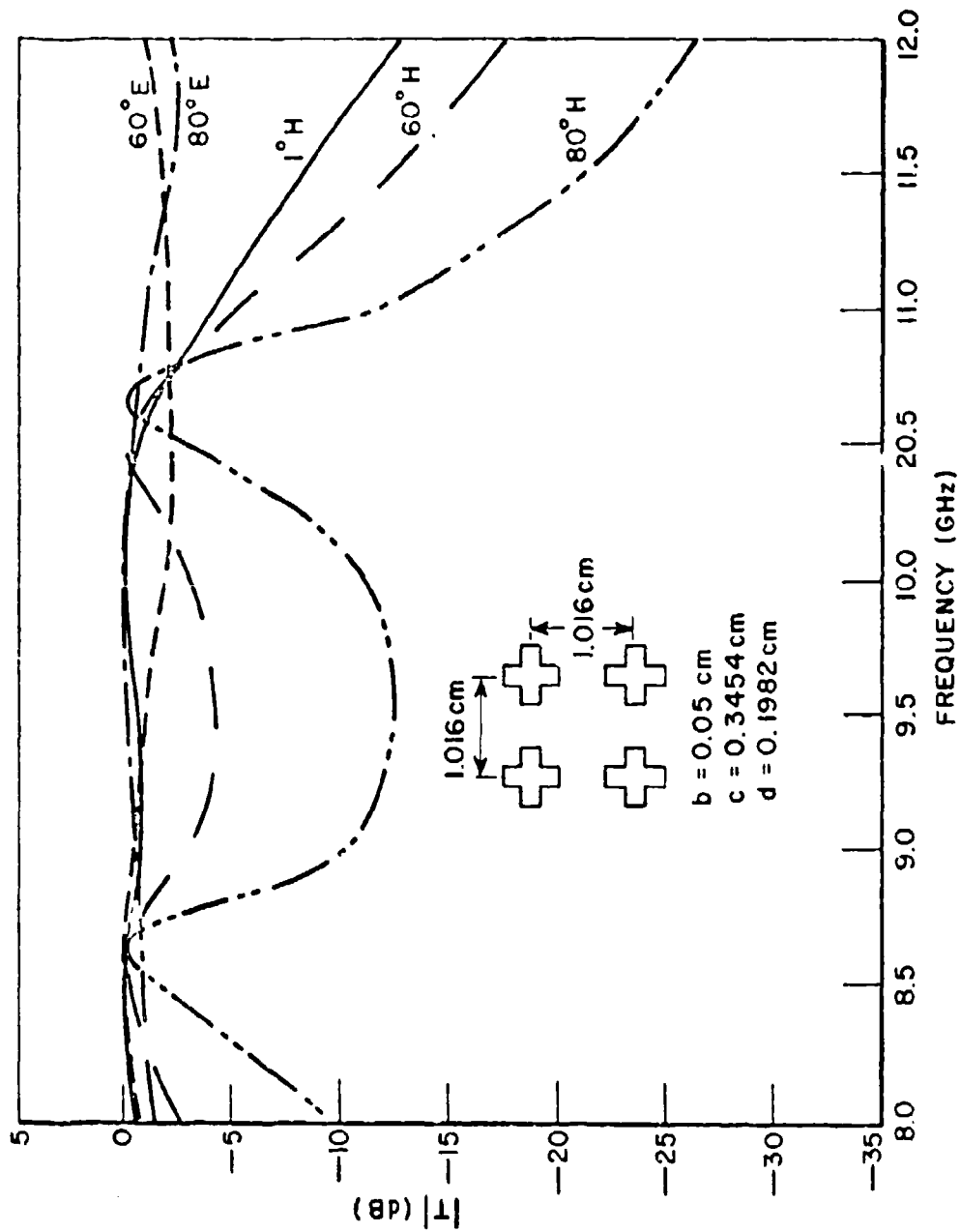
Before becoming involved in the complex behavior obtained from biplanar slot arrays filled and/or covered with dielectric layers, we shall present some calculated curves for two biplanar arrays which have only a thin dielectric substrate. The results obtained are confirmed by measured data obtained from Reference [19]. Convergence was obtained for the calculations presented in this section with 98 Floquet modes ($p_{\max}=q_{\max}=3$) and the first 5 sine modes for the 4-legged slot.

In Fig. 6-3 calculated transmission coefficient curves for a biplanar array with a panel separation of 0.43 cm ($\sim .13\lambda$ at resonance) are shown. The thin dielectric substrate is required for mechanical support. Electrically it is quite thin, with its main effect being a slight lowering of the resonance frequency of the slot array. For this spacing the near field coupling is quite strong, with the most prominent effect of this coupling being the deep dip in the resonance region for 60 and 80° H-plane scan ($\phi=0^\circ$; $\theta=60^\circ, 80^\circ$). The corresponding measured curves are shown in Fig. 6-4. The agreement is quite good.

If we increase the spacing between the two arrays to .83 cm ($\sim .25\lambda$ at resonance) the near field coupling will decrease, which should produce a corresponding decrease in the depth of the resonance region transmission coefficient dip for H-plane incidence angles. That this is indeed the case is confirmed by the calculated transmission coefficient curves of Fig. 6-5. The corresponding measured curves are given in Fig. 6-6. Again the agreement is quite good.

While these two biplanar configurations might be quite useful for certain applications, they have some shortcomings. One is the resonance region dip for high H-plane incidence angles. Now this dip could be lessened by moving the panels further apart, but there are reasons for not separating the panels much more than about 0.5λ . One reason is the appearance of unwanted resonances which can cause transmission losses in the passband. Another is the desirability of keeping the electrical spacing between screens ($2\gamma_{00}^{(2)}t_2 + \gamma_{00}^{(3)}t_3$) approximately $\pi/2$. This electrical spacing is proportional to the cosine of the incidence angle, and for wide spacings changes very rapidly with incidence angle. For further discussion of these points see Reference [19].

Another shortcoming is the change of the bandpass bandwidth with incidence angle. For many applications this is a very undesirable feature, but one which seems to be unavoidable in biplanar resonant surfaces which are not covered with dielectric.



6-3.--Calculated transmission curves for a biplanar array of 4-legged symmetric loaded slots. The two panels are separated 0.13λ at resonance ($t_1=0.079$ cm, $\epsilon_1=2.56\epsilon_0$; $t_2=0$; $t_3=0.43$, $\epsilon_3=\epsilon_0$).

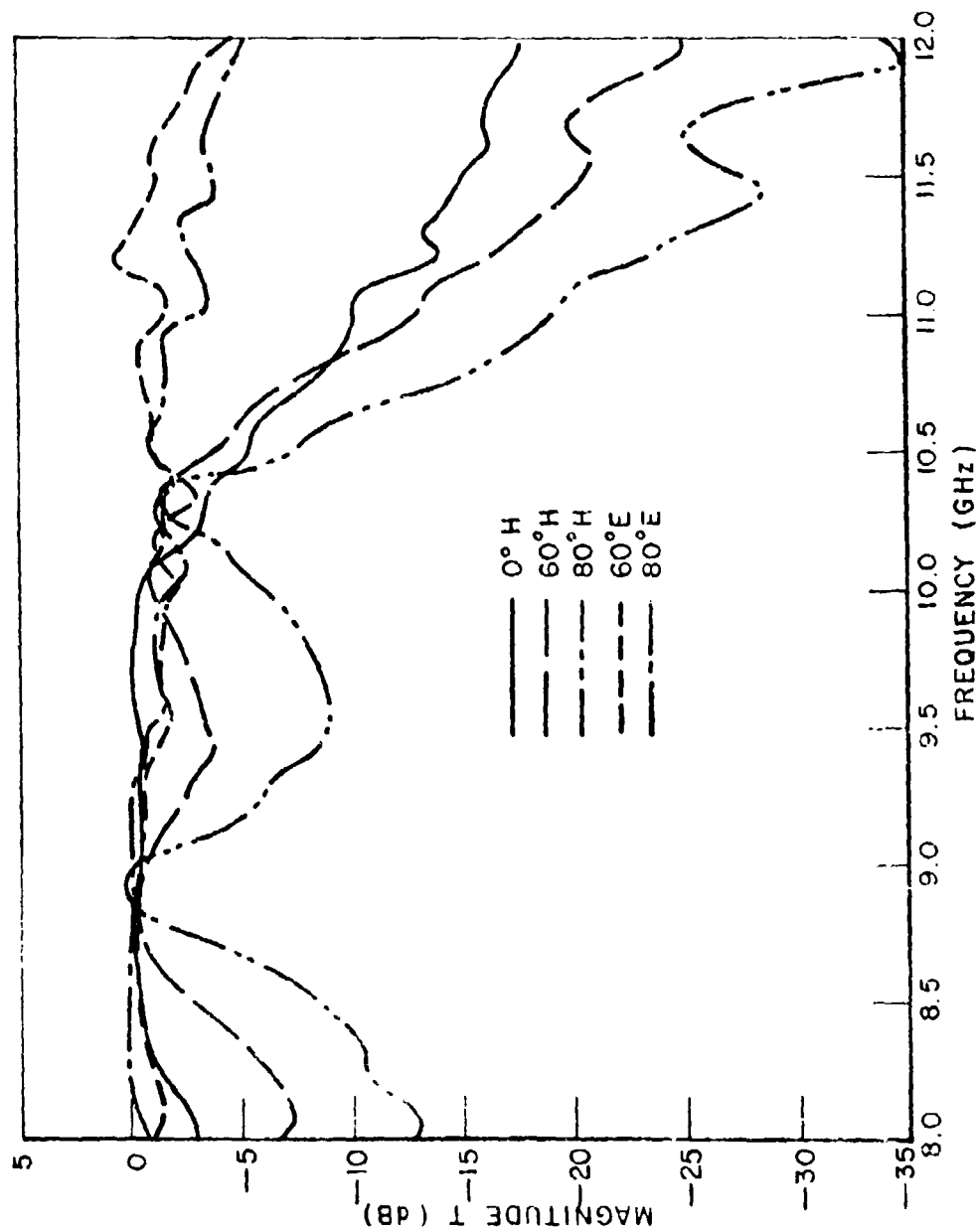


Figure 3-4.--Measured transmission curves corresponding to the calculated curves of Fig. 6-3.

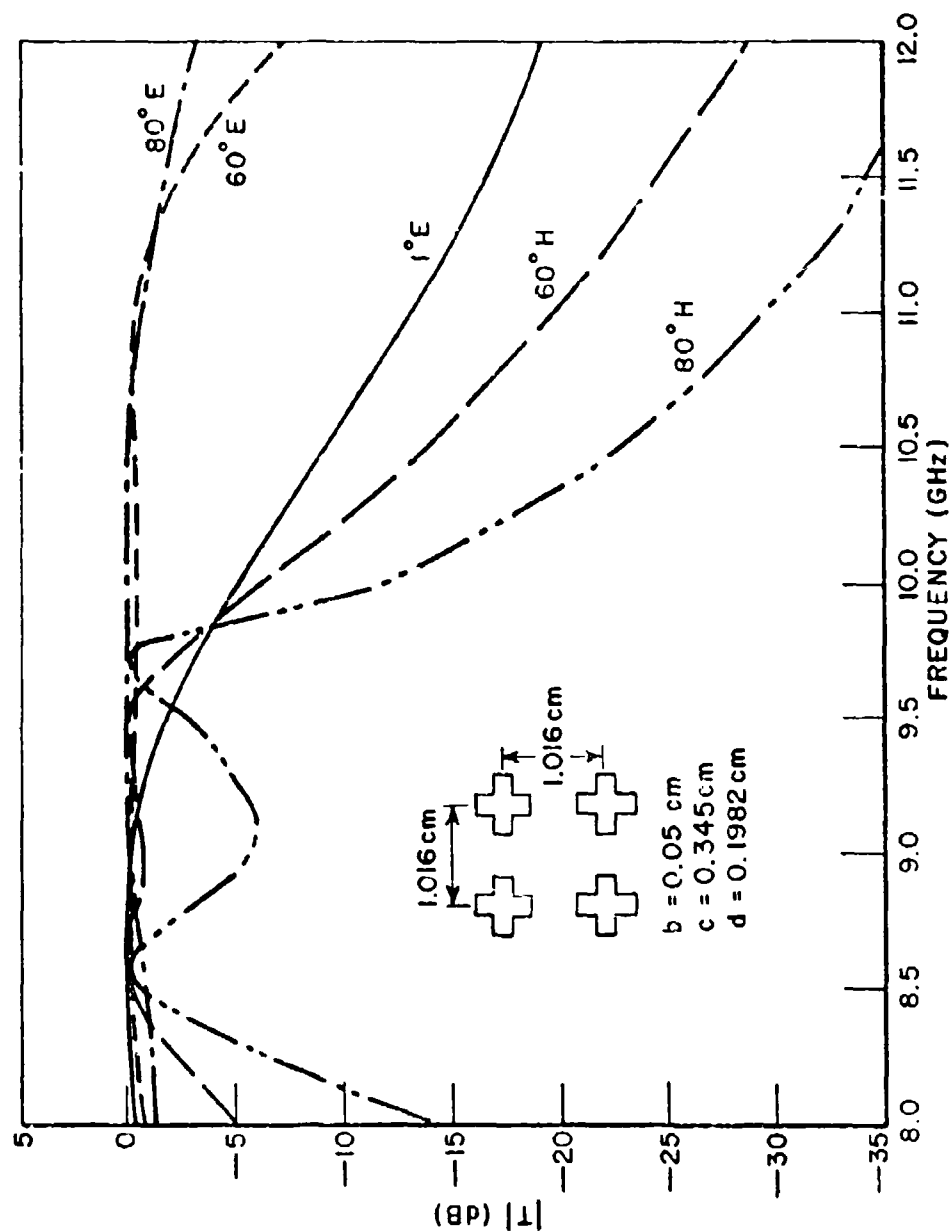


Figure 6-5.--Calculated transmission curves for a biplanar array of 4-legged symmetric loaded slots. The two panels are separated 0.25λ at resonance ($t_1=0.079$ cm, $\epsilon_1=2.56\epsilon_0$; $t_2=0$; $t_3=0.83$ cm, $\epsilon_3=\epsilon_0$).

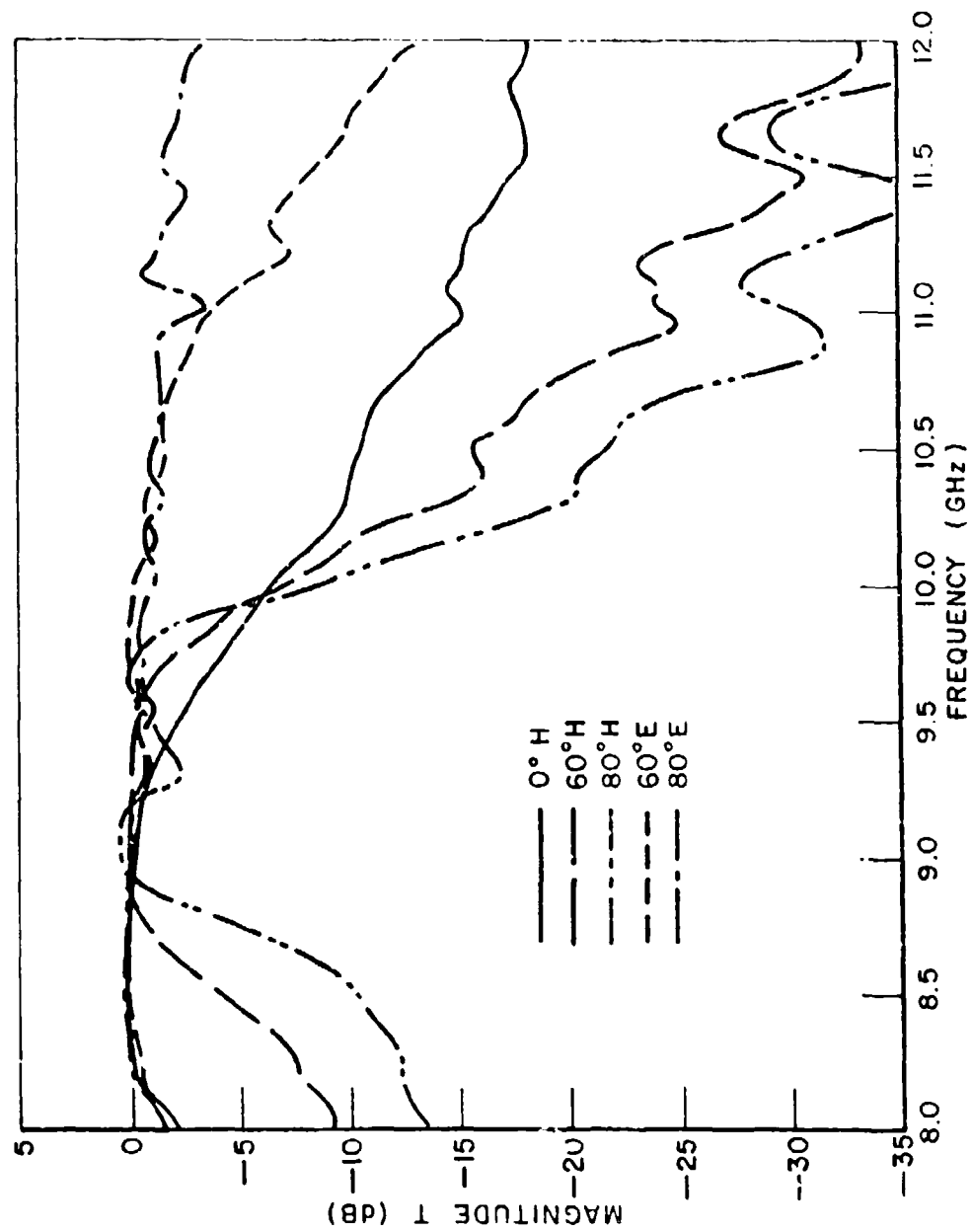


Figure 6-6.--Measured curves corresponding to the calculated curves of Fig. 6-5.

As pointed out in a previous chapter, the variation of bandwidth with incidence angle can be reduced considerably by covering the periodic surface with a properly designed dielectric layer. In the next section we will illustrate that, as suggested by Munk [4] this technique can be successfully applied to biplanar resonant surfaces with good results. Further, the resonance region dip for H-plane incidence angles can be reduced considerably by properly picking the thicknesses l_2 and l_3 and dielectric constants ϵ_2 , ϵ_3 of the material between the screens.

C. Dielectric Covered Biplanar Arrays

As mentioned previously, the modal solution presented in the first section of this chapter was the first solution to the biplanar array problem which included dielectric layer effects. With this solution several new phenomena related to dielectric covered biplanar arrays were discovered, and these will be presented in the following pages. However, shortly after this solution was developed Munk developed a solution using a mutual impedance method [5]. One advantage of his method is that it can more readily be used to design dielectric covered biplanar arrays with desirable properties than can the modal solution, which is primarily a means of analysis. One cannot merely cover the biplanar array with just any dielectric configuration and expect good performance. An example of this is shown in the calculated transmission curves of Fig. 6-7, where a biplanar slot array has been covered on the outside with 0.5 cm thick layers of $\epsilon_r=4.0$ dielectric, and filled in the center with a 0.7 cm dielectric with $\epsilon_r=1.9$. Note the shifts in resonance frequency for the H-plane incidence angles. Also, the 1° incidence angle curve has a loss at resonance of 3.5 db. This panel is clearly unsuitable for any practical applications.

Proper design is required to obtain a biplanar panel with stable resonance frequency and minimal change in bandwidth and phase delay with changing incidence angle. Later in this section transmission curves for a biplanar array designed by means of Munk's solution and calculated using the modal matching solution will be presented. These curves show a quite stable passband, minimal change in bandwidth with incidence angle, and a phase delay variation comparable to that for a conventional dielectric radome. A complete discussion of the design procedure is beyond the scope of the present work, and the interested reader is referred to Munk [5].

However, we shall first show a series of calculated and measured curves for a dielectric covered biplanar panel which does not have such good performance since the results will illustrate certain phenomena which must be taken into account when designing biplanar arrays. The calculated curves in this section required 242 Floquet modes ($p_{\max}=q_{\max}=5$) for convergence. In general the first 7 sine

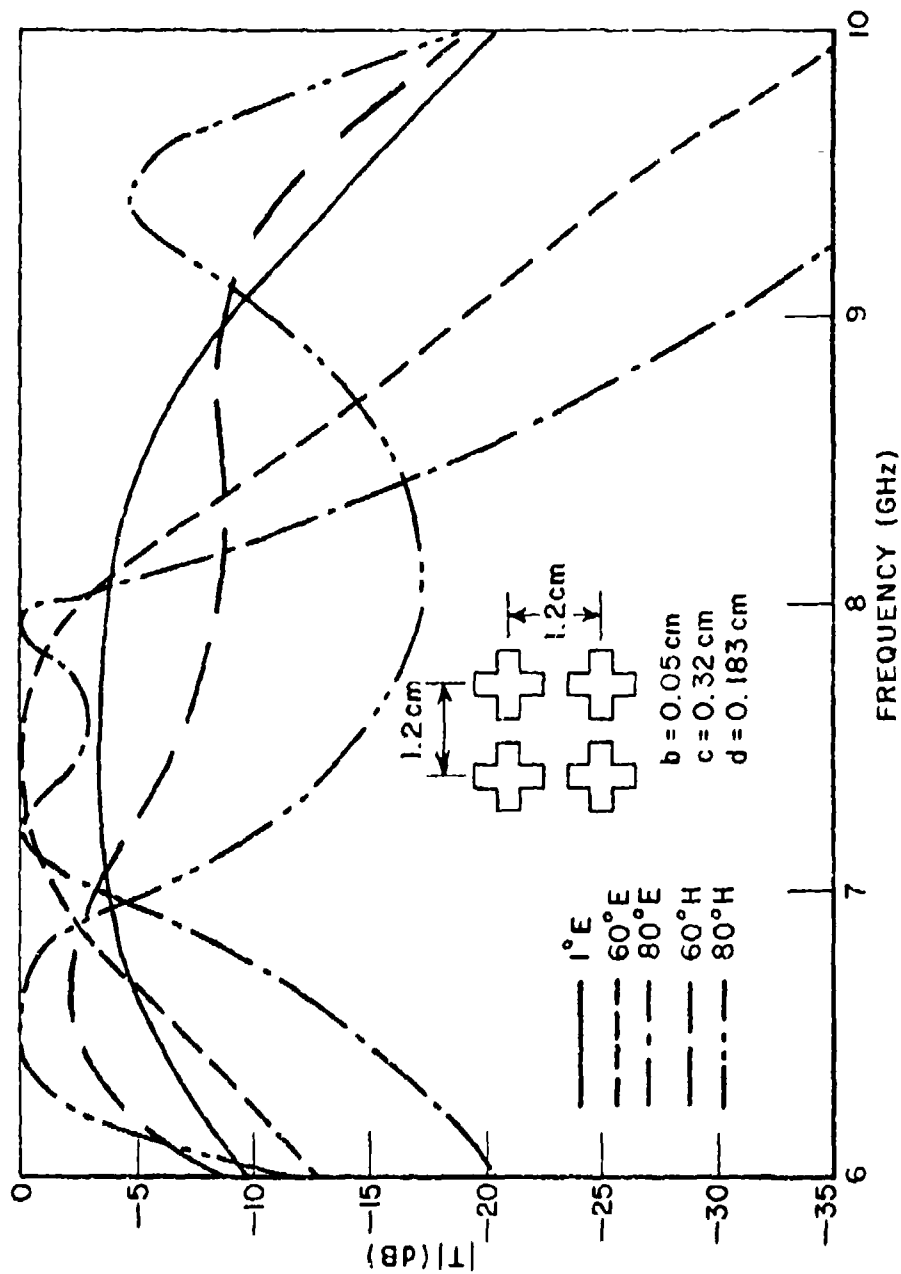


Figure 6-7.--Calculated transmission curves for a biplanar array of 4-legged symmetric loaded slots ($t_1=0.5$ cm, $\epsilon_1=4.0\epsilon_0$; $t_2=0$; $t_3=0.7$ cm, $\epsilon_3=1.9\epsilon_0$). These curves illustrate the bad performance which can result from a poorly designed dielectric covered biplanar array.

and cosine modes were used to expand the fields in the slot. However, for lower frequencies (i.e., below 12 GHz) the cosine modes were not included since they are only weakly excited.

The biplanar geometry of Fig. 6-8 represents an early attempt to design a dielectric covered biplanar array. As is evident from the calculated transmission curves of Fig. 6-9 this design attempt was a failure. The reason is that the 60°, 70°, and 80° E-plane transmission nulls fell in the passband of the panel. The existence of the passband nulls for biplanar arrays was not anticipated by previous theories, and was first demonstrated by the modal solution results of Fig. 6-9. Only later were these results confirmed by the measured curves of Fig. 6-11.

These passband nulls are related to the surface wave nulls discussed extensively in Chapter IV. It was shown there that the frequency of the null would be reduced by coating the array with a dielectric layer. The amount of reduction would depend, in a somewhat complicated fashion, on the thickness of the dielectric layer. The lowest possible frequency could be quite easily determined, however, and would be given by Eq. (4-29) with $K_w = K_1$. For a square array ($d_x d_y$, $\alpha = 90^\circ$) this means that the surface wave null frequency cannot be lower than f_e , where

$$(6-28) \quad f_e = c/[d_x(\sqrt{\epsilon_r} + \sin\theta)]$$

and where c is the speed of light and ϵ_r is the relative dielectric constant of the dielectric layer. For the outer layer, with $\epsilon_r = 1.5$, and taking $\theta = 70^\circ$, Eq. (6-28) predicts a null no lower than 10.23 GHz for $d_x = 1.355$ cm. Thus, according to previous theory, the null should have been above the desired passband frequencies and the biplanar design of Fig. 6-8 should have been a viable one.

The source of the null was evidently not in the exterior region of the biplanar array (i.e., the t_1 layers) but in the area between the arrays. Note that if the spacing between the slots (d_x and d_y) is increased the frequency of the null is moved upwards in frequency (i.e., see Fig. 6-18). This behavior is similar to that of the surface wave null discussed in Chapter IV. If we proceed to apply Eq. (6-28) to the region between the panels, we find that for a 70° incidence angle and a relative dielectric constant of 1.9 the Wood's anomaly null would normally occur at a frequency above 9.55 GHz. Our calculated frequency from Fig. 6-9 is 8.9 GHz, well below the frequency predicted by Eq. (6-28). Equation (6-28) corresponds to a phase difference of 2π radians between adjacent slots. Thus, assuming that the null occurs when adjacent slots differ in phase by a multiple of $2n\pi$, the presence of the 2nd array must affect the phasing between the slots on the first array, and vice versa. This is not really that unexpected. What was not known previously, however, was that this

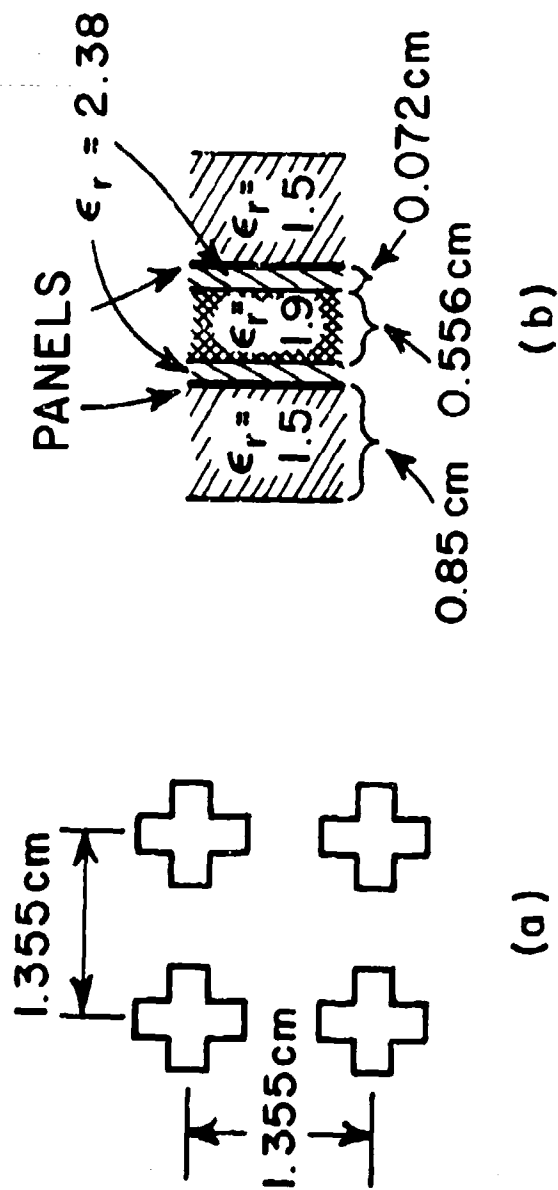


Figure 6-8.--Geometry of the biplanar array analyzed in the following series of calculated and measured curves:

- Grid arrangement for the 4-legged symmetric slots with dimensions $b=0.051 \text{ cm}$, $c=0.32 \text{ cm}$, $d=0.183 \text{ cm}$.
- Arrangement of the dielectric layers showing $t_1=0.85 \text{ cm}$, $\epsilon_1=1.5\epsilon_0$; $t_2=0.072 \text{ cm}$, $\epsilon_2=2.38\epsilon_0$; and $t_3=0.556 \text{ cm}$, $\epsilon_3=1.9\epsilon_0$.

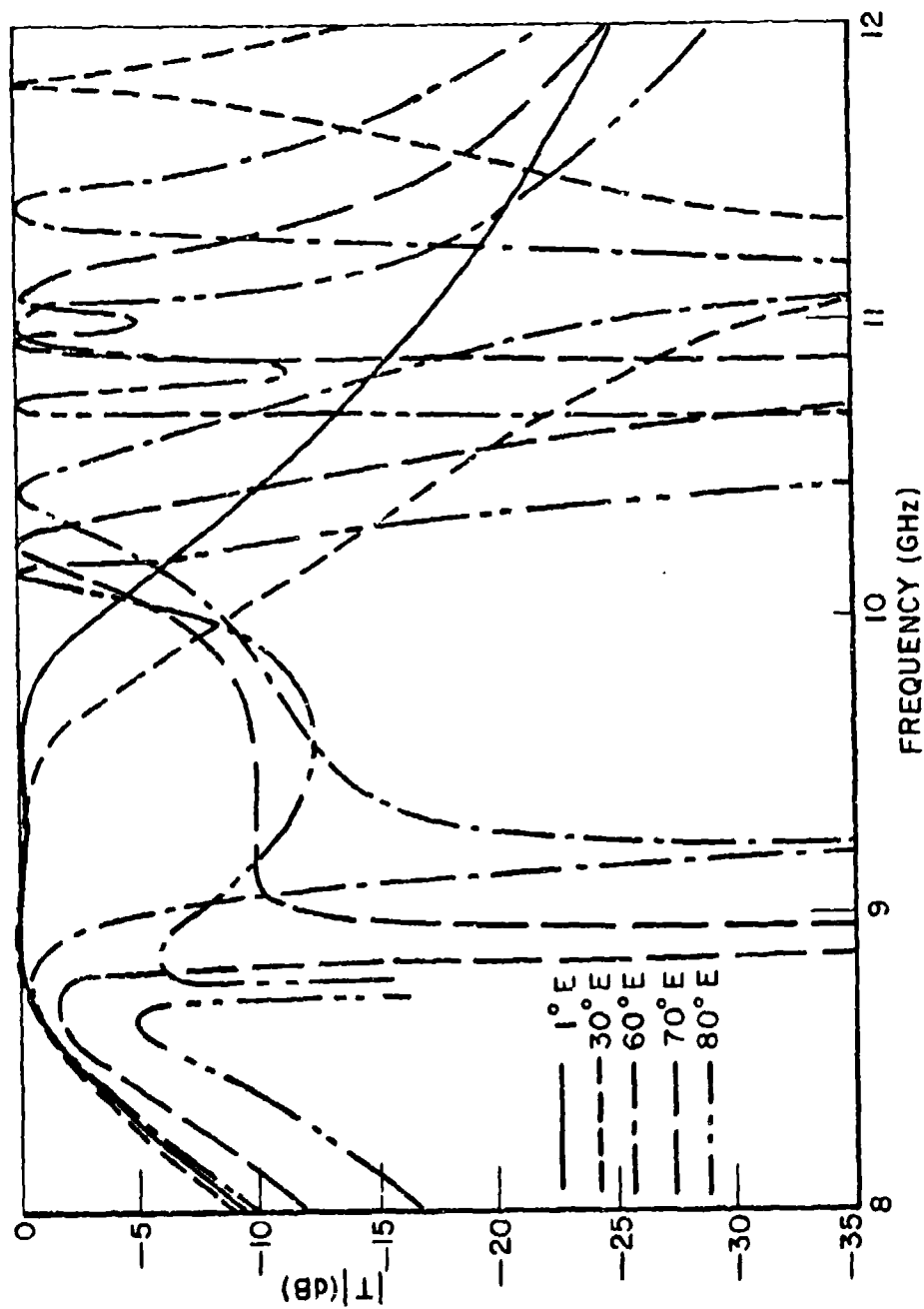


Figure 6-9.--Calculated transmission curves for a biplanar array of 4-legged symmetric loaded slots arranged as shown in Fig. 6-8. E-plane incidence.

shift in the frequency of the null would 1) be so pronounced, and 2) be downward (in frequency) rather than upward.

One might argue that it is the t_2 substrate layers with $\epsilon_r=2.38$ which lower the null frequency. However, a layer of dielectric this thin will have little effect on the surface wave null frequency, as is evident from the results of Fig. 4-17. To confirm this conclusion calculations for the array of Fig. 6-8 were made with the relative dielectric constant of the t_2 substrate layers changed to 1.9. The results are shown in Fig. 6-10. For 70° incidence the null

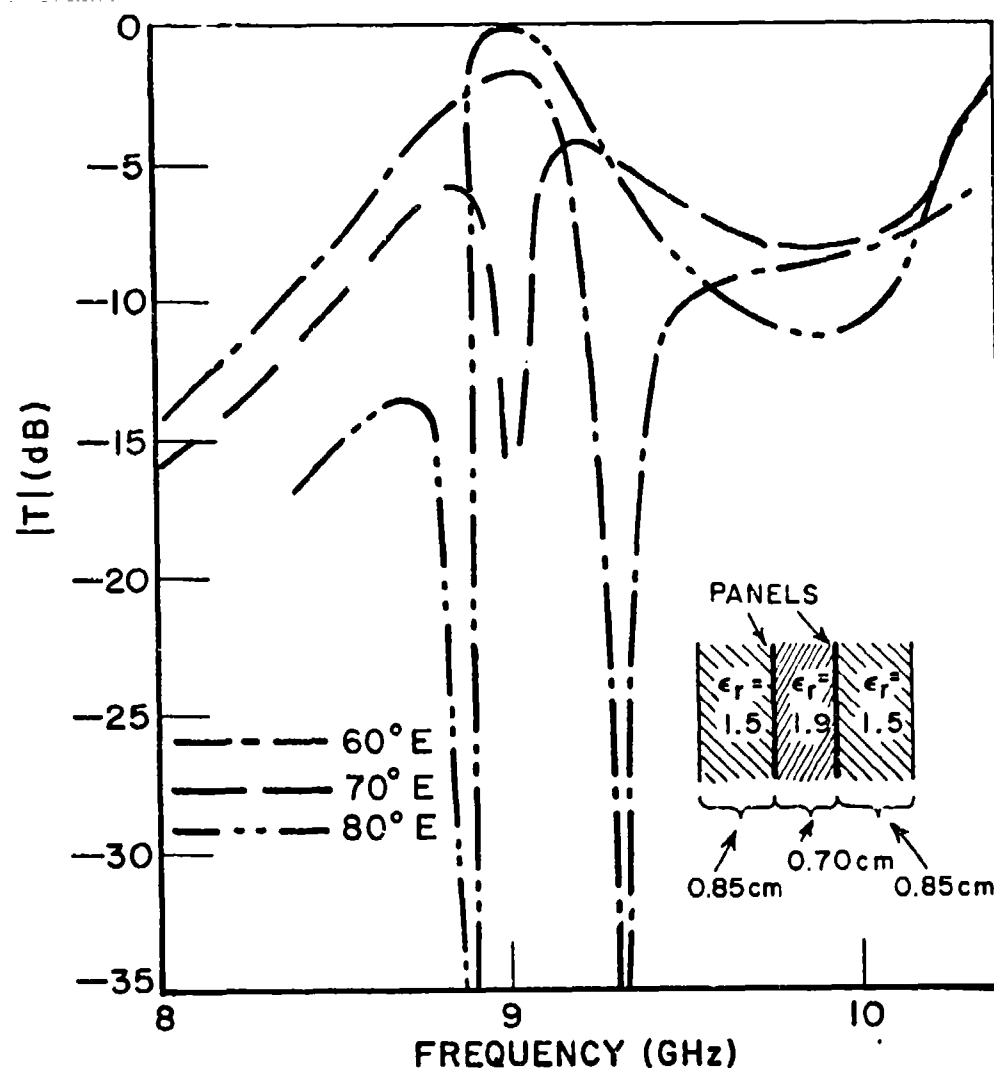


Figure 6-10.--Calculated transmission curves for the same biplanar array of Fig. 6-9 but with the relative dielectric constant of the t_2 substrate layer set equal to that of the t_3 center layer. E-plane incidence.

frequency increased slightly (from 8.9) to 9.02 GHz. This frequency is still well below the 9.55 GHz frequency predicted by Eq. (6-28), and supports our conclusion that the frequency of the null is lowered by the coupling between the panels.

As previously mentioned, the experimental confirmation of the calculated curves of Fig. 6-9 is shown by the curves of Fig. 6-11. The overall agreement is quite good. The forced resonances above 10 GHz due to the rapid changes in $Z_{pq}^{(2)}$ (see Chapter IV) are lossy in the measured curves because of the finite size of the measured panels. Note that their frequencies are, for the most part, quite accurately predicted by the calculations. The measured loss is actually good in terms of possible applications, since for most applications one would like to depress the out of passband transmission as much as possible.

Calculated and measured transmission curves for the other incidence plane (H-plane) are shown in Figs. 6-12 and 6-13. Again the agreement is quite good. The amount of the $\theta=80^\circ$ resonance band dip is predicted quite accurately. The passband nulls and forced resonances evident in the E-plane transmission curves are suppressed by the element pattern for H-plane incidence angles. The exception to this is the narrow null produced at the onset of the external, free space grating lobe (11.4 GHz for $\theta=70^\circ$, 11.15 for $\theta=80^\circ$). This null is not completely suppressed by the element pattern. Because of the presence of the dielectric layer, the grating lobe (which leaves the structure at a grazing angle ($\theta=90^\circ$)) is not grazing at the surface of the panel, but is tilted up and out of the element pattern null [48]. As a final comment, note that the dip in the 80° curve at 10.3 GHz is a measurement error; in fact, no null exists at this frequency.

Calculated and measured transmission curves for the same bi-planar geometry over the second resonance region (13 to 18 GHz) are shown in Figs. 6-14 and 6-15 for E-plane incidence and in Figs. 6-16 and 6-17 for H-plane incidence. The agreement between the calculated and measured curves is not as good as it was for the first resonance region. The calculated higher order resonance peaks are often not confirmed by the measurements. Again, this is to be expected for a finite size panel.

As mentioned previously, the passband nulls for E-plane incidence can be raised in frequency by decreasing d_x and d_y . The results which can be obtained by this means are illustrated in Fig. 6-18. The arrangement of the dielectric layers is the same as in Fig. 6-10. However, decreasing the interelement spacing has moved the unwanted null upward in frequency and out of the passband. Thus this panel design has a 0.6 GHz wide passband where the transmission loss is evidently less than one dB for incidence angles up to 80° in both cardinal planes. In addition, the ratio of the 80° E-plane

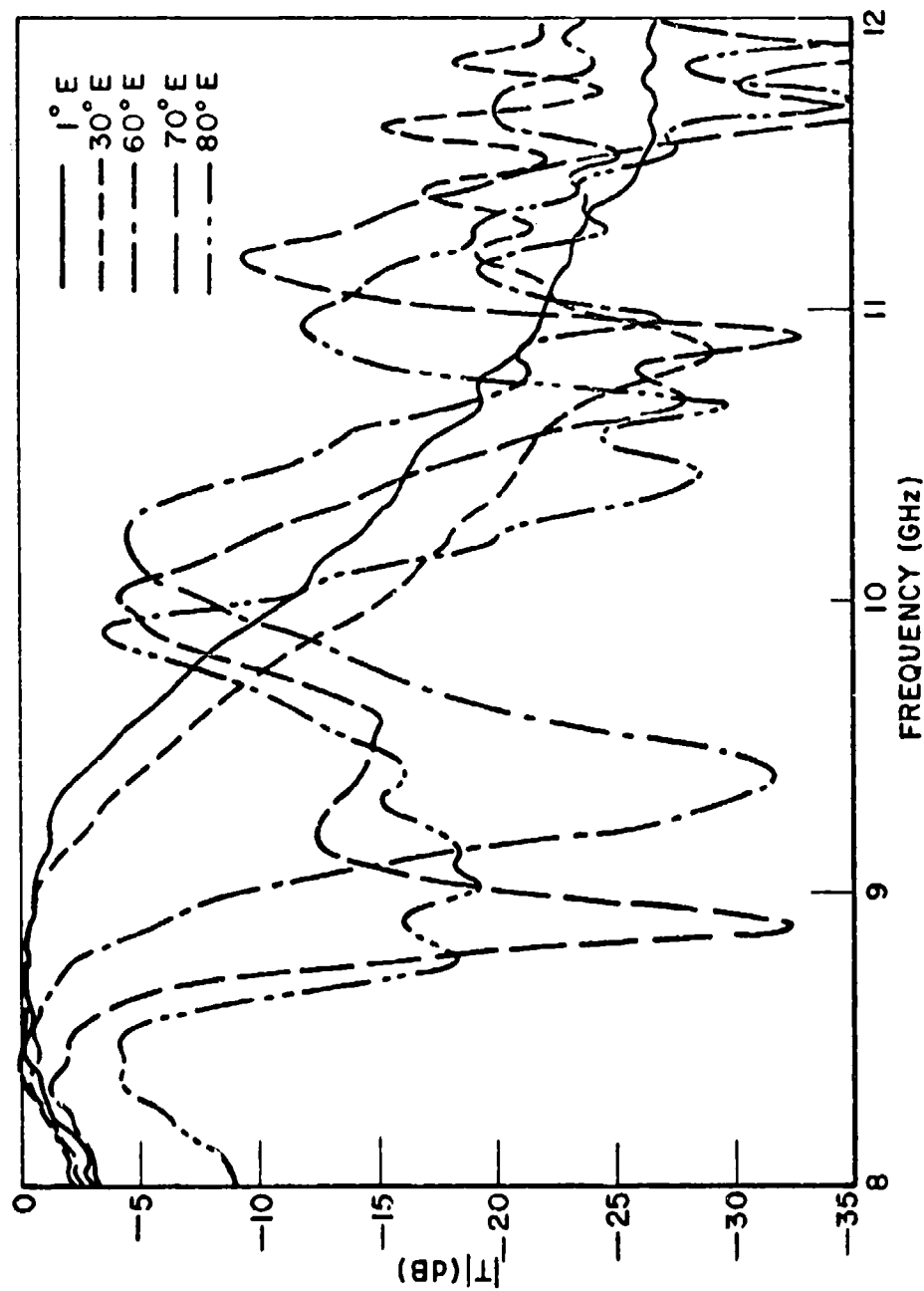


Figure 6-11.--Measured transmission curves corresponding to the calculated curves of Fig. 6-9.

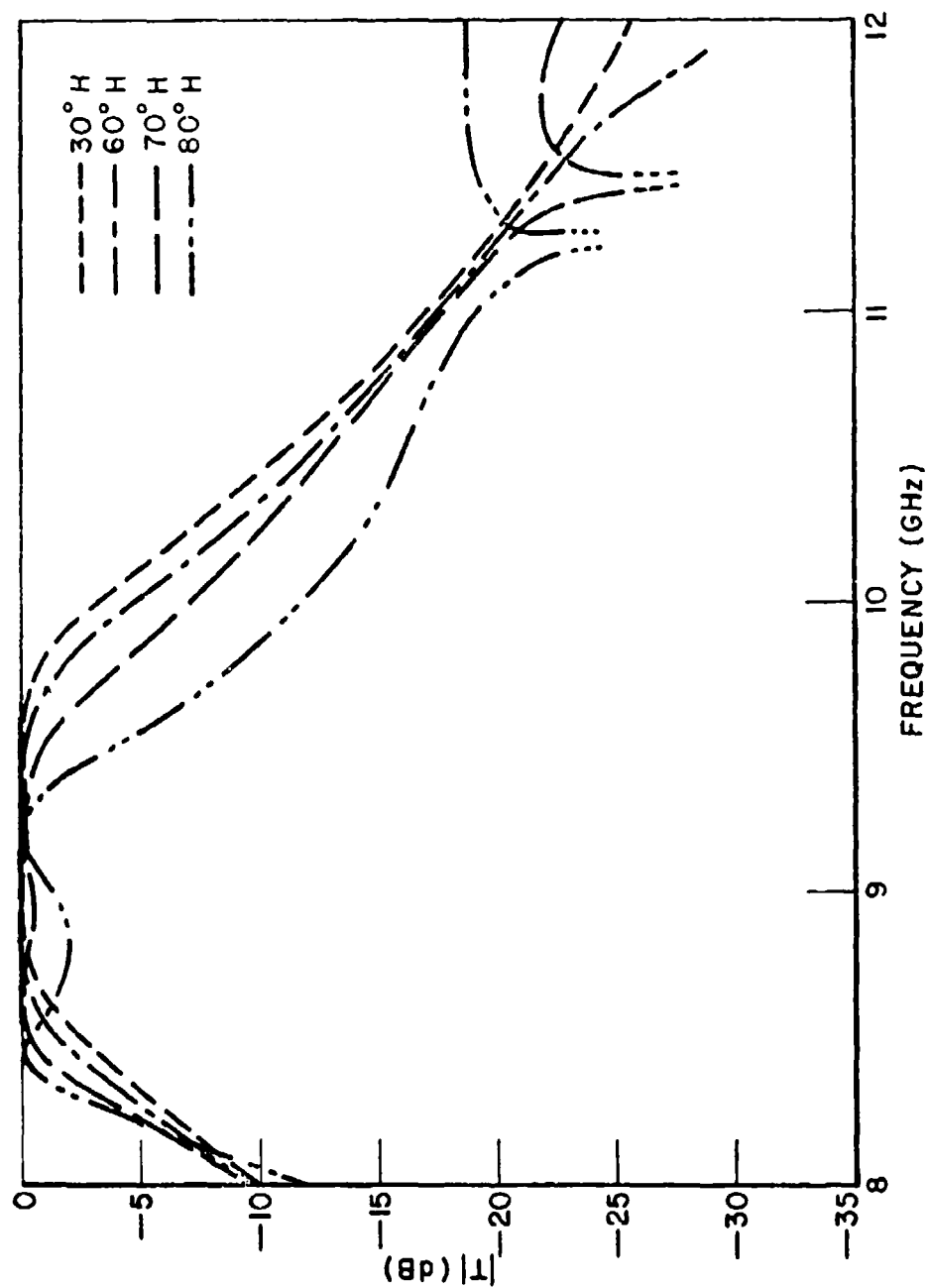


Figure 6-12.--Calculated transmission curves for a biplanar array of 4-legged symmetric loaded slots arranged as shown in Fig. 6-8. H-plane incidence.

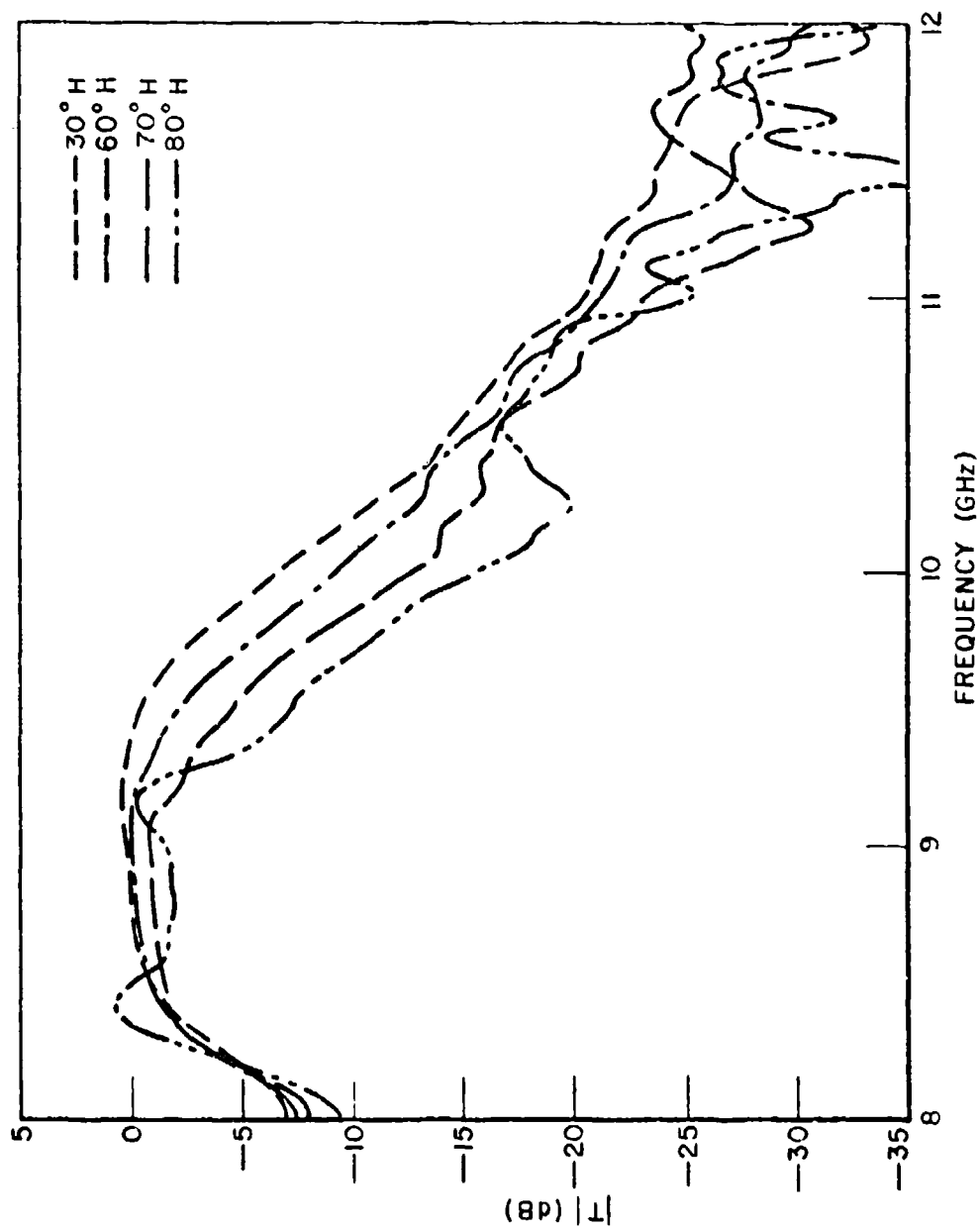


Figure 6-13.--Measured transmission curves corresponding to the calculated curves of Fig. 6-12.

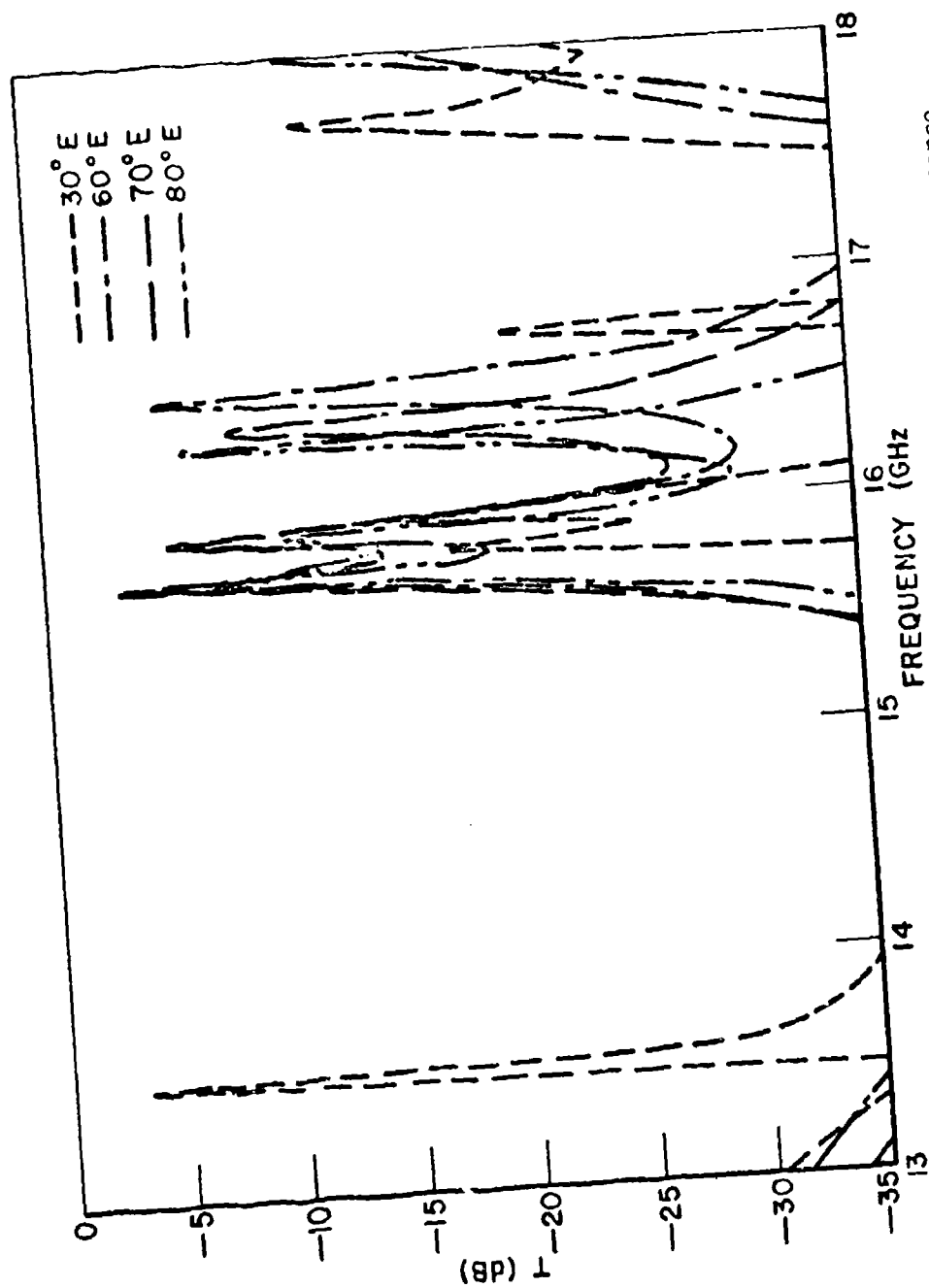


Figure 6-14.---Calculated transmission curves showing the second resonance for a biplanar array of 4-legged symmetric loaded slots arranged as shown in Fig. 6-8. E-plane incidence.

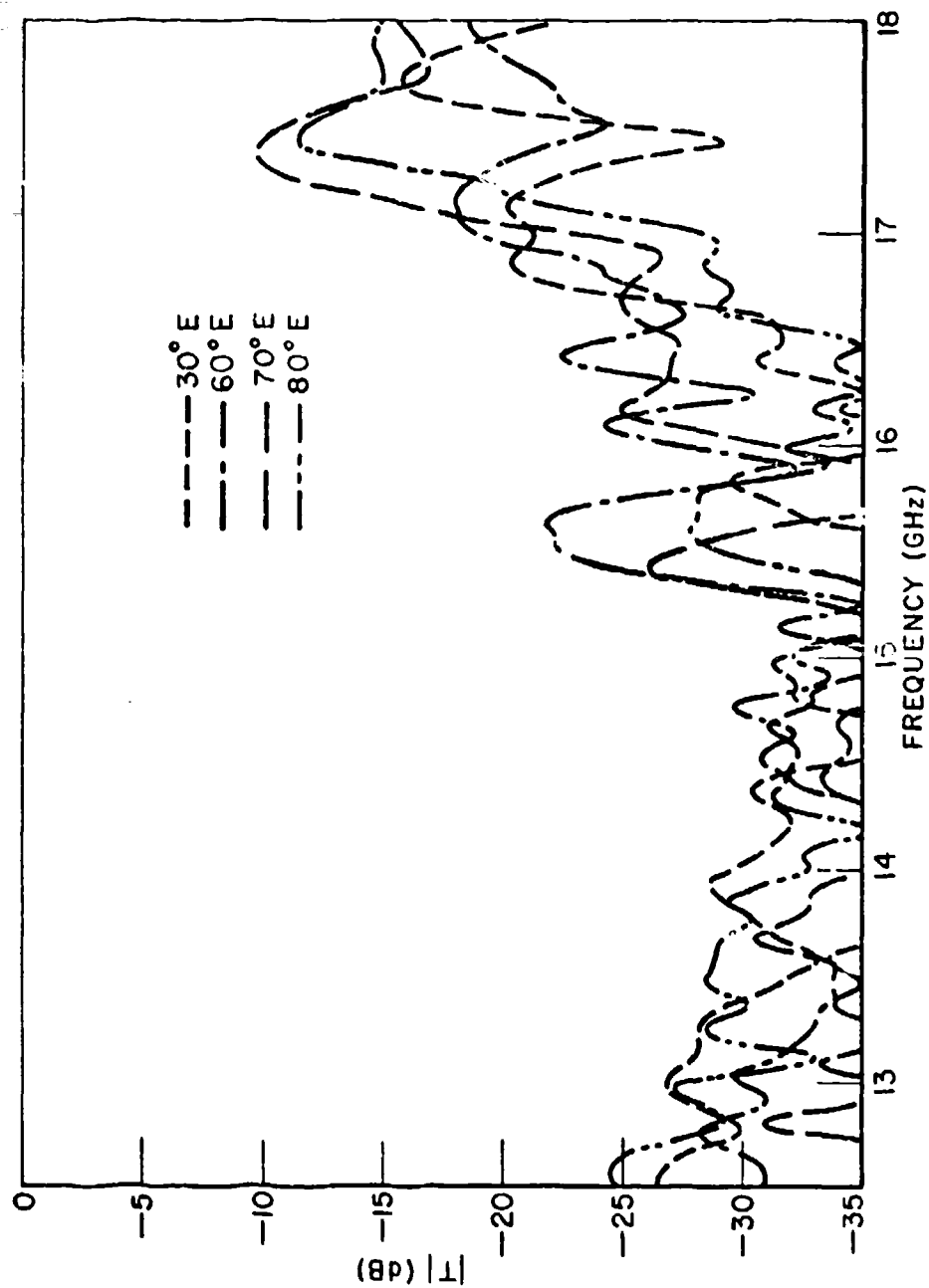


Figure 6-15.--Measured transmission curves corresponding to the calculated curves of Fig. 6-14.

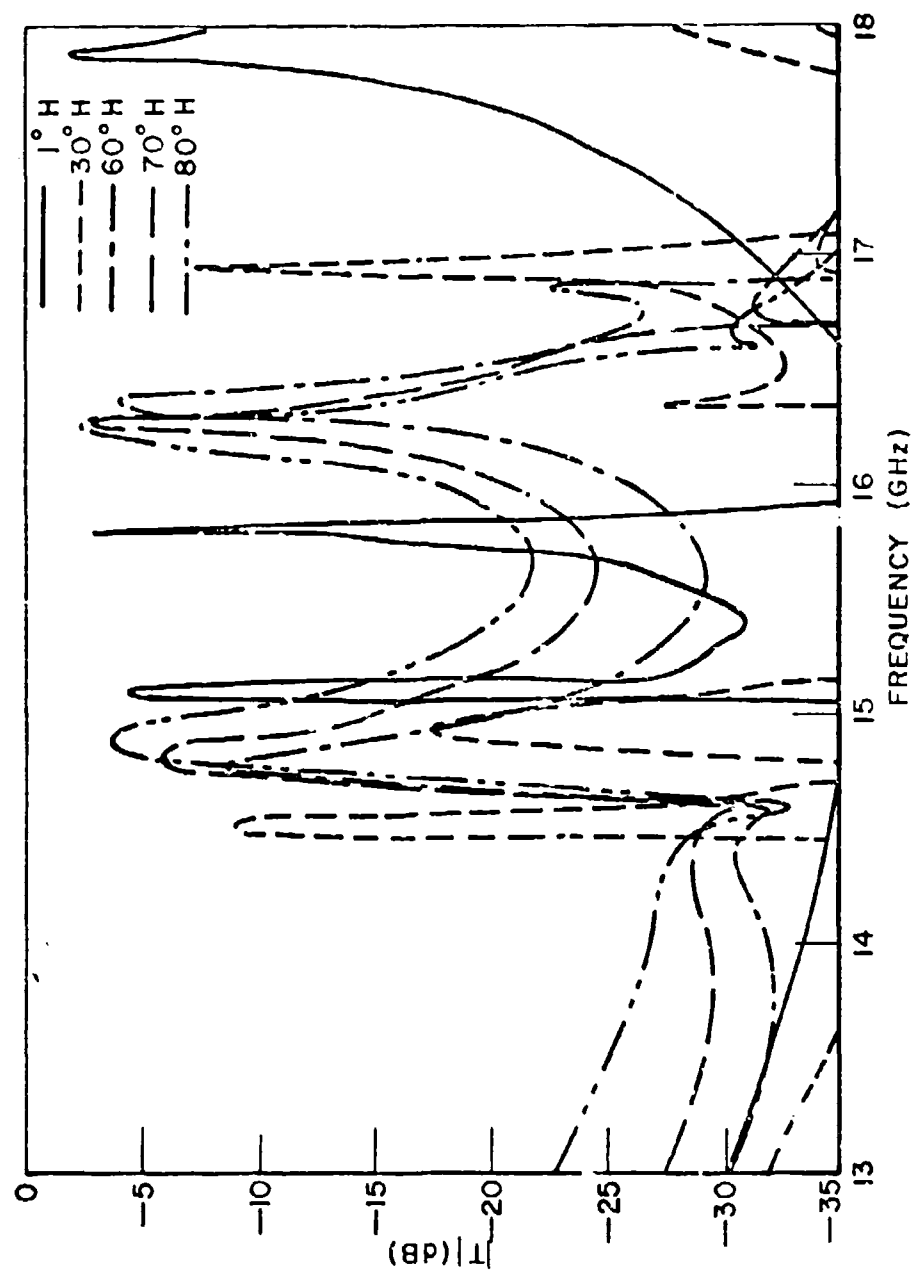


Figure 6-16.--Calculated transmission curves showing the second resonance for a biplanar array of 4-legged symmetric loaded slots arranged as shown in Fig. 6-8. H-plane incidence.

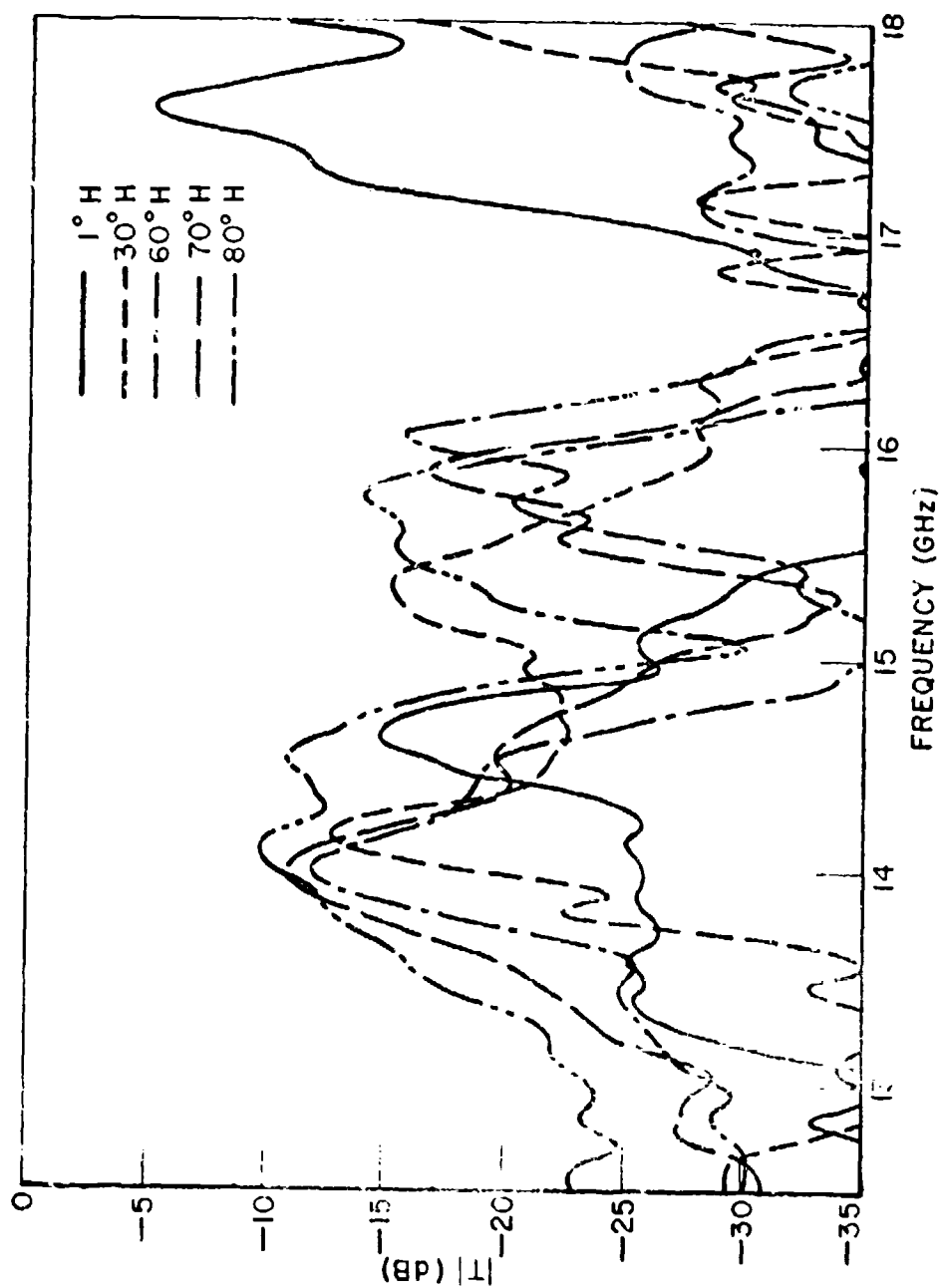


Figure 6-17.--Measured transmission curves corresponding to the calculated curves of Fig. 6-15.

3 dB bandwidth to the 80° H-plane 3 dB bandwidth is approximately 2:1. This is a substantial improvement over the situation shown in the preceding section for biplanar arrays without dielectric layers.

For such a thick structure the variation of the insertion phase delay with incidence angle can be a problem. In Fig. 6-19 we show curves of the phase ψ of the transmission coefficient, where $T = |T|/e^{j\psi}$. These phase curves are plotted vs. frequency for 1° E-plane and 60° E and H-plane incidence. The curves marked square correspond to the biplanar panel of Fig. 6-18. The "interlaced" curves are for the same biplanar panel with the one change that the slots are arranged in an interlaced grid (i.e., $\alpha=45^\circ$ instead of 90° , see Fig. 6-1). The transmission curves for the interlaced panel are virtually the same as those in Fig. 6-18.

If we examine the square grid ($\alpha=90^\circ$) curves in the resonance region (at $f=9.4$ GHz, for instance) we find that when the incidence angle changes from 1° E-plane to 60° H-plane the insertion phase delay decreases by about 46° . When the incidence angle is changed from 1° E-plane to 60° E-plane the phase delay is decreased by 74° . A few degrees improvement in each case can be obtained by going to an interlaced grid ($\alpha=45^\circ$). This change in phase delay is undesirable. It can be reduced somewhat by more sophisticated panel designs. Yet it should be pointed out that this change in phase delay is no greater than that introduced by a typical dielectric radome [5].

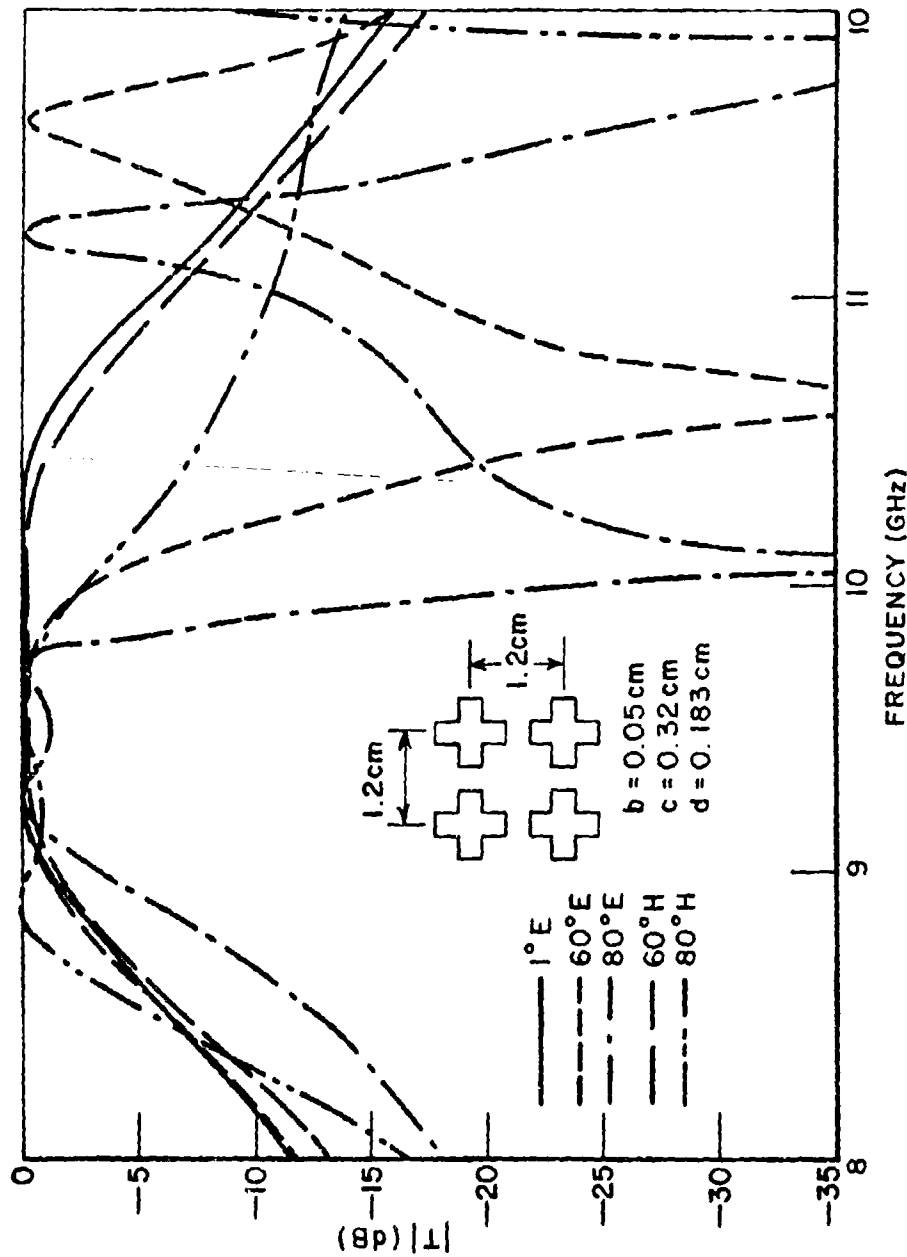


Figure 6-18.--Calculated transmission curves for a biplanar array of 4-legged symmetric loaded slots with d_x and d_y reduced to 1.2 cm to eliminate the passband null. $t_1=0.85$ cm, $\epsilon_1=1.5\epsilon_0$; $t_2=0$, $t_3=0.7$ cm, $\epsilon_3=1.9\epsilon_0$.

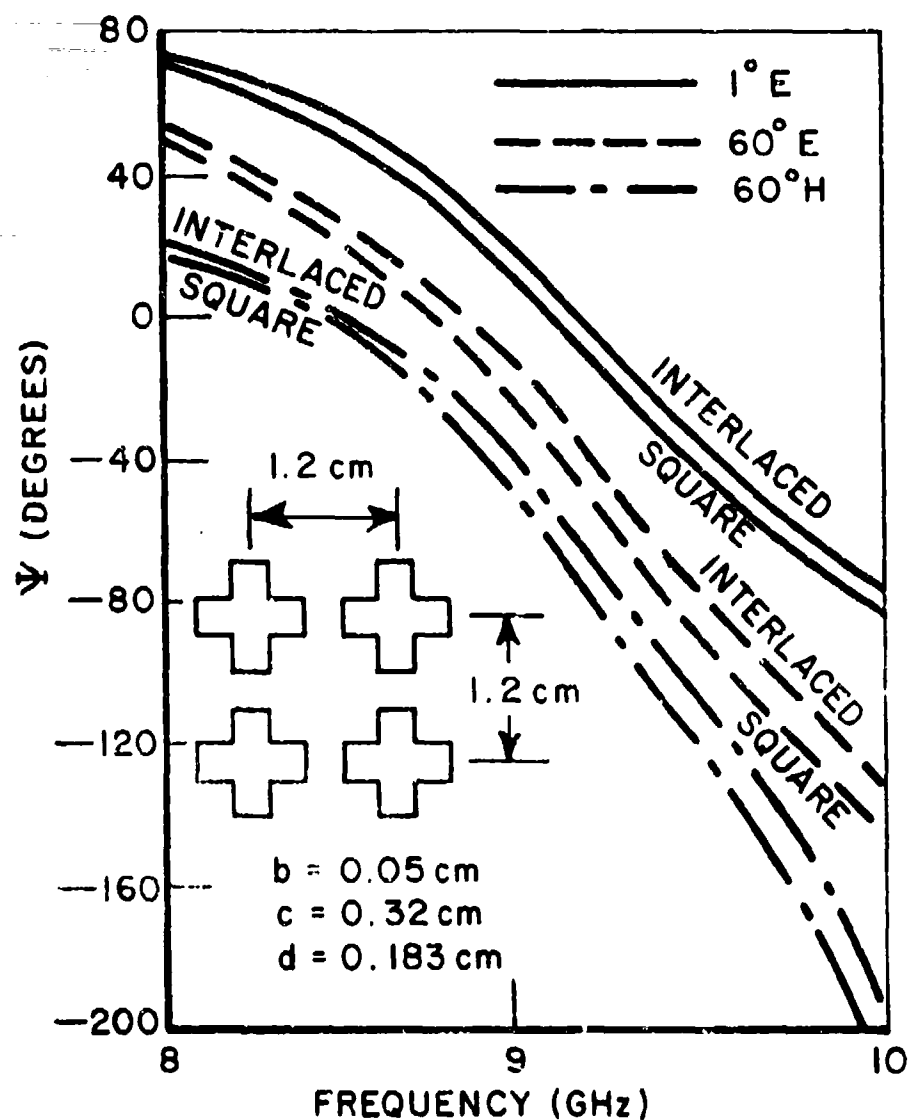


Figure 6-19.--Phase of transmission coefficient for a biplanar array. The curves marked "square" are for the biplanar array of Fig. 6-18. The curves marked "interlaced" are for the biplanar array of Fig. 6-18 but with the slots arranged in an interlaced grid, i.e., every other row of slots shifted right by $d_x/2$.

CHAPTER VII SUMMARY

Moment method solutions have been developed which enable the designer of metallic radomes to calculate the transmission coefficients for metallic slot arrays. The geometries considered were 1) thick slot arrays covered with dielectric, 2) thin slot arrays covered with dielectric, and 3) biplanar slot arrays covered with dielectric. The slot shapes considered were 1) rectangular slots, 2) single loaded slots, 3) 4-legged symmetric slots, and 4) 3-legged symmetric slots. The wide range of geometries and slot shapes considered makes this set of solutions a powerful tool for resonant slot array analysis and design, and thus will aid considerably in designing new metallic radomes for a wide variety of applications.

In conjunction with investigations of the effects of thickness on resonant slot arrays a solution for the transmission through a thick rectangular waveguide iris was obtained, and from this solution considerable insight into the effects of thickness on metallic radomes was obtained.

In order to obtain a proper understanding of this work certain basic information on resonant slot arrays and their application as metallic radomes is required. Thus a concise review of the basic properties of resonant surfaces is contained in the introduction.

APPENDIX A WAVEGUIDE MEASUREMENT OF EQUIVALENT IMPEDANCE

The waveguide hardware used to determine the reflection coefficient for a slot in a waveguide is shown in Fig. A-1. The waveguide frequency range is 2.6 to 3.95 GHz. The Polorad source is modulated externally by a 1,000 Hz fork. Frequency is measured with a resonant cavity frequency meter since a precise determination of the frequency is necessary for this measurement technique. The SWR and voltage minimum are measured with the slotted line and SWR meter.

In order to verify the Modal Analysis calculations of Chapter II we need to determine the equivalent impedance. The concept of the equivalent impedance is discussed in Chapter II. To determine the equivalent impedance of a slot the following data must be measured: 1) Frequency; 2) SWR; and 3) distance between slot in flange and the first voltage minimum. With this information the calculation of the equivalent impedance is straightforward.

If one desires to measure transmission loss for a thick slot, the apparatus sketched in Fig. A-1 may be also used to determine the magnitude of T . With the apparatus connected as shown in Fig. A-1 the maximum voltage V_{\max} and the minimum voltage V_{\min} of the standing wave on the input side of the slot are measured with the slotted line and SWR meter. Then the slot is removed from between the flanges connecting the slotted line and the load and placed between the flanges connecting the slotted line and the waveguide to coax adapter. All flanges are tightened, and the value of V^t (see Fig. 2-2) is now measured on the slotted line. With this information one can readily evaluate $|T|$ using transmission line theory.

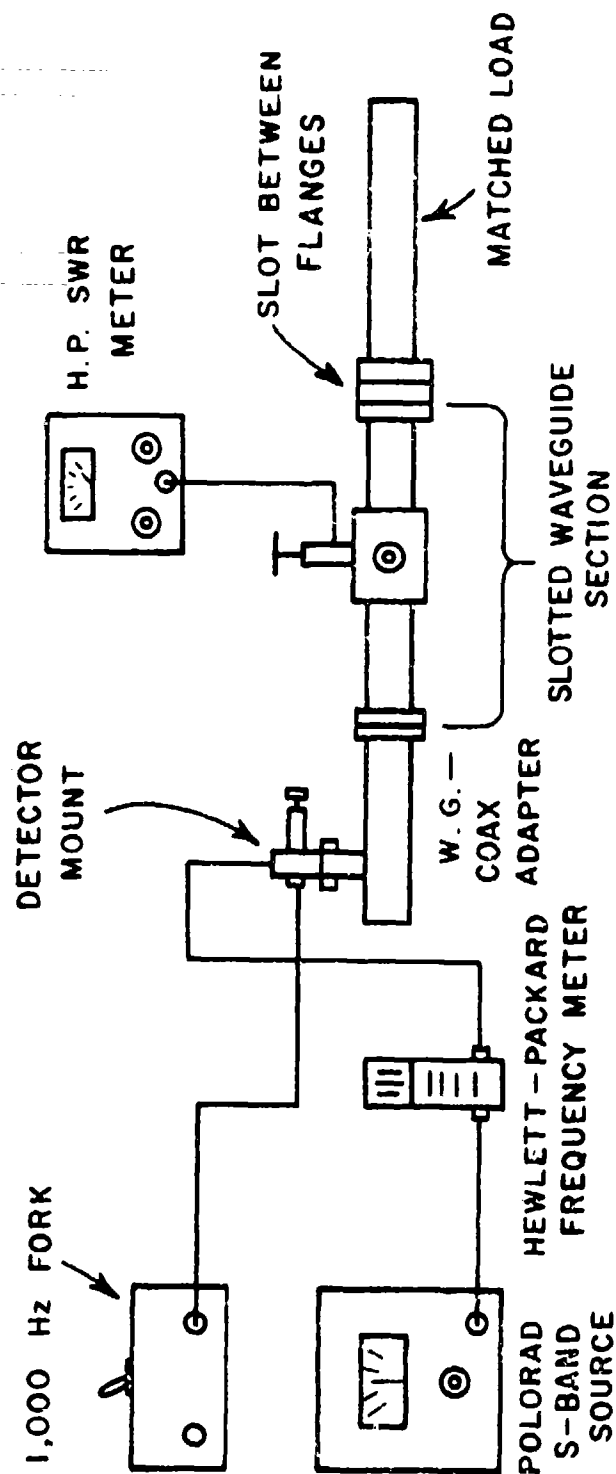


Figure A-1.--Waveguide equipment used to measure the reflection coefficient and equivalent shunt impedance of a slot.

APPENDIX B EVALUATION OF MODAL INTEGRATIONS

In order to solve the integral equations of Chapters IV, V, and VI, integrals of the form $\int_b \bar{e}_{bj} x \bar{\phi}_{pq}^* \cdot \hat{z} ds$ must be evaluated. The $\bar{\phi}_{pq}$ functions come from the transverse magnetic field Floquet mode functions, and from Eqs. (3-14), (3-15), and (3-50) are given by

$$(B-1) \quad \bar{\phi}_{pq}^1 = \frac{1}{\sqrt{d_x d_y}} \left(\frac{U_p}{T_{pq}} \hat{x} + \frac{V_{pq}}{T_{pq}} \hat{y} \right) \psi_{pq}, \quad \text{TE}$$

$$(B-2) \quad \bar{\phi}_{pq}^2 = \frac{1}{\sqrt{d_x d_y}} \left(-\frac{V_{pq}}{T_{pq}} \hat{x} + \frac{U_p}{T_{pq}} \hat{y} \right) \psi_{pq}, \quad \text{TM}$$

with U_p , V_{pq} , T_{pq} , and ψ_{pq} given by Eqs. (3-7), (3-8), (3-19), and (3-18), respectively. The \bar{e}_{bj} modes are defined in Eq. (3-69) for rectangular slots, Eq. (3-73) for single loaded slots, and Eq. (3-76) for the 3-legged and 4-legged symmetrical loaded slots.

The integral can be evaluated in closed form for all of the \bar{e}_{bj} modes in a quite straightforward, although somewhat tedious, manner. We shall illustrate this for the single loaded slot, and then give a Fortran computer code which can be used to evaluate the integral for any of the \bar{e}_{bj} modes given in Chapter III. The integral $\int_b \bar{e}_{bj} x \bar{\phi}_{pq}^{r*} \cdot \hat{z} ds$ can then be quite easily obtained, since

$$(B-3) \quad \int_b \bar{e}_{bj} x \bar{\phi}_{pq}^{r*} \cdot \hat{z} ds = \left[\int_b \bar{e}_{bj} x \bar{\phi}_{pq}^r \cdot \hat{z} ds \right]^*$$

This follows from noting that all of the \bar{e}_{bj} mode functions are real functions.

In Fig. B-1 we have divided the single loaded slot into 5 straight regions with the 6 points P_1 through P_6 . Referring to Eq. (3-73) we can, with suitable coordinate substitutions, express the \bar{e}_{bj} modes in each of the 5 regions at $z=0$ as:

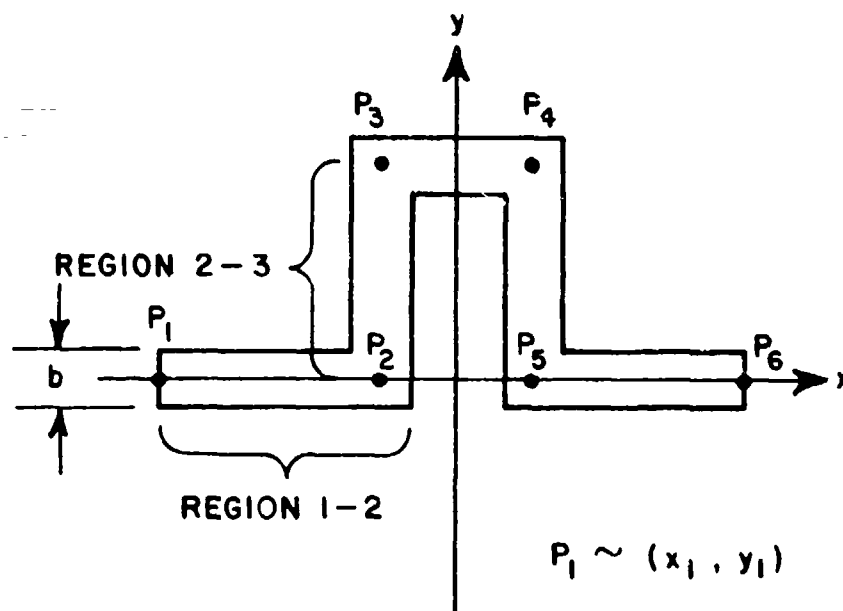


Figure B-1.--Single loaded slot divided into linear regions by points P_1 through P_6 .

$$(B-4) \quad \text{Region 1-2: } \bar{e}_{bj} = \hat{y} \sin\left(\frac{j\pi}{T}(x-y_4) - \frac{j\pi}{2}\right) = \hat{y} e_{bj}$$

$$(B-5) \quad \text{Region 2-3: } \bar{e}_{bj} = -\hat{x} \sin\left(\frac{j\pi}{T}(y-x_4-y_4) - \frac{j\pi}{2}\right) = \hat{x} e_{bj}$$

$$(B-6) \quad \text{Region 3-4: } \bar{e}_{bj} = \hat{y} \sin\left(\frac{j\pi x}{T} - \frac{j\pi}{2}\right) = \hat{y} e_{bj}$$

$$(B-7) \quad \text{Region 4-5: } \bar{e}_{bj} = \hat{x} \sin\left(\frac{j\pi}{T}(x_4+y_4-y) - \frac{j\pi}{2}\right) = \hat{x} e_{bj}$$

$$(B-8) \quad \text{Region 5-6: } \bar{e}_{bj} = \hat{y} \sin\left(\frac{j\pi}{T}(x+y_4) - \frac{j\pi}{2}\right) = \hat{y} e_{bj}$$

where T is the total length of the slot ($T=2x_6+2y_4$). Due to symmetry, once the quantities x_4 , y_4 , x_6 , and b are specified the dimensions of the slot are completely determined.

We now have the \bar{e}_{bj} modes, the scalar e_{bj} modes, and the $\bar{\phi}_{pq}^r$ function expressed in the same coordinate system, and can proceed to evaluate the integral. We note that the $\bar{\phi}_{pq}^r$ function is constant

except for the ψ_{pq} term. Therefore we shall first evaluate the integral $\int_b e_{bj} \psi_{pq} ds$ over the 5 straight segments of the loaded slot. After these results are obtained, it will be quite simple to take the required dot and cross products, include the constant terms in Eqs. (B-1), (B-2), and obtain the final results.

Let us begin with the region of the slot between points P_3 and P_4 . We thus define

$$(B-9) \quad \text{TEM3} = \int_{-x_4}^{x_4} \int_{y_4-b/2}^{y_4+b/2} \sin\left(\frac{j\pi x}{T} - \frac{j\pi}{2}\right) \psi_{pq} dy dx$$

Substituting for ψ_{pq} , and noting again that $z=0$, we obtain

$$(B-10) \quad \text{TEM3} = \int_{-x_4}^{x_4} \sin\left(\frac{j\pi x}{T} - \frac{j\pi}{2}\right) [\cos(U_p x) - j \sin(U_p x)] dx \\ \int_{y_4-b/2}^{y_4+b/2} e^{-j V_{pq} y} dy$$

In order to make our bookkeeping a little easier, we shall at this point define the following computer subroutine calls in terms of the tabulated integrals [54] which they evaluate:

$$(B-11) \quad \text{SS}(A, \alpha, B, \beta, x_1, x_2) = \int_{x_1}^{x_2} \sin(Ax + \alpha) \sin(Bx + \beta) dx$$

$$(B-12) \quad \text{SC}(A, \alpha, B, \beta, x_1, x_2) = \int_{x_1}^{x_2} \sin(Ax + \alpha) \cos(Bx + \beta) dx$$

$$(B-13) \quad \text{CC}(A, \alpha, B, \beta, x_1, x_2) = \int_{x_1}^{x_2} \cos(Ax + \alpha) \cos(Bx + \beta) dx$$

If we now define and evaluate the integral

$$(B-14) \quad I7 = \int_{y_4-b/2}^{y_4+b/2} e^{-jV_{pq}y} dy = \begin{cases} \frac{2}{V_{pq}} \sin(V_{pq} \frac{b}{2}) e^{-jV_{pq}y_4} \\ b; & V_{pq} = 0 \end{cases}$$

then

$$(B-15) \quad TEM3 = [SC(\frac{j\pi}{T}, -\frac{j\pi}{2}, U_p, 0, -x_4, x_4) - jSS(\frac{j\pi}{T}, -\frac{j\pi}{2}, U_p, 0, -x_4, x_4)] \cdot I7$$

where all of the quantities to the right of the equal sign can be readily evaluated via the computer.

One might now anticipate that we can similarly deal with each of the remaining straight regions of the loaded slots separately, combine the results, and obtain the desired answer. This would be the case were it not for round off error. For an example of the difficulties which may arise, consider a certain Φ_{pq} mode which, because of the symmetry of the loaded slot, couples with a given \bar{e}_{bj} mode such that $\int_b \bar{e}_{bj} \cdot \Phi_{pq} \cdot \hat{z} ds$ is a real quantity. When evaluating this integral one might find in evaluating the contributions of the various straight segments that the integrations over region 2-3 and region 4-5 had non-zero imaginary parts. These two imaginary contributions would then cancel when added together. Due to round off error these two imaginary contributions would not cancel exactly when added on the computer, but instead the result would have a small imaginary part. It was found that this incorrect result could lead to incorrect answers when the resulting system of equations was solved.

In order to eliminate this source of error the contributions of segments of the slot which might cancel one another must be added in closed form rather than by the computer. Thus we now combine the portions of the $\int_b \bar{e}_{bj} \psi_{pq} ds$ integral taken over regions 1-2 and 5-6 as follows:

$$(B-16) \quad TEM15 = \int_{-x_6}^{-x_4} \int_{-b/2}^{b/2} \sin[\frac{j\pi x}{T} - \frac{j\pi y_4}{T} - \frac{j\pi}{2}] \psi_{pq} dy dx \\ + \int_{x_4}^{x_6} \int_{-b/2}^{b/2} \sin[\frac{j\pi x}{T} + \frac{j\pi y_4}{T} - \frac{j\pi}{2}] \psi_{pq} dy dx \quad .$$

After some simplification this integral can be written as

$$(B-17) \quad \text{TEM15} = \int_{-b/2}^{b/2} \cos(V_{pq}y) dy \cdot \int_{x_4}^{x_6} \sin\left[\frac{j\pi x}{T} + \frac{j\pi y_4}{T} - \frac{j\pi}{2}\right] \\ \{-\cos(j\pi)[\cos(U_p x) + j\sin(U_p x)] + \cos(U_p x - j\sin(U_p x))\} dx.$$

We now define and evaluate

$$(B-18) \quad I1 = \int_{-b/2}^{b/2} \cos(V_{pq}y) dy = \begin{cases} \frac{2}{V_{pq}} \sin\left(\frac{V_{pq}b}{2}\right), & V_{pq} \neq 0 \\ b, & V_{pq} = 0 \end{cases}$$

$$(B-19) \quad I2 = \text{SC}\left(\frac{j\pi}{T}, \frac{j\pi y_4}{T} - \frac{j\pi}{2}, U_p, 0, x_4, x_6\right)$$

$$(B-20) \quad I3 = \begin{cases} \text{SS}\left(\frac{j\pi}{T}, \frac{j\pi y_4}{T} - \frac{j\pi}{2}, U_p, 0, x_4, x_6\right) \\ 0, & U_p = 0. \end{cases}$$

Now combining B-17 through B-20 we obtain

$$(B-21) \quad \text{TEM15} = I1 \cdot \begin{cases} 2 I2 & ; \quad j=1,3,5,7,\dots \\ -2j I3; & j=2,4,6,8 \end{cases}.$$

In a similar manner we proceed to evaluate the portions of the $\int b e_{bj} \psi_{pq} ds$ integral taken over regions 2-3 and 4-5:

$$\begin{aligned}
 (B-22) \quad \text{TEM}_{42} = & - \int_{-x_4-b/2}^{-x_4+b/2} \int_0^{y_4} \sin\left[\frac{j\pi y}{T} - \frac{j\pi x_4}{T} - \frac{j\pi y_4}{T} - \frac{j\pi}{2}\right] \psi_{pq} \, dy \, dx \\
 & + \int_{x_4-b/2}^{x_4+b/2} \int_0^{y_4} \sin\left[-\frac{j\pi y}{T} + \frac{j\pi x_4}{T} + \frac{j\pi y_4}{T} - \frac{j\pi}{2}\right] \psi_{pq} \, dy \, dx
 \end{aligned}$$

where the negative sign in front of the first integral is due to the -x vector direction of the mode in region 2-3 as expressed in Eq. (B-5). After some simplification we can obtain

$$\begin{aligned}
 (B-23) \quad \text{TEM}_{42} = & - \int_0^{y_4} \sin\left(\frac{j\pi x}{T} - \frac{j\pi x_4}{T} - \frac{j\pi y_4}{T} - \frac{j\pi}{2}\right) [\cos(V_{pq}y) - j \sin(V_{pq}y)] \, dy \cdot \left\{ \cos(j\pi) \cdot \left[\int_{x_4-b/2}^{x_4+b/2} (\cos(U_p x) - j \sin(U_p x)) \, dx \right] + \right. \\
 & \left. \int_{x_4-b/2}^{x_4+b/2} (\cos(U_p x) + j \sin(U_p x)) \, dx \right\}.
 \end{aligned}$$

We now decompose Eq. (B-23) into the following expressions:

$$\begin{aligned}
 (B-24) \quad I_4 = & \text{SC}\left(\frac{j\pi}{T}, -\frac{j\pi x_4}{T} - \frac{j\pi y_4}{T} - \frac{j\pi}{2}, V_{pq}, 0, 0, y_4\right) \\
 & - j \text{SS}\left(\frac{j\pi}{T}, -\frac{j\pi x_4}{T} - \frac{j\pi y_4}{T} - \frac{j\pi}{2}, V_{pq}, 0, 0, y_4\right)
 \end{aligned}$$

$$(B-25) \quad I_5 = \int_{x_4-b/2}^{x_4+b/2} \cos(U_p x) \, dx = \begin{cases} \frac{2}{U_p} \cos(U_p x_4) \sin(U_p b/2), & U_p \neq 0 \\ b, & U_p = 0 \end{cases}$$

$$(B-26) \quad I_6 = \int_{x_4-b/2}^{x_4+b/2} \sin(U_p x) dx = \begin{cases} \frac{2}{U_p} \sin(U_p x_4) \sin(U_p b/2), & U_p \neq 0 \\ 0, & U_p = 0. \end{cases}$$

Combining Eqs. (B-23) to (B-26) we have

$$(B-27) \quad TEM_{42} = - I_4 \cdot \begin{cases} 2j I_6, & j=1,3,5,7 \\ 2 I_5, & j=2,4,6,8 \end{cases}$$

Finally, if we now combine the results of Eqs. (B-1) through (B-27) and take the required dot and cross products we obtain

$$(B-28) \quad \int_b \bar{e}_{bj} \times \bar{\phi}_{pq}^1 \cdot \hat{z} ds = \frac{1}{T_{pq}} \cdot \frac{1}{\sqrt{d_x d_y}} \cdot [-U_p (TEM_{15} + TEM_3) + V_{pq} \cdot TEM_{42}]$$

$$(B-29) \quad \int_b \bar{e}_{bj} \times \bar{\phi}_{pq}^2 \cdot \hat{z} ds = \frac{1}{T_{pq}} \cdot \frac{1}{\sqrt{d_x d_y}} [V_{pq} (TEM_{15} + TEM_3) + U_{pq} \cdot TEM_{42}]$$

for the single loaded slot modes. In a similar fashion the integral has been evaluated for the 3-legged and 4-legged symmetric loaded slots, and the results for all three slot types were programmed in Fortran. The resulting program is listed at the end of this appendix. Note that the rectangular slot mode integration for $g=0$ (see Eq. (3-69) can be obtained from the single loaded slot results if we let $Y_4=0$ and set $X_4=X_6$.

We will now give a brief description of the input and output variables of the computer program. Referring to line 1, the output is the complex variable EBPHI. The value of the computer function EBPHI and the calling parameters are most easily defined for the single loaded slot \bar{e}_{bj} modes as follows:

$$(B-30) \quad EBPHI(IP, IQ, IR, IF) = \int_b \bar{e}_b(IF) \times \bar{\phi}_{(IP(IQ))}^{(IR)} \cdot \hat{z} ds.$$

The remaining input variables, located in the COMMON blocks of lines 12 and 15-17, are defined as follows for the single loaded slot \bar{e}_{bj} modes:

TABLE B-1
COMMON INPUTS FOR SINGLE LOADED SLOT

Variable Name	Value or Description
IANTP	1
ICALC	1
DX, DY, ALPHA	dx, dy, α of Fig. 3-2
ADIM	T; total length of slot
BDIM	b; slot width
XX4, YY4, X6	x_4, y_4, x_6 of Fig. B-1
UPOD, VPQD, TPQD	U_p, V_{pq}, T_{pq}

Note that consistent length units must be used, e.g., if the slot dimensions, etc., are expressed in meters then U_p, V_{pq}, T_{pq} will have units (meters)⁻¹. The COMMON block variables of Function EBPHI which are not listed in Table B-1 are not used for the single loaded slot calculations.

Using the subroutines to evaluate $\int \bar{e}_{bj} x_{pq}^2 \cdot \hat{z} ds$ for the 3-legged or 4-legged symmetric slots requires only a few changes in the input variables. The \bar{e}_{bj} modes for these two slots are given by Eq. (3-76) as:

$$(3-76) \quad \bar{e}_{bj} = \begin{cases} \sin\left(\frac{2n\pi\ell}{S}\right) e^{\pm j\Gamma_n z} \bar{G}(\ell) & j=1,3,5; \quad n = \frac{j+1}{2} \\ \cos\left(\frac{2n\pi\ell}{S}\right) e^{\pm j\Gamma_n z} \bar{G}(\ell) & j=2,4,6,8; \quad n = \frac{j}{2} \end{cases}$$

Thus for these symmetric slots there are two modes, the sine and the cosine mode, for each value of n.

For the 4-legged symmetric slots not all of the modes will be excited when the incidence angles are in the cardinal planes. For the calculations of Chapter V only the sine modes were used for H-plane ($\phi=0^\circ$) incidence angles. For E-plane ($\phi=90^\circ$) the sine modes

were used for n odd and the cosine modes for n even. The EBPHI function is thus programmed as follows for the 4-legged slot modes:

- 1) The input variable IF corresponds to n in Eq. (3-76).
- 2) For H-plane incidence angles the integral will be evaluated for the $n=IF$ sine mode.
- 3) For E-plane incidence angles the integral will be evaluated for the $n=IF$ sine mode if IF is odd; for the $n=IF$ cosine mode if IF is even.

The remaining input variables are explained in the following table:

TABLE B-2
COMMON INPUTS FOR 4-LEGGED SLOTS

Variable Name	Value or Description
IANTP	4
IEH	1 for E-plane Incidence; 2 for H-plane Incidence
ICALC	1
DX, DY, ALPHA	d_x, d_y, α , of Fig. 3-2
ADIM	$4 \cdot c + 2 \cdot d$
BDIM	b , slot width
XX4	$d/2$
Y4	0.
X6	$d/2 + c$
UPQD, VPQD, TPQD	U_p, V_{pq}, T_{pq}

The b , c , and d dimensions are defined in Fig. 3-11. Again, those COMMON block variables not specified in Table B-2 are not used for the 4-legged modes

The input variable descriptions for the 3-legged slot integration are quite similar to those for the 4-legged case. The major difference is that for the 3-legged slots both the sine and cosine mode integration values may be required for a given value of n (Eq. (3-76)). Therefore the EBPHI subroutine is programmed to evaluate the desired integral with the 3-legged \bar{e}_{bj} modes as follows:

- 1) The input variable IF corresponds to n in Eq. (3-76).
- 2) The sine mode integration will be evaluated if the input variable ISC (line 12) is set = 1.
- 3) The cosine mode integration will be evaluated if $ISC = 2$.

The input variables for the 3-legged slot modes are given below:

TABLE B-3
COMMON INPUTS FOR 3-LEGGED SLOTS

Variable Name	Value or Description
IANTP	3
ICALC	1
ISC	1 for sine mode 2 for cosine mode
DX, DY, ALPHA	d_x, d_y, α ; Fig. 3-2
ADIM	$3 \cdot c + 1.5 \cdot d$
BDIM	b
XX4	c
YY4	d
UPQD, VPQD, TPQD	U_p, V_{pq}, T_{pq}

The b , c , and d dimensions are defined in Fig. 3-12 for the 3-legged slot modes.

The Fortran listing of the computer program follows.

Computer Listings

```

1      COMPLEX FUNCTION EBPHI(IP,IO,IK,IF)
2      FOR SINGLE LOADED SLOTS IANTP=1
3      FOR 3-LEGGED SLOTS IANTP=3
4      FOR 4-LEGGED SLOTS IANTP=4
5      COMPLEX FL4,IF5,FL2,IF12,FL3,IF11,FL1
6      COMPLEX IT10,TL1,TL23,IT11,IT14,TL45X,TL45Y,TL67X,TL67Y,
7      2TL89X,TL89Y,IT7,IT17,IT20
8      REAL IT1,IT2,IT3,IT4,IT5,IT6,IT8,IT9,IT12,IT13,IT15,IT16,
9      2IT18,IT19,IT21,IT22,IT23,IT24,IT25,IT26,IT27,IT28,IT29,
10     3IT30,IT31,IT32,IT33,IT34,IT35,IT36,IT37,IT38,IT39,IT40
11     REAL IF1,IF2,IF3,IF4,IF6,IF7,IF8,IF9,IF10
12     COMMON /FOUR/ IANTP,IEH,ICALC,ISC
13     REAL LAMBDA,I1,I2,I3,I5,I6,EROL(2),THKOL(2)
14     COMPLEX J
15     COMMON THETA,PHI,LAMBDA,EROL,DX,DY,ALPHA,THKOL,ADIM,
16     2PDIM,XX4,YY4,Y6
17     COMMON /MARKET/ UPQD,VPQD,TPQD
18     COMPLEX TEM15,TEM42,TEM3,I4,I7,SUM
19     REAL IC2,IC6,IC8
20     COMPLEX IC3,IC1,IC4,IC5,IC7,IC9
21     REAL I9
22     COMPLEX I8,INT14,INT5
23     F20=1.
24     CON=1.
25     PI=3.14159265
26     J=(0.,I.)
27     IF(IANTP.EQ.4) GO TO 22
28     IF(IANTP.EQ.3) GO TO 60
29     IF(ICALC.NE.1) GO TO 221
30     X4=XX4
31     Y4=YY4
32     IG=0
33     I1=BDIM
34     IF(ABS(VPQD).LT.1.0E-5) GO TO 1
35     I1=2.*SIN(VPQD*BDIM/2.)/VPQD
36     1   FPA=IF*PI/ADIM
37     FP2=IF*PI/2.
38     T2=SC(FPA,FPA*Y4-FP2,UPQD,0.,X4,X6)
39     T3=0.
40     IF(ABS(UPQD).LT.1.0E-5) GO TO 2
41     T3=SS(FPA,FPA*Y4-FP2,UPQD,0.,X4,X6)
42     2   TEM15=2.*I1*(I2*FLOAT(MOD(IF,2))-CON*J*I3*FLOAT(1-MOD(IF,2)))
43     I4=SC(FPA,-FPA*(X4+Y4)-FP2,VPQD,0.,0.,Y4)+J*0.
44     IF(ABS(VPQD).LT.1.0E-5) GO TO 3
45     T4=I4-CON*J*SS(FPA,-FPA*(X4+Y4)-FP2,VPQD,0.,0.,Y4)
46     3   T5=BDIM
47     I6=0.
48     IF(ABS(UPQD).LT.1.0E-5) GO TO 4
49     T5=2.*COS(UPQD*X4)*SIN(UPQD*PDIM/2.)/UPQD
50     I6=2.*SIN(UPQD*X4)*SIN(UPQD*PDIM/2.)/UPQD
51     4   TEM42=2.*I4*(CON*J*I6*FLOAT(MOD(IF,2))+I5*FLOAT(1-MOD(IF,2)))
52     I7=BDIM+J*0.
53     IF(ABS(VPQD).LT.1.0E-5) GO TO 10
54     I7=2.*SIN(VPQD*BDIM/2.)*CEXP(-CON*J*VPQD*Y4)/VPQD
55     10  SYSTEM=0.

```

```

56      IF (ABS(UPQD).LT.1.0E-5) GO TO 6
57      SSTEM=SS(FPA,-FP2,UPQD,0.,-X4,X4)
58  A      TEM3=I7*(SC(FPA,-FP2,UPQD,0.,-X4,X4)-J*CON*SSTEM)
59      TEM42=-TEM42
60  221    CONTINUE
61      IF (IR.(0.2) GO TO 7
62      SUM=-E20*UPQD*(TEM15+TEM3)+E20*VPQD*TEM42
63      GO TO A
64  7      SUM=E20*VPQD*(TEM15+TEM3)+E20*UPQD*TEM42
65  8      CONTINUE
66      FBPHI=SUM/(TPQD*SQRT(DY*DY))
67      GO TO 21
68  22      CONTINUE
69      IF (ICALC.NE.1) GO TO 51
70      X4=XX4
71      Y4=YY4
72      FPA=IF*PI/ALIM
73      C=X6-X4
74      D=2.*X4
75      Y1=X4
76      Y2=X6
77      FP2=IF*PI/2.
78      IF (IEH.EQ.2) GO TO 40
79      IF (MOD(IF,2).EQ.0) GO TO 41
80  40      CONTINUE
81      IF1=SC(FPA,-FP2,UPQD,0.,-X4,Y4)
82      IF2=0.
83      IF6=BDIM
84      YF6=0.
85      YF11=(0.,0.)
86      IF (ABS(SIN(UPQD*BDIM/2.)).LT.1.0E-5) GO TO 30
87      IF2=SS(FPA,-FP2,UPQD,0.,-X4,Y4)
88      YF8=2.*SIN(UPQD*X4)*SIN(UPQD*BDIM/2.)/UPQD
89      YF6=2.*COS(UPQD*X4)*SIN(UPQD*BDIM/2.)/UPQD
90  30      CONTINUE
91      IF3=2.*BDIM
92      YF4=2.*BDIM
93      YF7=SS(-FPA,FPA*(X6+X4),VPQD,0.,X4,X6)
94      YF9=SC(VPQD,0.,-FPA,FPA*(X4+X6),X4,X6)
95      YF10=SS(FPA,0.,VPQD,0.,0.,X4)
96      IF (ABS(SIN(VPQD*BDIM/2.)).LT.1.0E-5) GO TO 31
97      YF3=4.*COS(VPQD*Y2)*SIN(VPQD*BDIM/2.)/VPQD
98      YF4=4.*COS(VPQD*X4)*SIN(VPQD*BDIM/2.)/VPQD
99  31      CONTINUE
100     IF (MOD(IF,2).EQ.0) GO TO 32
101  C      IF IS ODD
102     YF5=-2.*CC(FPA,FPA*C,UPQD,0.,X4,X6)*SIN(FP2)+J*0.
103     IF (ABS(SIN(UPQD*BDIM/2.)).GT.1.0E-5) IF11=-4*J*SIN(UPQD*Y6)
104     2 *SIN(UPQD*BDIM/2.)/UPQD
105     YF12=YF8*YF9*SIN(FP2)+J*0.
106     GO TO 33
107  32      CONTINUE
108  C      IF IS EVEN
109     YF5=-2.*J*SS(FPA,FPA*C,UPQD,0.,X4,X6)*COS(FP2)
110     IF11=2.*BDIM+J*0.

```



```

111      IF (ABS(SIN(UPQD*RDIM/2.)).GT.1.0E-5) IF11=4.*COS(UPQD*X6)
112      2*SIN(UPQD*RDIM/2.)/UPQD+J*0.
113      IF12=-J*IF6*IF7*COS(FP2)
114 33      CONTINUE
115      FL1=2.*J*IF10*IF11
116      FL2=IF4*IF5
117      FL3=4.*IF12
118      FL4=IF3*(IF1-J*IF2)
119      GO TO 31
120 41      CONTINUE
121      IC2=0.
122      IC5=J*0.+2.*CC(UPQD,0.,FPA,-FPA*(X6+X4),X4,X6)*FLOAT(
123      21-MOD(IF,2))
124      IC7=-2.*B01M*FLOAT(MOD(IF,2))+J*0.
125      IC9=J*0.-2.*B01M*FLOAT(MOD(IF,2))
126      IF (ABS(UPQD).LT.1.0E-5) GO TO 44
127      IC2=SC(UPQD,0.,FPA,2.*FPA*X6,-X4,X4)
128      IC5=2.*FLOAT(1-MOD(IF,2))*CC(UPQD,0.,FPA,-FPA*(X6+X4),
129      2X4,X6)+2.*J*FLOAT(MOD(IF,2))*SC(UPQD,0.,FPA,-FPA*
130      3(X6+X4),X4,X6)
131      IC7=-4.*J*FLOAT(1-MOD(IF,2))*SIN(UPQD*X4)*SIN(UPQD
132      2*RDIM/2.)/UPQD -4.*FLOAT(MOD(IF,2))*COS(UPQD*X4)
133      3*SIN(UPQD*RDIM/2.)/UPQD
134      IC9=-4.*SIN(UPQD*RDIM/2.)*(FLOAT(MOD(IF,2))*COS(UPQD*X6)
135      2+FLOAT(1-MOD(IF,2))*SIN(UPQD*X6)*J)/UPQD
136 44      CONTINUE
137      IC3=J*0.
138      IC4=J*0.
139      IF (ABS(VPGD).LT.1.0E-5) GO TO 45
140      IC3=-4.*J*SIN(VPGD*X6)*SIN(VPGD*RDIM/2.)/VPGD
141      IC4=-4.*J*SIN(VPGD*X4)*SIN(VPGD*RDIM/2.)/VPGD
142 45      CONTINUE
143      IC1=CC(FPA,2.*FPA*X6,UPGD,0.,-X4,X4)
144      2-J*IC2
145      IC6=2.*CC(VPGD,0.,FPA,FPA*C,X4,X6)
146      IC8=CC(FPA,0.,VPGD,0.,-X4,X4)
147      FL4=IC1*IC3
148      FL2=IC6*IC5
149      FL3=IC6*IC7
150      FL1=IC8*IC9
151 51      CONTINUE
152      IF (IR.F0.2) GO TO 34
153      FBPHI=VPGD*(FL1+FL3)-UPGD*(FL2+FL4)
154      GO TO 35
155 34      FBPHI=UPGD*(FL1+FL3)+VPGD*(FL2+FL4)
156 35      CONTINUE
157 25      FBPHI=FBPHI/(TD01*SQRT(OX*OY))
158 21      CONTINUE
159      RETURN
160 40      CONTINUE
161      IF (ICALC.NE.1) GO TO 8(
162      FPA=IF*PI/ADIM
163      SQ3=SQRT(3.0)
164      O=YY4
165      C=XX4

```

```

166      A=3.*C+3.*D/2.
167      Y2=D/2.
168      X3=C/4.-D*SQ3/4.
169      X2=-C+X3
170      X5=C/2.+D*SQ3/2.+X3
171      Y5=C*SQ3/2.
172      Y4=C*SQ3/2.+D/2.
173      X4=X3+D/2.
174      X6=D*SQ3/2.+X3
175      P=Y4-SQ3*Y4
176      Q=X4+SQ3*Y4
177      R=FPA*(Y.+2.*C+2.*Y4)
178      S=FPA*(Y2+D-2.*X2)
179      V3=VPQD*SQ3
180      FPA2=2.*FPA
181      U3=UPQD*SQ3
182      ISC=1 FOR SINE TERMS; 2 FOR COSINE TERMS
183      IF (ISC.EQ.2) GO TO 70
184      IT1=SC(FPA,0.,VPQD,0.,-Y2,Y2)
185      IT2=0.
186      IT5=2.*BOIM
187      IT6=0.
188      IT9=4.*BOIM
189      IT10=0.*J
190      IT12=SC(FPA2+V3,VPQD*P+S,UPQD,0.,X3,X4)
191      2 +SC(FPA2-V3,-VPQD*P+S,UPQD,0.,X3,X4)
192      IT13=0.
193      IT15=0.
194      IT16=0.
195      IT24=2.*BOIM
196      IT25=SC(-FPA2+VPQD,R,U3,-Q*UPQD,Y5,Y4)
197      2 +SC(-FPA2-VPQD,R,U3,-Q*UPQD,Y5,Y4)
198      IT26=0.
199      IT27=0.
200      IT28=0.
201      IT33=SC(FPA2+V3,-(FPA2+V3)*X6,UPQD,0.,X6,X5)
202      2 +SC(FPA2-V3,-(FPA2-V3)*X6,UPQD,0.,X6,X5)
203      IT34=0.
204      IT35=0.
205      IT36=0.
206      IF (ABS(VPQD).LT.1.0E-5) GO TO 61
207      IT2=SS(FPA,0.,VPQD,0.,-Y2,Y2)
208      IT5=4.*COS(VPQD*Y2)*SIN(VPQD*BOIM/2.)/VPQD
209      IT9=4.*SIN(VPQD*BOIM)/VPQD
210      IT10=-J*IT9
211      IT15=CC(FPA2-V3,S-VPQD*P,UPQD,0.,X3,X4)
212      2 -CC(FPA2+V3,S+VPQD*P,UPQD,0.,X3,X4)
213      IT27=CC(-FPA2-VPQD,R,U3,-Q*UPQD,Y5,Y4)
214      2 -CC(-FPA2+VPQD,R,U3,-Q*UPQD,Y5,Y4)
215      IT35=CC(FPA2+V3,-(FPA2+V3)*X6,UPQD,0.,X6,X5)
216      2 -CC(FPA2-V3,-(FPA2-V3)*X6,UPQD,0.,X6,X5)
217      IF (ABS(UPQD).LT.1.0E-5) GO TO 61
218      IT16=SC(UPQD,0.,FPA2-V3,S-VPQD*P,X3,X4)
219      2 -SC(UPQD,0.,FPA2+V3,S+VPQD*P,X3,X4)
220      IT28=SC(U3,-Q*UPQD,-FPA2-VPQD,R,Y5,Y4)

```

```

221      2 -SC(U3,-Q*UPQD,-FPA2+VPQD,R,Y5,Y4)
222      IT36=SC(UPQD,0.,FPA2-V3,(-FPA2+V3)*X6,X6,X5)
223      2 -SC(UPQD,0.,FPA2+V3,-(FPA2+V3)*X6,X6,X5)
224  61  CONTINUE
225      TL1=-8*DIM*(IT1-J*IT2)
226      IF(ABS(UPQD).LT.1.0E-5) GO TO 62
227      TL1=-2.*CEXP(-J*UPQD*X2)*SIN(UPQD*8*DIM/2.)*(IT1-J*IT2)/UPQD
228      IT6=SS(FPA,FPA*(Y2-X2),UPQD,0.,X2,X3)
229      IT13=SS(FPA2+V3,VPQD*P+S,UPQD,0.,X3,X4)
230      2 +SS(FPA2-V3,-VPQD*P+S,UPQD,0.,X3,X4)
231      IT24=2.*SIN(UPQD*8*DIM)/UPQD
232      IT26=SS(-FPA2+VPQD,R,U3,-Q*UPQD,Y5,Y4)
233      2 +SS(-FPA2-VPQD,R,U3,-Q*UPQD,Y5,Y4)
234      IT34=SS(FPA2+V3,-(FPA2+V3)*X6,UPQD,0.,X6,X5)
235      2 +SS(FPA2-V3,-(FPA2+V3)*X6,UPQD,0.,X6,X5)
236  62  CONTINUE
237      TL23=IT5*(SC(FPA,FPA*(Y2-X2),UPQD,0.,X2,X3)-J*IT16)
238      IT11=(IT12-J*IT13)/2.
239      IT14=(IT15-J*IT16)/2.
240      TL45X=-IT10*IT14*SQ3/2.
241      TL45Y=IT9*IT11/2.
242      TL67X=-(J*IT27-IT28)*IT24/2.
243      TL67Y=IT24*SQ3*(IT25+J*IT26)/2.
244      TL89X=-0.5*CCS(IF*PI)*SQ3*IT10*(IT35-J*IT36)/2.
245      TL89Y=0.5*CCS(IF*PI)*0.5*IT9*(IT33-J*IT34)
246      GO TO 60
247  70  CONTINUE
248  C
249  C  COSINE MODES
250  C
251      IT3=CC(FPA,0.,VPQD,0.,-Y2,Y2)
252      IT4=0.
253      IT7=0.*J
254      IT8=0.
255      IT9=4.*8*DIM
256      IT10=0.*J
257      IT24=2.*8*DIM
258      IT18=0.
259      IT19=0.
260      IT21=CC(FPA2+V3,S+VPQD*P,UPQD,0.,X3,X4)
261      2 +CC(FPA2-V3,S-VPQD*P,UPQD,0.,X3,X4)
262      IT22=0.
263      IT29=CC(-FPA2+VPQD,R,U3,-Q*UPQD,Y5,Y4)
264      2 +CC(-FPA2-VPQD,R,U3,-Q*UPQD,Y5,Y4)
265      IT30=0.
266      IT31=0.
267      IT32=0.
268      IT37=0.
269      IT38=0.
270      IT39=CC(FPA2+V3,-(FPA2+V3)*X6,UPQD,0.,X6,X5)
271      2 +CC(FPA2-V3,-(FPA2+V3)*X6,UPQD,0.,X6,X5)
272      IT40=0.
273      IF(ABS(VPQD).LT.1.0E-5) GO TO 71
274      IT9=4.*SIN(VPQD*8*DIM)/VPQD
275      IT10=-J*IT9

```

```

276      IT4=SC(VPQD,0.,FPA,0.,-Y2,Y2)
277      IT7=-4.*J*SIN(VPQD*Y2)*SIN(VPQD*BDIM/2.)/VPQD
278      IT18=SC(V3+FPA2,VPQD*P+S,UPQD,0.,X3,X4)
279      2      +SC(V3-FPA2,VPQD*P-S,UPQD,0.,X3,X4)
280      IT31=SC(VPQD-FPA,R,U3,-Q*UPQD,Y5,Y4)
281      2      +SC(VPQD+FPA,-R,U3,-Q*UPQD,Y5,Y4)
282      IT37=SC(FPA2+V3,-(FPA2+V3)*X6,UPQD,0.,X6,X5)
283      2      -SC(FPA2-V3,(-FPA2+V3)*X6,UPQD,0.,X6,X5)
284      IF(ABS(UPQD).LT.1.0E-5) GO TO 71
285      IT19=SS(V3+FPA2,VPQD*P+S,UPQD,0.,X3,X4)
286      2      +SS(V3-FPA2,VPQD*P-S,UPQD,0.,X3,X4)
287      IT32=SS(VPQD-FPA,R,U3,-Q*UPQD,Y5,Y4)
288      2      +SS(VPQD+FPA,-R,U3,-Q*UPQD,Y5,Y4)
289      IT36=SS(FPA2+V3,-(FPA2+V3)*X6,UPQD,0.,X6,X5)
290      2      -SS(FPA2-V3,(-FPA2+V3)*X6,UPQD,0.,X6,X5)
291  71      CONTINUE
292      TL1=-BDIM*(IT3-J*IT4)
293      IF(ABS(UPQD).LT.1.0E-5) GO TO 72
294      TL1=-2.*CEXP(-J*UPQD*X2)*SIN(UPQD*BDIM/2.)*(IT3-J*IT4)/UPQD
295      IT8=SC(UPQD,0.,FPA,FPA*(Y2-X2),X2,X3)
296      IT22=SC(UPQD,0.,FPA2+V3,S+VPQD*P,X3,X4)
297      2      +SC(UPQD,0.,FPA2-V3,S-VPQD*P,X3,X4)
298      IT24=2.*SIN(UPQD*BDIM)/UPQD
299      IT30=SC(U3,-Q*UPQD,-FPA2+VPQD,R,Y5,Y4)
300      2      +SC(U3,-Q*UPQD,-FPA2-VPQD,R,Y5,Y4)
301      IT40=SC(UPQD,0.,FPA2+V3,-(FPA2+V3)*X6,X6,X5)
302      2      +SC(UPQD,0.,FPA2-V3,(-FPA2+V3)*X6,X6,X5)
303  72      CONTINUE
304      TL23=IT7*(CC(FPA,FPA*(Y2-X2),UPQD,0.,X2,X3)-J*IT8)
305      IT17=0.5*(IT18-J*IT19)
306      IT20=0.5*(IT21-J*IT22)
307      TL45X=-IT20*IT9*SQ3/2.
308      TL45Y=0.5*IT17*IT10
309      TL67X=IT24*0.5*(IT29+J*IT30)
310      TL67Y=-IT24*SQ3*0.5*(J*IT31-IT32)
311      TL89X=0.5*COS(IF*PI)*SQ3*0.5*IT9*(IT35-J*IT40)
312      TL89Y=-0.5*COS(IF*PI)*0.5*IT10*(IT37-J*IT38)
313  80      CONTINUE
314      IF(IR.EQ.2) GO TO 84
315      FBPHI=VPQD*(TL1+TL45X+TL67X+TL89X)-UPQD*(TL23+TL45Y+
316      2      TL67Y+TL89Y)
317      GO TO 85
318  84      CONTINUE
319      FBPHI=UPQD*(TL1+TL45X+TL67X+TL89X)
320      2      +VPQD*(TL23+TL45Y+TL67Y+TL89Y)
321  85      CONTINUE
322      FBPHI=FBPHI/(TPQD*SQRT(OX*OY))
323      RETURN
324      END
325
326  FUNCTION SS(A,ALPHA,B,BETA,X1,X2)
327      IF(ABS(A).GT.1.0E-10) GO TO 1
328      IF(ABS(B).GT.1.0E-10) GO TO 1
329      SS=SIN(ALPHA)*SIN(BETA)*(X2-X1)
330      RETURN

```

```

331 1    CONTINUE
332      DIV=ABS(A)+ABS(B)
333      IF (ABS((A-B)/DIV).GT.1.0E-4) GO TO 2
334      SS=-SIN(2.*A*X2+ALPHA+BETA)/(4.*A)+.5*X2*COS(ALPHA-BETA)
335      2 +SIN(2.*A*X1+ALPHA+BETA)/(4.*A)-.5*X1*COS(ALPHA-BETA)
336      RETURN
337 2    CONTINUE
338      IF (ABS((A+B)/DIV).GT.1.0E-4) GO TO 3
339      SS=-SIN(2.*A*X2+ALPHA-BETA)/(4.*A)+SIN(2.*A*X1+ALPHA-BETA)
340      2/(4.*A)+.5*(X2-X1)*COS(ALPHA+BETA)
341      SS=-SS
342      RETURN
343 3    CONTINUE
344      SS=-SIN((A+B)*Y2+ALPHA+BETA)/(2.*(A+B))+SIN((A-B)*X2+ALPHA
345      2 -BETA)/(2.*(A-B))+SIN((A+B)*X1+ALPHA+BETA)/(2.*(A+B))-SIN
346      3 ((A-B)*X1+ALPHA-BETA)/(2.*(A-B))
347      RETURN
348      END
349 C
350      FUNCTION SC(A,ALPHA,B,BETA,X1,X2)
351      IF (ABS(A).GT.1.0E-10) GO TO 1
352      IF (ABS(B).GT.1.0E-10) GO TO 1
353      SC=SIN(ALPHA)*COS(BETA)*(X2-Y1)
354      RETURN
355 1    CONTINUE
356      DIV=ABS(A)+ABS(B)
357      IF (ABS((A-B)/DIV).GT.1.0E-4) GO TO 2
358      SC=-COS(2.*A*X2+ALPHA+BETA)/(4.*A)+.5*X2*SIN(ALPHA-BETA)
359      2 +COS(2.*A*X1+ALPHA+BETA)/(4.*A)-.5*X1*SIN(ALPHA-BETA)
360      RETURN
361 2    CONTINUE
362      IF (ABS((A+B)/DIV).GT.1.0E-4) GO TO 3
363      SC=-COS(2.*A*X2+ALPHA-BETA)/(4.*A)+COS(2.*A*X1+ALPHA-BETA)
364      2/(4.*A)+.5*(X2-X1)*SIN(ALPHA+BETA)
365      RETURN
366 3    CONTINUE
367      SC=-COS((A+B)*Y2+ALPHA+BETA)/(2.*(A+B))-COS((A-B)*X2+ALPHA
368      2 -BETA)/(2.*(A-B))+COS((A+B)*X1+ALPHA+BETA)/(2.*(A+B))+COS
369      3 ((A-B)*X1+ALPHA-BETA)/(2.*(A-B))
370      RETURN
371      END
372 C
373      FUNCTION CC(A,ALPHA,B,BETA,X1,X2)
374      IF (ABS(A).GT.1.0E-10) GO TO 1
375      IF (ABS(B).GT.1.0E-10) GO TO 1
376      CC=COS(ALPHA)*COS(BETA)*(X2-Y1)
377      RETURN
378 1    CONTINUE
379      DIV=ABS(A)+ABS(B)
380      IF (ABS((A-B)/DIV).GT.1.0E-4) GO TO 2
381      CC=SIN(2.*A*X2+ALPHA+BETA)/(4.*A)+.5*X2*COS(ALPHA-BETA)
382      2 -SIN(2.*A*X1+ALPHA+BETA)/(4.*A)-.5*X1*COS(ALPHA-BETA)
383      RETURN
384 2    CONTINUE
385      IF (ABS((A+B)/DIV).GT.1.0E-4) GO TO 3

```

```

386      CC=SIN(2.*A*X2+ALPHA-BETA)/(4.*A)-SIN(2.*A*X1+ALPHA-BETA)
387      2/(4.*A)+.5*(X2-X1)*COS(ALPHA+BETA)
388      RETURN
389 3      CONTINUE
390      CC=SIN((A+B)*X2+ALPHA+BETA)/(2.*(A+B))+SIN((A-B)*X2+ALPHA
391      2 -BETA)/(2.*(A-B))-SIN((A+B)*X1+ALPHA+BETA)/(2.*(A+B))-SIN
392      3 ((A-B)*X1+ALPHA-BETA)/(2.*(A-B))
393      RETURN
394      FEND$

```

BIBLIOGRAPHY

1. Pelton, E.L. and B.A. Munk, "A Streamlined Metallic Radome," IEEE Transactions on Antennas and Propagation, Vol. AP-22, pp. 799-804, November 1974.
2. Pelton, E.L., "A Streamlined Metallic Radome with High Transmission Performance," Report 2989-11, March 1973, The Ohio State University ElectroScience Laboratory, Department of Electrical Engineering; prepared under Contract F33615-70-C-1439 for Air Force Avionics Laboratory, Wright-Patterson Air Force Base, Ohio. (AFAL-TR-73-100) (AD 909360L)
3. Munk, B.A., R.G. Kouyoumjian, and L. Peters, Jr., "Reflection Properties of Periodic Surfaces of Loaded Dipoles," IEEE Transactions on Antennas and Propagation, Vol. AP-19, pp. 612-617, September 1971.
4. Munk, B.A. and R.J. Luebbers, "Transmission Properties of Dielectric Coated Slot Arrays," Report 2989-8, February 1973, The Ohio State University ElectroScience Laboratory, Department of Electrical Engineering; prepared under Contract F33615-70-C-1439 for Air Force Avionics Laboratory, Wright-Patterson Air Force Base, Ohio. (AFAL-TR-73-26) (AD 907628L)
5. Munk, B.A., R.D. Fulton, and R.J. Luebbers, "Plane Wave Expansion for Arrays of Dipoles or Slots in Presence of Dielectric Slabs," Report 3622-6, The Ohio State University ElectroScience Laboratory, Department of Electrical Engineering; prepared under Contract F33615-73-C-1173 for Department of the Air Force, Wright-Patterson Air Force Base, Ohio. (In preparation).
6. Bathker, D.A., S.A. Brunstein, and A.C. Ludwig, "Dual Frequency Microwave Reflex Feed," U.S. Patent Application Ser. No. 290,022, filed September 18, 1972.
7. Ryan, C.E., Jr., "Experimental Study of the Ohio State University Tuned Reflector," Report 2148-1, February 1966, The Ohio State University ElectroScience Laboratory, Department of Electrical Engineering; prepared under Contract AF33(615)-3461 for Air Force Avionics Laboratory, Wright-Patterson Air Force Base, Ohio. (AD 371062)
8. Booker, H.G., "Slot Aerials and Their Relation to Complementary Wire Aerials (Babinet's Principle)," IEEE, Vol. III-A, pp. 620-626, 1946.

9. Robinson, L.A., "Electrical Properties of Metal-Loaded Radomes," Wright Air Development Division Technical Report No. 60-84 on Contract AF33(615)-5539, Project No. 4161, February 1960.
10. Oh, L.L. and C.P. Lunden, "A Slotted Metal Radome Cap for Rain, Hail, and Lightning Protection," Microwave Journal, Vol. 2, No. 3, pp. 105-108, March 1968.
11. Rope, E.L., T.E. Fiscus, and G. Tricoles, "Perforated Metallic Shells for Radome Applications," Report R-70-032-F, July 1971, Electro Dynamic Division of General Dynamics; prepared under Contract H00019-70-C-0290 for Naval Air Systems Command, Department of the Navy, Washington, D.C.
12. DiCaudo, V.J., et.al., "Antenna Camouflage Study," Goodyear Aerospace Corporation Report No. GER-15734, October 1972. Air Force Avionics Laboratory, Wright-Patterson Air Force Base, Ohio. (AFAL-TR-72-375)
13. Oliver, T.L., "Design Curves for Mono-Planar Arrays of Short Loaded Flat Dipoles," Report 2382-19, April 1970, The Ohio State University ElectroScience Laboratory, Department of Electrical Engineering; prepared under Contract F33615-67-C-1507 for Air Force Avionics Laboratory, Wright-Patterson Air Force Base, Ohio. (AD 508445) (AFAL-TR-70-36)
14. Woo, R.T. and A.C. Ludwig, "Low Loss Dichroic Plate," U.S. Patent #3,769,623.
15. Munk, B.A. "The Backscattering From a Tuned Resonant Surface Made of an Array of Short Loaded Dipoles," Report 2148-6, March 1967, The Ohio State University ElectroScience Laboratory, Department of Electrical Engineering; prepared under Contract AF 33615-3461 for Air Force Avionics Laboratory, Wright-Patterson Air Force Base, Ohio. (AD 808571)
16. Pelton, E.L., "Scattering Properties of Periodic Arrays Consisting of Resonant Multi-Mode Elements," Report 3622-3, March 1975, The Ohio State University ElectroScience Laboratory, Department of Electrical Engineering; prepared under Contract F33615-73-C-1173 for Air Force Avionics Laboratory, Wright-Patterson Air Force Base, Ohio. (In preparation)
17. Munk, B.A., R.J. Luebbers and C.A. Mentzer, "Breakdown of Periodic Surfaces at Microwave Frequencies," Report 2989-1, June 1971, The Ohio State University ElectroScience Laboratory, Department of Electrical Engineering; prepared under Contract F33615-70-C-1439 for Air Force Avionics Laboratory, Wright-Patterson Air Force Base, Ohio. (AD 516254) (AFAL-TR-71-116)

18. Munk, B.A. and R.J. Luebbers, "Reflection Properties of Two Layer Dipole Arrays," IEEE Trans. on Antennas and Propagation, Vol. AP-22, pp. 766-773, November 1974.
19. Munk, B.A., R.J. Luebbers, and R.D. Fulton, "Transmission Properties of Bi-Planar Loaded Slot Arrays," Report 2989-10, March 1973, The Ohio State University ElectroScience Laboratory, Department of Electrical Engineering; prepared under Contract F33615-70-C-1439 for Air Force Avionics Laboratory, Wright-Patterson Air Force Base, Ohio. (AD 909359L) (AFAL-TR-73-103)
20. Munk, B.A., R.J. Luebbers, and R.D. Fulton, "Transmission Through a Two Layer Array of Loaded Slots," IEEE Trans. on Antennas and Propagation, Vol. AP-22, pp. 804-809, November 1974.
21. Luebbers, R.J. and B.A. Munk, "Reflection From N-layer Dipole Array," Report 2989-12, July 1973, The Ohio State University ElectroScience Laboratory, Department of Electrical Engineering; prepared under Contract F33615-70-C-1439 for Air Force Avionics Laboratory, Wright-Patterson Air Force Base, Ohio. (AD 912113L) (AFAL-TR-73-256)
22. Mentzer, C.A. and B.A. Munk, "Resonant Metallic Radome," Report 2382-21, June 1970, The Ohio State University ElectroScience Laboratory, Department of Electrical Engineering; prepared under Contract F33615-67-C-1507 for Air Force Avionics Laboratory, Wright-Patterson Air Force Base, Ohio. (AD 509525) (AFAL-TR-70-86)
23. Kiebertz, R.B. and A. Ishimaru, "Scattering by a Periodically Apertured Conducting Screen," IRE Trans. on Antennas and Propagation, Vol. AP-9, pp. 506-514, November 1961.
24. Ott, R.H., R.G. Kouyoumjian, and L. Peters, Jr., "Scattering by a Two-dimensional Periodic Array of Narrow Plates," Radio Science, Vol. 2 (New Series), No. 11, November 1967.
25. Munk, B.A., "Periodic Surfaces for Large Scan Angles," U. S. Patent #3,789,404.
26. Chen, C.C., "Transmission Through a Conducting Screen Perforated Periodically with Apertures," IEEE Trans. on Microwave Theory and Techniques, Vol. MTT-18, pp. 627-632, September 1970.
27. Chen, C.C., "Scattering by a Two-dimensional Periodic Array of Conducting Plates," IEEE Trans. on Antennas and Propagation, Vol. AP-18, pp. 660-665, September 1970.
28. Amitay, N. and V. Galindo, "The Analysis of Circular Waveguide Phased Arrays," Bell System Technical Journal, Vol. 47, pp. 1903-1932, November 1968.

29. Montgomery, J.P., "Scattering by an Infinite Periodic Array of Thin Conductors on a Dielectric Sheet," IEEE Trans. on Antennas and Propagation, Vol. AP-23, pp. 70-75, January 1975.
30. Chen, C.C., "Diffraction of Electromagnetic Waves by a Conducting Screen Perforated Periodically with Circular Holes," IEEE Trans. on Microwave Theory and Techniques, Vol. MTT-19, pp. 475-481, May 1971.
31. Luebbers, R.J. and B.A. Munk, "Cross Polarization Losses in Periodic Arrays of Loaded Slots," IEEE Trans. on Antennas and Propagation, Vol. AP-23, pp. 159-164, March 1975.
32. Munk, B.A., "Reflection Properties of Mono- and Bi-Planar Double Loaded Periodic Surfaces," Report 2382-10, October 1968, The Ohio State University ElectroScience Laboratory, Department of Electrical Engineering; prepared under Contract F33615-67-C-1507 for Air Force Avionics Laboratory, Wright-Patterson Air Force Base, Ohio. (AD 394983) (AFAL-TR-68-257)
33. Chen, C.C., "Transmission of Microwaves Through Perforated Flat Plates of Finite Thickness," IEEE Trans. on Microwave Theory and Techniques, Vol. MTT-21, pp. 1-6, January 1973.
34. Luebbers, R.J. and B.A. Munk, "Analysis of Thick Rectangular Waveguide Windows with Finite Conductivity," IEEE Trans. on Microwave Theory and Techniques, Vol. MTT-21, pp. 461-468, July 1973.
35. Luebbers, R.J. and B.A. Munk, "Rectangular Arrays of Resonant Slots in Thick Metallic Panels with Finite Conductivity," Report 2989-4, August 1972, The Ohio State University ElectroScience Laboratory, Department of Electrical Engineering; prepared under Contract F33615-70-C-1439 for Air Force Avionics Laboratory, Wright-Patterson Air Force Base, Ohio. (AD 902936L) (AFAL-TR-72-237)
36. Lewin, L., Advanced Theory of Waveguides, Iliffe and Sons, p. 96, 1951.
37. Marcuvitz, N., Waveguide Handbook, McGraw-Hill, pp. 248-257, 404-408, 1951.
38. Wexler, A., "Solution of Waveguide Discontinuities by Modal Analysis," IEEE Trans. on Microwave Theory and Techniques, Vol. MTT-15, No. 9, pp. 508-517, September 1967.
39. Lewin, L., Advanced Theory of Waveguides, Iliffe and Sons, p. 21, 1951.

40. Lee, S.W., W.R. Jones, and J.J. Campbell, "Convergence of Numerical Solutions of Iris-Type Discontinuity Problems," IEEE Trans. on Microwave Theory and Techniques, Vol. MTT-19, No. 6, pp. 528-536, June 1971.
41. Harrington, R.F., Time-Harmonic Electromagnetic Fields, McGraw-Hill, p. 73, 1961.
42. Collin, R.E., Field Theory of Guided Waves, McGraw-Hill, p. 193, 1960.
43. Marcuvitz, N., Waveguide Handbook, McGraw-Hill, p. 21, 1951.
44. Harrington, R.F., Time-Harmonic Electromagnetic Fields, McGraw-Hill, pp. 148-155, 1961.
45. Johnson, C.C., Field and Wave Electrodynamics, McGraw-Hill, p. 142, 1965.
46. Mittra, Raj, T. Itoh, and T. Li, "Analytical and Numerical Studies of the Relative Convergence Phenomenon Arising in the Solution of an Integral Equation by the Moment Method," IEEE Trans. on Microwave Theory and Techniques, Vol. MTT-20, pp. 96-104, 1972.
47. Wood, R.W., "Anomalous Diffraction Gratings," Physical Review, Vol. 48, pp. 928-936, December 1925.
48. Munk, B.A., private communication.
49. Harrington, R.F., Time-Harmonic Electromagnetic Fields, McGraw-Hill, pp. 163-169, 1961.
50. Farrel, G.F. and D.H. Kuhn, "Mutual Coupling in Infinite Planar Arrays of Rectangular Waveguide Horns," IEEE Trans. on Antennas and Propagation, Vol. AP-16, pp. 405-414, July 1968.
51. Stark, Louis, "Microwave Theory of Phased-Array Antennas - A Review," IEEE Trans. on Antennas and Propagation, Vol. 62, pp. 1661-1701, December 1974.
52. Woo, R., "A Low-loss Circularly Polarized Dichroic Plate," 1971 G-AP International Symposium Program and Digest, pp. 149-152.
53. Pelton, E.L., private communication.
54. Bois, G. Petit, Tables of Indefinite Integrals, Dover Publications, Inc., pp. 119-125, 134, 1961.